CUSTOM-MADE, TITANIUM ALLOY HIP JOINT PROSTHESES: A COMBINED MATHEMATICAL MODELLING, FATIGUE STRENGTH AND MICROSTRUCTURE STUDY

BY

MAREK GORYWODA, Dipl.-Ing.

Doctoral Thesis
Submitted in partial fulfilment of the requirements
for the award of
Doctor of Philosophy
of
Loughborough University of Technology

September 1990

Supervisors: Dr. R. G. Faulkner, Dr. T. Chung,
Institute of Polymer Technology and Materials Engineering, and
Mr. J. Ascough,
Department of Mechanical Engineering
Industrial supervisors: Dr. D. Lupton and Dr. A. Weipert
W. C. Heraeus GmbH, Hanau, W. Germany

ABSTRACT

Three mathematical models were developed in order to calculate stresses which occur in custom-made HERAMED prostheses during mechanical testing according to DIN 58840. Two of the models performed a three-dimensional stress analysis by using either the boundary element method or the finite element method. The third model was called the simple model and relied on a mixture of the simple bending theory, the beam-on-elastic-foundation theory and the finite element method. Results from the mathematical models were compared with results from three-dimensional photoelasticity by stress freezing. The use of three-dimensional scattered-light photoelasticity was also evaluated. On the basis of the theoretical and experimental results, it was found that stresses in the prostheses can satisfactorily be calculated with the simple model. The simple model was also much less expensive in terms of computer resources than both the boundary and finite element methods.

The high-cycle fatigue strength of the material of the prostheses: Ti-5Al5-2.5Fe, was investigated in three point bending tests in conditions, which approximated that of the human body. The material was perfectly notch sensitive in respect to mild notches. The fatigue strength can be improved by appropriate heat treatment and surface finish. Two different microstructures of the material were investigated using light microscopy, X-ray diffraction and transmission electron microscopy. They were described in detail. Dislocation structures introduced by the fatigue process into the material were also investigated. The majority of dislocations had a screw character and their Burgers vector was equal to $[11\bar{2}0]$. A simple explanation of the high-cycle fatigue strength was proposed on the basis of dislocation pile-up theory.

The application of the simple model together with the results obtained from the fatigue tests of the material enables the fatigue performance of the prostheses to be predicted and points out the possibilities of its improvement.

ACKNOWLEDGEMENTS

The author would like to thank the following:-

W. C. Heraeus GmbH for sponsoring the project.

Dr. D. Lupton for his continuous support and encouragement throughout the project.

Dr. A. Weipert for his supervision and introduction into the subject of HERAMED prostheses.

Dr. R. Faulkner for his supervision and critical discussion of the work.

Mr. J. Ascough for his supervision, patience and for always having time for discussion.

Dr. T. Chung for his supervision and interesting discussions on fatigue of metals.

Mr. J. Bates for his help in electron microscopy.

Mr. D. Britton for his help during photoelastic experiments and in the workshop.

All the technical staff of the Department of Mechanical Engineering and the Institute of Polymer Technology and Materials Engineering for their technical help.

My parents for their understanding.

All my friends and especially Vicky for her having time to correct my English.

CONTENTS

Page No.

VOLUME 1

VOLUME 2

1. INTRODUCTION

It is estimated that 250,000 total hip joint replacement operations are being performed in Western Europe and the United States every year [1, 2, 4]. In the majority of these operations, a prosthetic stem is fixed in the thigh bone (femur) of a patient by means of a bone cement, polymethylmethacrylate (PMMA). In the years following the hip replacement about 10 percent of the patients will need a revision operation because of a malfunction of the initial implant [1]. The bone cement is often blamed for this high rate of failure. The main problem of the cemented total hip arthroplasty is the so-called loosening of the implant due to an aseptic separation at the bone-cement interface [2, 6]. A loosened prosthesis is painful for a patient and can break out of the femur, or even fracture in extreme cases [3]. A revision of a cemented implant is difficult and it often leads to damage to the bone substance of the femur [2, 5]. The failure rate of a reoperation is estimated to be as high as 30 percent [1, 5].

It is well accepted in the literature that the failure rate of cemented total hip replacements increases with the time in service. The relationship is exponential, i.e. more and more failures are recorded with time [2]. This fact is very unsatisfactory in cases where young patients need a hip joint replacement. If one assumes an average life of a prosthesis being say, fifteen years, it becomes clear that with a life expectancy of more than seventy years a twenty year old patient will need at least two revision operations. This situation combined with the poor results of the revision total hip arthroplasties has stimulated considerable activity among surgeons to develop cementless artificial hip joint prostheses.

One of the new designs in the field of cementless hip joint prostheses is the subject of this work. The HERAMED® CAT cementless, prosthetic hip stem was developed by Priv.-Doz. G. Aldinger[1] in close collaboration

---

[1] Priv.-Doz. G.M.D. Aldinger, Orthopädische Universitätsklinik und Poliklinik Tübingen, Tübingen, West Germany

with W. C. Heraeus GmbH[2]. The prosthesis is a custom-made one, which in this case means that the shape of the prosthesis is determined by the shape of the marrow cavity of a patient's femur. The prosthesis is designed on the basis of a series of pictures obtained with X-ray computer tomography and manufactured by means of computer aided technology (CAT). The design process is carried out semi-automatically on a computer. A qualified and experienced person initiates and oversees each step of the design. The final product of the design process is a set of digital data which is then passed on to a computer-controlled machine where the prostheses are manufactured. Each prosthesis has a unique and rather complicated shape. Not until the manufacturing of a prosthesis is completed, can the entire shape of the prosthesis be visualized. It sometimes appears that the finished prosthesis is thin and this leads to fears that such a prosthesis could break soon after it has been implanted into a patient. In cases when such a prosthesis is encountered, a second, dummy prosthesis is manufactured which is destined for mechanical fatigue testing under simulated working conditions of a severely loosened prosthesis [7]. If the dummy prosthesis breaks during the mechanical testing, there are several ways of changing the design in order to reduce stresses.

A redesigned prosthesis is then once more subjected to the mechanical fatigue testing. The redesign procedure can be repeated several times until a satisfactory product is achieved. Only if the dummy prosthesis withstands the fatigue testing, is the prosthesis given the 'go ahead' for implantation [8].

The assurance that a prosthesis would not break after implantation is very important from the point of view of the manufacturer. A broken prosthesis can easily injure the patient. If the failure of the prosthesis can be related to a mistake in the design or in the manufacturing, the manufacturer could be made liable for any damage caused by the

---

[2]W. C. Heraeus GmbH, Produktbereich Material-Technik, Hanau, West Germany

failure [9, 10]. All the manufactured prostheses must therefore be designed and manufactured under state-of-the-art quality assurance controls.

A second important point for the manufacturer of the prostheses is the cost of production. If prostheses had to be continuously fatigue tested and redesigned, the price (of the prostheses) would have to be very high. The combined situation of product liability and the production costs has led, on the side of the manufacturer, to the desire to be able to estimate the fatigue performance of a prosthesis in advance of the manufacturing process.

The task of developing a method for predicting the fatigue performance of the HERAMED custom-made prostheses was the object of this work. The objective was to develop a mathematical model of the prostheses in the form of a computer programme which could be included as a new step in the design process. The computer program should perform a numerical stress analysis of the design of a prosthesis. The results of the analysis would then be compared with the appropriate fatigue data of the material from which the prostheses are manufactured. The comparison would then enable a decision to be made regarding whether or not the particular design is safe enough to be manufactured.

Closely related to the object of the work, was an investigation of the material of the prostheses. The HERAMED prostheses are manufactured in a recently-developed titanium alloy, Ti-5Al-2.5Fe. In particular, high cycle fatigue data for this alloy, in the form which is required for the application of the computer programme for predicting the fatigue performance of the prostheses, is not available from previous investigations.

2. MODELLING OF PROSTHESES

2.1. Introduction

With the introduction of new designs, materials and testing methods, a (fatigue) fracture of common prosthetic stems is regarded as a problem which could be dealt with without any particular difficulties. Provided that the prostheses have been properly manufactured, a fracture can only occur in case of severe loosening of the stem. It is the responsibility of the surgeons to ensure that loosened prostheses are removed before a dangerous situation can develop. The HERAMED prostheses differ from the standard ones in that their design is determined by the geometry of the hip joint and the shape of the femoral canal of each individual patient. In this sense, each HERAMED prosthesis is unique.

The recently-proposed mechanical testing method for prostheses was developed with serially manufactured prostheses of the same design in view. The HERAMED prostheses are tested according to the same method despite the fact that each prosthesis has a different shape. A method of comparing the results of different tests is therefore needed. The method will enable an evaluation of the results from mechanical testing and provide a feed-back into the prosthesis design process. It can also be used for an a priori estimation of the fatigue performance of the prosthesis.

An obvious choice for such a method is to develop a computer-based, mathematical model which simulates the conditions of the mechanical tests. In developing such a model, several options were investigated. The use of the Boundary Element Method and the Finite Element Method was evaluated with commercially available software. A simple model based on the Simple Bending Theory was written 'in house'. Experimentally, the mechanical tests were simulated with the help of three-dimensional photoelasticity. The use of three-dimensional scattered light photoelasticity was also investigated. The experimental and theoretical results have been compared and discussed.

2.2. LITERATURE REVIEW

2.2.1. The HERAMED Prosthesis

As has already been mentioned in Chapter 1, the HERAMED prosthetic stems were developed by Priv.-Doz. G. Aldinger in collaboration with W. C. Heraeus GmbH. Aldinger had initially investigated the possibility of designing standardized, cementless prostheses. He advocated the opinion that the omission of cement demands high conformity of the implant to the femoral cavity, since, without cement, only bone was capable of stabilizing the stem. With X-ray computer tomography, he measured 50 healthy hip joints and tried to estimate how many types of prostheses would be needed in order to reconstruct the hip joints. He found that 4000 different prostheses would be necessary if the prostheses were manufactured with tolerances of 5 mm for the position of the head of the prostheses and 4 mm for their diameter in the femur shaft. He concluded that if anatomical and/or therapeutical aspects of hip joint replacements were taken into consideration, only prostheses manufactured individually for each patient would be satisfactory [3].

The HERAMED prostheses were developed with the view of satisfying the demand for cementless prostheses. This development focused on a design which would reflect the state-of-art knowledge on cementless prosthetic systems [2, 3, 11]. The HERAMED-CAT prostheses (Fig. 1) are manufactured for each patient individually to closely fit into the bony cavity. Computer Aided Technology (CAT) enables a precise design, production and control of the manufacturing of the prostheses. The femur, including the cavity, the curvatures, the neck shaft angle, and the angle of femoral torsion[3] (the antetorsion) of the coxal femoral end, is reconstructed three-dimensionally on the basis of a series of computer tomographic section images. The position of the joint head determines the biomechanics of the joint. The HERAMED prostheses make it possible for the surgeon to freely select the position of the head, the antetorsion and neck length as required by anatomical or therapeutical considera-

[3] See Figure 2 for explanation of some of the medical terms.

tions. The conformity of the stem ensures a stable long-lasting fixation and that the load is uniformly introduced into the bearing bone. The fixation and the load transfer are enhanced by the stepped, tapered shape of the prostheses. The steps enlarge the fixation area and promote the transfer of favourable pressure forces. Harmful shear and radial forces are reduced. The taper enables the "self-press-fit" fixation. The taper also ensures that if required, the prostheses can be removed without further harm to the bone.

The feasibility of implantation is assured by a computer simulation. The highest possible resection level of the femur is determined in order to preserve as much of the bone substance as possible. The broach, the tool for preparing the femoral cavity, is shaped according to the corresponding stem, and is manufactured in parallel with the stem.

A schematic flow chart of the activities connected with the design, manufacture and implantation of HERAMED prostheses is shown in Figure 3. The area concerned with this work is outlined in the chart.

More than 200 HERAMED prosthesis have been implanted up to date. The results of clinical monitoring of the operations are good. No complications connected with the prostheses such as fracture of the femoral shaft or shaft perforation have been reported [8, 12]. In their short history, the HERAMED prostheses have had some very encouraging results. Some surgeons see the HERAMED prostheses as the last resource of providing a total hip replacement for patients with thin or unorthodox shaped femora. These patients were refused an operation because no standard cemented prostheses could be found to satisfy preoperative requirements. Using the HERAMED technology, however, some of the patients were successfully supplied with prostheses. In one case, a woman had both hips operated on, and was able to walk without severe pain for the first time in her life[4].

[4]Private communication

2.2.2 Mechanical Testing of HERAMED Prostheses

The major problem in the cemented prosthetic systems is the loosening of the stem. The loosening usually starts at the proximal end and progresses towards the distal end of the implant. In areas where there is no contact between the implant and the bone, the load is carried entirely by the prosthetic stem. The stems are subjected to severe overstressing under conditions of cyclic bending and torsion. The cement often cracks exposing the material of the prostheses to the corrosive body fluids. The stability of the fixation is severely affected by the loosening. Patients experience considerable pain so that eventually, a loosened prosthesis has to be removed.

It is good practice to remove a loosened stem as soon as possible. Firstly, the patients are spared the pain and secondly, a possible fracture of the overstressed stem is avoided. It is generally accepted that it is much more difficult to remove a loosened femoral prosthesis with a fatigue-fractured stem than a loosened implant with an intact stem. There could, however, be several months before a re-operation takes place. Thus, the prostheses have to be designed in such a way that they are able to withstand several million cycles of fatigue loading in a loosened condition.

In order to prevent stem breakage in the event of loosening of the femoral stem, elaborate criteria for fracture-proof prosthesis stems have been proposed [13]. The German DIN Standardization Group adopted the International Organisation for Standardization Draft Proposal (ISO/DP 7206/3) 'Implants for surgery - Partial and total hip joint prostheses - Part 3: Method for determination of the endurance properties of stemmed femoral components without application of torque', and issued its own corresponding standard proposal, DIN 58 840 'Hip joint prostheses; method for determination of the endurance properties of metallic stemmed femoral components' [14]. The major concept behind the proposals is that the endurance properties of hip joint prostheses should be determined in fatigue tests simulating conditions of a severe

loosening. According to the DIN proposal[5], a prosthesis is embedded prior to testing in a specimen holder by means of bone cement in such a way that 50 mm of the upper part of the stem remains uncemented (Fig. 4). This absence of the cement simulates the loosened condition. The embedding angle, i.e. the angle between the axis of the prosthesis and the vertical (the loading axis) is 10°. The embedding angle represents the so-called neutral position of the prosthesis in the femur. The prosthesis is loaded by a pulsating load at a frequency between 1 and 10 Hz. The loading acts in such a way that the prosthesis remains under load during the whole duration of the testing procedure. The minimum load is at least 300 N, whereas the maximum load is suggested to be at least three times the average body weight, i.e. about 2.3 kN. The load is applied through the centre of the head of the prosthesis, parallel to the to the vertical direction by means of a low-friction loading mechanism that minimizes loads not parallel to the loading axis. During the testing, the embedded prosthesis is submerged in an aerated, physiological fluid medium, Ringer's solution (see Chapter 3.3.2), which is kept at 37±1°C and which has a pH value between 7.0 and 7.4. The test is conducted under these conditions until a fracture of the prosthesis occurs or until a specified number (usually several million) cycles is completed.

It is pointed out that the above described method was designed for cemented prosthetic stems. There is no generally approved method for mechanical testing of cementless prostheses. Although the HERAMED prostheses are cementless, the manufacturer decided however to test the prostheses according to DIN 58 840. This decision was taken after a careful consideration of the concept of the HERAMED prostheses. This concept states that by modelling the exact contour of the femoral cavity, the load transfer takes place already in the proximal part of the bone, the calcar. Therefore, the proximal part of the prostheses carries the load, whereas the distal part has the mere function of stabilizing the stem. Although long term result are not yet available,

---

[5]The related BSI Draft Proposal DD 91:1986 differs in some aspects from the ISO approach [15].

preliminary findings show that the bone indeed responds positively to the HERAMED prostheses: it remodels and adapts itself to the steps of the prostheses in the calcar [12]. However, if the bone resorbs from the prosthesis in the proximal region, the distal end will have to carry the entire load. At this stage, the patient would feel increasingly greater pain. The prosthesis is ready for revision.

The scenario described here for the HERAMED prostheses is very similar to the case of loosened cemented prostheses, so that the application of DIN 58 840 for the determination of the endurance properties of the prostheses is justified. However, the important condition that the load transfer takes place primarily in the calcar region, has to be yet confirmed by long term medical trials. In the meantime, the HERAMED prostheses are tested according to the DIN proposal. The starting maximum load is 3.1 kN and the frequency of fatigue cycling is 10 Hz. If the prostheses sustain $3*10^6$ cycles, the load is raised to 4.6 kN and the testing continues for next 10^6 cycles. In the last stage of the testing, the load is increased to 6.2 kN and the test carried out for the final 10^6 cycles. If the prostheses survive this very tough testing procedure without failure, they are allowed to be implanted. Initially every manufactured prosthesis was subjected to the testing. With growing experience and confidence, the number of tests could be reduced to about 10 percent of the total number of prostheses [8].

2.2.3. Experimental and Mathematical Modelling of Prostheses

The continuous, large demand for total hip joint replacements has led to considerable efforts aimed at a better understanding of the complex problems associated with them. These efforts which combine researchers from the fields of medicine, engineering and material science are already bearing fruit in designing better, longer-lasting and safer prostheses. Many investigations concentrated on the problem of bio-mechanical interaction between implant and bone.

In the first instance, the forces which act on the femur have to be calculated. On the basis of movement studies and simple mechanistic models it is estimated that during walking, the femur is exposed to static and

dynamic forces which can reach between three and four times the body weight [16, p. 76]. It is pointed out that similar values are suggested for the minimum force in the fatigue testing of prostheses. There are research programs under way which will eventually enable a telemetric, in-vivo monitoring of forces acting on an implanted prosthesis. The prostheses are equipped with miniature, encapsulated measuring devices which send signals related to their stress levels [17].

The mechanical properties of the bone substance have been investigated [18]. It is found that the bone consists roughly of two types of bone substance. The cancellous bone which is present inside the femur is spongious and therefore mechanically very weak. The cancellous bone is regarded as not suited for transfering any loads and is therefore removed from the femoral cavity before the implantation of a prosthesis. In contrast, the cortical bone is compact and capable of carrying major loads. The mechanical properties of the cortical bone are anisotropic. This means, for example, that the tensile strength and the elasticity modulus changes with different directions. The density of the cortical bone which is closely correlated with the mechanical properties also varies from place to place [16, p. 299]

The stress distribution in loaded femora has been modelled experimentally with photoelasticity [16] and numerically with finite elements [19]. Measurements of the stress distribution were carried out by instrumenting the femora with strain gauges [19, 20]. The bone is a living structure and there is a strong indication that the spatial distribution of the density of the bone is related to the stress distribution [16]. Mathematical models investigating this finding predict a density distribution similar to the one found in real bones [21].

Investigations show that the stress distribution of an intact femur is significantly altered by inserting a prosthesis [19, 20, 22]. The bone can react to the new situation by adopting its shape or density to the changed stress distribution. This process is called the adaptive bone remodelling. Losses of bone substance are sometimes observed in the calcar region. This is explained by the so-called 'stress shielding' of the bone by the prosthesis. The stress shielding occurs when a load, normally carried by the bone alone, is shared with the implant. As a re-

sult, the bone stresses are subnormal and the bone loses mass [23]. The opposite situation can occur at the distal tip of the prostheses. If the stresses there are, for some reason, too high, the bone can increase the cortical diameter by building up its mass.

One obvious method of ensuring that the stress distribution after implantation will change as little as possible is to make sure that the geometry of the hip joint is accurately reconstructed by the operation. The direction of loads in this case will change little giving less stimulus for the bone to remodel.

The stress-shielding effect is only one of several, essentially mechanical problems encountered in total hip replacements. These problems include plastic deformation and (fatigue) fracture of prostheses, breakdown of the cement, loosening at the boundaries between different material (interfaces) and stress-related bone resorption. All the problems are interdependent and thus, they can be regarded as one problem of artificial hip joint design and fixation.

Models show that the flexural rigidity of the prosthetic stem plays an important role. A stiff stem tends to carry a larger proportion of the load along its length than a less stiff one [24]. The bone is therefore stress shielded to a larger extent in the case of a stiff stem. The rigidity of a stem depends on its cross sectional area and the elasticity modulus of the material of the stem. The value of the cross sectional areas can be adjusted only in certain limits set by stability and strength requirements. Prostheses made of a strong material with elasticity modulus closer to the elasticity modulus of the bone are therefore desirable. Many prostheses are currently manufactured of high quality stainless steels with the modulus of elasticity nearly 15 to 30 times greater than that of the bone. However, the stainless steels are being gradually replaced by recently developed titanium alloys. Apart from similar strength, the titanium alloys have only half the modulus of elasticity, better biocompatibility, and, better corrosion resistance than stainless steels [26]. There are numerous efforts to develop new prosthetic materials with even better properties than titanium alloys [22, 26].

The length of a prosthetic stem also influences the stress distribution. Surgically, an implantation of a short prosthesis is much easier than of a long one. A sharp increase of stresses was measured when a extremely short stem (40 mm) had been implanted into a cadaver femur [25]. The stresses were much lower for a stem with length of 100 mm. There was little change in stresses, however, when the length of the stem was further increased. These results can be understood with the help of the results presented in [27]. On the basis of a simple, beam-on-elastic-foundation model it was shown that in general, the load transfer from the prosthesis to the bone takes place in three different regions along the implant. In the first transition region at the proximal end, the stresses in the stem decrease sharply. They have constant value[6] in the middle region where no load is transferred, and finally, drop to zero in the second transition region at the distal end. In the case of a 'long' stem, the transition regions are not significantly changed; only the middle region is extended. In the case of a 'short' stem, the load is transferred linearly from the stem to bone, and the stem behaves rigidly relative to the bone. Ideally, a prosthetic stem should therefore be long enough to enable the two transition regions to be present with little or no middle region.

It is pointed out that in practice, the ideal length of a (standardized) stem is very difficult or nearly impossible to calculate. The type of stem, whether long or short, depends sensitively on the rigidities of the stem, bone and cement, and of the properties of the interfaces between them, e.g. continuous or loose. The rigidities depend on the geometry, the modulus of elasticity and the interface conditions of the components. They vary therefore from patient to patient.

Many cemented hip stems have some kind of collar near the neck. The collar is designed in order to transmit the axial components of load into the resected neck of the femur. The collar is a logical answer to

---

[6] In the case of constant cross sections and loading by a pure bending moment.

the demand of loading the femur directly, the stem plays only a stabilizing role in this case, and therefore avoids the stress shielding effect. Mathematical models indicate that theoretically, the idea of a collar is correct. Loads are indeed transmitted directly from the collar to the femur, and stresses in the stem and the cement are reduced. Medical experience, however, shows that the bone often resorbs around collared stems. In practice, it is often difficult to assure a uniform contact between the resection area of the femur and and the collar which is essential for the desired load transfer mechanism [28].

The cement has received much attention in the modelling of hip joint prostheses. Interestingly, mathematical models predict that stresses in the cement increase with increasing flexibility of the stem. It appears, however, that in any case of a well-performed hip joint replacement, the cement would not fail under a typical loading. The results indicate that a poor operational technique is often to be blamed for a failure of the hip replacements. This is confirmed by clinical experience [31].

Cementless prosthetic stems rely on a different mechanism of fixation than the cemented ones. It is believed that the long-term performance of the cementless stems is greatly influenced by the amount of micromovements between the bone and the implant. Medical trials show that excessive micromovements can lead to a development of a mechanically worthless, soft fibrous tissue at the bone/implant interface. The fibrous tissue obviously builds up as a reaction of the bone to accommodate the mismatch of the relative bone/implant movements[7] [32]. In order to reduce the amount of micromovements, the cementless prostheses rely on the so-called 'press-fit' fixation or/and on porous surface coating enabling the fixation by an ingrowth of bone tissue. A mathematical model of porous and smooth interface conditions has been investigated [33]. The model showed that the main difference between the two surface conditions was the site and the amount of load transmission from

[7] This situation is also valid in the case of loosened cemented prostheses [33]

the stem to the bone. The micromovements were chiefly influenced by the rigidity of the stem. Intriguingly, flexible stems showed much larger relative movements than stiff stems. It was concluded that in view of the relative movements between a prosthesis and the bone, flexible stem designs are disadvantageous.

It can be seen from this literature review that the problems connected with the hip joint replacements are very complex. These problems have been investigated experimentally by means of mechanical testing, photoelasticity and strain gauging. In addition to the experiments, mathematical calculations, ranging from simple mechanistic to complex three-dimensional finite element models, have been developed. In particular, the finite element models have found wide application in calculating stress-related problems of artificial hip joint fixation [20]. It is pointed out that however complex the models, they can only give an approximate, idealized picture of the problems. There are pronounced difficulties in correctly modelling the geometry, the material properties and the interface conditions. As these factors change with every patient, the models have to be regarded as very useful and powerful tools for developing and verifying ideas and concepts. The ultimate test can only be provided by clinical experience.

2.3. MATHEMATICAL MODELS

2.3.1. Input Data

At the end of the design process of the HERAMED prosthesis, which is carried out with the help of a computer, a set of digital data is created which is the basis for the manufacturing of the prostheses on a computer numerically controlled (cnc) milling machine. A part of this set describes the geometry of the prosthesis, and was therefore required as the input data for the mathematical model.

The design process is performed on a Hewlett Packard (HP) computer with the help of a computer program written in the HP BASIC programming language. The program writes the final set of data in a format which can only be read by the cnc-machine. In order to provide the geometrical data of the prosthesis for this work, the computer program, therefore, had to be extended. A subroutine was included in the program in such a way that on request, it became possible to output the geometrical data of the prosthesis in the form of a file written in the ASCII[8] format. This file could then be transferred on to a VAX computer, and recorded on a magnetic tape. It was possible to read this tape on a PRIME computer at the Loughborough University Computer Centre.

The file which was stored on the magnetic tape consisted of a series of records. Each record had the length of 80 ASCII symbols. The contents of each record were as follows:

1st record: designation of the prosthesis; four characters,
2nd record: not used in the mathematical model; integer number,
3rd record: not used in the mathematical model; integer number,
4th record: not used in the mathematical model; integer number,
5th record: the number of the basis-scan; integer number,
6th record: the last 8mm step; integer number
7th record: total number of steps; integer number,

[8] American Standard Code for Information Interchange

8th record: number of points per step; integer number,
9th record: neck angle; integer number,
10th record: not used in mathematical model; integer number,
11th record: not used in mathematical model; integer number,
12th record: not used in mathematical model; integer number,
13th record: x-coordinate of the first point of the first step; real number,
14th record: y-coordinate of the first point of the first step; real number,
15th record: z-coordinate of the first point of the first step; real number,

.
.
. N records containing the (x,y,z)-coordinates of the
. points describing the contours of the steps;
. real numbers;
. N=(number of points per step)*(number of steps),
.
.

(N+1) record: y-coordinate of the centre point of the head of the prosthesis; real number,
(N+2) record: x-coordinate of the centre point of the head of the prosthesis; real number,
(N+3) record: z-coordinate of the centre point of the head of the prosthesis; real number.

The meaning of the contents of each record is explained with the help of Figures 5 and 6. Figure 5 shows a schematic drawing of a prosthesis. It can be seen that there are two values of the step height. Starting from the distal end, the steps are 8 mm apart and after the last 8 mm step, the step height changes to 4 mm. Very important information is provided by the number of the so-called basis-scan (or basis-step). This number defines the last step, the contour of which is manufactured to the contour of the bone. Above this step, the shapes of the contours are affected by the manufacture of the neck of the prosthesis. The basis-step is therefore the step from which the 50 mm are measured in order to define the embedding level for the DIN-tests (see Chapter 2.2.2). The shapes of

the contours of each step are defined by series of (x,y,z)-coordinates of points lying along the contours. The point coordinates are given in respect to a Cartesian coordinate system, as shown in Figure 5. The number of points per contour is constant for each each step. Figure 6 shows a schematic drawing of how the points are arranged along the contours. The points are defined in such a way that the angles between the vectors, from the centre point to two adjacent points on the contour, are equal. It should be noted that the coordinates of the last point describing each contour are the same as these of the first point.

The data which is contained in the records 2-4 and 10-12 is not used in the mathematical model. These records give information on how the position of the z-axis of the coordinate system has been defined, and on the shape of the neck of the prosthesis respectively.

The last three records contain the coordinates of the centre point of the head of the prosthesis (see Figure 5). These records define therefore the coordinates of the point to which the loading force is attached during the DIN-tests.

It has to be mentioned that in a healthy femur, there is an offset between the position of the axis of the neck and the axis of the bone (see Figure 7). Because of the fact that the HERAMED prosthesis reconstructs the coxal femur, there also is an offset between the neck and the axis[9] of the prosthesis. This offset is given indirectly in the data file, by the way in which all the point coordinates are defined. The position of the Cartesian coordinate system is chosen in such a way that the neck axis is parallel to the x-axis of the coordinate system. The y-coordinate of the centre point of the head gives, therefore, the value of the offset (see Figure 7).

---

[9] Because of the complex shape, the axis of a prosthesis is not to be understood as an axis of symmetry. The axis of the prosthesis is defined as that passing through the centroids of two cross sections of the bone (records 3 and 4 in the geometry file).

One important item of information is not included in the data file. This is the value of the transition radius in the steps, which is introduced during the manufacturing of the prostheses. This value is important for two reasons. Firstly, the smaller the radius, the better is the conformity of the prosthesis with the bony cavity. Secondly, the smaller the radius, the higher are the stress increases (stress concentration factors) due to changes in in the geometry of the prosthetic stems.

In current designs of the prosthesis, the transition radii are not standardized. They can have values ranging from 1 mm to 2 mm, but once chosen, the value of the transition radius remains constant for each prosthesis.

An example of the input data for one of the prostheses investigated is shown in Appendix 1. The format of the data in Appendix 1, however, is different from that described above. This was done in order to save space. The average size of the files written in the format which was described in this chapter is approximately 70 kB[10], and, if such a file was printed, the text would require approximately 6,100 lines. A graphical example of the complex shapes of the contours is shown in Figure 8.

2.3.2. Finite Element Model

2.3.2.1. Concept of the Finite Element Method

The Finite Element Method (FEM) is probably the most popular numerical method for solving differential equations which represent problems encountered in engineering practice. In this chapter, a very brief description of this method is provided in order to provide a basis for understanding the ideas and terms used in the following chapters. The

[10] The unit for describing the sizes of files on a computer is called the Byte. One Byte (1 B) is necessary in order to describe one ASCII character. 1 kB is equal to 1000 B.

following sections are not original, as they rely heavily on the literature, in particular on [35]. A detailed description of the Finite Element Method is given in the literature, e.g. in [36, 37].

Basic definitions

Assume that a differential equation which describes a physical problem, is represented by an operator L such that:

$$L(u)=b \quad \text{in } \Omega. \tag{1}$$

The operator L is defined as a process which when applied to the function u produces an another function b. Ω represents the spatial domain, usually represented by coordinates x_i (i=1,2,3).

The homogeneous version of (1) is:

$$L(u)=\emptyset \quad \text{in } \Omega. \tag{2}$$

An inner product of two functions can be defined as:

$$\int_{\Omega} L(u)w\,d\Omega = \emptyset.$$

Such products are some times represented by a bracket expression $\langle L(u),w\rangle$. The inner product can be integrated by parts until all derivatives in u have been eliminated. This leads to the 'transposed' form of the inner product and, as a result of integrating by parts, produces a series of boundary terms. In general, it can be written:

$$\int_{\Omega} L(u)w\,d\Omega=\int_{\Omega} uL^*(w)\,d\Omega+\int_{\Gamma} [S^*(w)G(u)-G^*(w)S(u)]\,d\Gamma. \tag{4}$$

Γ is the exterior surface of the domain Ω and S and G are differential operators arising from the integration by parts. By definition, $S^*(w)$ contains the w terms resulting from the initial phase of integration, and S(u) contains the corresponding u terms.

The operator L^* is called the adjoint of L. If $L^*=L$, L is said to be self-adjoint. In this case also $G=G^*$ and $S=S^*$. Self-adjointness of an operator is analogous to symmetry of a matrix. In addition to determining if the operator is self-adjoint, the integration by parts also generates two different types of boundary conditions. The set S(u) prescribed are called the essential boundary conditions and G(u) prescribed are the natural boundary conditions[11]. The essential boundary conditions must be enforced at some point of the surface Γ in order for the solution to be unique. Letting Γ_1 and Γ_2 represent complementary positions of the total surface Γ, one can state the boundary conditions for the self-adjoint problem as

$$\begin{aligned} &G(u) \text{ prescribed on } \Gamma_2, \\ &S(u) \text{ prescribed on } \Gamma_1, \\ &\Gamma=\Gamma_1+\Gamma_2. \end{aligned} \tag{5}$$

A self adjoint operator is positive definite if

$$\int_{\Omega} L(u)u\,d\Omega \geq 0 \tag{6}$$

---

[11] If the order of the differential operator is 2m, there can be a total of 2m boundary conditions. These 2m terms form m pairs of conjugated boundary terms. Under regular conditions of two such terms, one term is prescribed and the other is unknown. (Two boundary terms are conjugated if the sum of their indices is 2m-1.) The lower terms

$$\delta^0 u,\ \delta^1 u,\ \ldots,\ \delta^{m-1} u,$$

are the essential boundary conditions (displacements), and the higher terms

$$\delta^m u,\ \delta^{m+1} u,\ \ldots,\ \delta^{2m-1} u,$$

are the natural boundary conditions (forces).

for all u, and only equal to zero for the case $u \equiv 0$. Positive definiteness is an extremely valuable property in establishing solution schemes.

Approximate solution

Most engineering problems which are expressed in a differential form can only be solved in an approximate manner due to their complexity. In FEM, the infinite degrees of freedom of a continuous system are reduced to a finite set which can then be solved numerically (on a computer). This is done by dividing the domain and the boundary of the system in a series of regions called elements (the process is called discretization). These elements are considered to be interconnected at discrete points on their boundaries joints called nodes or nodal points, at which the values of the unknowns are to be approximated. The discrete version of the differential equation or its inner product version is satisfied in an average sense over the elements. To understand this, the following equations are considered:

$$L(u_o)=b \quad \text{in } \Omega \tag{7}$$

with boundary conditions

$$\begin{aligned} S(u_o)&=s \quad \text{on } \Gamma_1, \\ G(u_o)&=g \quad \text{on } \Gamma_2. \end{aligned} \tag{8}$$

u_o represents the exact solution of the problem which is usually impossible to find. The function u_o can be approximated by a set of functions $\phi_k(x)$ such that

$$u=\sum_{k=1}^{n} \alpha_k \phi_k + \alpha_o . \tag{9}$$

The α_o coefficient is included to satisfy the nonhomogeneous part of the boundary conditions. α_k are undetermined parameters and ϕ_k are linearly independent functions taken from a complete sequence of functions such as

$$\phi_1(x), \phi_2(x), \ldots, \phi_n(x); \tag{10}$$

x represents the spatial coordinates in the Ω domain.

These functions are usually chosen to satisfy certain given conditions, called admissibility conditions, relating to the boundary conditions and the degree of continuity.

A sequence of functions such as these in (10) is said to be linearly independent if

$$\alpha_1\phi_1+\alpha_2\phi_2+\ldots+\alpha_n\phi_n=\emptyset \qquad (11)$$

is true only when all α_k are zero.

A sequence of linearly independent functions is said to be complete if a number n of terms and a corresponding set of constants α_k can be found in a certain way. Given an admissible but otherwise arbitrary function u_o, this is achieved if the square root of the inner product of the difference between u_o and its approximation u can be made as small as one requires, i.e.:

$$\int\{(u_o-u)^2dx\}^{1/2}\leq\beta,$$

where β is a small positive quantity.

Assuming that the approximate functions satisfy all the boundary conditions of the problem given by Equation (7), and have the necessary degree of continuity to make the left-hand side of Equation (7) different from zero (i.e., $L(u)\neq\emptyset$).

Substituting the approximation for u_o into Equation (7) produces a 'residual' or 'error' function R such that

$$R=L(u)-b\neq\emptyset. \qquad (12)$$

If the function u does not satisfy all boundary conditions one may have two types of error, or residual functions:

- error in the essential boundary conditions

$$R_1 = S(u) - s \neq \emptyset \qquad \text{on } \Gamma_1 ;$$

-error in the natural conditions

$$R_2 = G(u) - g \neq \emptyset \qquad \text{on } \Gamma_2 . \tag{13}$$

These errors can be forced to zero in certain average sense, and this can be done in different ways. This leads to the method of weighted residuals.

Weighted Residuals

In this method, a set of linearly independent functions θ_k such as

$$\theta_1(x), \theta_2(x), \ldots, \theta_m(x) \tag{14}$$

is defined. A set of arbitrary coefficients β_k is then defined which combined with the functions θ_k leads to the expression for a function w:

$$w = \beta_1 \theta_1 + \beta_2 \theta_2 + \ldots\ldots\ldots \tag{15}$$

If it is assumed that the approximate function u identically satisfies all the boundary conditions, the residual functions R_1 and R_2 are equal to zero. The residual R can now be distributed in Ω by multiplying it by the function w which is now called the weighting function, i.e.,

$$\langle R, w \rangle = \int_{\Omega} w R \, d\Omega = \emptyset . \tag{16}$$

This ensures that the error R is distributed according with the function in w. As the β_k coefficients are arbitrary, Equation (16) implies that

$$\int_{\Omega} R \theta_k \, d\Omega = \emptyset \qquad \text{for } k = 1, 2, \ldots m. \tag{17}$$

Several approximate techniques are in use, which apply different weighting functions. These methods are: the point collacation, sub-domain collocation, least squares, least squares collocation, variational methods and the Galerkin method. The majority of FEM applications use the last technique.

Galerkin Method

The Galerkin method is a particular weighted residual method for which the weighting functions belong to the same set as the approximating functions. Given the system

$$L(u_o)=b \quad \text{in } \Omega \tag{18}$$

with homogenous boundary conditions, an approximate function which satisfies theses conditions can be proposed such that

$$u_o \approx u=\sum_{k=1}^{n} \alpha_k \phi_k . \tag{19}$$

The approximation produces a residual

$$R=L(u)-b=\emptyset \tag{20}$$

which in Galerkin method is then orthogonalized with respect to the same functions ϕ_k used in the approximation, i.e.,

$$\int_{\Omega} R w d\Omega=\emptyset, \tag{21}$$

where

$$w=\beta_1 \phi_1+\beta_2 \phi_2+.... \tag{22}$$

For a linear operator L(), Equation (21) produces a linear system of algebraic equations from which the β_k coefficients can be calculated.

As the same functions are used for u and w and the β's are arbitrary it is common to write the w function as a variation of u, i.e.,

$$w=\delta u=\delta\alpha_1\phi_1+\delta\alpha_2\phi_2+\ldots, \tag{23}$$

where $\delta\alpha_k\equiv\beta_k$. These variations can be associated with virtual quantities such as virtual displacements or velocities.

The property of having the same functions for the weighting and approximating functions is important as it produces symmetrical coefficients in many cases.

Weak Formulation

The weighted residual method can be used for solving problems by approximate functions, identically satisfying the boundary conditions. This is called the strong formulation of the problem. The weighted residual method can also be used in such a way that the boundary conditions are approximately satisfied. This enables the use of approximate functions which have relaxed continuity requirements, and leads to the so-called weak formulation.

In practice, it is often encountered that different orders of continuity of functions u and w are required. The continuity of a function can be classified as follows. It is assumed that a function f is discontinuous as discrete points but finite throughout the region. If its norm satisfies the condition

$$\int f^2 dx < \infty, \tag{24}$$

the function f is said to be square integrable. The function f is said to be a first derivative square integrable if the the function and its first derivative satisfy the condition

$$\int\{f^2+(df/dx)^2\}dx < \infty. \tag{25}$$

This definition of continuity can be easily extended to higher derivatives.

The order of continuity becomes important in cases where the solution of a particular problem is sought by the method of reducing the order of derivatives of the function u by integrating by parts. The integration by parts introduces new differential operators which are prescribed on the boundary of the problem. One can now look for a solution which approximately satisfies the problem in the domain Ω and the natural boundary conditions.

In general, two residual, or error functions can be defined:

$$\begin{aligned} R &= L(u)-b \qquad \text{in } \Omega, \\ R_2 &= G(u)-g \qquad \text{on the } \Gamma_2 \text{ part of the boundary.} \end{aligned} \tag{26}$$

Both residuals can now be weighted by the function w,

$$\int_{\Omega} (L(u)-b)w\,d\Omega = \int_{\Gamma_2} (G(u)-g)w\,d\Gamma. \tag{27}$$

The operator L() in Equation (27) can be integrated by parts.

If the operator is self-adjoint, it will produce two equal operators of reduced order which can be called D(), i.e.,

$$\int_{\Omega} D(u)D(w)\,d\Omega + \int_{\Omega} bw\,d\Omega = \int_{\Gamma_2} gw\,d\Gamma. \tag{28}$$

The natural boundary conditions g, in Equation (28), have to be replaced by their known values q.

The weak formulation is often used in solving problems with the Finite Element Method.

A more explicit formulation of FEM

It is assumed that the function u represents a physical quantity,the field variable, which varies subject to a differential equation L(u)=b

in the domain Ω, and to boundary conditions $G(u)=q$ on the boundary Γ. The form taken by $L(u)$ and $G(u)$ is determined by the physical problem under investigation.

The solution for a continuum involves an infinite number of points and hence an infinite number of values of the variables. This number is reduced by dividing the domain Ω into numbers of finite elements. In FEM it is assumed that the values of u vary within an element according to a simple law. The values of u are defined only at special points called nodes, such as the variation of u within an element can be approximated by the equation:

$$u=\sum_{k=1}^{n} N_k u_k, \qquad (29)$$

where n is the number of nodes of the element, and u_k is the value of u at node k. The variables $N_1, N_2, \ldots, N_n$ are functions of x, y and z, and are called shape functions. The shape functions have the following property:

$$N_k=1 \quad \text{at node k,}$$
$$N_k=0 \quad \text{at all other nodes.} \qquad (30)$$

Equation (29) can be written in matrix notation as:

$$u=[N]\{u\}^e \qquad (31)$$

where $\{u\}^e$ is a vector containing all the nodal values of u for the element, and [N] is a row matrix of all shape functions, i.e.,

$$[N]=[N_1, N_2, \ldots, N_n],$$
$$\{u\}^e=[u_1, \ldots, u_n]^T,$$

for the case of one field variable u.

In general, there has to be continuity of the field variable u from element to element. This continuity is assured by choosing suitable elements and shape functions. In FEM, the shape functions are usually chosen as a polynomial, i.e,

$$N=a_0+a_1x+a_2x^2+\ldots. \tag{32}$$

for a one-dimensional case.

The weighted residual can be written as:

$$\int_\Omega (\{w\}L([N])\{u\})^e-\{w\}b)d\Omega=\{\emptyset\} \tag{33}$$

where

$\{\emptyset\}$ is a null vector,
$\{w\}$ is a vector of weighting functions.

Equation (33) can be expressed in matrix form:

$$[k]\{u\}^e-\{v\}=\{\emptyset\} \tag{34}$$

where

$$[k]=\int_\Omega \{w\}L([N])d\Omega,$$

$$\{v\}=\int_\Omega \{w\}bd\Omega. \tag{35}$$

In the Galerkin method, the weighting functions are chosen in such a way that $\{w\}=[N]^T$. Equation (33) can now be written as:

$$\int_\Omega [N]^TL([N])d\Omega\{u\}^e - \int_\Omega [N]^Tbd\Omega = \{\emptyset\} \tag{36}$$

The first term in Equation (36) is often integrated by parts in order to reduce the the order of derivatives in L(u). The integration by parts introduces contour integrals which can be dealt with in terms of known boundary conditions. The integration by parts leads also to the weak formulation of the problem, which means that the approximate solution will satisfy the initial differential equation and a part of the boundary conditions (natural boundary conditions) in an average sense.

Equation (34) gives a general form of the equations (matrices) describing one finite element. In practice, the domain Ω is divided into many finite elements. The (local) matrices for each element, therefore, have to be assembled in order to form a (global) matrix describing the whole domain. The assembly process is nothing else but a summation over the entire domain for all elements. The summation process leads to a matrix equation for the whole domain Ω

$$[k_\Omega]\{u\}^\Omega-\{v_\Omega\}=\{0\}. \tag{37}$$

At this stage, the coefficient matrix $[k_\Omega]$ is singular. It is made non-singular by inserting known (essential) boundary conditions. The system of simultaneous equations represented by Equation (37) can then be solved. In many engineering problems, such as e.g. linear stress analysis, the matrix $[k_\Omega]$ is symmetric and has the so-called 'banded' form. A matrix is said to be symmetric if the coefficients satisfy the relation:

$$k_{ij}= k_{ji}, \tag{38}$$

where

$i,j=1,2,....,m$
m=number of rows and columns in the matrix.

A matrix is said to be banded if all coefficients which are different from zero, are grouped along the diagonal of the matrix.

Powerful methods have been developed in order to solve systems of equations which are represented by symmetric and banded matrices on the computer.

Procedure in FEM

In the preceding sections, a introduction into the concept of the finite element method has been presented. From this introduction, it can be re-

cognized that in order to solve a problem by FEM, the following steps are carried out:

1. The spatial domain of the problem is divided into suitable elements.
2. Element matrices are constructed for each element.
3. The element matrixes are assembled into a global matrix.
4. Constrains for boundary conditions are inserted.
5. The system of equations is solved for all nodal values of the field variable u.
6. Post-processing, such as graphical representation of the solution is carried out.

2.3.2.2. FEM-model of Prosthesis

In Chapter 2.2.3, it was shown that the finite element method had been successfully applied for modelling problems associated with artificial hip joint prostheses. The finite element method was therefore an obvious choice of the method for modelling the HERAMED prostheses. It was decided that the FE-analysis should be conducted with the help of a commercially-available finite element system. A good reason for this decision was that it could be expected that a commercial finite element program, with a good record in the literature, would provide reliable results of the analysis. Such a system was provided at Loughborough University in the form of PAFEC[12] (Program for Automatic Finite Element Calculations) and PIGS[12] (PAFEC Interactive Graphic Suite; pre- and post-processor for PAFEC). The use of the PAFEC package reduced the task of this work to the writing of a computer program which would provide the first step of the finite element analysis, i.e., it would define the nodes and the elements needed. Such a program is called, in the FEM-language, the mesh generator. Because of the complex, three-dimensional shape of the prosthesis, it was decided that only a three-dimensional FE-analysis would lead to the desired results. It was also decided that

---

[12] Pafec Ltd., Nottingham, England

the FE-analysis would be conducted as a linear elastic analysis, due to the fact that the loading of the prosthesis in the the DIN-test does not lead to any plastic deformation of the prostheses.

The whole procedure which was envisaged for analysing the stresses in a prosthesis subjected to the DIN-test with FEM can now be described as consisting of the following steps:

1. Design process: File containing the geometrical data of the prosthesis.
2. Mesh generator: File containing the geometrical input data for FE-analysis with PAFEC.
3. PAFEC: File containing the results of the analysis.
4. PIGS: Graphical representation of the results.
5. Design process: Evaluation of the results.

The complex shape of the prosthesis made it necessary to develop two mesh generators. The first program, called PROEM, generates geometrical data for FE-analysis in the case of embedded prosthesis with a 'smooth' shape. The term smooth means that the shape of the prosthesis is simplified by omitting the steps. The second program, called COSCF, generates data which enables the estimation of the stress concentration factors along the contour of one chosen step. Both the programs are written in the FORTRAN 77 programming language. Listings of these programs are given in Appendix 2. The mesh generators produce input files which are destined for the FE-analysis with PAFEC. These files are therefore written in a format which is specific for PAFEC, and cannot be directly used with other FE-packages. However, the principal idea behind the mesh generation is common for the majority of the FE-packages, so that the programs which have been developed in this work, can easily be changed in order to suit these packages. The format of the input files, and the expressions which have to be included in these files in order to conduct the FE-analysis with PAFEC, are given in the PAFEC reference manuals [38, 39].

As has been previously mentioned, the program PROEM generates a mesh for the case of embedded prosthesis with smooth shape. This is done in the following way (see Appendix 2):

In the first step, the main program calls the subroutine READAT. This subroutine reads the input file which contains the geometrical data of the prosthesis. In the second step, the subroutine SECT is called. This subroutine calculates a 'centre' point and redefines the coordinates of the points for each section (each contour). The effect of the subroutine SECT is illustrated in Figures 9 and 10.

The convergence, and thus the accuracy of the results of a FE-analysis over a domain, depends on the number of elements and on the way in which the elements are defined. The accuracy is increased by increasing the number of elements, but attention must be paid to fact that the elements should be evenly distributed over the domain, and that the shapes of the elements should not be too distorted. In Figure 9, a schematic drawing of a contour is shown. The z-axis intersects the plane of the contour in the point O. The points which describe the contour are defined in such a way so that all the angles between the vectors from the point O to two adjacent points on the contour are equal (see Chapter 2.3.1). If the point O lies near the contour, the points are unevenly distributed along the contour. The points near to O are denser, and the points far from O are leaner distributed (see Figure 9). The subroutine SECT attempts to change this distribution of points along the contour so as to be more even. Firstly, SECT calculates a new centre point of the contour which is on average equally distant from the edges of the contour. This is done using the formula:

$$x_c = (x_i w_i) / (\sum_{i=1}^{n} x_i),$$

$$y_c = (y_i w_i) / (\sum_{i=1}^{n} y_i),$$

where

x_c, y_c - coordinates of the centre point,
n - number of points per contour,
x_i, y_i - coordinates of point i; $i=1,2,\ldots,n$,
w_i - weighting factor equal to the half of the distance between the point i and its two neighbours.

Secondly, SECT calculates new points of the contour around the centre point in such a way that the x-coordinate of the first point is equal to zero, and the y-coordinate of this point is positive. Starting from this point, new points which are apart by the same angle around the centre point are calculated. This is shown schematically in Figure 10.

In the next step of the main program, a file called PROEM.DAT is created. All the information needed for PAFEC will be written into this file. The file PROEM.DAT is therefore the input file for PAFEC. The file begins with the TITLE[13] for the PAFEC job. This is followed by the so-called CONTROL module. The CONTROL module states that PAFEC will conduct a linear elastic FE-analysis, at the end of which, STRESSes will be calculated. The analysis will be carried out invoking the PHASEs 1, 2, 4, 6, 7 and 9 of PAFEC. In PHASE 1, the input data are read. In PHASE 2, the so-called PAFBLOCKS are replaced by a full nodal coordinate and topological description of the complete mesh of elements. PAFBLOCKS is a facility in PAFEC which enables an automatic subdivision of an element into a series of elements of the same type according to a given set of parameters. These parameters define in how many (sub-) elements the element under consideration will be divided. If these parameters are all set to one, PAFBLOCKS are equivalent to ELEMENT definition which defines only one element. The PAFBLOCKS-facility enables a mesh refinement, and it is therefore used through the program PROEM. In PHASE 4 the constraints are considered and a numbering system for the degrees of freedom is derived. The stiffness matrices of all elements are found and assembled in a global matrix in PHASE 6. In PHASE 7, the system of equations is solved, which, in the case of stress analysis, means that the displacements in the nodes are calculated. From these displacements, stresses are calculated in PHASE 9.

The CONTROL module is followed by the definition of NODES. The nodes are defined by specifying the NODE.NUMBER and the X,Y,Z-coordinates. The nodes are found in subroutines DEFSTEM, DEFTOP and DEFEMBE. It has to be

---

[13] In the following description, the terms in capitals are PAFEC program terms unless otherwise stated.

born in mind that the definition of nodes has to be carried out in a way which is suitable for the definition of elements. Two types of elements are used in the analysis:

The twenty-noded, isoparametric brick element for three dimensional stress analysis (PAFEC TYPE 37110), is a generally shaped brick type element with six curvilinear faces and twelve edges. The nodes are positioned in the corners and in the centres of each of the edges (see Figure 11). Reasonable distortion (from the basic cubical shape) of the element is permitted, but PAFEC aborts the analysis if the element is too distorted[14]. The element has three translatory degrees of freedom (displacements in x,y and z-direction) at each node. Principal stresses are given at each of the nodes and also at the centre of the faces and at the centre of the element.

The fifteen-noded, triangular prism (wedge) element for three dimensional stress analysis (PAFEC TYPE 37210), is a generally shaped prism element with five curvilinear faces and nine edges. The nodes are positioned in the corners and in the centres of each of the edges (see Figure 12). Otherwise, the prism element is similar to the brick element described above.

DEFSTEM defines the nodes of the prosthesis up to the level of the basic-step. This is done in the following way:

---

[14] The element is too distorted if the radius of curvature of any of the edges is too small, or, if the angles between neighbouring faces are too small or too large, or, if the proportion of the element, given by the relation of the shortest to the longest edge, is too large. The geometrical validation of the input data is performed in PHASE 2.

In the first step, the nodes with the z-coordinate equal to zero are defined. In the input file which contains the geometry of the prosthesis, the points describing the contour of the first section have the z-coordinate equal to 8 mm (see Figure 5). It has to be noted that, strictly speaking, these points describe each contour with the z-coordinate between zero and 8 mm less the value of the transition radius. In this way, the points which are given in the input file for the second section, describe the contours with the z-coordinate between 8 and 16 mm less the value of the transition radius, and so on. In order to define nodes with z=0, the coordinates of the points of the first section of the prosthesis are therefore taken. Figure 13 shows a schematic drawing of the definition of nodes. The first node has the x,y-coordinates equal to the first point of the contour. The second node has the x,y-coordinate of the point of the contour, the number of which is determined form the number of elements into which the contour is being divided and the number of points per contour.

In the example shown in Figure 13, it can be seen that eight brick elements (along the boundary), and eight wedge elements (inside the contour) will be used. If the number of points per contour is seventeen (the coordinates of the last point and the first point are the same), the x,y-coordinates of the second node would be equal to that of the second point. If the number of points per contour is thirty three however, the coordinates of the second node would be equal to that of the third point.

Apart from the boundary, nodes have to be defined inside the contour. The coordinates of these nodes are calculated as the coordinates of the centres of the distances between the nodes on the boundary and the centre point of the contour (coordinates of which were calculated in SECT). The last node which is defined for the contour has the coordinates of the centre point.

In Figures 11 and 12, the topologies of the brick and the wedge elements are shown. These topologies are given by the shape of the elements, and by the local numbering schemes of the nodes. By comparing Figures 11 and 13, it can be seen that one face of the brick element defined (locally) by e.g. the nodes 1, 2, 3 and 4, can be made equivalent to the face de-

fined in Figure 13 by e.g. the nodes 1, 3, 17 and 19 respectively. From Figure 11, it can be seen that apart from the corner nodes, a face of the brick element is also defined by nodes on the midpoints of the edges, i.e. by nodes 9, 10, 11 and 12. Nodes 2 and 18 in Figure 13 can be set equivalent to nodes 9 and 12, but no nodes have been defined which could be set equivalent to the nodes 10 and 11 of the brick element. The reason for this is that if an entry for a midside node is omitted, PAFEC automatically calculates the coordinates of such a node from the coordinates of the corner nodes. The definition of the coordinates of all midside nodes is therefore not necessary in PAFEC.

In the second step of the subroutine DEFSTEM, the nodes with the z-coordinate equal to 4 mm are defined. Continuing the example which was given above, nodes equivalent to the midside nodes 13, 14, 15, 16 and 17 of the brick element have to be defined. For the whole contour, this is simply done by taking the x,y-coordinates of the previously defined nodes and increasing the value of the z-coordinate to 4 mm. Because of the fact that less nodes are needed for the definition of the midside nodes, the nodes equivalent to the nodes 2, 4,..., 16, 18,..., 32 and 33 in Figure 13 are omitted.

In the third step, the nodes with the z-coordinates equal to 8 mm are defined. The procedure is exactly the same as in the case of the definition of the nodes at the level z=0 mm. The nodes are defined on the basis of the point coordinates which describe the contour of the first section of the prosthesis.

In the fourth step, the nodes with the z-coordinate equal to 12 mm are defined. The procedure is the same as described for the second step. The x,y-coordinates of the nodes are taken from the points describing the first section of the prosthesis.

In the next steps of the definition of the nodes, the procedure, similar to that described in the steps three and four, is followed. From the point where the sections in the prosthesis are 4 mm apart, points of every second section are used in the manner described in step three. The points of the remaining sections are used in order to define nodes at the midsides of the elements according to step four. If the number of basis-section less the number of the sections which are 8 mm apart is

even, the points of the basis-section are included into the definition of nodes. In the opposite case, these points are not included, and the shape of the prosthesis is modelled up to the section with the number of one less than the number of the basis-section.

From the description of the definition of the nodes by the subroutine DEFSTEM, it can be seen that the nodes define a smooth prosthesis, as the transition radii between the sections have been ignored. The shapes of the sections, however, are defined as accurately as possible. The nodes are defined in such a way that they model a smooth prosthesis, the shape of which lies inside the shape of the real, stepped prosthesis. It has to be mentioned that the number of points per contour in the file containing the geometry of the prosthesis is, in current designs, equal to seventy three. The program PROEM, as it is shown in Appendix 2, is preset to this value of the number of the points. The program is also preset to model each section of the prosthesis with twelve brick and twelve wedge elements. These preset values can easily be changed if required.

The next subroutine which defines nodes, is called DEFTOP. This subroutine defines nodes of the neck of the prosthesis in a very simplified fashion. DEFTOP calculates nodes around the centre of the head of the prosthesis for an assumed circular shape of the section in a manner similar to that shown in Figure 13.

In the subroutine DEFEMBE, the nodes of the embedding are defined. The first steps in DEFEMBE are equivalent to the steps one, two and three in the subroutine DEFSTEM. The z-coordinate of the nodes starts, however, with the value of -8 mm. This value was arbitrarily chosen for the thickness of the embedding under the distal end of the prosthesis. In addition to the nodes which are defined similarly to these in DEFSTEM, new nodes are defined which are 20 mm distant from the z-axis of the coordinate system. This is shown schematically in Figure 14. It can be seen that the embedding is modelled in the shape of a cylinder around the prosthesis. The value of 20 mm for the radius of the cylinder was chosen arbitrarily. The definition of the nodes of the embedding proceeds further in similar fashion to the definition of the nodes of the stem. The nodes are defined in layers along the z-axis in steps of 4 mm.

The nodes of the inner surface of the embedding (close to the stem) are defined using the points describing the contours of the prosthesis. The nodes of the outer surface of the embedding (surface of the cylinder) are defined 20 mm from the z-axis. The subroutine stops after the last nodes, with the z-coordinate equal to the z-coordinate of the basic-section less 50±2 mm, have been defined.

Two points are to be noted in the definition of the nodes of the embedding. Firstly, the coordinates of the nodes on the inner surface of the embedding are equal to these of the surface of the stem. If nothing else is specified, PAFEC will assume that these nodes are in fact the same. In this case, continuity will be automatically assumed for the interface condition between the embedding and the stem. By having two different numbers for nodes with the same coordinates, it is possible to introduce different interface conditions than the continuity condition. PAFEC enables the use of the so-called GAPS interface elements. The effect of these elements is such that if there is pressure between two facing elements, the interface condition is assumed to be continuous, but if there is tension, the elements are assumed to be separated from each other. Thus, GAPS enable the modelling of a separation of the stem from the embedding. Secondly, it should be noted in the definition of the embedding nodes that the embedding level can be 48 mm or 52 mm below the basis-section. This is dictated by the way in which the nodes are being defined. The embedding level will be 48 mm below the basis-section if the number of the basis-section, less the number of the sections which are 8 mm apart, is even. In the opposite case, the embedding level will be 52 mm below the basis-section.

After the definition of the nodes, the program PROEM defines the elements by calling the subroutines PROTE and EMBE. PROTE defines the elements of the prosthesis, and EMBE defines the elements of the embedding. The elements are defined by using the PAFBLOCKS facility in both the subroutines. PAFBLOCKS are defined by specifying BLOCK.NUMBER, TYPE, ELEMENT.TYPE, PROPERTIES, N1, N2, N5, and the TOPOLOGY. BLOCK.NUMBER defines the number of the PAFBLOCK to be defined. TYPE refers to the type of the PAFBLOCK, i.e, it specifies the way in which the PAFBLOCK will be divided into elements. ELEMENT.TYPE gives the type of element to be used in the PAFBLOCK, i.e., brick or wedge element. PROPERTIES refers

to the properties of the MATERIAL, i.e., the modulus of elasticity and the Poisson's ratio, to be used with the elements. N1, N2 and N5 refer to a list of factors which define in how many elements the PAFBLOCK will be divided. This list is given by defining the so-called MESH, REFERENCE and SPACING.LIST. It is to be noted that N1, N2 and N5 do not give the numbers of division of the PAFBLOCKS, but refer to a number in REFERENCE. The number of the divisions is given in SPACING.LIST. TOPOLOGY specifies the node numbers which define the PAFBLOCK according to the ELEMENT.TYPE. The subroutines PROTE and EMBE write the PAFBLOCKS into the PROEM.DAT output file in such a way that the local numbering schemes of the nodes of the elements (see Figures 11 and 12) are replaced by the appropriate node numbers which were defined in the subroutines DEFSTEM, DEFTOP and DEFEM.

In the last part of the program PROEM, the constraints and the loads are defined. The constraints are defined in the subroutine BOND. This subroutine imposes RESTRAINTS on all nodes on the outer and on the bottom surface of the embedding in such a way that all degrees of freedom of these nodes are set to zero. Loads are defined in the subroutine DEFLOAD. They are attached to the NODE.NUMBER which has the coordinates of the centre of the head of the prosthesis. Two loads are specified: the first one acts in the DIRECTION parallel to the z-axis, and the second, parallel to the x-axis of the coordinate system. The VALUEs.OF.LOADs are calculated according to the fact that the axis of the prosthesis during the DIN-tests is tilted by 10° from the vertical which, in turn, is the direction of the load applied during the tests. In order to calculate the loads for the FEM-model, this applied load has to, therefore, be resolved into the directions parallel to the axis of the (local) coordinate system of the prosthesis.

An example of the output file from the program PROEM is not shown. The reason for this is the large size of such a file of approximately 200 kB. If these 200 kB of data were printed, the text would occupy approximately 60 pages. Figure 15 shows a graphical representation of the mesh which is generated by PAFEC on the basis of the data provided by the program PROEM. The mesh shown in Figure 15 consists of 3,670 nodes, and

735 brick and wedge elements, and it has round 9,300 degrees of freedom (i.e., unknowns). The calculation of stresses for this particular model needed 100 MB of storage space and 80,000 cpu[15] seconds on an Apollo 2000 computer.

The program PROEM defines the mesh for the case of an embedded prosthesis with smooth shape. However, in reality, there are transition radii between the sections of the prosthesis. These transition radii cause an increase in stresses due to the changes in the geometry. In engineering practice, these increases in stresses are dealt with by defining the so-called geometrical (or theoretical) stress concentration factor (K_T). The stress concentration factor is defined as the ratio of the maximum stress in a structure with a geometrical discontinuity to the stress in a similar structure with no discontinuity. In the case, e.g. of a circular round bar with a fillet subjected to pure bending (Figure 16), the maximum stress is found in the root of the transition radius. The stress concentration factor for this case is defined as the ratio of this maximum stress to the stress in that part of the bar with the smaller diameter. In general, the stress concentration factor depends on the type of loading, the cross sectional geometry, the value of the transition radius, and the value of the height of the shoulder of the fillet.

In order to calculate the stress concentration factors for the case of the HERAMED prosthesis, the program COSCF was developed (see Appendix 2). The stress concentration factors cannot be calculated directly with COSCF. The program is similar to the program PROEM in that it generates a mesh for the FE-analysis with PAFEC. The results of the analysis have

[15] The abbreviation cpu stands for Central Processing Unit. The cpu time gives therefore the time during which the processor of the computer was occupied by the calculation. The cpu time is not the total time which was needed for calculation as it does not include the time which was needed in order to write and read data on the hard disc (the so-called Input/Output time).

to be processed further, in order to calculate the stress concentration factors. COSCF enables the stress concentration factors to be calculated for only one section at time. The number of the section to be modelled is specified interactively during the execution of the program. It has to be pointed out that in FEM, it is not possible to define a mesh which would describe a general form of a section of the prosthesis with the transition radius (form of the step). The major difficulty is that because of the irregular shape of the adjacent contours, the height of the step varies along the transition zone between the two contours. It is even possible that in some places, the transition radius will disappear altogether. It is obvious that the task of developing a mesh generator which would be able to model the general form of the stem is equivalent to a task of developing an automatic mesh generator for any three-dimensional shape. This is simply too difficult. With the program COSCF, a way around the problem of varying step height is proposed. For input data, COSCF uses the same file containing the geometrical data of the prosthesis as the program PROEM. After the number of the section which is to be modelled has been chosen, COSCF produces four files: COSF0.DAT, COSF1.DAT, COSF2.DAT and COSF3.DAT, for the FE-analysis with PAFEC. These files define the meshes for the section of the prosthesis with constant step heights along the contour. In the first file, a smooth structure, i.e. without the transition radius, is defined. In the consecutive files, structures, in which $^1/_3$, $^2/_3$ and the whole transition radius is modelled, are defined. All the structures are loaded with a bending moment of the same value. From the results of the FE-analysis, the stress concentration factors can be calculated at each position along the transition zone and for the given step height. These stress concentration factors can be presented graphically as a set of curves (one curve for each position along the transition zone) which show the dependence of the value of the stress concentration factors on the step height. From the file which contains the geometrical data of the prosthesis, the step heights along the transition zone of the modelled section can be calculated. Using these values for the step heights and the set of curves found from the results of the FE-analysis, the stress concentration factors for the section under consideration can be estimated.

A detailed description of the program COSCF is not presented. As the program COSCF uses the same technique as the program PROEM in order to

define the meshes, it is assumed that the listing of COSCF (see Appendix 2), can be understood on the basis of the detailed description of PROEM, which was previously presented. Graphical representations of the meshes generated on the basis of the output files form COSF are shown in Figures 17, 18, 19 and 20. Figure 17 shows the structure defined in the file COSF0.DAT, and which consists of 120 elements and 563 nodes with 1,542 degrees of freedom. Figure 18 shows the structure defined in the file COSF1.DAT, which consists of 264 elements and 1,151 nodes with 3,306 degrees of freedom. Figure 19 shows the structure defined in the file COSF2.DAT, which consists of 408 elements and 1,812 nodes with 5070 degrees of freedom. Finally, the structure defined in the file COSF3.DAT is shown in Figure 20. This structure consists of 516 elements and 2,306 nodes with 6,480 degrees of freedom. In order to calculate stresses in the case of the last model, 45 MB of storage space and round 23,000 cpu seconds were needed on PRIME C computer.

2.3.3. Boundary Element Model

2.3.3.1. Concept of Boundary Element Method

The Boundary Element Method (BEM) has been developed in recent years as an alternative to FEM. Similar to FEM, BEM is also a technique for solving complex physical problems numerically. The way in which this is done, however, is different. The method has some advantages over FEM, in particular, when a linear elastic stress analysis of a three-dimensional body with a complex shape is to be performed. This is the reason why BEM was used in order to model the HERAMED prostheses. The mathematics involved in the exact formulation of BEM are difficult and can be found in the literature [35, 41]. Here, an attempt is made to present the basic idea behind BEM and to show the major differences between practical applications of BEM and FEM.

Basic idea

In Chapter 2.3.2.1, the concept of FEM was presented. It is pointed out that the majority of what has been said in that chapter also applies to

BEM. In Chapter 2.3.2.1, it was stated that by integrating by parts the differential operator L(), a set of differential operators G() and S(), which are associated with boundary conditions of the problem described by L(), is generated (see Chapter 2.3.2.1, Equation (4)). If the solution of the differential equation given by L() is found in the form of a function u, which does not exactly satisfy the governing equation and the boundary conditions, a set of residual, or error functions can be defined, as shown below (see Chapter 2.3.2.1, Equations 12 and 13):

$$\begin{aligned} R &= L(u)-b && \text{residual in } \Omega, \\ R_1 &= S(u)-s && \text{residual on the } \Gamma_1 \text{ part of the boundary,} \\ R_2 &= G(u)-g && \text{residual on the } \Gamma_2 \text{ part of the boundary.} \end{aligned} \tag{1}$$

where

- L() - differential operator describing the problem,
- S() - differential operator resulting from the integration by parts and associated with the essential boundary conditions,
- G() - differential operator resulting from integration by parts and associated with the natural boundary conditions,
- u - approximating function,
- b - function which together with L() describes the problem (see Chapter 2.3.2.1, Equation (1)),
- s - essential boundary condition on the Γ_1 part of the boundary,
- g - natural boundary conditions prescribed on the Γ_2 part of the boundary,
- Ω - domain in which the problem is defined,
- Γ - boundary of Ω; $\Gamma=\Gamma_1+\Gamma_2$.

These residuals can be weighted with a weighting function w, and a general equation of the residuals can be formulated such that

$$\int_{\Omega} R w d\Omega = \int_{\Gamma_2} R_2 w d\Gamma - \int_{\Gamma_1} R_1 w d\Gamma, \tag{2}$$

If the approximating function u (the approximate solution) identically satisfies the boundary conditions and is approximate in the domain, the residuals R_1 and R_2 are equal to zero. Equation (2) can now be written as:

$$\int_{\Omega} R w d\Omega = 0, \tag{3}$$

This equation is also the starting point for the Finite Difference Method.

If the function u satisfies the essential, but not the natural boundary conditions and is approximate in the domain, the equation of the residuals can be written as:

$$\int_{\Omega} R w d\Omega = \int_{\Gamma_2} R_2 w d\Gamma, \tag{4}$$

Equation (4) is the starting point for the weak formulation of the Finite Element Method.

If the function u is chosen in such a way that it identically satisfies the governing equation, the integral over the domain Ω in Equation (2) is forced to zero and the equation of the residuals can be written in the following form:

$$0 = \int_{\Gamma_2} R_2 w d\Gamma - \int_{\Gamma_1} R_1 w d\Gamma, \tag{5}$$

This is the basic concept of the Boundary Element Method.

Inverse formulation

It has to be pointed out that from this point, a discussion of BEM in general terms becomes difficult without referring to examples of particular forms of the differential operator L(). Excellent illustrations

of the concept of BEM are given in the literature [35]. In practice, one often starts with the initial formulation of the residual of the problem (see Chapter 2.3.2.1, Equation (16)) in the form:

$$\int_{\Omega}(L(u)-b)w\,d\Omega = \emptyset. \qquad (6)$$

Equation (6) is then integrated by parts until all orders of L() disappear in u. This leads to an equation similar to Equation (4) in Chapter 2.3.2.1, i.e,

$$\int_{\Omega} uL^*(w)\,d\Omega + \int_{\Gamma} [\text{boundary terms}]\,d\Gamma = \emptyset, \qquad (7)$$

where

$L^*()$ - the adjoint operator of $L()$.

It can be seen that $L^*()$ has the same order as $L()$, but it acts on the weighting function w and not on the approximating function u. In order to apply the concept of BEM, i.e., to force the domain integral to zero, not u but the function w has to satisfy the equation given by the adjoint operator $L^*()$. (If $L()$ is self-adjoint, the function w also satisfies $L()$). This formulation is called the inverse formulation and is used in practical applications of BEM.

Fundamental solution

In BEM, the weighting function w is chosen in such a way that this function is the so-called fundamental solution of $L^*()$. This function will be indicated by an asterisk, i.e., w^*, to show its special character. The fundamental solution w^* has the following property:

$$L^*(w^*)=\delta_i, \qquad (8)$$

where δ_i indicates the Dirac delta function which is different from zero at the point i but zero everywhere else.

The domain integral in Equation (7) can now be written as:

$$\int_{\Omega} L^*(w^*)u\,d\Omega = \int_{\Omega} \delta_i u\,d\Omega = u_i\,, \qquad (9)$$

It can be seen that the domain integral has been replaced by the value of the function at the point i where the Dirac delta function is applied. Thus, a general form of Equation (7) can be written in the form:

$$(\text{constant value}) + \int_{\Gamma} (\text{boundary terms})\,d\Gamma = 0. \qquad (10)$$

This is the general form of equations used in BEM.

It is pointed out that the use of functions which identically satisfy the governing equation (or its adjoint form) has a very important practical consequence. Because of the fact that the domain integrals have been eliminated, in order to solve an equation of the type (10) numerically, only the division of the boundary, not the domain of the problem, into elements is required. This is the main advantage of BEM over FEM. It is much easier to define nodes on the surface of e.g. a three-dimensional body than to define nodes on the surface and in the interior of such a body. The definition of a mesh in BEM is therefore much simpler than in FEM. Also because of the fact that nodes in BEM need to be specified on the surface, fewer nodes have to be defined. This leads to a reduction in the number of unknowns and thus to a reduction of the size of the problem which is to be solved. As the weighting functions are the fundamental solutions of the governing equations, the results of BE-analysis tend to be more accurate than that of FE-analysis. This is in particular, if one is interested in the values of the unknowns on the boundary (surface) of a problem.

BEM in elastostatics

The basis of BEM in elastostatics is the constraint equation which relates the values of the surface displacements u_i to the surface traction t_i [35, 42], given by

$$u_i(P)/2 + \int_\Gamma T_{ij}(Q,P)u_j(Q)d\Gamma(Q) = \int_\Gamma U_{ij}(Q,P)t_j(Q)d\Gamma(Q), \qquad (11)$$

P and Q are points on the boundary Γ of the body Ω; T_{ij} and U_{ij} are second order tensors, singular at P=Q, which correspond to the tractions and displacements for the problem of three orthogonal unit loads in an infinite elastic body[16]. The tensors T_{ij} and U_{ij} are reported in the literature, e.g. in [35], and are functions of the distance between the boundary points P, Q given by

$$r(P,Q) = \sqrt{\{[x_i(Q)-x_i(P)][x_i(Q)-x_i(P)]\}}, \qquad (12)$$

where

$x_i(Q)$, $x_i(P)$ - the coordinates of the points P, Q,

and functions of the derivatives of r(P,Q). The tensors T_{ij} and U_{ij} are the fundamental solutions in the case of elastostatics. Equation (11) is solved numerically by carrying out the following steps:

1. The boundary Γ is discretized into a series of elements over which displacements and tractions are chosen to be piecewise interpolated between the nodal points;
2. Equation (11) is applied in discretized form to each nodal point P of the boundary Γ and the integrals are computed over each element. A system of M linear algebraic equations involving the set of M nodal tractions and M nodal displacements is therefore obtained;
3. Boundary conditions are imposed and consequently M nodal values (tractions or displacements in each direction per

[16] The coefficients of the tensors T_{ij} and U_{ij} are the tractions and displacements in the j direction due to a unit force at the point under consideration, acting in the i direction.

node) are prescribed. The system of M equations can therefore be solved by standard methods to obtain the remaining boundary data.

For the discretization of Equation (11), the boundary Γ is approximated by using a series of elements. Boundary displacements and tractions over each element are expressed in terms of interpolation (shape) functions and their nodal values. The boundary variables can be approximated as, e.g., piecewise constant. The continuous boundary can be replaced by N piecewise flat segments and the tensors T_{ij} and U_{ij} integrated for each segment. The result for Equation (11) is given as [42]:

$$u_i(P_m)/2 + \sum_{n=1}^{N} \Delta T_{ij}(Q_n, P_m) u_j(Q_n) = \sum_{n=1}^{N} \Delta U_{ij}(Q_n, P_m) t_j(Q_n). \qquad (13)$$

The new tensors ΔT_{ij} and ΔU_{ij} are computed using the geometric descriptions of the N segments and the elastic properties of the body. It is to be noted that Equation (13) is valid for a load point on the boundary at P_m. This equation can be written in a matrix form as

$$u_i/2 + [h_{i1}, h_{i2}, \ldots, h_{ii}, \ldots, h_{iN}]\{u_1, u_2, \ldots, u_{ii}, \ldots, u_{iN}\}^T = [g_{i1}, g_{i2}, \ldots, g_{ii}, \ldots, g_{iN}]\{t_1, t_2, \ldots, t_i, \ldots, t_N\}^T, \qquad (14)$$

where u_j and t_j are unknowns at nodes j. h_{ij} and g_{ij} are interaction coefficients which relate the node i with all the nodes on the surface of the body[17]. Equations, such as (14), can be written for each of the

[17] In the case where the interpolation functions are not constant, i.e., they are linear or quadratic, the form of the matrices $[h_{ij}]$ and $[g_{ij}]$ will not change, but more than one element will contribute to the coefficients of these matrices.

nodes. In three dimensions, the number of equations is 3N, so that the number of unknowns is also 3N. These equations can be written as one matrix equation:

$$[H]\{u\} = [G]\{t\}. \tag{15}$$

The known boundary conditions are now applied in the system of equations (15). These boundary conditions can be of two types: u_i on Γ_1 and t_i on Γ_2. If the displacements are known, the tractions can be found and vice versa[18]. The system of equations (15) can be rewritten in such a way that all the unknowns are written on the left-hand side in a vector Y and all the knowns on the right-hand side in a vector X. The final result can be written as:

$$[A]\{Y\} = [B]\{X\}. \tag{16}$$

The system of equations given by (16) can be solved by standard methods. It has to be mentioned, that the solution of the system of equations produces values for the unknown displacements and tractions on the surface of the body. In BEM, it is also possible to compute stresses and displacements at any point inside the body. This is done after the system of equations (16) has been solved by using the so-called Somigliana identity [35, 42]. The fact that the stresses (or the displacements) can be calculated at any point inside the body, after solving the system of equations, means that the internal points can be arranged in an arbitrary fashion and that the number of the internal points can theoretically be unlimited. This feature of BEM has found its application in the computation of stresses around cracks in bodies [42, 43].

---

[18]Note that at the surface of a body, there have to be at least one kind of boundary condition prescribed on each part of the surface. On a free surface, the tractions are equal to zero and the displacements are unknown. On a loaded surface, the tractions are known but not the displacements. However, displacements have to be prescribed for some elements in order to eliminate any rigid-body displacement in any one direction.

2.3.3.2 BEM-model of Prosthesis

The advantages of BEM over FEM, and in particular the ease with which a mesh of nodes can be defined for complex shapes in three dimensions, led to an attempt to model the HERAMED prosthesis with BEM. The overall procedure in the developing of this model was exactly the same as in the developing of the model for FEM. Two computer programs were written which used the same file for the input data as described in Chapter 2.3.1. These programs generated files which then could be used for BE-analysis with the commercial BEM package BEASY[19]. (The version 3.1 of BEASY [44] was available in the Department of Mechanical Engineering at Loughborough University on a PRIME C computer and in the University of Manchester Regional Computer Centre on a CDC CYBER 205 super-computer.) The first program generated data for the case of smooth prosthesis. The embedding was modelled with the help of 'linear-spring' elements. The second program generated data for BE-analysis of one step of the prosthesis. It is pointed out that by using BEM, it was possible to generate a mesh which described a step of the prosthesis with varying step height in a fully automatic way. This was not possible using FEM (see Chapter 2.3.2.2).

For reasons which will be given later in the discussion, the listings of the mesh generators for BEASY are not presented. The mesh for the case of smooth prosthesis is shown in Figure 21. The model consists of 164 quadrilateral elements, which in the BEM language are called patches, and 635 nodes. Figure 22 shows the mesh of one step. Round 130 patches and 500 nodes were needed in order to define the mesh shown in Figure 22. BEASY did not give the number of degrees of freedom (number of unknowns) for the meshes shown in Figures 21 and 22. However, this number can be estimated from the knowledge of how many unknowns there can be per element. For a three-dimensional analysis, the so-called discontinuous elements were used (default in BEASY). The term discontinuous means that the values of unknowns are not calculated in the points with coor-

---

[19] BEASY, the boundary element analysis system, Computational Mechanics, Southampton, U.K.

dinates equal to that of the nodes which describe the geometry of the elements, but in points inside the element. In the case of a doubly-curved quadrilateral element, this means that there are nine such points inside the element [44]. Each of these points is associated with three values of displacements and three values of tractions. In order for the solution to be unique, three of these values must be prescribed. This means that each element can be associated with with the number of 3*9=27 unknowns. Thus, the number of unknowns for the structure shown in Figure 21 can be estimated to be equal to 164*27=4,428 and for the structure shown in Figure 22, to be equal to 130*27=3,510. The model of the prosthesis required 2,700 cpu seconds and occupied 100 MB of storage space on CYBER 205 supercomputer.

2.3.4. Simple Model

In Chapters 2.3.2 and 2.3.3, the FEM-model and the BEM-model were described. In both the models, large equation systems (matrices) with several thousands of unknowns have to be solved in order to calculate stresses in the prosthesis. These models, therefore, require long computing time and large computer storage space[20]. In order to provide a model which would be less 'expensive', a simple model for calculating the stresses was developed. This simple model uses a mixture of the simple bending theory [45], finite elements [46] and beam on elastic foundation theory [47]. Several assumptions had to be made in developing the simple model. The major assumption is that the stresses in the prosthesis can be calculated with formulas which are valid for the case of a straight beam with constant cross section. Thus, the simple model provides approximate results for stresses in the prosthesis. The closer the prosthesis resembles a straight beam, the more accurate are the results. The simple model was written in FORTRAN 77 programming language and is shown in Appendix 3.

The main program is called PROCO. This program uses the same file for the input of the geometrical data of the prosthesis as the FEM and BEM

[20] See Discussion for details.

models (see Chapters 2.3.1, 2.3.2 and 2.3.3). The geometrical data is read in the subroutine READAT. READAT also reads data from a second file called SCFDAT which contains tables of stress concentration factors. These tables are used in the later stage of the program PROCO. The subroutine READAT is followed by the subroutine SECT. SECT performs a similar task as the subroutine SECT in the program PROEM (see FEM-model, Chapter 2.3.2.2). In the first step, SECT calculates approximate centre points of each of the contours and then calculates new coordinates of points of the contours around these centre points (see Chapter 2.3.2.2). In this way, the new positions of the points are more evenly distributed along the contours than the old ones. However, the old positions are stored in separate arrays. In the second step, SECT performs a series of transformation of coordinates. The coordinates of points of each contour and the coordinates of the centre of the head of the prosthesis are translated in such a way that the origins of the (local) coordinate systems lie in the centre points. The coordinate systems are then rotated until the y-coordinate of the first point of each contour is equal to zero. The aim of the subroutine SECT is to facilitate an accurate calculation of geometrical properties of the contours, such as the cross sectional areas, the coordinates of the centroids and the second moments of area of each section. The geometrical properties of the sections are calculated in the subroutine CENTRO. This is done in the following way:

1. Each part of the section which lies in one of the quadrants of the coordinate system is divided in a series of strips (Figure 23).

2. The areas, the products of inertia, the first and the second moments of area about the x- and y-axis of the coordinate system of each of of the strips are calculated:

$$A=H*B,$$

$$AX=A*Y,$$

$$AY=A*X, \qquad (1)$$

$$IX=(B*H^3)/3,$$

$IY=(H*B^3)/12 + A*X^2$,

$IXY=A*X*Y$,

where

A - area of one strip,
H - height of the strip,
B - width of the strip ,
AX- first moment of area about x-axis,
AY- first moment of area about y-axis,
IX- second moment of area about x-axis,
IY- second moment of area about y-axis,
IXY-product of inertia,
X - x-coordinate of the centre point of the strip,
Y - y-coordinate of the centre point of the strip.

Because of the fact that the shape of the section cannot be closely approximated using rectangular strips (trapezoids would be needed), the properties of two strips, one with a too large area and second with a too small area, are calculated (see Figure 23).

3. The properties of each strip are summed over each quadrant and added together.

4. The averages of the results of the summation for the 'too large' and the 'too small' strips are calculated:

$$A_t = (A_l + A_s)/2,$$

$$AX_t = (AX_l + AX_s)/2,$$

$$AY_t = (AY_l + AY_s)/2, \qquad (2)$$

$$IXX_t = (IXX_l + IXX_s)/2,$$

$$IYY_t = (IYY_l + IYY_s)/2,$$

$$IXYXY_t = (IXYXY_l + IXYXY_s)/2,$$

where

A - area,
AX,AY - first moments of area,
IXX,IYY - second moments of area; IXX=ΣIX; IYY=ΣIY,
IXYXY - product of inertia; IXYXY=ΣIXY,
t,l,s - subscripts denoting the average, 'too large' and 'too small' properties respectively.

5. Coordinates of the centroid of the section are calculated:

$$XBAR = AX_t/A_t,$$

$$YBAR = AY_t/A_t, \qquad (3)$$

where

XBAR - x-coordinate of the centroid,
YBAR - y-coordinate of the centroid.

6. The nominal moments of area, i.e., moments about axes which are parallel to the axes of the coordinate system but pass through the centroid, are calculated:

$$INAX = IXX_t - A_t*YBAR^2,$$

$$INAY = IYY_t - A_t*XBAR^2, \qquad (4)$$

$$INAXY = IXYXY_t - A_t*XBAR*YBAR,$$

where

INAX - nominal second moment of area of the section about an axis which is parallel to the x-axis of the coordinate system and which passes through the centroid,

INAY - nominal second moment of area of the section about an axis which is parallel to the y-axis of the coordinate system and which passes through the centroid,

INAXY - product of inertia.

7. Finally, the coordinate system of each section is translated in such a way that its origin coincides with the centroid.

The subroutine CENTRO is followed by the subroutine MPROT. MPROT calculates moments which act on each section due to the applied force in the centre of the head of the prosthesis. In general, there are three moments acting on each section. The first two moments are bending moments and the third one is a torsion moment. The torsion moment is not calculated in MPROT and it will be dealt with later. The first of the bending moments acts about the x-axis and the second, about the y-axis of the coordinate system. Each of the moments is a sum of a pure bending moment and a moment due to the shear force resulting from the fact that the axis of the prosthesis is tilted in respect to the axis of the applied force (see Figure 24). The general form of the equation for calculating the moments is as follows:

$$MX = -P*YL*COS(BETA) \pm P*ZL*SIN(BETA)*COS(ANG), \quad (5)$$

$$MY = P*XL*COS(BETA) \pm P*ZL*SIN(BETA)*SIN(ANG),$$

where

MX - moment about x-axis,

MY - moment about y-axis,

P - absolute value of the applied force,

XL,YL - coordinates of the centre of the head in the local coordinate system of the section,

ZL - distance along the z-axis of the prosthesis between the z-coordinate of the centre of the head and the z-coordinate of the section,

BETA - tilt angle of the prosthesis,

ANG - angle between the neck axis and the x-axis of the local coordinate system,

± - (+) if XL is positive and (-) if XL is negative.

The moments MX and MY cannot be directly used for calculation of stresses as they act about the axis of the coordinate system which, in general, are not the principal axis of the section[21]. In order to calculate values of moments which can be used for the calculation of stresses, MPROT uses the so-called method of effective moments [45]. The effective moments are calculated in the following way:

$$M1 = (MX + INAXY*MY/INAY)/(1 - INAXY^2/INAX/INAY), \qquad (6)$$

$$M2 = (MY + INAXY*MX/INYX)/(1 - INAXY^2/INAX/INAY),$$

where

M1 - effective moment about the x-axis of the coordinate system,
M2 - effective moment about the y-axis of the coordinate system.

It has to be mentioned that the subroutine MPROT calculates the effective moments for each section of the prosthesis and that in doing this, the influence of the embedding is not considered. The program PROCO, however, enables an estimation of the influence of the embedding on the value of the moments acting on embedded sections. If a value different from zero for the number of the last embedded section (LEVEL) is entered, the program executes the subroutine MPROEM. In the first step, MPROEM calculates the shear stresses acting on the last embedded section (Figure 24):

$$SX = \pm P*SIN(BETA)*COS(ANGLEV), \qquad (7)$$

$$SY = \pm P*SIN(BETA)*SIN(ANGLEV),$$

[21] The axes of the coordinate system are the principal axes of the section if the product of inertia for these axes is equal to zero.

where

SX - shear force acting along y-axis,
SY - shear force acting along x-axis,
ANGLEV - angle between the neck axis and the x-axis of the local coordinate system of the last embedded section.
± - (+) if XL is positive; (-) if XL is negative.

In the second step, MPROEM passes the shear forces SX and SY, and the moments M1 and M2 for the last embedded section to the subroutine ELBEAM. ELBEAM executes a series of subroutines which calculate the approximate reduction of the moments M1 and M2 along the embedding. The embedding is modelled as a series of linear springs which are attached to the prosthesis in distances 2 mm apart. The calculation is performed using the finite difference method [47]. It is assumed that the reductions in the values of both the moments M1 and M2 are independent from each other. The calculation is, therefore, carried out separately for each of the moments. The first subroutine in the series which is executed by ELBEAM is called PARAM. This subroutine calculates the stiffness of each of the linear springs using the following formula:

$$KN = 1.9*EC*g_1(\nu_c)*\{0.24 + DS/(1-DS)\}, \qquad (8)$$

where

KN - stiffness of the Nth spring,
EC - modulus of elasticity of the embedding,
ν_c - Poisson's ratio of the embedding,
g_1 - function shown in Figure 25,
DS - ratio of the 'diameter' of the section to the diameter of the embedding.

This formula was derived on the basis of analytical considerations combined with FEM calculations in [24,48]. The stiffnesses of the linear springs, calculated with the formula, approximate the stiffnesses of circular rings subjected to a transverse loading as shown in Figure 26. The formula is valid in the case of loose interface condition between the stem and the embedding, and in the case where there is no friction

in the interface[22]. The results of the calculation of the stiffnesses are the more accurate, the smaller is the value of DS.

It has to be noted that the term: diameter of the section (used in the calculation of DS), cannot be exactly defined because of the irregular shape of each section. For the diameter of the section, PARAM calculates the distance between two opposite, in respect to the centroid, points on the contour. For calculation of the reduction of the moment M1, the distance between points with y-coordinates equal to zero is taken, and for the calculation of the reduction of the moment M2, the distance between points with the x-coordinate equal to zero is taken.

The next subroutine executed from ELBEM is called MATRIX. This subroutine assembles a system of equations (matrix), which, if solved, enables the calculation of the moments along the embedding. The starting point of the assembly is the finite difference formulation of the moment equation of a beam:

$$d^2y/d^2x = M/EI, \qquad (9)$$

where

y - direction of displacements of the beam,
x - axis of the beam,
M - bending moment,
E - modulus of elasticity of the beam,
I - second moment of area of the beam section.

The differential on the left hand side of the above equation is replaced by the central difference operator:

$$d^2y/d^2x = (\delta_{i-1} - 2\delta_i + \delta_{i+1})/h^2, \qquad (10)$$

---

[22] In the case where the continuity between the embedding and the stem is assumed, the factor 1.9 and the function g_i have to be replaced by the factor 5.3 and the function g_f, (Figure 25), respectively.

where

δ_i - displacement at point i,
h - step width, i.e., distance between two adjacent points.

In Figure 27, the case of a beam on elastic foundation considered in the subroutine MATRIX is shown. The elastic foundation (the embedding) is approximated by a series of linear springs with stiffnesses k. On both the ends of the beam, it is assumed that the stiffnesses has the value of ½ k. The beam is loaded on the right hand side with a bending moment M and a shear force S. This loading produces reaction forces in the springs which are equal to k*h*δ, where h denotes the step width and δ, the displacements in the springs. Using Equations (9) and(10), and moving from the left-hand side of the beam in Figure 27, the following equilibrium equations of moments can be written:

Point 2: $(1+\frac{1}{2}k_1h^4/EI_1)\delta_1-2\delta_2+\delta_3=0,$

Point 3: $(\frac{1}{2}k_1h^4/EI_1)2\delta_1+(1+k_2h^4/EI_2)\delta_2-2\delta_3+\delta_4=0,$

Point 4: $(\frac{1}{2}k_1h^4/EI_1)3\delta_1+(k_2h^4/EI_2)2\delta_2+(1+k_3h^4/EI_3)\delta_3-2\delta_4+\delta_5=0,$

. (11)

Point (n-1): $(\frac{1}{2}k_1h^4/EI_1)(n-2)\delta_1+(k_2h^4/EI_2)(n-3)\delta_2+.....$

$.....+(1+k_{n-2}h^4/EI_{n-2})\delta_{n-2}-2\delta_{n-1}+\delta_n=0,$

where

k_i - stiffness of spring i,
h - step width,
E - modulus of elasticity of the beam,

I_i - second moment of area of section i,

δ_i - displacement in point i,

i=1,2,....,n,

n - number of points.

Equations (11), constitute a system of n-2 equations with n unknowns. The unknowns are the displacements δ of each spring. Two more equations can be written in order to be able to solve the system. The first equation is delivered from the equilibrium condition that the sum of all shear forces must be equal to zero:

$$\tfrac{1}{2}k_1 h\delta_1 + k_2 h\delta_2 + ... + k_{n-1} h\delta_{n-1} + \tfrac{1}{2}k_n \delta_n - S = 0, \qquad (12)$$

where

S - external shear force.

The second equation is delivered from the equilibrium of moments for point n if moving from the right-hand side of the beam:

$$\delta_{n-2} - 2\delta_{n-1} + \delta_n (1 + \tfrac{1}{2}k_n h^4 / EI_n) - (Mh^2 + Sh^3)/EI_n = 0, \qquad (13)$$

where

M - external bending moment.

Thus, Equations (11),(12) and (13) represent a system of n equations with n unknowns. It is to be noted, that although the equations are valid for a straight beam, the changes in the second moments of areas and changes in the stiffnesses of the embedding are modelled. The subroutine MATRIX calculates the coefficients of the system of equations according to Equations (11), (12) and (13), and writes them in the form of a matrix.

The next subroutines which are executed from ELBEAM are called FACTOR and SUBST. These subroutines solve the system of equations which was

assembled in the subroutine Matrix using the Gauss elimination procedure [49]. The results of the solution are the displacements δ in the springs.

Finally, in order to calculate bending moments along the embedding, the subroutine ELBEAM executes the subroutine MOMENT. MOMENT calculates the bending moments at each of the sections of the prosthesis from the finite difference form of Equation (10), i.e.:

$$M_i = EI_i(\delta_{i-1}-2\delta_i+\delta_{i+1})/h^2, \qquad (14)$$

where

M_i - moment at point i which is equivalent to the z-coordinate of a section,
E - modulus of elasticity of the stem,
I_i - second moment of area,
δ_i - displacement at point i.

The bending moments which are calculated in MOMENT are taken into consideration in subsequent calculation of stresses in the prosthesis.

After the calculation of moments in the embedding, the main program PROCO invokes the subroutine COSTRE. COSTRE calculates stresses in each point of the contours on the surface of the prosthesis. If the torsion moment is omitted, the loading of the prosthesis can be regarded as combined biaxial bending and axial loading due to an eccentric force. This is best visualized by refering to Figure 24. The prosthesis is loaded by a force P which does not act parallel to the axis of the prosthesis. This axis is tilted to the direction of the applied load by the angle BETA. The force P, therefore, has to be resolved into directions which are parallel to the axis of the coordinate system of the prosthesis. This produces two forces: the first one, S, is a shear force which acts perpendicular to the axis of the prosthesis and the second one, F, is an axial force which acts parallel to the z-axis. Because of the fact that F does not act on the z-axis, apart from axial loading, this force will produce two pure bending moments (about the x- and y-axis) which act on each of the sections of the prosthesis. The force S also produces

two bending moments on each of the sections. The value of these moments increases with the increase in the distance between the line of action of the force S and the position of the section. The stresses at each point of the section can be calculated from the following equations [45]:

```
SSUM = S1 + S2 + SL,

S1 = M1*Y/INAX,                                          (15)

S2 = M2*X/INAY,

SL = -P*COS(BETA)/A,
```

where

SSUM - stress at the point,
S1 - stress due to the effective moment M1,
S2 - stress due to the effective moment M2,
SL - stress due to the axial force F=-P*COS(BETA),
M1,M2 - effective moments,
INAX,INAY - nominal second moments of area,
X,Y - coordinates of the point,
P - absolute value of the load on the centre of the head of the prosthesis,
BETA - tilt angle,
A - area of the section.

Two further things have to be mentioned in order to explain the way in which the stresses are calculated by the subroutine COSTRE. Firstly, COSTRE calculates stresses for all points on the perimeter of the section. The points are chosen in such a way, that their positions are equivalent to those of the points in the original file which contains the geometrical data of the prosthesis (not the positions of the points which were calculated in the subroutine SECT). In this way, a direct reference to the geometry of the prosthesis is provided. Secondly, if stresses are calculated in the embedding, the last equation in (15) is not used. This means that it is assumed that the axial force is equal to

zero in the embedding. Because of the fact that the axial force is negative, this assumption means that the values of tensile stresses due to the bending moments in the embedding will be overestimated.

The subroutine COSTRE is followed by the subroutine CONCTR. In the first step, CONCNTR estimates the stress concentration factors at each point of the section. This is done in the following way:

1. The distance (DMIN) between the centroid of the section and the point under consideration is calculated.

2. The distance (DMAX) between the same centroid and the equivalent point to that which was considered above of the next section is calculated.

3. The following ratios are calculated:

$$RAT1 = DMAX/DMIN, \qquad (16)$$

$$RAT2 = RAD/DMIN,$$

where

RAD - value of the transition radius between the sections.

4. The values of the ratios RAT1 and RAT2 are then passed to subroutine SCFINT which returns the approximate value of the stress concentration factor.

According to the values of RAT1 and RAT2, the subroutine SCFINT interpolates between the values of stress concentration factors which were read in the subroutine READAT in the form of a table from the file SCFDAT. The file SCFDAT is shown in Appendix 3. It contains values of the stress concentration factors which were obtained from the literature [49] for the case of pure bending of a rectangular bar with a fillet (Figure 28). Instead of the values of the stress concentration factor for the case of rectangular bar, the file SCFDAT could have contained the values of the factors for the case of circular bar with a fillet

subjected to pure bending (Figure 29). However, because of the the irregular shapes of the sections of the prosthesis, it was decided that the factors for rectangular bars should be used. The values of these factors are slightly higher than the values of the factors for the case of circular bars. SCFINT, therefore, will overestimate the stress concentration factors.

In the second and final step of the subroutine CONCTR, the values of stresses which were calculated in the subroutine COSTRE are multiplied by the appropriate stress concentration factors:

$$FSUM = SSUM*K, \tag{17}$$

where

FSUM - factored stresses,
SSUM - stresses at each point of the contours,
K - stress concentration factor.

It has to be mentioned beforehand, that in this form, Equation (17) already includes a factor for the behaviour of the material of the prosthesis under fatigue loading. In the investigation of the material (see Chapter 3), it was found that under fatigue loading, the material behaves as a perfectly notch sensitive material. This means that Equation (17) does not have to be multiplied by an another factor (the so-called fatigue strength reduction factor) in order to compare the results of the calculation of stresses with the fatigue data of the prosthesis from the DIN-tests.

The subroutine CONCNTR is followed by the subroutine SSORT. SSORT has the task of finding the maximum and minimum stresses, and factored stresses along each contour. After SSORT, the values of the maximum and minimum stresses are written into the output file of the program PROCO, which is called STRESS. The file STRESS contains the maximum (tensile) and the minimum (compressive) stresses for each section. The numbers of points where the stresses were calculated are also included. An example of the file STRESS is shown in Appendix 3.

Apart from the stresses due to the bending moments, with the program PROCO it is also possible to estimate the stresses in the sections due to the torsion moments. The torsion moments arise due to the fact that the line of action of the force S (or their components SX and SY) does not pass through the centroids of the sections (see Figure 24). In the calculation of the stresses due to torsion, it is assumed that these stresses can be calculated with a method which is valid for the case of a straight bar with uniform noncircular shape of the cross-section. It is further assumed that no embedding is present around the prosthesis. The calculation is carried out using the finite element method as presented in [46].

The governing equation of the torsion of a noncircular bar is as follows:

$$\partial\tau_{yz}/\partial x + \partial\tau_{zx}/\partial y = 0, \tag{18}$$

where

τ_{yz}, τ_{zx} - shear stresses in the cross-section.

The shear stresses τ_{yz} and τ_{zx} are given as:

$$\tau_{yz} = \alpha G(\partial\phi/\partial y + x),$$
$$\tau_{zx} = \alpha G(\partial\phi/\partial x - y), \tag{19}$$

where

α - constant,
G - shear modulus of the material,
ϕ - the so-called warping function of the section.

The applied torsion moment, the torque, on the cross-section can be calculated from:

$$T = \iint_A (x\tau_{yz} - y\tau_{zx})dxdy, \tag{20}$$

where

T - applied torque,
A - area of the section,

The starting equation for the finite element formulations is the so-called virtual work balance equation:

$$\int_S (ut_x + vt_y)dS = 1/G * \int_V (\tau_{yz}^2 + \tau_{zx}^2)dV, \qquad (21)$$

where

u,v - displacements in x- and y- direction,
t_x, t_y - tractions at the surface Γ,
S - surface of the section,
G - shear modulus of the material,
V - volume.

The left-hand side of Equation (21) denotes the virtual work $T\alpha L$ done by the applied torque T trough the angle of twist αL. By taking Equation (20) for T and expressing the shear forces in this equation according to Equation (19), the left-hand side of (21) can be written as:

$$T\alpha L = \alpha^2 LG \iint_A (x\partial\phi/\partial y - y\partial\phi/\partial x + x^2 + y^2)dxdy, \qquad (22)$$

Using Equations (19), the right-hand side of (21) can be expressed as:

$$1/G*\int_V(\tau_{yz}^2+\tau_{zx}^2)dV = \alpha^2 LG \iint_A \{(\partial\phi/\partial y+x)^2+(\partial\phi/\partial x-y)^2\}dxdy, \qquad (23)$$

Equating the letf- and right-hand sides of the virtual work balance defined in (22) and (23) respectively, it can be written:

$$\iint_A (-x\partial\phi/\partial y + y\partial\phi/\partial x)dxdy = \iint_A \{(\partial\phi/\partial x)^2 + (\partial\phi/\partial y)^2\}dxdy, \qquad (24)$$

Equation (24) defines the problem of torsion of the bar completely in terms of variation of the warping function ϕ. Once the variation of this function is defined over the cross section, the stresses τ_{yz} and τ_{zx}, and the applied torque which causes these stresses can be calculated.

In the program PROCO, the subroutine TORO is invoked which, in turn, invokes a series of subroutines in order to solve Equation (24) for each of the sections of the prosthesis using finite element method. The first of the subroutines invoked by TORO is called SPEC. In this subroutine, the section under consideration is divided into 96 triangular elements using 61 nodes (Figure 30). Each node is specified by defining the node number and its coordinates. The nodes possess one degree of freedom. As Equation (24) is independent from any material properties, no properties are specified. IN order to eliminate rigid body displacements, the value of the warping function ϕ is set to zero in the node in the centre of the section.

The subroutine SPEC is followed by the subroutine ACTIVE. According to the number of nodes, the number of degrees of freedom per node and the number of prescribed boundary conditions, this subroutine calculates the number of active equations in the system. This number is passed to the next subroutine which is called called BWIDTH. BWIDTH calculates the semi-band width of the system of equations. This subroutine is followed by the subroutine ASSEM. The subroutine ASSEM assembles the system of equations which describe the problem in a special form which takes into account the number of active equations and the semi-band width. In this way, the system matrix does not contain unnecessary large number of coefficients which are equal to zero. However, by doing this, the number of nodes are being assigned new node numbers according toe their positions in the system matrix. In assembling the system matrix, ASSEM invokes the subroutine ELEMNT. This subroutine calculates the stiffness matrices and nodal point forces for each element. This is done in the following way:

The finite elements used in the division of each section is shown in Figure 31. The element is a triangular element which possesses three nodes i, j and k. Within the element e the warping function is approximated in terms of its nodal point values $[\delta^e]=[\phi_i, \phi_j, \phi_k]^T$ by

$$\phi = [N][\delta^e], \tag{25}$$

where

$[N]=[N_i, N_j, N_k]$ - shape functions.

Linear shape functions are used, such that

$$\begin{aligned} N_i &= 1/2A^*(a_i + b_i x_i + c_i y_i), \\ N_j &= 1/2A^*(a_j + b_j x_j + c_j y_j), \\ N_k &= 1/2A^*(a_k + b_k x_k + c_k y_k), \end{aligned} \tag{26}$$

where

N_i, N_j, N_k - shape functions,
A - area of the element:

$$A = \tfrac{1}{2}\det \begin{vmatrix} 1 & x_i & y_i \\ 1 & x_j & y_j \\ 1 & x_k & y_k \end{vmatrix} = \tfrac{1}{2}(a_i + a_j + a_k), \tag{27}$$

a,b,c - constants:

$$\begin{aligned} a_i &= x_j y_k - x_k y_j, \quad b_i = y_j - y_k, \quad c_i = x_k - x_j, \\ a_j &= x_k y_i - x_i y_k, \quad b_j = y_k - y_i, \quad c_j = x_i - x_k, \\ a_k &= x_i y_j - x_j y_i, \quad b_k = y_i - y_j, \quad c_k = x_j - x_i, \end{aligned} \tag{28}$$

x,y - coordinates of nodes i,j,k.

After substituting Equation (25) into Equation (24), the following equation for one element can be written:

$$[F^e] = [K^e][\delta^e], \tag{29}$$

where

$[F^e]$ - matrix of nodal point forces,

$[K^e]$ - element stiffness matrix.

The nodal point forces are defined by

$$[F^e] = \int_{S_e} (-x[\partial N/\partial x]^T + y[\partial N/\partial x])dS, \tag{30}$$

and the stiffness matrix is

$$[K^e] = \int_{S_e} ([\partial N/\partial x]^T[\partial N/\partial x] + [\partial N/\partial y]^T[\partial N/\partial y])dS, \tag{31}$$

Differentiating the shape functions (26) leads to

$$[\partial N/\partial x] = 1/2A * [b_i, b_j, b_k],$$
$$[\partial N/\partial y] = 1/2A * [c_i, c_j, c_k]. \tag{32}$$

With Equation (32), the stiffness matrix (31) and the nodal point forces (30) can be written as:

$$[K^e] = 1/4A \begin{vmatrix} b_i^2+c_i^2 & b_i b_j+c_i c_j & b_i b_k+c_i c_k \\ b_i b_j+c_i c_j & b_j^2+c_j^2 & b_j b_k+c_j c_k \\ b_i b_k+c_i c_k & b_j b_k+c_j c_k & b_k^2+c_k^2 \end{vmatrix}, \tag{33}$$

$$[F^e] = 1/2A \begin{vmatrix} -x_c c_i+y_c b_i \\ -x_c c_j+y_c b_j \\ -x_c c_k+y_c b_k \end{vmatrix}, \tag{34}$$

where

(x_c, y_c) - coordinates of the centroid of the element:

$$x_c = 1/3 * (x_i + x_j + x_k),$$
$$y_c = 1/3 * (y_i + y_j + y_k). \tag{35}$$

In the final step of the assembly of the system matrix, the subroutine ASSEM imposes the displacement boundary condition, i.e, the value of zero for the warping function in the centre of the section.

The system matrix is solved by the subroutine SOLVE. This is done by Gauss elimination procedure for banded symmetric system of equations [36, 46, 49]. Also in the subroutine SOLVE, the original numbers, as specified in SPEC, are assigned to the nodes. This is done by the subroutie RENUM.

Having calculated the values of the warping function ϕ at each node (by solving the system matrix), the subroutine STRESS is executed. This subroutine calculates stresses in the centroids of each of the elements using the finite element formulation of Equations (19), i.e,

$$\tau_{yz} = \alpha G/2A * (c_i \phi_i + c_j \phi_j + c_k \phi_k) + x_c,$$
$$\tau_{zx} = \alpha G/2A * (b_i \phi_i + b_j \phi_j + b_k \phi_k) + y_c, \qquad (36)$$

where

$\phi_{i,j,k}$ - values of the warping function at nodes i,j,k.

The applied torque on the section is also calculated in STRESS. The value of this torque is approximated using the finite element formulation of Equation (22) by summing over the system of n elements representing the section:

$$T = \alpha G \Sigma (I_e + J_e), \qquad (37)$$

where

$$I_e = \int (x\partial\phi/\partial y - y\partial\phi/\partial x)dA$$

$$= \int (x[\partial N/\partial y][\delta^e] - y[\partial N/\partial x][\delta^e])dA$$

$$= \tfrac{1}{2}(x_c c_i - y_c b_i)\phi_i + \tfrac{1}{2}(x_c c_j - y_c b_j)\phi_j + \tfrac{1}{2}(x_c c_k - y_c b_k)\phi_k,$$

and

$$J_e = \int (x^2 + y^2)dA$$

$$= A/6*(x_i^2+x_j^2+x_k^2+y_i^2+y_j^2+y_k^2+x_i x_j+x_j x_k+x_k x_i$$

$$+y_i y_j+y_j y_k+y_k y_i).$$

The last subroutine which is invoked from the subroutine TORO is called OUTPUT. This subroutine calculates the maximum shear stresses in the elements which are located at the boundary of the section. These maximum shear stresses are calculated from:

$$TMAX = (\tau_{yz}^2 + \tau_{zx}^2)^{\frac{1}{2}}, \qquad (38)$$

where

TMAX - maximum shear stress.

TMAX is then divided by the value of the torque T which was calculated from Equation (37). In this way, the values of TMAX represent the values of the maximum shear stresses in the section due to a unit torque. The value of the highest maximum shear stress and the corresponding point number in the section are subsequently calculated. These values are returned to the main program PROCO.

After the calculation of the maximum shear stresses in each of the sections has been completed, the main program PROCO approximately calculates the values of the torsion moments which act on each section due to the force S (see Figure 24). These values are calculated by multiplying the value of S by the distance from the line of action of S to the centre of each of the sections. (The offset between the line of action of S and the centroid of the section is calculated; see Figure 24.) The maximum values of the shear stresses in each section is derived form the multiplication of the appropriate values TMAX (maximum shear stresses due to unit torque) with the values of the torsion moments. PROCO writes the results of the torsion calculation into the output file STRESS. The section number, the number of the point and the maximum shear stress at the same point are given (see example of file STRESS in Appendix 3).

In the final part of the program PROCO, it is possible, on request, to estimate the influence of simple redesign measures on the magnitude of stresses in the prosthesis. Two such redesign measures are provided: firstly, the length of the neck of the prosthesis can be shortened, and secondly, the neck angle can be increased. If one of these measures is requested, the program PROCO calculates new values of the stresses according to the changed parameter. The results of the new calculation is also written to the output file STRESS.

2.4. EXPERIMENTAL WORK

2.4.1. 3D Photoelasticity

In order to verify the mathematical models, an alternative method for calculating the stresses in the prosthesis was needed. In the literature, results from calculations with mathematical models are often compared with experimental results from strain gauge measurements (see Chapter 2.2.3). In the case of the HERAMED prosthesis, however, this method was not suitable. The strain gauges available on the market need a relatively large space in order to be attached to the component under investigation. (For the smallest strain gauges, the space needed is approximately 4 mm x 2 mm.) This space is, in general, not available neither between the steps nor in the transition radii on the surface of the prosthesis[23]. Thus, it was decided to investigate the stresses in the prosthesis with the technique of three-dimensional photoelasticity by stress freezing.

Three-dimensional photoelasticity by stress freezing is a well-established and well-documented technique for stress analysis of three-dimensional components [51, 52]. In this technique, a scale model of the component under investigation is made from a photoelastic material. The model is then subjected to a heat treatment cycle under load. The material properties are such that on cooling, the stresses are effectively 'frozen' into the model. Thin slices in the areas of interest are cut from the model and they are subsequently investigated by two-dimensional photoelasticity. As a result of the investigation, the magnitudes of principal stresses and the directions of principal stresses can be obtained at each point of the slices.

---

[23] In fact, one prosthesis was investigated with the help of strain gauges [53]. The results showed that the measurement was strongly influenced by the stress concentrations in the transition radii and by the embedding. Thus, the interpretation of these result was difficult.

In the case of the prosthesis, the model was produced by casting. The mould which was used in the casting was prepared in the following way:

1. The prosthesis with connecting pipes and alignment pins were placed in a wooden box.

2. Plaster of Paris was poured into the box until approximately half of the prosthesis (along its axis) was covered.

3. After the plaster of Paris had hardened, silicone rubber[24] was poured into the box until the prosthesis was entirely covered.

4. The box was placed in an oven where the rubber was allowed to harden (to cure) for two days at 70°C.

5. The plaster of paris was removed and the surface of the prosthesis and the silicone rubber cleaned. The cleaned surfaces were then sprayed with silicon mould release agent.

6. The silicone rubber was poured over the second half or the prosthesis.

7. The rubber was cured as in 4.

8. The prosthesis was then removed. The adjacent surfaces of the two halves of the mould were covered with silica gel and connecting pipes, 15 mm in diameter, were attached in such a way that they enabled an ascending casting (Figures 32 and 33). The mould was subsequently clamped together and sealed with silicone sealing paste.

The photoelastic material used in the castings was Araldite CT200 with HT907 hardener[25]. This material has the property that above a certain

---

[24] SILASTIC, J RTV silicone rubber, Dow Corning, Senefee, Belgium

[25] Sharples, Stress Engineers, Ltd., Preston, U.K.

critical temperature (approximately 135°C), it changes its structure from glass-like to rubber-like. If the material is loaded in its rubber-like state and then cooled slowly until room temperature is reached, the strain induced by the loading does not vanish even if the loading is removed and the model cut into slices. The material also has the property that if stressed, it exhibits different refractive indices in each of the principal stress directions. Thus, when viewed in polarised light, fringe patterns can be seen, from which, using well-established techniques, the principal stress values can be obtained.

Prior to casting, 300 grammes of Araldite CT200 was melted at 140°C. 240 grammes of melted hardener HT907 at 100°C was then added through a fine sieve to the Araldite. The mixture was then mixed thoroughly and poured into the mould which had been preheated to 100°C. At the same time as the model of the prosthesis, a sheet of the material, 3 mm in thickness, was also cast. The mould for the prosthesis and for the sheet were then kept in an oven at 100°C for four days. After this, the oven temperature was reduced slowly at the rate of 2°C per hour to approximately 75°C. The castings were removed from the moulds and were finally cured at 130°C for one day in a Glycerine bath. The temperature was then reduced slowly to room temperature.

A hole, 1.5 mm in diameter, was drilled through the neck of the model of the prosthesis. This hole was used for attaching the load during the heat treatment cycle. The model was then embedded in Araldite in such a way that the axis of the model was tilted by 10° from the vertical and the embedding level was approximately 50 mm below the basic-step (Figure 34). Prior to the embedding, the model of the prosthesis was covered with a thin layer of silica gel in order to prevent melting of the model by the hot Araldite during the casting of the embedding. A disc, 30 mm in diameter was cut from the sheet of material which had been cast in parallel with the model of the prosthesis. This disc was placed in a rig which enabled compressive loading of the disc along its diameter (Figure 35). The model of the embedded prosthesis and the rig with the disc were placed in an oven. The temperature in the oven was then raised to 135°C. After one hour, the model and disc were loaded. After approximately thirty minutes more, the reduction of the temperature at the rate of 2°C per hour to room temperature was begun. From the model of the

prosthesis, a thin slice (approximately 2.7 mm in thickness), along the axis of the prosthesis and parallel to the axis of the neck was carefully machined. After machining, the surfaces of the slice were polished by hand in order to remove any machining marks. The slice and the disc were then ready for the photoelastic investigation.

The apparatus used in the photoelastic investigation was the so-called transmission polariscope (Figure 36). In this polariscope, a slice from the model under investigation is placed between two polaroids. The first polaroid is called the polarizer and the second, the analyser. White or monochromatic light is passed through the polaroids and the slice. The slice is observed behind the analyser with the help of a travelling microscope. If the polariscope consists only of the polaroids, it is called a plane polariscope. If, in addition to the polaroids, also quarter-wave plates are placed between the polaroids, it is called a circular polariscope. The plane polariscope works in the so-called dark-field mode if the optical axis of the polaroids are crossed (are perpendicular to each other). The circular polariscope works in the dark-field mode if the axis of the polaroids are crossed and the axis of the quarter-wave plates are crossed and at 45° to those of the polaroids.

Two types of fringes, i.e. line patterns in a stressed slice, can be observed in a polariscope. The fringes of the first type are called isochromatics. Isochromatics are lines of constant principal stress difference. If white light is used, these lines are coloured with the exception of the fringes of the so-called order zero, which are black. The second type of fringes are called isoclinics. These are black lines at which the directions of the principal axes of stresses are parallel to the axes of crossed polaroids. If the polaroids are rotated, the isoclinics pattern also rotates. The isochromatics, however, remain unchanged. From the pattern of isoclinics, the so-called stress trajectories can be drawn. Stress trajectories are lines drawn such that their direction at any point coincides with that of one of the principal stresses at the point. In the plane polariscope, the isochromatics and the isoclinics can be observed simultaneously. In the circular polariscope, only isochromatics can be seen. In the dark-field mode, the isochromatics are assigned fringe orders which are whole numbers starting from fringes with the fringe order zero. In the circular polariscope, it

is also possible to determine fractional fringe orders at any point of the slice. The method of doing this is called the Tardy compensation method. In this method, the axis of the polaroids are set parallel to the axes of principal stresses in the model at the point under observation. This is done by rotating the crossed polaroids with the quarter-wave plates removed, until an isoclinics passes through the point. The quarter-wave plates are then inserted with their axis crossed and at 45° from those of the polaroids. The analyser is then rotated until an isochromatics of known (whole) fringe order passes through the point under observation. The angle by which the analyser has to be rotated is called the angle of compensation. The value of this angle when divided by π gives the fractional fringe order which has to be added or subtracted from the fringe order of the fringe which was brought to the point under observation.

Equation which relates the fringe orders with the stresses in the slice is the so-called stress-optic law:

$$\sigma_1 - \sigma_2 = n*f/d,$$

where

$\sigma_1 - \sigma_2$ - difference between the principal stresses in the plane of the slice,
f - constant depending on the material and the wavelength of the light used. f is called the material fringe value or the fringe-stress coefficient [N/mm].
n - fringe order,
d - thickness of the slice.

At a free surface of, i.e., at the contour of the slice, one of the principal stresses (perpendicular to the surface) is equal to zero. Therefore, it can be seen that by measuring the fringe orders at a point on the surface leads directly to the value of the principal stress at this point, providing that the fringe-stress coefficient of the photoelastic material is known.

In the case of the model of the prosthesis, the fringe-stress coefficient of the material was established from measuring the fringe order

in the centre of the disc, which was cast and heat treated in parallel with the model. From the theory of elasticity, the magnitudes of the principal stresses in the centre of a disc subjected to a compressive force which acts along the diameter of the disc are as follows:

$$\sigma_1 = 2P/(\pi Dd),$$

$$\sigma_2 = 6P/(\pi Dd),$$

where

P - value of the force,
D - diameter of the disc,
d - thickness of the disc.

Substituting these expressions for the principal stresses into the stress-optic law leads to the following expression for the fringe-stress coefficient:

$$f = (\sigma_1-\sigma_2)d/n = 8P/(\pi Dn),$$

where

n - fringe order in the centre of the disc.

The value of the fringe-stress coefficient for the disc was used in calculating the stresses with the stress optic law along the surface of the slice which was machined from the model of the prosthesis. Fringe orders were measured at points on the surface of the slice. The points lay in the roots of the transition radii and in spaces between them. The fringe orders were measured using monochromatic light from a mercury vapour bulb. While measuring the fringe order at one point, the following procedure was used:

1. The cross-hair of the travelling microscope was positioned on the point under investigation.

2. The value of the fringe order was measured with the Tardy method and while doing this the analyser was rotated until a given fringe just disappeared at the surface of the slice.

3. The analyser was then rotated back until the fringe just emerged at the surface.

4. The average of the values of the fringe orders obtained in steps 2 and 3 was taken.

This procedure was conducted several times at the same point. The final value of the fringe order at one point was obtained by averaging the results of all the measurements at this point.

In this work, the total of three different prosthesis were investigated with the technique of 3D photoelasticity by stress freezing.

2.4.2. Scattered-light Photoelasticity

Scattered-light photoelasticity is a photoelastic method which enables an experimental stress analysis of a three-dimensional component without the need for the stresses to be frozen and without the slicing of the model [54]. The use of this method, therefore, seemed to be appropriate for the case of the prosthesis. The applicability of the scattered-light method was evaluated on a problem related to the estimation of the stress concentration factors in the transition radii between the steps of the prosthesis. In Chapter 2.3.2.2, it was stated that the calculation of the stress concentration factors for a generally shaped step of the prosthesis is not possible with the finite element method. In the simple mathematical model of the prosthesis (Chapter 2.3.4), the magnitude of the stress concentration factors is estimated on the basis of charts from the literature. These charts, however, do not take into account that the shapes of the sections of the prosthesis are highly irregular and that the sections are not 'symmetric' in respect to each other. They are not 'symmetric' in the sense that their centroids do not lie on a straight line, in other words, there is an offset or 'eccentricity' between the centroids. In the literature, there is no indica-

tion if such an eccentricity can influence the value of the stress concentration factors. Thus, it was decided to investigate this problem with the scattered-light photoelasticity. The problem was simplified, i.e, it was attempted to measure the stress concentration factors in round bars with a fillet and an eccentricity subjected to pure bending. In this way, the results of the investigation could be compared with the results from the literature for the case of concentric round bars with a fillet subjected to pure bending (Figure 29).

The theory and the methodology of scattered-light photoelasticity are well-described in the literature [54, 55, 56, 57, 58, 59]. The technique uses preferably a low power laser as the source of monochromatic light. The light is passed through a model of the component under investigation which is made of a photoelastic material, i.e, a material which is transparent and which if stressed, it exhibits different refractive indices in the directions of principal stresses. In order to reduce any disturbing scatter or reflection of the light at the surface, the model is usually submerged in an immersion fluid. In an ideal situation, the refractive index of the immersion fluid matches that of the photoelastic material. On its way through the model, the light is scattered on small inclusions which are always present in the model. The scattered-light is plane polarized and propagates in directions perpendicular to the direction of the incident light. If scattered-light from a stressed model is observed , its intensity is a minimum and maximum along the path of incident light. In this way, a fringe pattern is observed. From such fringe patterns, it is possible to calculate the magnitude of principal stresses at each point of the path of the incident light in the model.

The stress-optic law in scattered-light photoelasticity is as follows:

$$\sigma_1 - \sigma_2 = (dn/ds)*f,$$

where

$\sigma_{1,2}$ - principal stresses at point of interest,
n - fringe order at point of interest,
s - distance from the entry point of incident light to point of interest,
f - fringe-stress coefficient.

This equation is valid for the case where the direction of the incident light is parallel to the direction of the third principal stress[26], σ_3, and where the directions of the principal stresses σ_1 and σ_2 do not rotate along the path of the incident light [55]. If these conditions are satisfied, the difference between two of the principal stresses at any point along the path of the incident light can be obtained as follows:

1. The light is passed through the model in the direction parallel to that of the third principal stress[27].

2. Starting from the entry point of the light into the model, the fringes are assigned appropriate fringe orders, i.e., whole numbers.

3. Along the direction of propagation, the distances from the entry point of the light to the fringes and up to the point of interest are measured.

4. A curve which expresses the dependence of Δn from Δs is drawn, where Δn denotes the difference in fringe orders of two fringes and Δs, the difference in the distance between these fringes.

5. A tangent is then drawn at the point of interest. The slope of this tangent is directly proportional to the principal stress difference at the point.

---

[26]The stress-optic law is also valid in the case where the direction of the light propagation is not parallel to the direction of one of the principal stresses. In this case, the difference between two stresses with directions perpendicular to that of the light propagation is measured. These stresses, however, are not the principal stresses.

[27]The directions of the principal stresses can be found either from theoretical considerations or experimentally [54, 59].

In scattered-light photoelasticity, the incident light is usually plane or circular polarized. If the light is plane polarized, the maximum contrast of the fringe pattern is achieved if the plane of polarization is inclined 45° to the directions of principal stresses σ_1 and σ_2, and if the the fringe pattern is observed perpendicular to the direction of light propagation in the direction perpendicular or parallel to the plane of polarization [59]. If circular polarized light is used, the maximum contrast of the fringe pattern is observed perpendicular to the direction of light propagation and at 45° (or 135°) to the directions of the principal stresses [56]. In the case of plane polarized light, the first fringe from the entry point of the incident light into the model has an order equal to one or one half. In the case of circular polarized light, the first fringe has an order equal to one quarter or threequarters [58]. In any practical case, the value of the fringe order of the first fringe can be easily determined. This is done simply by comparing the fringe patterns observed from different directions.

It has already been mentioned that the scattered-light method was used for estimating the influence of an eccentricity on the value of the stress concentration factor. An attempt was made to measure this influence on round bars with a fillet which were subjected to pure bending. The preparation of specimens for investigation was conducted in the following way. Firstly a number of round bars with uniform diameter were cast from Araldite CT200. The method of the casting was equivalent to that for casting the models of the prosthesis (see Chapter 2.4.1). These bars were then machined to the desired shape. A schematic drawing of the shape of the specimens is shown in Figure 37. The specimens consisted of two sections which had the shape of round bars. The diameter of one section was equal to 20 mm and the diameter of the second section was equal to 30 mm. There was a transition radius between the sections. The specimens were machined in such a way that in some specimens, the sections were concentric and in others, eccentric. The eccentricity of the specimens was defined as the distance between the centres of the sections. The total of 13 specimens was produced. They were as follows:

1. Concentric with 5 mm fillet radius,
2. Concentric with 3 mm fillet radius,

3. Concentric with 1 mm fillet radius,
4. 1 mm eccentric with 4 mm fillet radius,
5. 1 mm eccentric with 3 mm fillet radius,
6. 1 mm eccentric with 2 mm fillet radius,
7. 1 mm eccentric with 1 mm fillet radius,
8. 2 mm eccentric with 3 mm fillet radius,
9. 2 mm eccentric with 2 mm fillet radius,
10. 2 mm eccentric with 1 mm fillet radius,
11. 3 mm eccentric with 2 mm fillet radius,
12. 3 mm eccentric with 1 mm fillet radius,
13. 4 mm eccentric with 1 mm fillet radius.

After the machining of the specimens, their surfaces were polished in order to remove any machining marks. The specimens were then subjected to a heat treatment cycle which was aimed at removing any stresses which could have been introduced into the specimens during the machining process. During this heat treatment cycle, the specimens were placed in a glycerine bath, kept for two hours at 140°C and then slowly cooled (2°C/1 hour) to room temperature.

The stress relieved specimens were then placed in a loading rig. This loading rig enabled the loading of one specimen at time in the four point bending mode (Figure 38). Thus, away from the supporting pins, the loaded specimen was subjected to a pure bending moment.

The experimental set-up which was used in this work is shown in Figure 39. As the light source, a helium-neon gas laser was used[28]. This laser had the output power of 20 mW and produced a continuous beam of plane polarized light. The laser was mounted on an adjustable support which enabled it to be rotated about its axis. The light from the laser was passed through a set of apertures onto an adjustable mirror. Optionally, a quarter-wave plate could be placed between the apertures. After having been reflected from the mirror, the light entered an immersion tank. The immersion tank was a rectangular glass container and it was filled with

[28]Helium-neon laser model 106-1, SPECTRA-PHYSICS Inc., Eugene, Oregon, U.S.A.

olive oil as the immersion fluid. The refractive index of the olive oil of approximately 1.56 does not exactly match the refractive index of the Araldite which is approximately 1.6. An exact match between the refractive indices of the immersion fluid and the Araldite would have been possible if a mixture of α-bromonaphtalene and liquid paraffin was used. The α-bromonaphtalene, however, can cause dermatitis and may be carcinogenic. Therefore, on the grounds of safety, olive oil was used. A video camera was positioned[29] perpendicular to the direction of propagation of the light in the immersion tank. This camera was connected to a video monitor[30].

During measurements, the loading rig with the specimen was placed in the immersion tank. Two positions of the rig were possible in the tank. In the first position, the specimen lay horizontally. This position was designed to measure stresses in the specimen away from the fillet. In the second position, the specimen was at 45° to the horizontal. This position was designed to measure stresses in the root of the fillet radius. The laser, the apertures and the mirror were adjusted until the light from the laser in the form of a beam was perpendicular to the surface of the specimen. Thus, the positions of the specimen with respect to the direction of the laser beam ensured that the beam entered the specimen in the direction parallel to that of one of the principal stresses at the surface (Figure 40). (The direction of the principal stresses are readily obtained by considering the bending theory.) The video camera was positioned in such a way that the direction of observation of the scattered-light was perpendicular to the direction of propagation of the laser beam and at 45° to the directions of the principal stresses in the specimen(Figure 41). Thus, a magnified picture of the scattered-light fringe pattern could be observed on the video monitor. The laser was then rotated along its axis until the fringe pattern showed a maximum contrast. In this position, the polarization plane of the laser light was at 45° to the directions of the principal stresses.

---

[29]Video camera model AVC-3250CE, SONY, Japan

[30]Video monitor model VM 900E/K, Hitachi, Japan

A quarter-wave plate was inserted between the apertures in such a way that one of its axes was parallel to the polarization plane of the light (Figure 41). By rotating the laser in steps of 45° about its axis, it was thus possible to make the light circular or plane polarized. (In the initial position of the laser, the light entering the specimen was plane polarized. After rotating the laser by 45°, the light was circularly polarized. By rotating the laser by further 45°, the light became once more plane polarized, but the direction of polarization was perpendicular to that in the initial position. After the laser was rotated by further 45°, the light was circularly polarized, but the direction of rotation of the light vector was opposite to that in the previous circularly polarized light (see Figure 42).) Also by rotating the laser, it was possible to establish the value of the fringe order of the first fringe in the pattern. In the case of plane polarized light, the first fringe was assigned the value of one half for the position of the laser in which the fringe was nearer to the entry point of the laser beam into the specimen, i.e., nearer to the surface of the specimen. Otherwise, the first fringe had the order equal to one. In the case of circularly polarized light, the first fringe was assigned the value of one quarter for the position of the laser, in which the fringe was nearer to the surface. Otherwise, the fringe had the order equal to three quarters. It has to be noted that by rotating the laser, the position of the fringe pattern is changed. This process is similar to the Tardy method of compensation and was used for determining fractional fringe orders at points along the light propagation in the specimen [59].

Two measurements were conducted on each of the specimens. The first measurement was carried out with the light entering the specimens away from the fillet and the second, with the light entering the specimens at the root of the fillet. During each of the measurements, the laser was positioned in such a way that the first fringe had a value of fringe order equal to one. The distances of the fringes in the fringe pattern from the surface of the specimen under investigation were measured on the video monitor. The laser was then rotated until a change in the position of the fringe patterns could be observed. In practice, this meant that the laser had to be rotated by 30°, or the laser was rotated by 45°. The distances of the fringes from the surface were once more measured. The procedure of rotating the laser and measuring the dis-

tances of the fringes was repeated until the laser was rotated to its initial position. A graph of fringe order against fringe distances from the surface was produced. A curve was drawn through the points of the graph. A tangent at the point of this curve which represented the surface of the specimen was than drawn and its slope calculated. In calculating the stress concentration factors it was assumed, in accordance with bending theory, that at the surface, the value of the principal stress σ_1 was much larger than that of the stress σ_2. The value of the principal stress σ_3, in the direction perpendicular to the surface, was equal to zero as the surface was not loaded externally. Taking into consideration the stress-optic law, the slope of the tangent was, therefore, directly proportional to the value of the slope of the tangent, the proportionality factor being the fringe-stress coefficient. The stress concentration factor is defined as the ratio of the maximum stress in the root of the fillet radius to the maximum stress away from the fillet (see Chapter 2.3.2.2). Thus, the stress concentration factor was calculated by dividing the value of the slope of the tangent obtained from measurement in the fillet, by that obtained from measurement away from the fillet. In doing this, the value for the fringe-stress coefficient was cancelled out. Therefore, there was no need to establish its value. This also meant, that the value of the bending moment did not have to be known, provided that the bending moment was not changed during the measurements on one specimen.

2.5. RESULTS

2.5.1. FEM-model

The finite element model was used for calculating stresses in three prostheses. These prostheses had the designations F063, F076 and G035. These prostheses were also investigated with three-dimensional photoelasticity by stress freezing. Calculations with the finite element model, using the program PROEM (see Chapter 2.3.2.2), were carried out for the following cases:

1. Stresses were calculated for each of the prostheses without the embedding. This case was aimed at comparing the results of the FE-analysis with the results from the simple model and with those from the photoelastic experiments. The models were loaded at points, coordinates of which were calculated for the point where the load was attached to the photoelastic model. The value of the load was equal to that used during the photoelastic experiments.

2. Stresses were calculated for embedded prostheses. As this case was aimed at comparing the results with the results from the photoelastic experiments, the material constants of the prostheses and of the embedding were set equal to those of Araldite at the stress freezing temperature, i.e., the elasticity modulus E was set equal to 15 N/mm² and the Poisson's ratio ν set equal to 0.4[31] [51]. The coordinates of the loading point and the value of the load were equal to these in the case one.

[31] The Poisson's ratio of Araldite above the critical temperature is equal to 0.48. This value, however, could not be used in the finite element model as in this case, the system matrix is ill conditioned. The value of 0.4 for the Poisson's ratio is therefore an approximation.

3. Finally, stresses were calculated for embedded prostheses. The load was applied in the centre of the head of the prostheses. For simplicity, the value of the load was assumed to be equal to 1N. The material constants were set equal to these of the material of the prostheses, i.e., Ti-5Al-2.5Fe alloy, and of the embedding, i.e., PMMA. These values were E = 112GPa and ν = Ø.32 for Ti-5Al-2.5Fe, and, E = 3.5GPa and ν = Ø.33 for PMMA [24]. This case was aimed at showing the influence of different material properties of the prostheses and the embedding on the stresses in the embedded part of the prostheses , and at estimating the stresses in the prostheses during DIN-tests.

The results of the finite element analysis were evaluated with the help of the PIGS package (see Chapter 2.3.2.2). Direct and von Mises stresses[32] were plotted along cross sections of the finite element models. The maximum (positive) and the minimum (negative) stresses were identified on each of these plots. The values of these stresses were then plotted along the z-axes of the prostheses.

Typical examples of plots of stresses along a cross section of the model of the prosthesis F076 are shown in Figures 43 and 44. Figure 43 shows the values of the stresses for a cross section above the embedding level and Figure 44, for a section at the embedding level. In both the figures, the values of the direct stresses: σ_x, σ_y and σ_z, and, the von Mises stress are shown against the node numbers.

---

[32] Direct stresses are stresses along the axes of the coordinate system, i.e, the stresses σ_x, σ_y and σ_z. The von Mises stress is an effective stress which is calculated form the following formula:

$$\sigma_e = {}^1/\sqrt{2}\,\{(\sigma_x-\sigma_y)^2+(\sigma_y-\sigma_z)^2+(\sigma_z-\sigma_x)^2\}^{1/2},$$

where

σ_e - the von Mises stress.

Plots of maximum (tensile) and minimum (compressive) stresses along the z-axes of embedded prostheses (analysis according to the case 2) are shown in Figures 45-56. Figures 45 and 47 show the maximum and minimum direct stresses, and, Figures 46 and 48, the respective von Mises stresses along the z-axis of the prosthesis FØ63. The same types of plots for the prostheses FØ76 and GØ35 are shown in Figures 49-52 and 53-56 respectively.

Figures 57-60 show the maximum and minimum direct stresses and the von Mises stresses for the prosthesis FØ76, which were calculated according to the case 3. The values of these stresses are plotted along the z-axis of the prosthesis.

The plots for the maximum and minimum von Mises stresses (Figures 46, 48, 50, 52, 54 and 56) and similar plots for prostheses without the embedding (acording to the case 1) served as the basis for comparing the result of the finite element analysis with the results from photoelastic experiments. The values of these von Mises stresses are shown in the tables below. By definition, the von Mises stresses are always positive. However, in order to be able to distinguish between the stresses which were calculated for positive direct stresses and these which were calculated for negative direct stresses, the values of the von Mises stresses were regarded as positive for positive direct stresses and negative for negative direct stresses. Table 2.5.1.1, Table 2.5.1.2 and Table 2.5.1.3 show the values of the von Mises stresses for the prostheses FØ63, FØ76 and GØ35 respectively. A graphic representation of theses values can be found in Figures 79, 80, 81, 85, 86 and 87.

Table 2.5.1.1. FEM-model of prosthesis F063. Values of von Mises stresses for comparison with the results from photoelasic experiments.

z-coordinate [mm]	without embedding σ_e x1000 [N/mm²]		with embedding σ_e x1000 [N/mm²]	
	max.	min.	max.	min.
8	400	-444	-	-
16	346	-356	-	-
24	331	-350	-	-
32	314	-327	-	-
40	306	-320	-	-
48	320	-334	3	-0.8
56	267	-336	3	-3.4
64	251	-273	8	-13.7
72	203	-235	53	-60
80	151	-197	120	-144
84	-	-	142	-180
88	111	-133	116	-142
96	77	-101	79	-100
104	40	-56	40	-81
112	20	-49	26	-67
120	-	-	19	-46

Table 2.5.1.2. FEM-model of prosthesis F076. Values of von Mises stresses for comparison with the results from photoelasic experiments.

z-coordinate [mm]	without embedding σ_e x1000 [N/mm²]		with embedding σ_e x1000 [N/mm²]	
	max.	min.	max.	min.
8	418	-446	-	-
16	372	-420	-	-
24	341	-372	-	-
32	307	-349	-	-
40	287	-327	3	-1
48	281	-318	3	-4
56	261	-318	12	-24
64	224	-236	55	-67
72	205	-259	163	-197
76	-	-	194	-234
80	182	-207	182	-215
88	162	-241	156	-234
96	139	-159	142	-165
100	-	-	101	-148
104	97	-151	76	-124
112	28	-137	12	-112

Table 2.5.1.3. FEM-model of prosthesis G035. Values of von Mises stresses for comparison with the results from photoelasic experiments.

z-coordinate [mm]	without embedding σ_e x1000 [N/mm²]		with embedding σ_e x1000 [N/mm²]	
	max.	min.	max.	min.
8	28	-116	-	-
16	72	-162	-	-
24	108	-192	-	-
32	146	-214	-	-
40	152	-238	2	-1.8
48	166	-224	4	-2.6
56	166	-232	6	-6.4
64	172	-238	8	-18
72	190	-254	44	-70
80	194	-252	154	-206
88	206	-250	204	-258
96	160	-206	160	-222
104	118	-164	124	-160
112	48	-108	70	-88
120	-	-	24	-96

As described in Chapter 2.3.2.2, a finite element model was developed (program COSCF) which enablend an estimation of stress concentration factors along the transition zone between two sections of the prosthesis. An example of such estimation is shown for the section 12 of the prosthesis F076 with the value of the transition radius equal to 2 mm. The geometry of this section is shown in Figure 61. Plots of maximum direct and von Mises stresses along the transition zone for the models representing the section of the prosthesis with no transition radius,

with one third of the transition radius, with two thirds of the transition radius and the whole transition radius (see Figures 17-20) are shown in Figures 62-69 respectively. The plots showing the von Mises stresses were used for calculating the stress concentration factors. The values of these stresses and the values of the stress concentration factors are shown in Tables 2.5.1.4 and 2.5.1.5 respectively.

Table 2.5.1.4. Values of von Mises stresses along the transition zone for model of section 12 of prosthesis F076.

Number	no radius $\sigma_e \times 10^{-3}$ [N/mm²]	one third $\sigma_e \times 10^{-3}$ [N/mm²]	two thirds $\sigma_e \times 10^{-3}$ [N/mm²]	whole radius $\sigma_e \times 10^{-3}$ [N/mm²]
1	4.01	4.40	5.64	5.73
2	3.02	3.24	4.03	4.19
3	1.41	1.41	1.77	1.95
4	0.19	0.42	0.57	0.61
5	1.94	2.03	2.55	2.89
6	3.39	3.72	4.53	4.84
7	3.91	4.13	5.09	5.35
8	3.06	3.38	4.03	4.41
9	1.78	1.84	2.67	2.69
10	0.33	0.47	0.60	0.62
11	1.65	1.67	2.12	2.24
12	2.87	3.14	3.82	3.85

Table 2.5.1.5. Values of stress concentracion factors calculated from Table 2.5.1.4.

Number	no radius	one third	two thirds	whole radius
1	1	1.10	1.41	1.43
2	1	1.07	1.33	1.39
3	1	1.00	1.26	1.40
4	1	2.21	3.00	3.21
5	1	1.05	1.31	1.49
6	1	1.10	1.34	1.42
7	1	1.06	1.30	1.37
8	1	1.10	1.32	1.44
9	1	1.03	1.50	1.51
10	1	1.42	1.82	1.85
11	1	1.01	1.28	1.36
12	1	1.09	1.33	1.34

In the literature, the valuas of stress concentration factors are usually presented in the form of graphs (see Figures 28 and 29). In such graphs, the stress concentration factors are shown against two factors. The first factor is equal to the ratio of the value of the transition radius (r) to the value of the smaller diameter of the section (d). The second factor is equal to the ratio of the value of the larger diameter (D) to that of the smaller diameter (d). Table 2.5.1.6 shows the values of the diameters for each of the point on the transition zone for each of the models. These diamenters were calculated as described in Chapter 2.3.2.2, i.e, they are the values for the distances from the points to the centre of the section plus a value which represents the height of the transition zone (see Figure 61). The height of the transition zone for the model with one third of the transition radius was calculated from the formula:

$h = r*(1-\cos 30°)$,

and the height of the transition zone for the modes with two thirds of the transition radius, from the formula:

$h = r*(1-\cos 60°)$

where

h - height of the transition zone,
r - value of the transition radius; r=2 mm.

The height of the transition zone for the model with the whole transition radius was equal to the value of the transition radius, i.e, h = 2 mm.

Table 2.5.1.6. Values of the diameters for each of the points in the transition zone of section 12 of prosthesis F076.

Number	no radius ½d [mm]	one third ½D [mm]	two thirds ½D [mm]	whole radius ½D [mm]
1	7.71	7.98	8.71	9.71
2	7.34	7.61	8.34	9.34
3	7.02	7.29	8.02	9.02
4	7.07	7.34	8.07	9.07
5	7.80	8.07	8.80	9.80
6	6.98	7.25	7.98	8.98
7	6.24	6.51	7.24	8.24
8	6.52	6.79	7.52	8.52
9	8.08	8.35	9.08	10.08
10	7.21	7.48	8.21	9.21
11	6.24	6.51	7.24	8.24
12	6.52	6.79	7.52	8.52

Table 2.5.1.7 shows the values of ratios between the diameters from Table 2.5.1.6.

Table 2.5.1.7. Values of ratios r/d and D/d for section 12 of prosthesis F076.

Number	r/d	one third D/d	two thirds D/d	whole radius D/d
1	0.13	1.04	1.13	1.26
2	0.14	1.04	1.14	1.27
3	0.14	1.04	1.14	1.28
4	0.14	1.04	1.14	1.28
5	0.13	1.03	1.13	1.26
6	0.14	1.04	1.14	1.29
7	0.16	1.04	1.16	1.32
8	0.15	1.04	1.15	1.31
9	0.12	1.03	1.12	1.25
10	0.14	1.04	1.14	1.28
11	0.16	1.04	1.16	1.32
12	0.15	1.04	1.15	1.31

Using the values of stress concentration factors from Table 2.5.1.5 and the values of the ratio D/d from Table 2.5.1.7, a series of graphs can be plotted, which show the stress concentration factors against the values of the ratios for each point in the transition zone. An example of one such graph is shown in Figure 70 for the point number 1 from Tables 2.5.1.5 and 2.5.1.7. From the geometrical data of the prosthesis,

and in this particular case, from the coordinates of points of sections 12 and 13, the value of D/d for point 1 can now be calculated[33]. (For the purpose of argument, this value in Figure 70 is assumed to be equal to 1.20.) Having calculated the value of D/d, the respective value of the stress concentration factor can be obtained from Figure 70. (For D/d=1.20, the stress concentration factor is found to be equal to 1.42.)

Using the values from Tables 2.5.1.5 and 2.1.5.7, the stress concentration factors can be compared with those from the literature. Table 2.2.5.8 shows values of stress concentration factors obtained from the chart in Figure 28 using the values of r/d and D/d from the Table 2.1.5.7. Figure 28 contains values of stress concentration factors from the literature for the case of a rectangular bar with a fillet, which is subjected to pure bending. The values in Table 2.1.5.8, therefore, show the values of the stress concentration which would be found by the simple model of the prosthesis (see Chapter 2.3.4). The stress concentration factors in Figure 28 are shown as a set of curves agains the values of r/d. Each of the curves is valid for one specific value of D/d. Because of the fact that the values of D/d in Figure 28 are not continuous, the values of the stress concentration factors for the values of D/d from Table 2.5.1.7 cannot be exactly calculated. Table 2.5.1.8 shows, therefore, a range of values of the stress concentration factors for each value of D/d from Table 2.5.1.7. (In the simple model, it is always the highest value in the range that is taken as the value of the stress concentration factor.)

[33]It is to be noted that the value of the ratio r/d will not change.

Table 2.5.1.8. Stress concentration factors from literature for values of D/d and r/d from Table 2.5.1.7.

Number	one third K_T	two thirds K_T	whole radius K_T*
1	1.30-1.41	1.52-1.60	1.64-1.70
2	1.30-1.40	1.50-1.58	1.62-1.66
3	1.30-1.40	1.50-1.58	1.62-1.66
4	1.30-1.40	1.50-1.58	1.62-1.66
5	1.30-1.41	1.52-1.60	1.64-1.70
6	1.30-1.40	1.50-1.58	1.62-1.66
7	1.28-1.38	1.48-1.52	1.56-1.60
8	1.28-1.40	1.48-1.55	1.58-1.64
9	1.32-1.44	1.56-1.62	1.68-1.74
10	1.30-1.40	1.50-1.58	1.62-1.66
11	1.28-1.38	1.48-1.52	1.56-1.60
12	1.28-1.40	1.48-1.55	1.58-1.64

* K_T - *stress concentration factor*

Figure 29 shows values of stress concentration factors for the case of a round bar with a fillet subjected to pure bending. If, instead of Figure 28, Figure 29 was used for obtaining the values of the stress concentration factors, the values in Table 2.5.1.8 would be up to 0.1 smaller.

2.5.2. BEM-model

With the boundary element model, stresses for only one of the investigated prostheses, F076, were calculated. The analysis was aimed at comparing the results from the boundary element model with these from the

finite element model and from the photoelasic experiments. The material properties of the prosthesis and the elastic constants of the linear springs modelling the embedding (see Figure 21) were set to equal these of Araldite at stress freezing temperature (according to the case 2 of the finite element models). Direct stresses along a section of the prosthesis above the embedding level and a section at the embedding level are shown in Figures 71 and 72 respectively. In Figures 73, 74, 75 and 76, direct and von Mises stresses along the z-axis of the prosthesis are shown. The values of the von Mises stresses for comparison with the results from the finite element analysis and from the photoelastic experiments were obtained from Figures 74 and 76. They are shown in Table 2.5.2.1. The corresponding values of the direct stresses are also shown in the same table. A graphic representation of the von Mises stresses can be found in Figure 80.

Table 2.5.2.1. BEM-model of prosthesis F076. Values of von Mises stresses for comparison with the results from finite element analysis and from photoelastic experiments.

z-coordinate [mm]	von Mises σ_e x1000 [N/mm²]		direct σ_z x1000 [N/mm²]	
	max.	min.	max.	min.
68	46	-104	-6	-6
72	46	-52	18	-45
76	160	-186	249	-336
78	292	-262	294	-417
80	166	-230	288	-413
82	292	-306	279	-384
84	108	-122	278	-242
86	240	-226	225	-202
88	90	-110	186	-210
96	174	-188	148	-243
103	60	-80	90	-177

2.5.3. Simple Model

Tables 2.5.3.1, 2.5.3.2 and 2.5.3.3 show values of stresses, as calculated with the simple model, along the z-axes of the prostheses F063, F076 and G035 respectively. These values were calculated in such a way that they can be directly compared with the results from the photoelastic experiments. The embedding was not considered in the calculation. The value of the transition radius for the prostheses F063 and F076 was equal to 1 mm, and that for the prosthesis G035 was equal to 2 mm. A graphic representation of the values in Tables 2.5.3.1, 2.5.3.2 and 2.5.3.3 can be found in Figures 79, 80, 81, 85, 86, and 87.

Table 2.5.3.1. Simple model of prosthesis F063. Stresses for comparison with the results from photoelasic experiments.

z-coordinate [mm]	tension		compression	
	σ_z x1000 [N/mm^2]	$\sigma_z * K_T$ [N/mm^2]	σ_z x1000 [N/mm^2]	$\sigma_z * K_T$ [N/mm^2]
8	391	602	-420	-602
16	286	375	-302	-396
24	229	332	-246	-353
32	220	319	-238	-345
40	224	329	-237	-345
48	250	309	-257	-409
56	208	306	-229	-365
64	213	347	-241	-361
72	186	324	-214	-371
80	169	225	-198	-339
84	123	205	-147	-252
88	101	173	-127	-248
92	86	148	-113	-201
96	77	123	-103	-192
100	69	122	-95	-195
104	58	107	-82	-182
108	54	111	-81	-140

^+K_T - stress concentration factor

Table 2.5.3.2. Simple model of prosthesis F076. Stresses for comparison with the results from photoelasic experiments.

z-coordinate	tension		compression	
[mm]	σ_z x1000	$\sigma_z * K_T$ [N/mm²]	σ_z x1000	$\sigma_z * K_T$ [N/mm²]
8	437	627	-438	-698
16	381	553	-409	-629
24	345	452	-389	-481
32	301	443	-328	-514
40	280	411	-318	-467
48	280	411	-319	-469
56	259	451	-287	-483
64	226	343	-252	-421
72	208	348	-249	-416
80	179	223	-221	-379
88	165	250	-215	-383
92	159	273	-215	-382
96	141	171	-194	-309
100	114	195	-168	-311
104	103	183	-146	-301
108	91	188	-136	-266
112	91	187	-127	-279

Table 2.5.3.3. Simple model of prosthesis G035. Stresses for comparison with the results of photoelasic experiments.

z-coordinate [mm]	tension		compression	
	σ_z x1000	$\sigma_z * K_T$ [N/mm²]	σ_z x1000	$\sigma_z * K_T$ [N/mm²]
8	57	65	-108	-141
16	96	119	-143	-188
24	100	131	-144	-191
32	120	169	-165	-228
40	159	224	-194	-274
48	165	235	-202	-273
56	188	270	-218	-298
64	204	249	-234	-297
72	210	289	-241	-331
80	227	278	-260	-318
84	223	310	-253	-324
88	222	308	-248	-304
92	196	293	-214	-297
96	173	260	-186	-291
100	149	211	-167	-254
104	114	176	-134	-218
108	94	147	-113	-189
112	71	105	-90	-122
116	59	95	-75	-122
120	47	62	-60	-107

In Tables 2.5.3.4 and 2.5.3.5, values of maximum stresses along the z-axis of the prosthesis F076 are shown. These values were calculated for the case of embedded prosthesis which was loaded in the centre of the head with the load equal to 1N. In order to show the influence of different values of transition radius, the stresses in Table 2.5.3.4 were calculated for a transition radius of 1 mm and the stresses in Table 2.5.3.5, for a transition radius of 2 mm. Also, the value of the elasticity modulus of the embedding was varied. Table 2.5.3.4 shows the results of the calculation in the case of the elasticity modulus of the embedding being equal to that of the prosthesis. Table 2.5.3.5 shows the results of the calculation in the case of the elesticity modulus of the embedding 32 times lower than that of the prosthesis. Table 2.5.3.6 shows values of stresses along the z-axis of the prosthesis F076 which were calculated with the FEM-model using the values of the elasticity modulus of the embedding as in the case of Tables 2.5.3.4 and 2.5.3.5. The values from Tables 2.5.3.4, 2.5.3.5 and 2.5.3.6 are shown in Figure 88.

Table 2.5.3.4. Simple model of prosthesis F076. Elasticity modulus of embedding equal to that of prosthesis

z-coordinate	tension		compression		Torsion
[mm]	σ_z x1000	$\sigma_z * K_T$ [N/mm²]	σ_z x1000	$\sigma_z * K_T$ [N/mm²]	$\tau_{max} x10^3$ [N/mm²]
8	-1.6	-2.2	1.6	2.5	10.8
16	-0.6	-0.8	0.6	1.1	9
24	0.	0.	0.	0.	7.7
32	0.	0.	0.	0.	5.3
40	0.	0.	0.	0.	4.3
48	0.2	0.2	-0.2	-0.3	4.4
56	0.2	0.2	-0.2	-0.3	3.4
64	-1.6	-2.	1.7	2.9	3
72	-4.9	-5.3	5.4	10	2.6
80	4.8	7.6	-5.5	-9	2.4
88	53	66	-63	-113	2.4
92	83	135	-118	-230	2.9
96	70	120	-104	-172	3.4
100	62	114	-95	-176	3.3
104	51	94	-79	-147	2.6
108	44	96	-69	-134	2.4
112	35	78	-56	-123	2.7
116	25	55	-39	-92	2.1
120	19	37	-31	-74	1.9

Stress concentration factor K_T for radius equal to 1 mm.

Table 2.5.3.5. Simple model of prosthesis F076. Elasticity modulus of embedding 32 times lower than that of prosthesis.

z-coordinate [mm]	tension		compression		Torsion
	σ_z x1000	$\sigma_z * K_T$ [N/mm²]	σ_z x1000	$\sigma_z * K_T$ [N/mm²]	$\tau_{max} x10^3$ [N/mm²]
8	-4	-5	4	5.6	10.8
16	-5.9	-7.1	5.8	8.4	9
24	-6	-7.4	6.4	9.3	7.7
32	-5.4	-6.5	5.8	8	5.3
40	-6.3	-7.7	6.5	9.2	4.3
48	-5.9	-7.2	6.2	8.7	4.4
56	-1.9	-2.4	1.8	2.7	3.4
64	9.8	12	-10.7	-15.8	3
72	33	41	-37	-57	2.6
80	56	75	-64	-94	2.4
88	81	99	-98	-149	2.4
92	83	118	-118	-191	2.9
96	70	102	-104	-150	3.4
100	62	93	-95	-151	3.3
104	51	77	-79	-125	2.6
108	44	75	-69	-112	2.4
112	35	61	-56	-100	2.7
116	25	42	-39	-72	2.1
120	19	29	-31	-61	1.9

Stress concentration factor K_T for radius equal to 2 mm.

Table 2.5.3.6. FEM-model of prosthesis F076. Elasticity modulus of the embedding equal, and also 32 times lower, than that of the prosthesis.

z-coordinate [mm]	Equal E		E 32xlower	
	σ_z ten.	σ_z compr.	σ_z ten.	σ_z compr.
	x1000 [N/mm²]		x1000 [N/mm²]	
8	0.	0.	-2	2.2
16	0.	0.	-1.	0.8
24	0.	0.	-1.5	1.2
32	0.	0.	-2.3	0.8
40	0.	0.	-3.8	0.4
48	0.	0.	-4.8	0.05
56	0.5	0.	-2	-1.5
64	1	-1	10	-8.5
72	2.2	-4	26	-18
80	10	-15	56	-46
88	49	-83	77	-118
92	84	-127	84	-129
96	76	-90	75	-87
100	69	-88	69	-88
104	52	-81	52	-85
108	51	-78	51	-85
112	22	-67	20	-66
116	13	-72	13	-71
120	8	-50	10	-54

2.5.4. Photoelastic Experiments

A typical exapmle of an isochromatic pattern in a slice from an Araldite model of prosthesis is shown in Figure 77. In Figure 78, a schematic drawing of the isochromatics, isoclinics and stress trajectories in a typical slice is shown. Tables 2.5.4.1, 2.5.4.2 and 2.5.4.3 contain the values of stresses as measured at the surface of the slices from the prosthesis F063, F076 and G035 respectively. These values are also shown in Figures 79, 80 and 81.

Table 2.5.4.1. Photoelastic results for the prosthesis F063.

z-coordinate [mm]	tension σ_z x1000 [N/mm²]	compression σ_z x1000 [N/mm²]
72	13	-8
76	41	-25
80	71	-46
82	91	-63
84	97	-63
86	103	-76
88	117	-117
90	107	-117
92	125	-119
94	94	-108
96	108	-97
98	67	-87
100	96	-78

Table 2.5.4.2. Photoelastic results for the prosthesis F076.

z-coordinate [mm]	tension σ_z x1000 [N/mm²]	compression σ_z x1000 [N/mm²]
70	36	-36
74	73	-58
78	102	-138
82	-	-218
84	202	-229
86	216	-248
88	189	-234
90	198	-218
92	156	-206
94	171	-184
96	109	-167
98	134	-156
100	116	-139
102	165	-131

Table 2.5.4.3. Photoelastic results for the prosthesis G035.

z-coordinate [mm]	tension σ_z x1000 [N/mm²]	compression σ_z x1000 [N/mm²]
76	111	-94
80	171	-128
84	214	-171
88	229	-233
92	227	-214
94	218	-195
96	197	-195
98	174	-188
100	170	-171
102	129	-147
104	133	-141
106	113	-126
108	116	-103

2.5.5 Scattered-light Photoelasticity

Figure 82 shows an example of the stattered-light pattern in one of the specimens under investigation. A typical set of result of measurment is shown in Figure 83. Table 2.5.5.1 shows values of stress concentration factors determined with scattered-light photoelasticity. It also includes the stress concentratio factors from the literature (Figure 29), A graphical representation of the values from Table 2.5.5.1 is shown in Figure 84.

Table 2.5.5.1. Stress concentration factors obtained with scattered-light photoelasticity.

Specimen r [mm]	r/d	D/d	K_{exp}			K_{lt}
concentric						
5	0.25	1.5	1.37	1.86	-	1.38
3	0.15	1.5	1.71	2.31	-	1.54
1	0.05	1.5	2.0	2.84	2.32	2.14
1mm eccentric						
4	0.2	1.6	1.88	1.91	-	1.46
3	0.15	1.6	2.12	2.60	1.67	1.56
2	0.1	1.6	2.03	3.31	-	1.76
1	0.05	1.6	1.80	3.71	-	2.26
2mm eccentric						
2	0.1	1.7	1.93	-	-	1.76
1	0.05	1.7	1.77	1.98	1.98	2.26
3mm eccentric						
2	0.1	1.8	1.96	1.91	-	1.78
1	0.05	1.8	3.53	3.41	2.05	2.26
4mm eccentric						
1	0.05	1.9	3.14	3.60	2.70	2.26

2.6. DISCUSSION

2.6.1. 3D Photoelasticity by Stress Freezing

The results from the 3D photoelasticity by stress freezing serve as the experimental check of the results from the mathematical models. Therefore, it is appropriate to discuss them first.

The major problem during the casting of the photoelastic models of the prostheses (see Chapter 2.4.1) was the possibility of air bubbles being trapped in the models. It is obvious that models with air bubbles could not be used in stress freezing experiments. The problem could be, to a large extent, eliminated by very carefully sealing off the mould and strictly observing the casting temperatures, i.e., the temperatures of the mould and Araldite. Prior to casting, it was found to be advantageous to keep the Araldite for approximately 10 minutes at casting temperature after mixing with the hardener. This enables the air bubbles introduced by the mixing procedure to escape. No problems were encountered with the scale of the photoelastic models. After casting, the largest dimensions of each section of the models were measured with callipers. These dimensions were then compared with that measured on the original prostheses. It was found that these dimensions did not vary by more than ±0.02 mm. Thus, it can be concluded that the photoelastic models were true to the scale of the prostheses.

One of the major problems of the photoelastic experiments was the positioning of the models. The models had to be positioned according to the position of the prostheses in the DIN-tests (see Chapter 2.2.2), i.e., the axis of the models had to be tilted by 10° from the vertical. During the positioning, the models were held in a clamp which enabled the models to be smoothly rotated and moved in a horizontal and vertical direction. A specially machined cap, which fitted smoothly on the neck of the models and which had a 200 mm long, straight pointer, was then tightly attached to the necks of the models. The position of the pointer was such that it was parallel to the neck axes of the models. The neck angles, i.e. the angles of the neck axes and the axes of the prostheses were known from the geometrical data of the prostheses (see Chapter

2.3.1). Using the position of the pointer relative to the vertical direction, the models cold be rotated to the required position. By repeating the positioning of the models several times, it was estimated that the maximum error in the tilt angle of the axis of the models from the vertical was ±1°.

While casting the embedding around the photoelastic models, it was generally difficult to ensure that the embedding level was exactly 50 mm below the basis sections of the prostheses. This problem was caused by difficulties in estimating the change between the volume of as-cast, hot Araldite and Araldite after the entire curing procedure. It seems that this change in volume depends on the casting temperature and on the amount of air present in hot Araldite. During curing, the air escapes causing a reduction of the volume of the finished casting. Because of the fact that the results from the photoelastic experiments were used only for the purpose of comparison with the results obtained from the mathematical models (and not for the purpose of finding the values of stresses in the prostheses during the DIN-tests), the problem of not having the models embedded exactly 50 mm below the basis sections was not regarded as a major one. This is because the comparison of the experimental results with the results from the mathematical models does not depend on the embedding level.

The second major problem during the photoelastic experiments was the value of the load with which the models were loaded during the stress freezing procedure. This value of the load should be high enough to produce a sufficient number of fringes but it should not lead to an excessive plastic deformation of the models. Initially, a predecessor of the simple model for predicting the stresses in the prostheses (see Chapter 2.3.4) was used in order to estimate the load required in the stress freezing experiments. However, one or two models had usually been destroyed before a satisfactory value of the load was found. It is important to note that the models used in the stress freezing experiments were always deformed. This deformation consisted of plastic and frozen elastic deformations. The plastic deformation is undesirable but it cannot be avoided. Because of the fact that the maximum stresses in the models of the prostheses were found at the embedding level (the proximal part of the prostheses and the neck were thicker than the sec-

tions of the models at the embedding level), it can be assumed that the major proportion of the plastic deformation occurred at the embedding level. If it is assumed that the whole deformation was plastic and that it occurred at the embedding level, the result of such deformation can be seen as leading to the parts of the models above the embedding to be rotated about an axis lying in the embedding level. This rotation causes a reduction in the tilt angle of the models and a change in the position of the point where the load was attached during the experiments. Thus, it also causes the stresses in the model to rise on the tension side and to decrease on the compression side. This,' worst case', scenario leads to the conclusion that the values of the stresses as obtained from the photoelastic experiments can be overestimated in the case of tensile and underestimated in the case of compressive stresses.

The 'worst case' scenario is useful in order to estimate the errors in the results from the photoelastic experiments, which could have been caused by plastic deformation of the models. Using the positioning procedure of the models it was found that the tilt angles changed by less than 2° during the stress freezing procedure. The errors were estimated using the simple model of the prostheses, i.e., the program PROCO (see Chapter 2.3.4), by calculating the stresses for the tilt angles equal to 10° and 8°. The comparison between the results of the calculation led to the conclusion that the value of the stresses depended strongly on the value of the tilt angle. The relative difference between the values of stresses along the z-axes calculated with the tilt angle of 10° and these with the tilt angle of 8° increased along the z-axes in the direction towards the distal end of the models. The relative difference at the embedding level was as high as ±30 percent. This results means that under the assumption that the deformation of the models was caused entirely by plastic deformation, the values of the stresses as measured in the photoelastic experiments can be overestimated by 30 percent on the tensile side and underestimated by 30 percent on the compression side.

A second class of errors in the photoelastic experiments were caused by the accuracy with which the models were positioned and the accuracy with which the coordinates of the loading point could be determined. In order to estimate these errors, the simple model was used. A series of calcu-

lations was carried out, during which the value of the tilt angle and the coordinates of the loading point were varied by ±1° and ±1 mm respectively. These calculations led to the conclusion that the results from the photoelastic experiments have a maximum relative error of ±20 percent for both the tensile and compressive stresses at the embedding level. This result is not only important in view of the photoelastic experiments but also in view of the application of the mathematical models for the purpose of predicting the stresses in HERAMED prostheses subjected to the DIN-tests. Because of the fact that the accuracy of positioning of the prostheses in the DIN-tests is similar to that of the models in the photoelastic experiments, it can be seen that any calculation can predict the value of the stresses with an accuracy in the range of ±20 percent. It is to be noted that that this range can be larger or smaller than 20 percent for each individual prosthesis as it depends on the coordinates of the point of load application relative to the embedding level.

The last class of errors in the results from the photoelastic experiments is connected to measurements errors, i.e, with the accuracy with which the fringe orders could be measured. These errors can be estimated by using the stress-optic law (see Chapter 2.4.1). The relative errors can be calculated from the following equation:

$$\Delta\sigma/\sigma = \Delta f/f + \Delta n/n + \Delta d/d \qquad (1)$$

where

σ - stress,
f - fringe-stress coefficient,
n - fringe order,
d - thickness of slice,
Δ - denotes the absolute accuracy for each value.

In Equation (1) the value $\Delta f/f$ can be regarded as equal to the value of $\Delta n/n$ as the fringe-stress coefficient f was obtained experimentally by measuring fringe orders in the centre of a disk subjected to a compressive loading (see Chapter 2.4.1). During the measurements of the fringe orders, their value could be easily determined with an accuracy of ±0.02. The values of fringe orders in the slices taken from the models

of the prostheses and in the centres of the discs were in the range of 1 to approximately 3.5. Taking as the 'worst case' the value of 1 for the fringe orders, the relative error $\Delta n/n$ can be calculated as equal to ±2 percent. The thicknesses of the slices were approximately equal to 2.7 mm and they were measured with an accuracy of ±0.01 mm. Thus, the relative error $\Delta d/d$ was equal to ±0.4 percent. Substituting the values of the errors $\Delta n/n$ and $\Delta d/d$ into Equation (1) leads to the value for the relative error of the results for the stresses $\Delta\sigma/\sigma$ as equal to ±4.4 percent.

If the plastic deformation is regarded as having a negligible effect on the accuracy of the results from the photoelastic experiments, the total error of these results can be calculated by adding the measurement errors to the errors connected with the positioning of the models. Thus, the total error of the results is estimated to be approximately ±25 percent.

In Figure 78, a schematic drawing of isochromatics, isoclinics and stress trajectories is shown, which was observed in slices machined from the photoelastic models. The isochromatics pattern above the embedding level is typical for bending, i.e., the fringe with the order equal to zero lies in the centre of the slice and the remaining fringes are parallel to this fringe. The isoclinics and the stress trajectories also confirm the fact that above the embedding, the models were subjected to bending. An increase in fringe orders can be noticed in the proximity of transition radii. This increase is directly related to the stress concentrations in the radii. Starting with the embedding level, the situation becomes complicated. The isoclinics pattern at the embedding level resembles that of a bar subjected to three-point bending below the loading point (compare Figure 89 [52]). In the embedding, the fringe orders decline rapidly, but it seems that a broad resemblance with the pattern above the embedding is maintained.

Stresses along the edges of the slices taken from the models of the three prostheses under investigation were obtained by measuring the fringe orders. These stresses are shown in Figures 79, 80 and 81. It can be seen from these figures that the maximum stresses, on both the compression and the tension side, were always found at the embedding level.

The stresses were smaller above, and rapidly declined, in the embedding. Especially on the tensile side, the curves representing the stress distributions, have a zig-zag shape. This shape is obviously cased by the presence of stress concentrations at the transition radii.

2.6.2. FEM-model

It was mentioned in Chapter 2.5.1 that the FEM-model was used for calculating stresses in the prostheses with and without embedding. The first case was used for comparing the results from the FE-analysis with the results from the photoelastic experiments. The second case served as a comparison for the simple model. This second case was also used in order to estimate the accuracy of the FEM-model. This was done principally by using the geometrical data of the prosthesis FØ76. The accuracy of a FE-analysis depends on the number of elements which are used in the analysis and on the degree of distortion of these elements (see Chapter 2.3.2). The larger is the number of elements and the less these elements are distorted, the more accurate are the results of the analysis. It is to be noted that little can be done in order to reduce the distortions of the elements while modelling such complex geometries as these of the HERAMED prostheses. One can only hope that the elements will not be too distorted. The way in which the mesh generator for the FE-analysis was written, i.e., the program PROEM, enabled an easy way of increasing or reducing the number of elements. Several FE-analyses were carried out, during which the number of elements were varied along the axis and in the sections of the models. These analyses led to the result that in the case of the prosthesis FØ76, the stresses were calculated correctly if each section was modelled by at least twelve brick and twelve wedge elements, and if each of the sections was 8 mm high. Any attempt to reduce the number of elements by either reducing the number of elements in each of the sections or by increasing the heights of the sections to 16 mm, led to inconsistent results. On the other hand, if the number of elements were increased either by increasing the number of elements in the sections or by reducing the height of the sections to 4 mm, the results of these analyses showed little change. Thus, the program PROEM was preset in such a way that by default, it generated a mesh in which each of the sections was modelled by 12 brick and 12 wedge elements and in which

the height of the sections was equal to 8 mm. However, if these values were used for the prostheses FØ63 and GØ35, the FE-analyses showed inconsistent results. These results showed that the models were apparently buckling. However, no buckling effects can be calculated with linear elastic FE-analysis. Thus, the 'buckling' resulted from errors in the FE-analyses and disappeared when the number of elements was doubled by reducing the height of the sections to 4 mm. While carrying out the FE-analyses of the prostheses FØ63 and GØ35, problems related to distortions of elements were also encountered. The FE-analyses of these two prostheses could not be conducted without changing the coordinates of some of the nodes in the FEM-models. This had to be done by entering the output file from the program PROEM and changing the coordinates by hand. It is to be noted that the height of the sections was equal to 4 mm only during the analyses of the prostheses without the embedding. Because of the very large number of nodes needed in the analyses with the embedding, the height of the sections had to be increased to 8 mm. Thus, while full confidence can be placed in the results of the FE-analysis for the prosthesis FØ76, the results for the prostheses FØ63 and GØ35 can be much less accurate.

Figure 43 shows a plot of direct stresses: σ_x, σ_y and σ_z, along a section of the prosthesis FØ76. Such plots were typical for sections of the FEM-models above the embedding level and for all sections of the FEM-model without the embedding. It can be seen that the stress σ_z is much larger than the two other stresses. The shape of the curve for the stress σ_z confirms that the section was subjected predominantly to bending. No effects which could be related to torsion can be recognized in Figure 43.

Figure 44 shows a plot of direct stresses along a section at the embedding level. It can be seen that the stresses σ_x and σ_y are larger compared to that in Figure 43. This increase is caused by the interaction of the prosthesis with the embedding. The stress σ_z, however, is still the dominant stress in Figure 44. This shows that also in the embedding the prostheses are subjected chiefly to bending.

In Figures 79-81, the results from the FEM-analysis and from the photoelastic results are compared. In Figures 79 and 80, it can be seen that

the embedding level in the photoelastic experiments differed from that in the FEM-analysis. This was caused by difficulties in ensuring that the photoelastic models were embedded exactly 50 mm below the basis-sections (see Chapter 2.6.1). However, the difference in the embedding levels does not influence the comparison of the results. This can be seen from Figures 79-81 which also show the results from the FE-analysis without the embedding. By comparing the results from the FE-analysis with and without the embedding, it can be seen that the embedding level simply defines a level from which the stresses start to decrease. Above the embedding level, the stresses from the FE-analysis with and without the embedding are virtually the same. It can, therefore, be concluded that the embedding influences stresses only in the embedding but not above.

It can be seen from Figures 79-81 that the FE-analysis produced results well within the range of the results from the photoelastic experiments. The rate of decrease of stresses in the embedding as calculated by the FEM-models appears to be very similar to that obtained from the photoelastic experiments. Comparing the results above the embedding level, it can be said that the results from the photoelastic experiments are larger on the tension side and that they tend to be smaller on the compression side compared to the results from the FEM-analysis. Because of the fact that the FEM-analysis was carried out for 'smooth' models, i.e., the influence of the transition radii was omitted (see Chapter 2.3.2.2), the results from this analysis can be seen as a lower limit for the values of the stresses obtained from the photoelastic experiments. This seems to be confirmed on the tension side, but contradicted on the compression side. However, in the discussion of the photoelastic experiments in Chapter 2.6.1 it was shown that if the photoelastic models deformed plastically, the tensile stresses would have increased and the compressive stresses, decreased. This seems to explain why the results from the photoelastic experiments are smaller than that from the FE-analysis on the compression side.

In Chapter 2.5.1, the results of an attempt to calculate stress concentration factors due to the presence of a transition radius in a section of the prosthesis F076 were presented. Figures 62, 64, 66 and 68 show the direct stresses along the section with no radius, with one third,

two thirds and the whole transition radius respectively. It can be seen that the higher is the proportion of the radius, the higher are the stresses. It is interesting to note that compared to the case with no radius, the stresses σ_x and σ_y increase with the portion of the transition radius. Because of the fact that in the case with no radius, the stresses σ_x and σ_y are much smaller than the stress σ_z, the state of stress can be, with good accuracy, approximated by the stress σ_z only. This situation changes if a transition radius is introduced. In this case, if the state of stress is approximated only by the stress σ_z, an error is introduced. It is interesting to estimate how the calculation of stress concentration factors is influenced by the use of the von Mises stress and by use of the stress σ_z only. The von Mises stress is calculated from the following formula:

$$\sigma_e = {}^1/\sqrt{2}\{(\sigma_x-\sigma_y)^2+(\sigma_y-\sigma_z)^2+(\sigma_z-\sigma_x)^2\}^{1/2} \qquad (1)$$

where

σ_e - von Mises stress,
$\sigma_{x,y,z}$ - direct stresses.

In the case with no transition radius, the von Mises stress can be, with good accuracy, approximated by the stress σ_z. In the case of a transition radius, it is important to note that the stresses σ_x and σ_y have the same sign as the stress σ_z at each point along the section (see, e.g., Figure 68). If, for simplicity, it is assumed that the values of the stresses σ_x and σ_y are equal to each other, by substituting such values into Equation (1), it can be seen that the von Mises stress will be smaller than the stress σ_z. This finding is interesting from the point of view of experimentally measuring the stress concentration factors. In such experiments, not all of the stress components in the transition radius are usually measured. Thus, the experimentally obtained values of the stress concentration factors are slightly larger than that obtained from a FE-analysis by using the von Mises stresses.

The values of the stress concentration factors calculated with the FEM-model are shown in Chapter 2.5.1 in Table 2.5.1.5. It can be seen from Table 2.5.1.5 that the highest stress concentration factors were found

for the points 4 and 10. It should be noted that these points were near the neutral plane of bending. The stresses calculated for this points had the lowest value of all the points of the section. This means that the values of stress concentration factors for the points 4 and 10 contain a large error. The maximum stresses were calculated for points 1 and 7. The stress concentration factors calculated at these points were equal to 1.43 and 1.37 respectively for the case of the whole transition radius. In Table 2.5.1.8 in Chapter 2.5.1, stress concentration factors from the literature were shown. For the case of the whole radius, Table 2.5.1.8 gives the maximum stress concentration factors for points 1 and 7 as equal to 1.7 and 1.6 respectively. By comparing the values from the Table 2.5.1.5 with that from Table 2.5.1.8, it can be seen that the stress concentration factors from the literature are on average 25 percent higher. On the basis of this comparison, it is difficult to decide which values of the stress concentration factors should be used for estimating the stresses in the prostheses. The FE-analysis indicates that the stress concentration factors are lower than that from the literature. However, this analysis is very expensive in terms of computing resources. Due to this, no efort was made to increase the number of elements in the FE-analysis in order to see if the difference between the results from such an analysis and the values from the literature would disappear. Such an analysis would be needed in order to confirm (or contradict) the finding that lower than that in the literature, stress concentration factors could be used in the estimation of stresses in the prostheses. As the values of the stress concentration factors from the literature were found to be larger than that obtained from the FE-analysis, it is concluded that on the grounds of safety, the former ones should be used in the estimation of the stresses in the HERAMED prostheses.

Several conclusions can be drawn from the experience with the FEM-models. They are as follows:

1. The finite element method can be used for calculating stresses in prostheses subjected to a DIN-tests. The results form the FE-analysis compared well with the results from the photoelas-

tic experiments. The calculation of stress concentration factors is possible with FEM, but it is advisable to use stress concentration factors from the literature instead.

2. The FE-analysis requires large computer resources. It needs a sophisticated software and a fast computer. A full analysis of an embedded prosthesis takes approximately three days and requires 150 MBytes storage space. In some cases, the analysis cannot be conducted automatically. If the elements are too distorted, they have to be changed by hand. Thus, highly qualified person is needed in order to carry out the analysis.

3. The FE-analysis is advantageous in the sense that it enables an estimation of the influence of different parameters. These parameters can be, for example, different modulus of elasticity, interface, or even different, non-linear behaviour of the materials of the embedding and the prostheses. It has to be mentioned that during all the FE-analyses presented in this work, a rigidly connected interface between the embedding and the prostheses was assumed. In practice, this does not need to be the case. The prostheses can separate from the embedding. A FE-analysis was in fact conducted, in which the interface was modelled by non-linear elements, the so-called GAPS (see Chapter 2.3.1.2). This analysis took several times longer computing time, but unfortunately the solution did not converge, and was therefore interrupted. It is obvious that more effort is needed in order to calculate the influence of non-linear interface condition. The possibility of using non-linear material characteristic in the FE-analysis is pointed out because it seems that such analysis could lead to interesting results. It is commonly found in the DIN-tests that the prostheses break 3 mm below the embedding level [1]. This could not be confirmed either by the photoelastic experiments of by the FE-analysis. The maximum stress, and therefore the most likely place for the prostheses to break, was always found to be at the embedding level. The fact that the prostheses used to break 3 mm below the embedding level can be caused by a

separation of the embedding from the prostheses, or by a non-linear behaviour of the material of the embedding. This can indeed be the case, as PMMA has a much lower modulus of the elasticity and strength than titanium. The low modulus of elasticity means that under a loading, displacements in the embedding are much larger than in the prostheses. The relative difference in these displacements can cause problems during a FE-analysis. Because of the fact, that the stresses are calculated from the displacements, they can have large errors. This problem can, in theory, be avoided if the so-called large displacement FE-analysis is conducted. It is needless to say that such an analysis would require even more resources and specialized software. It seems, however, that it is worth considering in the future.

2.6.3. BEM-model

It was expected initially that the use of the boundary element method would lead to a reduction in modelling efforts and in computational resources (see Chapter 2.3.3.2). Indeed, the modelling effort, i.e., the writing of a computer program for mesh generation was found to be much less than in the case of the finite element method. As it has already been mentioned in Chapter 2.3.3.2, this program is not shown in this work. The reason for this is that it was found that, contrary to the expectations, the computational resources needed for a BE-analysis were found to be greater than for a FE-analysis. The BE-analysis of the prosthesis F076, during which the embedding was (rather unsatisfactorily) modelled by a set of linear springs, needed approximately 100 MBytes of computing space. Some results of this analysis are presented in Figures 71-76. In Figure 71, direct stresses along a section above, and in Figure 72, direct stresses along a section at the embedding level are shown. If the curves representing the direct stresses are compared with that from the finite element analysis (see Figures 43 and 45), it can be seen that their shapes are similar. In both the figures, the stress σ_z is larger than the stresses σ_x and σ_y. Above the embedding level, the stresses σ_x and σ_y are virtually equal to zero. Due to the interaction of the embedding with the prosthesis, these stresses rise at the embed-

ding level. The shape of the curves in Figure 71 does not show any effects which could be related to large torsional stresses. Therefore, the BE-analysis leads to the same conclusion as the FE-analysis (see Chapter 2.6.2) that the loading of the prostheses can be described primarely as bending.

Figures 73 and 75 show the maximum tensile and compressive direct stresses along the z-axis of the prosthesis FØ76 respectively. By comparing Figures 73 and 75 with the results from the FE-analysis (Figures 49 and 51), it can be seen that the shapes of the curves in the respective figures are similar. However, two major differences can be recognized. Firstly, the values of the direct stresses obtained from the BEM-model are nearly two times higher than these, from the FEM-model (compare also Tables 2.5.1.2 and 2.5.2.1). Secondly, the rate in which the stresses decrease in the embedding is higher in the case of the BEM-model. The second difference can be explained by difficulties in modelling the embedding with a set of linear springs. It is generally very difficult to calculate the elasticity constants of such springs in such a way that they would represent a three dimensional body (the embeding) correctly. The comparison of the Figures 73 and 75 with Figures 49 and 51 shows that in this particular case, the springs were too stiff. The first difference can be explained by comparing the values of the direct stresses from Figures 73 and 75 with the respective values of the von Mises stresses (Figures 74 and 76). It can be seen that the results of the BE-analysis are inconsistent. Apparent is the 'wavy' shape of the curves in Figures 74 and 76 and the large difference between the direct stress σ_z and the von Mises stresses (see also Table 2.5.2.1, Chapter 2.5.2). This means that the mesh used in the BEM-model was too coarse. Because of the fact that the BE-analysis has already taken a large computing space (comparable with the FEM-model), a refinement of the mesh was not carried out. The literature on the boundary element method indicates that the advantages of this method, as regarding the computational effort, can disappear if thin, long structures are modelled. This is obviously the case with the modelling of the prostheses. Thus, it was decided to abandon the BEM-model in the further course of this work.

2.6.4. Simple Model

The simple model was initially designed as a rough help for estimating the load needed in photoelastic experiments. By comparing the results from this model with the results from the FE-analysis, it soon became apparent that the simple model can be used instead of the expensive FEM-model. This is illustrated in Figures 79-81 and 85-88. In Figures 79-81, the results from the simple model are compared with the results from the photoelastic experiments and from the FE-analysis. The simple model was used in these cases without the embedding. This was done because the FE-analysis showed that the embedding influences only the stresses in the embedding but not above (see Chapter 2.6.2). In Figures 79-81 stresses, and stresses multiplied by appropriate stress concentration factors (see description of the simple model in Chapter 2.3.4), are shown. It can be seen that the results from the simple model without the stress concentration factors are very well in accordance (up to the embedding level) with the results from the FE-analysis. The factored stresses are always above the measured stresses from photoelastic experiments. Thus, it seems that the factored stresses lie on the 'safe' side. In Figures 85-87, the results from the simple model are compared with the results from FE-analysis without the embedding. It can be seen that in the case of the prosthesis F076 (Figure 86), an excellent agreement between the results from the simple model and from the FE-analysis is found. In the case of the prostheses F063 and G035 (Figures 85 and 87 respectively), the results from the simple model are smaller the that from the FE-analysis at the distal ends of the prostheses (on the graphs, at the distance near to 0 mm). It was previously mentioned that there were problems with the FE-analysis of the prostheses F063 and G035. The distal ends of these prostheses were quite thin. This led to the results of the FE-analysis to show a 'buckling' effect (see Chapter 2.6.2). However, there were no such problems with the FE-analysis of the prosthesis F076. It is therefore concluded that the difference between the results from the simple model and from the FE-analysis for the prostheses F063 and G035 were caused by the errors in the FE-calculations. (This is strengthened by the fact that although thin, the prostheses F063 and G035 were straight. The more straight the prostheses, the more accurate are the results from the simple model (see Chapter 2.3.4)).

An interesting observation can be made by comparing the shape of the curves in Figures 85-87 with each other. In Figures 85 and 86, the stresses fall starting from the distal end (at the distance equal to Ø mm) towards the proximal end. In Figure 87, however, the maximum stress is found in the middle between the distal and proximal ends. The shape of the curves in Figure 87 is caused by the fact that the neck of the photoelastic model of the prosthesis GØ35 was relatively short. Thus, when the model was tilted and loaded, the direction of the load passed near the geometrical centre of the section at the distal end. In this way, the bending moment induced by the load decreased quickly along the z-axis of the model and was small at the distal end. This small value of the bending moment is the reason for the small values of stresses which were calculated for the distal end of the prosthesis GØ35.

Generally, it can be said that the shape of the curves, such as in Figures 85-87, is determined by two competing effects: the taper of the shape of the prostheses and the rate of decrease of the bending moment (which, in turn, depends on the position of the centre of the head of the prostheses). If the rate with which the thickness of the prostheses decrease is greated than that of the bending moment, the shapes of the curves will be such as in Figures 85 and 86. Otherwise, the shape will be similar to that in Figure 87. It has to be pointed out that in real prostheses, the shape of the curves should not resemble that in Figure 87. Such a shape indicates that the neck of the particular prosthesis is too short or the neck angle is too large. The load (the weight of the patient) will not be introduced ito the femur in an advantageous, physiological way.

In Figure 88, results from the simple model with different modulus of elasticity of the embedding are compared with results from FE-analysis for the prosthesis FØ76. It can be seen that despite the many assumptions, the simple model correctly predicts the influence of the embedding on the stresses there. The simple model does this in a fraction of the time needed for the FE-analysis, and on a home computer. It has to be mentioned that both the analyses, with the simple model and with the FEM-model, showed that the actual values of the modulus of elasticity of the prosthesis and the embedding do not influence the values of the

stresses. What is important, however, is how many times the modulus of elasticity of the embedding is lower than that of the prosthesis. The lower is this modulus, the higher are the stresses in the embedding. From the analysis of the prosthesis F076 with the modulus of elasticity 32 times lower that that of the prosthesis, it can be seen that the stresses in the embedding decrease rapidly. Thus, the maximum stress is found at the embedding level. If this was the case for all prostheses, the calculation of the stresses in the embedding could be removed from the model. This could have been done if the prostheses had a uniform shape. However, the prostheses have a tapered shape. The taper can change from prosthesis to prosthesis. If the increase in stresses due to the taper along the axes of the prostheses is not compensated by the rate of the decrease of stresses due to the embedding, stresses in the embedding could be larger than that at the embedding level. It is therefore concluded that the calculation of the stresses in the embedding is an important part of the model.

It was shown in Chapter 2.3.4, that the simple model enables an estimation of stresses due to torsion. In this estimation, the influence of the embedding is not considered. In Table 2.5.3.4, the maximum torsional stresses for the prosthesis F076 are shown. It can be seen, that these stresses are much lower than the bending stresses. In calculations for the prostheses F063 and G035, the torsional stresses did not exceed 5 percent of the bending stresses. Also, the FE-analysis showed no effects which could have been related to large torsional stresses (see Chapter 2.6.2). Thus, it is concluded that the calculation of the stresses due to torsion can be removed from the simple model.

From the discussion of the simple model, it can be seen that it provides a valuable alternative to the finite element model. The comparison of the results showed that the simple model is as accurate as the FE-analysis. It also requires fewer computing resources. No specialized software and therefore, no specially qualified person is required in order to use this model. In particular, the short time needed for the calculation of stresses (a few seconds if the calculation of the torsional stresses is omitted), enables the simple model to be used as an 'on-line' facility in the design process of the HERAMED prostheses. Thus, several calculations can be carried out and simple redesign measures checked in a reasonably short time.

2.6.5. Scattered-light Photoelasticity

The results from the scattered-light photoelasticity, i.e, stress concentration factors for eccentric, circular bars (see Chapter 2.4.2), are summarized in Table 2.5.5.1 in Chapter 2.5.5. The last column in this table contains the maximum stress concentration factors from the literature. These values were obtained from Figure 29 by using the values for r/d and D/d shown in the second and third column of Table 2.5.5.1. It is interesting to note, that the stress concentration factors from the literature vary by a very little amount with the increase in eccentricity. This can be seen in the best way by comparing the factors for the value of the transition radius equal to 1 mm. This leads to the conclusion that an eccentricity has little influence on the values of the stress concentration factors. This observation is important because it justifies the use of the stress concentration factors from the literature in the simple model without any alternation.

The averaged experimental values, and these from the literature, of the stress concentration factors are shown against the values of r/d in Figure 84. It can bee seen that the experimental values are, on average, significantly higher than the values from the literature. This seems to indicate that an eccentricity has a large impact on the values of stress concentration factors. However, Figure 84 shows also that the experimental results are inconsistent. The stress concentration factors in the case of the eccentricity equal to 2 mm, for example, are lower than that from the literature. It was mentioned in Chapter 2.4.2 that the laser had to be rotated by approximately 30° in order to observe a change in the scattered-light fringe patterns. This was caused by the fact that the fringe patterns were usually very faint and lacking contrast (see Figure 82). This means that the accuracy with which the fringe order could be measured with the scattered-light method was equal to ±0.3 of fringe order. In the experiments, the stress concentration factors were calculated as the ratio between two values. These values were the slopes of the curves representing the dependence of the value of fringe order on distance at the surface of the specimens (see Figure 83). According to the stress optic law, they were directly proportional to the stresses at the surface (see Chapter 2.4.2). One slope was measured away from the

fillet, and the second, at the root of the fillet radius. The value of the stress concentration factors can be expresses by the following equation:

$$K_{exp} = [\lim_{s \to 0} (dn/ds)_{in}] \; / \; [\lim_{s \to 0} (dn/ds)_{away}] \qquad (1)$$

where

K_{exp} - stress concentration factor,
$\lim (dn/ds)_{in}$ - slope at the surface ($s \to 0$) in fillet,
$\lim (dn/ds)_{away}$ - slope at surface ($s \to 0$) away from fillet.

In practice, Equation (1) is replaced is replaced by:

$$K_{exp} = [\Delta n/\Delta s]_{in} \; / \; [\Delta n/\Delta s]_{away} . \qquad (2)$$

If one assumes that the error in measuring the distance Δs is small compared to that in the fringe order Δn, and by further assuming that the value of the fringe order Δn is equal to one, with the accuracy of the measurement of the fringe order equal to ± 0.3, the maximum error obtained for Equation (2) is as high as ± 60 percent. It is obvious, that this error will increase with the decrease in the measured value of the fringe order[34]. It can be seen from this simple estimation of errors, that the results from the scattered-light photoelasticity are quite inaccurate. Therefore, the statement that an eccentricity can significantly increase the values of stress concentration factors is not permitted on the basis of these results. The major problem identified in the scattered-light experiments is the accuracy with which the value of the fringe order could be measured. This accuracy can be increased if larger photoelastic models are used. For the purpose of this work, it would mean that new models would have to be cast and a new loading rig, produced. It was mentioned in Chapter 2.4.2 that with the scattered-

[34] Theoretically, the maximum error, exctly at the surface, is infinite.

light experiments, not only the stress concentration factors were supposed to be measured, but also the possibility evaluated weather the scattered-light method could be used for measuring stersses in models of proshteses. As the experiments showed that large photoelastic models would be needed in order to measure the stresses in these models, the scattered-light method was not further pursued. This was because a manufacture of large scale photoelastic models of prostheses would be much more time consuming than an investigation of the stresses by 3D photoelasticity by stess freezing.

3. MATERIAL INVESTIGATION

3.1 Introduction

The material investigation had three objectives. The first and the major objective was to establish the fatigue strength of the material used in the HERAMED prostheses, the Ti-5Al-2.5Fe alloy, at 10^7 cycles in order to provide data for the application of the mathematical model. The second, was to give a detailed description of the microstructure of the material, as this has not previously been done. The fatigue strength in titanium alloys depends on their microstructure. Finally, in view of recently developed ideas on the role of dislocations in fatigue of metals, the dislocation structure in Ti-5Al-2.5Fe induced by the fatigue process was to be described.

Before presenting the experiments, methods and results, the relevant literature on titanium and titanium alloys has been reviewed.

3.2. LITERATURE REVIEW

3.2.1. Some Properties of Titanium [59]

Titanium belongs to the fourth group of the table of elements. It has the atomic number of 22, the atomic mass of 47.9 and the specific weight of 4.51 g/cm³. Titanium has two allotropic forms: a low temperature form, Ti_α, which is stable up to 882.5°C and a high temperature form, Ti_β, which is stable up to the melting point of pure titanium at 1668±5°C.

The alpha phase crystallizes in the hexagonal close-packed structure (hcp), type A3 (space group $P6_3/mmc$). The unit cell parameters are: a_α= Ø.2950 nm, c_α= Ø.4683 nm and c/a= 1.5873. The beta phase possesses the body-centred cubic (bcc) structure, type A2 (space group Im3m) with the lattice parameter a_β= Ø.3283 nm. The lattice parameters of both the phases are influenced by the amount of alloying elements. In general, the lattice parameters of the alpha phase increase with the increase in the concentration of impurities or alloying elements. For example, this is true in the case of oxygen, which occupies the octahedral spaces between the titanium atoms in the hcp structure, and of aluminium, which forms an substitutional solid solution with titanium. The lattice parameter of the beta phase decreases with the increase in the concentration of elements such as vanadium or iron.

Polycrystalline titanium has a Young's modulus E of 112 GPa, a shear modulus G of 41 GPa and the Poisson ratio μ of Ø.32. At room temperature, titanium is paramagnetic.

3.2.2. Alloying of Titanium

The aim of the alloying of the titanium is to improve the mechanical properties of the material according to its application. A wide variety of microstructures, containing of α-phase, α- and β-phase mixtures or β-

phase only, can be achieved. As can be seen from the examples shown in Table 3.2.2.1, alloying[1] improves the tensile strength of the material.

Table 3.2.2.1. Typical tensile strength of titanium and titanium alloys [60].

Material	Tensile strength (MPa)
CP titanium annealed	680
cold worked	800
α Ti6Al12Nb1Ta1Mo	910
α/β Ti6Al4V	970
α/β Ti5AlFe2.5	1000
β Ti11.5Mo6Zr4.5Sn	1200

Broadly speaking, the alloying of titanium is dominated by the ability of elements to stabilize either of the alpha- or beta-phases. The most important alpha stabilizers are oxygen and aluminium. In engineering practice, however, oxygen is regarded as an impurity. On the other hand, aluminium is seen to be as important for titanium as carbon is for iron. It is to be noted that the concentration of aluminium is restricted in binary alloys to about 8% Al. Above this concentration the ordered phase α_2 (Ti_3Al) is formed, causing embrittlement of these alloys. In multi-component alloys, this critical amount could be moved to lower concentrations of Al [62]. The group of the beta stabilizers includes iron and vanadium, the latter being the component of the commonly used Ti-6Al-4V alloy. Figures 90, 91 and 92 show the phase diagrams of Ti-Al, Ti-V and Ti-Fe.

[1] In order to achieve the best properties, the alloys often have to be thermo-mechanically processed. The difficulty being that the processing parameters, like temperature and deformation rate, have to be strictly observed.

3.2.3. Phase Transformations in Titanium and its Alloys

The basic transformation in titanium is the allotropic transformation $Ti_\alpha <=> Ti_\beta$. On cooling from the β-field, at about 882°C in the case of high purity titanium, the cubic β-phase transforms into the hexagonal α-phase. In pure titanium the entire β-phase is transformed into the α-phase, so that no untransformed β is found at room temperature. On slow cooling, a cellular microstructure is formed due to the diffusion controlled nucleation of the α-phase at the grain boundaries of β and their subsequent, fast growth. At higher cooling speeds the $Ti_\beta \rightarrow Ti_\alpha$ transformation has a martensitic character and a needle-like microstructure is formed.

During the transformation $Ti_\alpha <=> Ti_\beta$ there is a relationship between the crystallographic orientations of the initial and transformed phases. This orientation relationship is found to be:

$$(0001)_\alpha \,||\, (110)_\beta, \quad [11\bar{2}0]_\alpha \,||\, [111]_\beta$$

where $(0001)_\alpha$ and $(110)_\beta$ denotes the planes and $[11\bar{2}0]_\alpha$ and $[111]_\beta$ the directions which are parallel to each other in the hexagonal (α) and cubic (β) lattices during the transformation (Fig. 93). The above relationship is called the Burgers orientation relationship after W. C. Burgers who was the first to describe it [63].

The phase transformations in titanium are strongly influenced by the presence of alloying elements and impurities. In alloys with sufficient concentration of β stabilizing elements it is possible to retain the β phase at room temperature. The amount of the retained β-phase depends on the temperature of the transformation $\beta \rightarrow \alpha+\beta$ and the concentration of the alloying elements. Also, a number of intermediate, metastable phases can be formed during the transformation of the β- into the α-phase. The intermediate phases can form on cooling or on heating the alloys. Certain characteristics of some of the metastable phases are given below:

The martensitic phase α'

The martensitic phase α' has a hexagonal structure. It represents a supersaturated solid solution of elements in Ti_α and is formed as a result of quenching from the temperature in the range of the stability of the β-phase or during annealing of the retained, metastable β [60]. The microstructure of α' consists of colonies of parallel plates or laths in more dilute alloys. The laths are separated by thin layers of the β-phase which is enriched in β-stabilizing solute elements. With increasing solute content, these colonies decrease in size and may degenerate into individual plates which are randomly oriented [64, 65]. The orientation relationship of the β-phase and α' martensite obeys the Burgers relation. In martensitic transformations in titanium alloys only a small strengthening effect is achieved as compared to iron alloys [60].

The martensitic phase α''

The martensite α'' is reported to have an orthorhombic structure and its lattice parameters are a=0.301 nm, b=0.490 nm, c=4.63 nm [66]. Formation of α'' is strongly composition dependent, i.e. it is present in alloys with only some solute elements. The α'' martensite can be formed on quenching, annealing or during plastic deformation. In the latter case the martensite is called the athermal or stress induced, and in the former, the isothermal martensite. The α'' phase has gained in importance in recent years as its formation is associated with remarkable strengthening in β alloys, and it is thought to play an important role in shape memory effects [67].

Other martensites

Two other martensites have been reported in the literature. A face-centred cubic martensite was found at grain boundaries between alpha and beta phases. This martensite forms very fine, needle like structures. These structures are called the interface phase. They are caused by spontaneous transformation during electropolishing of specimens for electron microscope studies due to an uptake of hydrogen [65, 114]. A face-centred orthorhombic martensite, termed as α''' or β', can be formed in some alloys with high concentration of β stabilizing elements e.g. Ti-12V [68].

The omega phase ω

The omega phase can be formed in certain titanium alloys on quenching or during isothermal aging at temperatures in the range of 100-500°C. These two forms of the omega phase have been named the athermal and isothermal omega respectively. The athermal omega phase manifests itself in electron diffraction patterns by extensive diffuse streaking effects. The isothermal omega produces well defined diffraction spots. The omega phase forms rapidly as homogeneously nucleated, coherent precipitates which can have a cuboidal or ellipsoidal shape. The beta to athermal omega transformation has been described as a fully reversible, displacement controlled transformation [71]. The exact tranformation mechanism has not yet been entirely clarified but it is thought that it is very similar for the both omega phases [69, 70]. The ideal (isothermal) omega structure can be viewed as having a hexagonal unit cell with the parameters a=0.460 nm, c=0.282 nm, c/a=0.613. The orientation relationship of the beta and omega phases is [72]:

$$[111]_\beta \,||\, [0001]_\omega,\ (110)_\beta \,||\, (11\bar{2}0)_\omega.$$

The formation of high volume fraction of the omega phase is associated with embrittlement of the alloys. The formation of the omega phase can be suppressed by an increased oxygen content or by the addition of at least 3% aluminium; for example, omega is formed in binary Ti-V alloys, but is absent in the important ternary alloy Ti-6Al-4V [69, 64].

3.2.4. Fatigue Properties

In this chapter, only some aspects of the fatigue properties of titanium and its alloys are presented. The emphasis is put on the high cycle fatigue (HCF) strength[2] of α+β alloys as most relevant for this study. The

[2]Here, the high cycle fatigue strength is understood to be the maximum stress level at which test samples of the material endure a large number (more than 10^5) of cycles without failure.

majority of the results presented here are obtained from the literature on Ti-6Al-4V.

It is generally accepted that the high cycle fatigue properties are strongly influenced by the microstructure, surface treatment and the environment.

The geometrical arrangement of the α and β phases can be influenced to a great extent in α/β-alloys by heat treatment (Fig. 94). Slow cooling from the β field produces a coarse lamellar arrangement of the α and β phases. Quenching from the β field causes the β-phase to transform martensitically and a subsequent annealing leads to a fine lamellar structure. The lamellar structure can be then deformed and after a recrystallization annealing, an equiaxed structure can be generated. The equiaxed structure consists of primary α and untransformed β grains. The grain size can be controlled by the degree of deformation, the annealing temperature and the annealing time.

The next type of structure is achieved when the equiaxed microstructure is annealed in the two phase field, quenched and subsequently annealed. This, so-called bi-modal, microstructure contains primary α grains surrounded by a fine lamellar microstructure of β and transformed β. The content of the primary α is varied by the annealing temperature in the α/β field [77].

It is found that the bi-modal microstructure exhibits a superior HCF strength as compared to the equiaxed and lamellar microstructures (Fig. 95). Also, the HCF strength increases with decreasing grain size (Fig. 96) [73, 74].

Reports in the literature point out that the Ti-6Al-4V alloy exhibits an abnormal dependence of the HCF strength on the mean stress. This dependence is usually judged according to the Goodman rule[3], which expresses a simple linear relationship between the fatigue strength at different mean stress levels [94]. It has been found that the application of the Goodman rule to the Ti-6Al-4V alloy leads to an overestimation of the HCF strength at low positive mean stress levels for the equiaxed and bi-modal microstructures. The lamellar microstructures show a normal dependence of the HCF strength on the mean stress [93].

The equiaxed and the bi-modal microstructures have sharp textures[4] as a result of the mechanical deformation and subsequent recrystallization. Test samples which are used to find the HCF strength can therefore show different values of the HCF strength according to the direction in which they are cut from the bulk material [74].

Figure 97 shows the influence of various mechanical surface treatments on the HCF strength. It is important to observe that the HCF strength is affected to a greater extent by the surface treatment than by microstructural changes [73, 78].

---

[3] Goodman rule: $\sigma_a = \sigma_{fat}(1-\sigma_m/\sigma_{ts})$

where σ_a - fatigue strength in terms of stress amplitude, where σ_m is not equal zero

σ_m - mean stress

σ_{fat} - fatigue strength in terms of stress amplitude, where $\sigma_m = \emptyset$

σ_{ts} - tensile strength

[4] Texture in this context means a distribution of crystallographic orientations of the grains relative to the geometry of the piece of the material. In deformed or recrystallized, polycrystalline materials some orientations of the grains relative to a reference system, which could be connected to the geometry of the sample of the material, are found to be more common then other. If the majority of the grains assume this special orientation, one speaks of a sharp texture.

The environment in which the HCF tests are carried out can significantly alter the results [79]. Materials tested in vacuum show higher HCF strength as compared to tests conducted in air or in various corrosive liquid solutions (Fig. 95). As the environment can have different effects on the HCF strength of different microstructures, it is important to test the material in an environment as similar as possible to that in which the material is going to be applied.

3.2.5. The Ti-5Al-2.5Fe Alloy

Commercial purity (CP) titanium has long been used as an implant material, e.g. in the heart surgery, because of its outstanding bio-compatibility [86]. The yield strength of CP titanium is about 650 N/mm² which makes it unsuitable for implants which have to withstand high stresses, such as hip joint prostheses. In these cases titanium alloys have to be used. The most commonly used is the Ti-6Al-4V alloy, but it contains the element vanadium which is classified as toxic [88]. As long term implants (e.g. hip joint prostheses), have to remain in the patient for many years, there is a fear among surgeons that the corrosion products of the implant material can adversely effect the health of the patient, or cause an allergic reaction of the tissue surrounding the implant which, in turn, would make a revision operation necessary[5]. The Ti-5Al-2.5Fe titanium alloy was developed in order to provide an alloy with similar mechanical properties to the Ti-6Al-4V alloy but without the inclusion of the poisonous element vanadium [80].

Figure 98 shows the phase diagram Ti-Fe at 5 wt.% Al [80], from which it could be recognized that there is an eutectoid transformation at around 650°C in the system (compare also the phase diagram Fe-Ti in Fig. 92 and

[5]Minds are divided on this subject: recent analysis by Zitter [91] shows, that there is no proof that the corrosion products of Ti-6Al-4V would affect the patient.

the diagram Ti-V in Fig. 91). As a result of this reaction, the iron rich alpha phase can, on cooling, transform into alpha and the intermetallic phase TiFe. The TiFe phase has a body centred, A_2 type (CsCl) structure with unit cell vector a=0.297 nm [113]. The eutectoid reaction, however, is very sluggish [60] and has no practical effect on the microstructure of the alloy. As the time-temperature-transformation (TTT) diagram in Figure 99 shows, the reaction can be initiated only by long annealing times near the eutectoid temperature [92].

The Ti-5Al-2.5Fe alloy can be processed in exactly the same ways as the Ti-6Al-4V alloy and its formability in elevated temperatures is even better than that of Ti-6Al-4V. It is usually hot worked at approximately 850°C, solution treated in the sub-transus temperature range and subsequently annealed (900°C/1 h/water quench + 700°C/2 h/air cooled). The above treatment produces material with equiaxed α+β microstructure with grain size of less than 10 µm. If the alloy is hot worked at approximately 1000°C, the resulting microstructure is lamellar. The influence of different Ti-5Al-2.5Fe microstructures on the mechanical properties of the alloy is compared in the Figure 100, which shows that the fine equiaxed microstructure has better mechanical properties than the lamellar microstructure.

The Ti-5Al-2.5Fe alloy is available commercially as semi-finished products manufactured by forging, rolling or extrusion [89].

Table 3.2.5.1 summarises the results of fatigue tests performed on Ti-5Al-2.5Fe alloy from the literature. It can be seen from the table that the fatigue strength of Ti-5Al-2.5Fe in the wrought condition, as found in rotating bending tests, lies around 550 N/mm² in the case of smooth specimens, and falls down to about 300 N/mm² for specimens with a stress concentration factor of 3.6. These values compare favourably with the fatigue strength of Ti-6Al-4V which lies in the range 500-600 N/mm² [83].

Table 3.2.5.1. Fatigue strength of Ti-5Al-2.5Fe.

Condition	Method	SCF*	Fatigue strength**	
hot rolled	rotating bending	1	550 N/mm²	[80]
	"	3.3	300 N/mm²	"
hot rolled	tension-tension	1	825 N/mm²	"
	in 0.9% NaCl	3.3	450 N/mm²	"
wrought annealed	tension-tension	1	725 N/mm²	[89]
	in air and RT			
wrought solution treated annealed	"	3.6	300 N/mm²	"
cast, hot isostatically pressed	"	1	450 N/mm²	"
		3.6	300 N/mm²	"
forged solution	rotating bending	1	550 N/mm²	[81]
treated annealed	"	1	580 N/mm²	[90]

* Stress concentration factor is equal to 1 for smooth specimens

** at more than 10^7 cycles

In tension-tension tests the fatigue strength of the alloy can be as high as 725 N/mm². This result is surprising, as one would expect that the fatigue strength found in the tension-tension tests would be lower than that found in the rotating bending tests. The tension-tension loading is regarded as more severe than the rotating bending loading . One of the differences between these two types of loading is that the mean stress in the tension-tension loading is higher than that in the case of rotating bending. According to the Goodman rule, the higher the mean stress the lower is the fatigue limit [94]. Presumably, the higher than expected values of the fatigue strength in tension-tension loading have arisen through different surface treatment of the test specimens.

Apart from mechanical testing, the Ti-5Al-2.5-Fe has been submitted to various corrosion, abrasion and biocompatibility tests [81-84, 86, 88]. The results show that the electrochemical properties of the material are virtually the same as in case of the Ti-6Al-4V alloy.

Because of its good mechanical and electrochemical, properties the Ti-5Al-2.5Fe titanium alloy has been applied as an implant material since 1980. In 1987, it was proposed to include this alloy in ISO Specification 5832 [81].

3.2.6. Dislocation Structures in Fatigued Metals

In recent years, a phenomenological understanding of the development of dislocation structures during cyclic deformation of metals seems to be emerging [95, 96, 97]. In carefully designed experiments on fcc materials, copper and aluminium in particular, the researchers were able to describe the fatigue process in terms of changes in the dislocation structures. It must be pointed out that these investigations shed light on the microstructural changes in the material due to the fatigue process up to the point of crack initiation. They are, therefore, very interesting from the point of view of the high cycle fatigue, where the majority of the specimen life is occupied by the crack initiation and not by the crack propagation process.

It is accepted by many researchers that the fatigue process of fcc metals is dominated by the formation of distinctive dislocation structures, the so-called persistent slip bands (PSBs), in the bulk of the material. The PSBs are easily recognizable in the electron microscope as they consist of regular, ladder like arrangements of dislocations (Fig. 101). The PSBs appear to form above a particular, well defined threshold stress amplitude. Cracks originate and propagate along the PSBs. If a material is fatigued below the threshold stress amplitude, no PSBs and also no cracks are formed. The material can endure an infinite number of cycles. This threshold stress amplitude, below which no PSBs are formed, can be therefore regarded as the fatigue limit of the material.

The behaviour of bcc metals differs from that of the fcc metals [95, 99]. The form of dislocation structures in bcc metals is thought to be dominated by different relative velocities of edge and screw dislocations. The most commonly observed dislocation structure in fatigued bcc metals is a cell structure. Cracks originate at the surface of the material in ill defined slip bands. It is still being discussed if bcc me-

tals possess a fatigue limit. There is experimental evidence that there is a region in which the plastic deformation induced by the fatigue process is accommodated by a to-and-fro gliding of dislocations in quasi reversible fashion. This region can be associated with the fatigue limit [99].

The literature search revealed that the dislocation structures in fatigued titanium, which has a hcp structure, has not so far been investigated in detail. Fatigue studies on pure titanium show that cracks initiate an the surface in narrow slip bands or along twin boundaries [100, 101]. In Ti-6Al-4V cracks were found to form in narrow slip bands in alpha grains [74] or at grain boundaries between alpha and beta phases [75]. It was suggested in [102] that the fatigue damage in Ti-6Al-4V accumulates preferentially in a 25 µm deep surface layer. However, a localized damage in the bulk of the material was not excluded. It was also shown in the same reference that beta grains did not contain any dislocations after fatiguing. The conclusion was that the beta phase could be regarded as hard inclusion in softer alpha matrix. The existence of the fatigue limit has not yet been decided for titanium and its alloys.

3.3. EXPERIMENTS AND METHODS

3.3.1. Material

Material investigated in this study, the Ti-5Al-2.5Fe titanium alloy, material number 3.7110 according to DIN 17851, was supplied by W. C. Heraeus GmbH, Hanau, West Germany. The material was delivered in the form of a forged and annealed rectangular bar with section dimensions of 40 mm x 90 mm. The composition and mechanical properties as given by the manufacturer are shown in the table 3.3.1.1.

Table 3.3.1.1. Composition and mechanical properties of Ti-5Al-2.5Fe.

Al (%)		4.9
Fe (%)		2.6
C (ppm)		< 100
O (ppm)		1350
N (ppm)		< 100
H (ppm)		< 30
σ_{rb}*	(N/mm²)	> 575
R_m	(N/mm²)	995
$R_{p\ 0.2}$	(N/mm²)	815
A (%)		15
HV30		300

* σ_{rb} denotes the endurance limit found in rotating bending tests at more than 10^7 cycles

The supplied material is used directly in the manufacturing of the HERAMED hip joint prostheses. The microstructure of this material is equiaxed. In Chapter 3.2.4, it was shown that in the case of Ti-6Al-4V the bi-modal microstructure exhibits better fatigue properties than the equiaxed microstructure. In order to establish if this finding is also valid in the case of Ti-5Al-2.5Fe alloy, part of the delivered material

was, therefore, subjected to a heat treatment aimed at creating of a bimodal microstructure. The heat treatment consisted of annealing at 900°C in air for 1h and subsequent water quenching followed by aging at 520°C and furnace cooling down to the room temperature.

In the following sections, the 'as delivered' material, the material after water quenching and the material after the entire heat treatment will be referred to respectively as: as-delivered, quenched and heat-treated material.

3.3.2. Investigation of Mechanical Properties

Before the material is admitted to the manufacturing of the prostheses, it has to undergo a series of mechanical tests which ensure its quality, and during which it has to fulfil set minimum requirements [104]. The test programme consist of monotonic tensile and of rotating bending tests. During the tensile test the tensile strength (R_m), the yield strength ($R_{p0.2}$) and elongation (A) satisfy the requirements if their values are found to be greater than 860 N/mm², 780 N/mm² and 8% respectively[6]. In the rotating bending test which is carried out up to 10^7 cycles, the fatigue strength should exceed 525 N/mm². The test is conducted in air on smooth specimens with a mirror-like surface finish.

The hip joint prostheses are manufactured from the initial bar of the material by milling, in such a way that their axes are parallel to the long axis of the bar. The cutter of the milling machine moves perpendicular to the axis of the prostheses. A characteristic feature of the final products is their stepped shape with unsymmetric sectional geometries. Between the adjoining sections (or steps), there is a transition

[6] The yield strength $R_{p\ 0.2}$ is defined as the stress value at 0.2 % strain offset, the tensile strength R_m as the maximum load divided by the initial cross-sectional area and the elongation at rupture A as the percentage increase in the length of the test specimen (see, for example, ASTM Standard E 8-69).

radius, which in current designs can have the value between 1 mm and 2 mm. The transition radii represent places where there will be an increase in stresses due to change in geometry when the prostheses are loaded. After the machining, the surface roughness values R_a and R_t have to lie below 0.6 µm and 63 µm respectively[7] [105]. The surface finish remains further unchanged, starting from the distal end up to a point above the level where maximum stresses are expected during subsequent endurance tests. The surface roughness of the proximal end is deliberately increased to about R_a= 20 µm by shot peening in order to enable implant fixation by bone ingrowth. The endurance of the prostheses under cyclic loading is tested according to DIN 58840 [106] (see Chapter 2.2.2). During these tests the prostheses are embedded partially in acrylic bone cement with their axes approximately 10° from the vertical direction and loaded at their heads by a pulsating, negative force. The prostheses are submerged in a Ringer's solution at 37°C in order to simulate the environment of the human body. The composition of the Ringer's solution as given by DIN 58840 is shown in the table 3.3.2.1.

Table 3.3.2.1. Composition of physiological, Ringer's solution.

NaCl	9.01 g/l
$NaHCO_3$	0.084 g/l
KCl	0.298 g/l
$CaCl_2 \times 6H_2O$	0.548 g/l
destilled water	rest

In the research programme presented here, a mathematical model of the prostheses was developed with the aim of estimating the stresses which

[7] The surface parameters are described in BS1134:1972 as follows:
R_a - arithmetical mean deviation or centre line average height,
R_t - maximum peak to valley height in the sample.

occur in the prostheses during the DIN-test. This model can further be used for predicting the endurance performance of the prostheses provided that appropriate material data, in particular the high cycle fatigue strength, is available. The reliability of the prediction depends strongly on the quality of the data. From the information presented in this chapter, on initial testing of the material, and on fatigue properties of titanium alloys and of the Ti-5Al-2.5Fe presented in, in Chapter 3.2.5, it can be seen that the data of the quality needed in the mathematical model is not available. The major drawbacks of the values of the fatigue strengths found in the literature are:

> The fatigue strength was determined chiefly in rotating bending tests on smooth specimens with polished surface or on specimens with a sharp notches with stress concentration factor (SCF) of more than 3.3 tested in air at room temperature. The loading of the prostheses can be approximately described as biaxial bending due to an eccentric axial force. The major difference between the rotating bending and the loading of the prostheses is that the mean stress in the former is positive, and in the latter is equal to zero. The polished surface of the rotating bending specimens does not reflect the much inferior properties of the milled surface of the prostheses. The transition radii between the steps of the prostheses represent mild notches which can have different influence on the fatigue strength of the material than the sharp ones. Also, no consideration was paid to the influence of the environment of a human body on the fatigue strength, as the rotating bending tests were not carried out in Ringer's solution at 37°C.

In order to provide the material data which could be applied in the mathematical model, a high cycle fatigue test programme of the Ti-5Al-2.5Fe alloy was designed and performed.

The material was tested in three point bending mode. The machine used was a DARTEC[8] servo-hydraulic universal testing machine. The three point bending mode was chosen for testing, because it simulates better the loading conditions of the prostheses during the DIN-tests than the rotating bending mode. The minimum stresses (σ_{min}) in the load cycles were kept in the range of five percent of the maximum stresses (σ_{max}) , thus defining the stress ratio, $R=\sigma_{min}/\sigma_{max}$, as 0.05 and the mean stress, $\sigma_m=(\sigma_{max}-\sigma_{min})/2$, as always positive during the tests. The testing frequency was 20 Hz which is twice as high as the frequency during the DIN-tests. The higher frequency had to be chosen because of the limited time of the entire research programme. The loading form was sinusoidal.

A special testing rig was constructed to enable the specimens to be tested in the Ringer's solution. A schematic drawing of the rig is shown in the Figure 102. All fretting parts of the testing rig were machined of the Ti-5Al-2.5Fe alloy and the remaining parts of stainless steel or perspex. The surfaces of the stainless steel which could come into contact with the Ringer's solution were painted and coated with wax. In Figure 103, a schematic drawing of the entire test setup is presented. The Ringer's solution was pumped through the testing rig in the rate of about 2 l/min and came from a closed container equipped with a heat element and temperature controller. The container contained about 10 l of the Ringer's solution. The pump used in the testing rig was a RENA[9] C 40 centrifugal pump, the heater was UNO[10] 'REGAL' heater and the temperature controller was a UNO 'NOVA' solid state electronic thermostat. These items are widely available in shops with equipment for aquariums and their performance proved to be sufficient for the purpose of this study. This was notably due to the fact that neither the pump nor the heater and the temperature controller have metallic parts which, under normal conditions of operation, can come into contact with the corrosive solution.

---

[8]DARTEC Ltd., Nottingham, England

[9]RENA S.A., Annency, France

[10] UNO Products, C. Ellson & Co. Ltd., Nantwich, England

Test specimens had a shape of rectangular bars with corners rounded off in order to avoid premature crack initiation at the corners. Three types of specimens were manufactured (Fig. 104):

- smooth specimens with dimensions 10x10x80 mm,
- U-notched specimens with dimensions 10x11x80 mm and notch width of 4 mm, notch depth and radius of 1 mm,
- U-notched specimens with dimensions 10x12x80 mm and notch width of 4 mm, notch depth and radius of 2 mm.

The geometrical stress concentration factors of the notched specimens were determined from charts published in the reference [107]. According to those charts, the notch with the radius of 2 mm had the stress concentration factor of 1.44 and the notch with the radius of 1 mm had the stress concentration factor of 1.6.

The test specimens were cut from the initial bar of the material with their long axis parallel to the axis of the bar. In the case of the heat-treated material, care was taken to cut the specimens at least 5 mm away from the surface. The purpose of this precaution was to ensure that any hardening effects due to diffusion of oxygen during the heat treatment would not affect the results of the fatigue tests. The final shape of the specimens were manufactured by milling in the direction perpendicular to the long axes of the specimens. The roughness of the surface of the specimens was measured[11] after the machining in order to ensure that the surface quality was in accordance with the surface finish specified for the HERAMED prostheses. In order to investigate the influence of a different surface quality on the fatigue strength, the surface of some smooth specimens was mechanically brushed after the machining. The brushing was performed using a rotating, 1000 rev/min, steel brush with the disk diameter of 200 mm. In the result of the brushing, a plastically deformed surface layer was created.

[11] Talysurf, Taylor-Hobson, Leicester, England

Several test series were performed during the testing programme. The material, specimen type and testing conditions were as follows:

- as delivered material, smooth specimens, machined surface, Ringer's solution at 37°C, up to $2*10^7$ cycles
- as delivered material, 2 mm notch, machined surface, Ringer's solution at 37°C, up to 10^7 cycles
- as delivered material, 1 mm notch, machined surface, Ringer's solution at 37°C, up to 10^7 cycles
- as delivered material, smooth specimens, brushed surface, Ringer's solution at 37°C, up to 10^7 cycles
- as delivered material, smooth specimens, brushed surface, room temperature, up to 10^7 cycles
- heat-treated material, smooth specimens, brushed surface, Ringer's solution at 37°C, up to 10^7 cycles

The fatigue strength in each of the test series was defined as the maximum stress at which at least three specimens withstood the total number of cycles without fracture. The stresses were calculated from the formula:

$$\sigma_{max} = M*y/I,$$

where

M - bending moment resulting from applied force F_{max};
$M = F_{max}*30/2$ Nmm (see Fig. 102),
y - half of the thickness of the specimens;
y = 5mm for all specimens (see Fig. 104),
I - second moment of inertia of the critical cross-sections of the test specimens; $I = 10^4/12$ mm^4 for all specimens.

Hardness was measured and tensile tests were performed on the as-delivered and the heat-treated material in addition to the fatigue tests. In the VICKERS hardness testing machine, the load of 20 kg was used. The

tensile tests were carried out in accordance with ASTM Standards [108] in an INSTRON[12] TT-CM mechanical testing machine. In each case, three round specimens, with the gauge length of 30 mm and the diameter of 6 mm, were tested. The tensile strength, the yield strength and the elongation at rupture were determined from the tests.

3.3.3. Microstructure Investigation

In Chapter 3.2.3, it was shown that a number of different phases could be encountered in titanium alloys. In order to determine which phases were present in the material investigated in this study, the X-ray diffraction method was used [109]. Specimens with the section dimensions of 10 mm x 20 mm, and of approximately 2 mm in thickness, were cut from the as-delivered, quenched and heat-treated material. One of the section surfaces of each specimen was ground on emery paper with grades of 240, 400, 600 and finally 800. The surface was then polished on a fast rotating (up to 1500 rev/min) woollen cloth with a paste, consisting of alumina with ¼ µm particle size and of 10% aqueous oxalic acid solution as the polishing medium. After the polishing, the surface was slightly etched in a solution consisting of:

50 ml H_2SO_4
20 ml HNO_3
20 ml HF (40%)

The X-ray diffraction experiments were carried out in a PHILIPS diffractometer equipped with a X-ray detector and graphite monochromator which were mounted on a goniometer. A copper tube was used as a X-ray source and the intensity of the diffracted X-rays was recorded with a chart recorder. The X-ray spectrum thus obtained was indexed using the Bragg's Law:

[12] Instron Ltd., High Wycombe, England

$$\lambda = 2d_{hkl}\sin\theta,$$

where λ - wavelength of the X-radiation; λ = 0.1542 nm in case of copper CuK_α radiation,
d_{hkl} - apparent interplanar spacing of the (hkl)-planes from which the X-rays are diffracted,
θ - Bragg angle of the diffracted rays.

Knowing the crystallographic structure of the phases, e.g. hexagonal or cubic, the Bragg angles θ can be calculated for different interplanar spacings d_{hkl} and compared with the measured Bragg angles from the X-ray spectrum. The following formulae were used for the calculation:

cubic structure $$d = a/\sqrt{(h^2+k^2+l^2)},$$

hexagonal structure $$d = \sqrt{(3a^2/2(h^2+k^2+i^2+\lambda^{-2}l^2))},$$

where d - interplanar spacing,
a - unit cell vector,
h,k,i,l - plane indices,
λ - factor equal $2(c/a)^2/3$
c - second unit cell vector in hexagonal structure.

The presence of a particular phase is identified if the measured and calculated values of θ match each other.

The geometrical arrangement of the phases in Ti-5Al-2.5Fe alloy was investigated using optical microscopy. Specimens for observation were cut from the as-delivered, water quenched and heat- treated material. The surface of the specimens was ground on emery paper with grades 240, 400, 600 and 1000 and polished on fast rotating woollen cloth with ¼ µm alumina in 10% aqueous oxalic acid solution. The specimens were cleaned by rinsing with methanol, followed by an ultrasonic bath. They were then etched with the Kroll's reagent, consisting of:

10 ml HF (40%),
30 ml HNO_3,
and 50 ml H_2O,

which selectively attacks the beta phase. The investigation was carried out in a REICHERT[13] MeF3 metallographical microscope and the quantitative analysis, such as determining the volume fraction of the phases and the mean grain diameter, was performed in a QUANTIMET 800[14].

In addition to the X-ray diffraction and optical microscopy, a detailed transmission electron microscopy study of the microstructure was carried out. Specimens for the transmission electron microscopy were prepared from the as-delivered, water quenched and heat-treated material. In the first step of the specimen preparation, 0.8 mm thick plates were spark eroded from the bulk material in a SPARK EROSION UNIT[15]. Distilled water was used as the dielectric medium during the spark erosion process. From the plates, small discs of 3 mm diameter were produced also by spark erosion. The discs were then ground from both sides on emery paper with grades 240, 400 and 800 until their thickness was reduced down to about 0.1 mm. These foils were electrochemically thinned in a TENUPOL 3[16] twin jet thinning equipment. The thinning electrolyte, 5 Vol.% H_2SO_4 in methanol [110], was cooled to -45°C with liquid nitrogen, the voltage was 10V and the pumping velocity of the electrolyte was kept low. The thinning process was immediately stopped after a small hole had appeared in the foil. If the right conditions had been chosen, the areas in the foil near the hole were thin enough to permit an observation in the transmission electron microscope. The investigation was carried out in a JEOL TEMSCAN 100CX[17] transmission electron microscope equipped with a double tilt specimen holder at 100 kV acceleration voltage.

A large number of photographs were taken in the electron microscope under bright-field (BF), dark-field (DF) and selected area diffraction (SAD) conditions. The techniques used are well described in the literature, e.g. in references [111, 112]. Under bright- and dark-field condi-

---

[13]Reichert-Jung, Wien, Austria

[14]Cambridge Instruments, Cambridge, England

[15]Material Science (North West) Ltd., England

[16]Struers

[17]JEOL

tions, the geometrical arrangement of the phases present in the material can be investigated. With the selected area diffraction technique, the phases can be identified on the grounds of their diffraction patterns, and also, the crystallographic orientation of the grains, with respect to the direction of the electron beam, can be measured. As there could be a number of phases which can have different crystallographic structure in a titanium alloy, a computer program was developed in order to facilitate the indexation of diffraction patterns. The program calculated all possible diffraction patterns which would, with certain degree of accuracy, match the experimentally measured input data for hexagonal, body-centred cubic, face-centred cubic and orthogonal structure and displayed them on a computer screen or optionally printed on a matrix printer. The calculated, and the experimentally obtained diffraction patterns could then be compared with each other. From the comparison the calculated pattern which matched the experimental pattern was easily chosen. The measuring procedure and the computer program are described in detail in Appendix 4.

The investigation of the microstructure in the transmission electron microscope was complemented by the energy dispersive X-ray analysis (EDXA). In this method, the energy spectrum of the X-ray radiation emanated from the specimen on entry point of the electrons is measured. By analysing the spectrum, the relative concentrations of elements in different areas of the foils can be determined. The apparatus used in this study was a LINK EDXA System 860.

3.3.4 Dislocations

A combination of bright-field and selected area diffraction techniques together with very careful tilting of the specimens in the electron microscope was applied in order to find the Burgers vectors (b) and the line direction (l) of dislocations.

The Burgers vector of a dislocation can be calculated from the so called invisibility criterion [112]. The criterion is valid when the dislocation is observed under two beam conditions. In this case, the picture in the electron microscope is built up by electrons originating from the prima-

ry electron beam, and by electrons diffracted by only one set of planes of the crystal. Under certain two-beam conditions, the dislocation becomes invisible which is mathematically expressed by the equation:

$$\mathbf{g} \cdot \mathbf{b} = \emptyset,$$

where $\mathbf{b}$ - Burgers vector of the dislocation,
$\mathbf{g}$ - reciprocal vector of the diffracting planes.

A unique calculation of b is possible only if the invisibility criterion is satisfied by several sets of planes with different g. Some values of $\mathbf{g} \cdot \mathbf{b}$ for the hexagonal crystal structure are shown in Figure 105.

The line direction of a dislocation can be approximately determined from a series of photographs taken with at least three different primary beam directions in the crystal. The procedure is as follows [111]:

- The diffraction patterns corresponding to each of the beam directions are indexed, and traces of a suitable strongly reflecting plane marked on the photographs.
- The angles θ between the plane chosen and the normals to the projected line directions of the dislocation are measured on each photograph.
- The normals are plotted on a stereogram using the exact beam directions and the angles θ.
- A great circle is then drawn through the normals. The pole of this great circle is the line direction l of the dislocation in the crystal.

Knowing the Burgers vector and the line direction of a dislocation enables the determination of the type of the dislocation. A dislocation is of the pure screw type if the Burgers vector is parallel to the line direction and a dislocation is of the pure edge type if the Burgers vector is perpendicular to the line direction of the dislocation.

3.4. RESULTS

3.4.1. Mechanical Properties

Figures 106-111 show the results of the fatigue testing of the Ti-5Al-2.5Fe alloy. Each figure includes a table which contains values of forces applied in the three point bending test, the resulting maximum stress, and the number of cycles sustained by the test specimens. A graphical representation of the stresses against the logarithm of the number of cycles is shown underneath the tables.

From Figure 106 can be seen that the fatigue strength of smooth specimens with the surface finish unaltered after machining was 560 N/mm² at 10^7 cycles. The fatigue strength was reduced by the presence of a notch with 2mm notch radius to 400 N/mm² (Fig. 107) and by a notch with 1mm notch radius to 330 N/mm² (Fig. 108).

The dependence of the fatigue strength from the geometrical stress concentration factor is shown in Figure 112. From this, it can be seen that the dependence of the fatigue strength from the stress concentration factor is approximately linear. This dependence can be expressed by the equation:

$$\sigma_f = -370 * K_T + 933,$$

where

σ_f - fatigue strength at 10^7 cycles in N/mm²,

K_T - geometrical stress concentration factor (see Chapter 3.3.2).

Results of the fatigue testing of un-notched specimens with brushed surface are presented in Figure 109. The fatigue strength at 10^7 cycles in this case was 720 N/mm².

Results of the fatigue testing of specimens prepared from the heat-treated material are shown in Figure 110. The test specimens were un-notched and their surface was brushed after machining. The results for

the heat-treated material can therefore be compared with the results for the as-delivered material with brushed surface, which are presented in Figure 109. The fatigue strength of the heat-treated material has been found to be 760 N/mm².

In Figure 111, results of the last series of the fatigue testing are presented. During this series, specimens of as-delivered material with brushed surface were tested under different environmental conditions from the previous series. Instead of being conducted in the Ringer's solution at 37°C, the test were carried out in air at room temperature. The fatigue strength in this case was 810 N/mm². This value is 90 N/mm² higher compared to the result of the fatigue testing in the Ringer's solution (Fig. 109).

Table 3.4.1.1 summarizes the results of tensile testing of the as-delivered and heat-treated material.

Table 3.4.1.1. Comparison of material condition.

	as-delivered	heat-treated
$R_{p\ 0.2}$	795 N/mm²	885 N/mm²
R_m	935 N/mm²	990 N/mm²
A	14.6 %	8 %
HV20	320	370
σ_f*	720 N/mm²	760 N/mm²

* un-notched specimens with brushed surface

It can be seen that the heat-treated material was stronger and harder than the as-delivered material. The yield strength ($R_{p0.2}$) increased by 90 N/mm², and the tensile strength (R_m) by 60 N/mm² compared to that of the as-delivered material. The value of the elongation (A) of 8%, determined for the heat-treated material, was smaller than the value of 14.6% for the as-delivered material. The heat-treated material showed a 40 N/mm² higher fatigue strength than the as-delivered material.

3.4.2. Microstructure

Figures 113-115 show the results of the X-ray diffraction of the Ti-5Al-2.5Fe alloy. Each figure contains parts of the recorded X-ray spectrum. In each part, the intensity of reflected X-rays is plotted against the double value of the reflection angle (θ). The spectra were evaluated according to the method described in Chapter 3.3.3.

The following phases were identified in the X-ray diffraction spectra:

In the as-delivered material, Figure 113, the alpha and the beta phase.

In the quenched material, Figure 114, the alpha and the beta phase.

In the heat-treated material, Figure 115, the alpha phase, small amounts of the beta phase and the intermetallic phase TiFe.

Figures 116, 117 and 118 show the microstructures of the as-delivered, quenched and heat-treated material photographed in the optical microscope. While observing the photographs, it has to be kept in mind that the etchant used for the preparation of the specimens preferentially attacked the beta phase. Thus, there is a relief between alpha and beta regions of the specimens. The beta phase having been etched away leaves the alpha phase standing out.

Figure 116 shows a characteristic microstructure after forging and annealing. On the whole, the microstructure can be described as equiaxed. The impression of an equiaxed microstructure disappears at higher magnification, at which the beta phase appears to be elongated in one direction. The direction of elongation varies locally from place to place. The microstructure is very fine. The mean distance between the regions of the beta phase has been measured to be 6.5 µm. The average length of the beta phase particles is 5 µm and their width 1.5 µm. The beta phase covers about 18% of the surface area of the specimens.

Figure 117 depicts the microstructure of the quenched material. The beta phase can not be easily recognized. The microstructure is equiaxed with the mean grain diameter of 7 µm.

In Figure 118, the microstructure of the heat-treated material is presented. Numerous, small etch-pits are visible in the picture. These etch-pits are present only in the interior of some of the grains and at grain boundaries. It appears that the pits indicate sites of the beta phase which has been retained after the entire heat treatment. The average grain diameter of the microstructure is 7 µm as measured without taking into account the size of the etch-pits. The grains containing the etch-pits occupy about 60% of the surface area.

The photographs shown in Figures 119-126 were taken in the transmission electron microscope. In the photographs showing the microstructure, two methods of finding out which grains consisted of the beta phase were used. In the first method, the concentration of iron was measured with the EDX. Those grains which contained iron were identified as beta phase due to the fact that iron stabilizes the beta structure. The second method relied on taking a selected area diffraction (SAD) picture from the grain under question. After indexing the diffraction pattern, the grain could be assigned to the beta or alpha phase. Although more cumbersome in evaluation, the second method was used more extensively. This is because this method is not only restricted to the beta or alpha phases but enables an identification of any of the phases which can be present in a titanium alloy. The indexing of the diffraction pictures was greatly facilitated by the computer program for indexing diffraction patterns (see Appendix 4).

Figure 119 shows the microstructure of the as-delivered material. Grains of the beta phase have thin, elongated morphology. They appear darker in this particular photograph because they are thicker than grains of the alpha phase. The grains of the beta phase are often surrounded by a very fine, needle-like structures. These structures are called the interface phase and are caused by an uptake of hydrogen during the preparation procedure of thin foils for the electron microscope (see Chapter 3.2.3 and [114]). The interiors of each alpha grain contains a number of cells.

The cells are built up of dislocations introduced into the material by forging. They had not been removed by the annealing procedure.

The photograph in Figure 120a shows a typical picture of a region near a grain boundary between the alpha and beta phase in the as-delivered material. At the grain boundary, the fine interface phase can be seen. In the alpha grain, there are numerous dislocations whereas the beta grain appears dislocation free. There seem to be very fine precipitates in the beta grain. A diffraction pattern taken from the beta grain is shown in Figure 120b. Extensive diffuse streaking can be seen on this diffraction pattern. Such diffuse streaking could be observed on diffraction patterns of the beta phase with different electron beam directions. The streaking was caused by the fine precipitates in the beta phase. Despite numerous efforts, however, the morphology of these precipitates could not be resolved with the dark-field technique.

It was in general very difficult to obtain a reasonably good foil of the quenched material for observation in the electron microscope with the applied foil preparation method. The difficulties are apparent in Figure 121 which shows the microstructure of the material. The beta phase was identified by the SAD-method. It can be easily recognized in the picture, because there are many rib-like features present in the interior of the beta grains. The EDXA showed that there were no differences in element concentrations between the ribs and the matrix of the grains. A number of diffraction patterns taken from different regions of beta grains showed that there also were no differences in their mutual orientations. It is concluded, then, that the rib-like features are nothing more than variations in the thickness across the beta grains, caused by the uneven thinning operation of the electrolyte during foil preparation. This finding is important because it shows that the beta phase in the Ti-5Al-2.5Fe did not transform martensitically on quenching.

A region of a beta grain is shown at successively higher magnifications in Figures 122a and 122b. Especially in Figure 122b, features which appear to consist of parallel rows of particles are clearly visible. A diffraction pattern taken from the same area is shown in Figure 122c. Diffuse streaking, similar to that seen in Figure 120b, can be seen in Figure 122c. Again, the morphology of the precipitates could not be resolved with the dark-field technique.

The microstructure of the heat-treated material is shown in Figure 123. The microstructure is bi-modal, i.e. it consists of large primary alpha grains which are surrounded by regions with a very fine lamellar structure. In some regions, the lamellae are parallel to each other but regions with no apparent direction of the lamellae are also frequently encountered. The lamellae were formed during the transformation of beta grains and consist primarily of the alpha phase. No particular orientation relationship was found between the lamellae and the large primary alpha grains.

The investigation of the lamellae with the SAD-method was difficult because the lamellae were so fine that it was impossible to take a diffraction picture from an individual lamella. Figures 124a-e show a series of photographs taken from the lamellar structure under the bright-field, dark-field and diffraction conditions. Figure 124a depicts the region of the structure from which the photographs were taken. The average thickness of the lamellae is Ø.1 µm. Figure 124b shows the diffraction pattern from the region. The diffraction pattern is indexed in Figure 124c. It is shown in Figure 124c that the diffraction pattern can be constructed from a diffraction pattern of the alpha phase with the beam direction B=[1$\bar{2}$1$\bar{3}$] and the same diffraction pattern rotated by 18Ø° about the plane vector g=(1$\bar{1}$Ø1). Such diffraction patterns are typical for twinned structures.

In Figures 124d and 124e, dark-field pictures are presented which were taken with different operating reflections. These reflections were chosen in such a way that they belonged to the two different orientations of the alpha phase shown in Figure 124c. Figures 124d and 124e are complementary, and show that the diffraction pattern in Figure 124b originates from differences in orientation of adjacent lamellae.

In Figure 125a, a bright-field picture of a different region in the lamellar structure is shown. The diffraction pattern of the region is shown in Figure 125b. In Figures 125c, 125d and 125e, theoretical diffraction patterns of the alpha, beta and the TiFe phases are plotted. The theoretical diffraction patterns are assembled together in Figures 125f and 1256g. From a comparison of Figures 125f and 125g with Figure

125b, it can be seen that the experimental diffraction pattern is composed of the diffraction patterns of the alpha, beta and TiFe phases shown in Figures 125c-125d. This result implies that there is an orientation relationship between the alpha and the beta phases of the form:

$$(0001)_\alpha \,||\, (110)_\beta \;,\; [11\bar{2}0]_\alpha \,||\, [100]_\beta .$$

The morphology of the beta phase and the TiFe phase is revealed in Figure 126. Figure 126a shows a bright-field photograph of the lamellar structure. The diffraction pattern of the region is depicted in Figure 126b and is similar to the diffraction pattern shown in Figure 126b. Figure 126c shows a dark-field photograph which was taken with operating reflections belonging to the beta and TiFe phase. Figure 126d depicts a dark-field photograph taken with an operating reflexion belonging to the alpha phase.

The microstructure investigation showed that the beta and TiFe phase are unevenly distributed in the lamellar structure. No reflections belonging to the beta or TiFe phases could be observed in regions where the lamellae were parallel to each other. Regions where the lamellae were irregular in shape often showed the presence of the beta and TiFe phases.

3.4.3. Dislocations

An attempt was made to investigate dislocation structures which develop during fatigue testing of the Ti-5Al-2.5Fe alloy. Thin foils for the investigation were prepared from the as-delivered and heat-treated material. They were cut from test specimens which had been fatigued at stress levels close the fatigue strength.

The investigation of the dislocation structures in the as-delivered material was difficult. The major problem was that it could not be decided whether the observed dislocation structures resulted from the fatigue process or whether they had been present in the material before it was fatigued. The investigation of the microstructure of the as-delivered

material had shown that many dislocations could be found in the unfatigued material (see Chapter 3.4.2). The observations were also affected by the formation of the hydrogen-induced interface phase around beta grains (see Chapters 3.2.3 and 3.4.2). Some common features could however be identified in all foils prepared from the as- delivered material. Firstly, no cell structures and no persistent slip bands were present in the fatigued microstructure. Secondly, no dislocations were observed in the beta phase. All dislocations were confined to the alpha phase.

Figure 127 shows a frequently observed dislocation structure in the alpha phase of fatigued, as-delivered material. The photograph in Figure 127 was taken from a foil which was prepared from a specimen which sustained 10^7 cycles at 720 N/mm², but similar pictures were observed in foils prepared from specimens which broke during fatiguing. The dislocation structure contains rows of parallel, long dislocations. The dislocations are straight and appear to form elongated, narrow U-shaped loops.

During the investigation of the dislocation structures in fatigued, heat-treated material no attempt was made to resolve dislocations in the fine lamellar part of the microstructure. The investigation concentrated on the primary alpha grains. Before fatiguing, these grains were free of dislocations. Figure 128 shows an example of a dislocation structure observed in a specimen which sustained 10^7 cycles at 760 N/mm² and which was also present in broken specimens. The dislocation structure shown in Figure 128 can be seen as a direct result of the fatigue damage. The dislocations form parallel slip lines. Seemingly perpendicular to the slip lines lie a number of U-shaped dislocation loops. No persistent slip bands or cells were observed in the heat-treated material.

A region near to one of the dislocation loops was investigated more closely. Figure 129 shows a series of photographs taken with different two beam conditions. The photographs served as the basis for the analysis aimed at finding Burgers vectors and line directions of the dislocations (see Chapter 3.3.4). Figure 129a shows the investigated dislocation loop and the adjacent area. On the right hand side of the picture, a part of a slip line is visible. The slip line lies along the trace of the prismatic $(10\bar{1}0)$-plane and consists of a dense array of parallel

dislocations. The photograph in Figure 129b was taken with operating reflection from the (0001)-planes, and shows no dislocations. This extinction of the dislocation contrast indicates that the dislocations are likely to have the Burgers vector of the type $^1/_3\langle 11\bar{2}0\rangle$ (see Figure 105). The operating reflection in Figure 129c was $(01\bar{1}2)$. The dislocations forming the dislocation loop are extinct. According to Figure 105, the extinct dislocations have the Burgers vector equal $\pm^1/_3[\bar{2}110]$. On the left hand side of Figure 129c, dislocations are visible which have a different direction, and therefore a different Burgers vector, from the dislocations in the slip line on the right hand side. Figure 129d shows a photograph where the dislocations of the slip band are not visible. The operating reflexion in this case was $(\bar{1}10\bar{1})$, and the dislocations therefore have the Burgers vector equal to $\pm^1/_3[11\bar{2}0]$.

Figure 130 shows a schematic stereographic projection and a schematic drawing of the dislocation loop. The stereographic projection shows the line directions of the dislocations determined by graphical analysis of the dislocations from Figure 129 described in Chapter 3.3.4. The dislocation line of the long dislocations in the dislocation loop lay close to the $\pm[\bar{2}110]$-direction, the dislocations in the slip line were close to $\pm[11\bar{2}0]$ and the short segment in the dislocation loop, forming the bottom of the shape U, was close to the $\pm[0001]$-direction.

Figure 131 shows the surface of a fatigued test specimen of the heat-treated material as seen in a scanning electron microscope. The surface was polished and slightly etched prior to the fatigue testing in order to be able to observe a crack initiation site. In Figure 131, a crack in the interior of a primary alpha grain is clearly visible. Numerous slip lines are present in all primary alpha grains. Similar pictures, and pictures with cracks apparently initiated at grain boundaries between two primary alpha grains, were observed in several places at the surface of the test specimen. Figure 131 implies that cracks in the heat-treated material presumably initiate at slip lines in the primary alpha grains.

The crack initiation site was not be established in the case of the as-delivered material. Figure 132 shows a picture of the starting point of a fully developed crack in a test specimen of the as-delivered material.

3.5. DISCUSSION

3.5.1. Mechanical Properties

The fatigue strength at 10^7 cycles of the Ti-5Al-2.5Fe alloy in the as-delivered condition was 560 N/mm². This value was found in three point bending tests on un-notched specimens, which were submerged in a physiological Ringer's solution kept at 37°C. The fatigue strength compares favourably with the fatigue strength of the Ti-5Al-2.5Fe alloy of 550 N/mm² reported in the literature (see Chapter 3.2.5). However, the drop in the fatigue strength due to a presence of notches is shown to be greater than is indicated by data from the literature. In this study, the fatigue strength was reduced to 330 N/mm² by a stress concentration factor of 1.6, whereas a comparable reduction in the value of the fatigue strength in the literature was associated with a stress concentration factor of 3.6.

The knowledge of the fatigue strength of smooth and notched specimens enables the calculation of the so called fatigue notch factor K_F. The fatigue notch factor is defined as the ratio of the fatigue strength of an un-notched specimen to that of a notched one having the same critical cross-sectional area [94]. The fatigue notch factor is the equivalent of the stress concentration factor for the case of cyclical loading. Having calculated the fatigue notch factor, the notch sensitivity factor q can be defined as:

$$q = K_F / K_T ,$$

where q - notch sensitivity factor,
K_F - fatigue notch factor,
K_T - geometrical stress concentration factor.

The notch sensitivity factor relates the fatigue notch factor to the geometrical stress concentration factor. The notch sensitivity factor is equal to one for a perfectly notch sensitive material [94].

The results of the calculation of the fatigue notch factor and the notch sensitivity factor for the two values of the stress concentration factor in the test specimens (see Chapter 3.3.2) are summarized in the table below.

Table 3.5.1.1. Notch sensitivity factors.

K_T	K_F	q
1.44	1.4	0.97
1.6	1.7	1.06

From this table, it can be seen that the Ti-5Al-2.5Fe alloy behaved as a perfectly notch sensitive material under the fatigue test conditions. This finding is important in respect to the mathematical model for predicting the endurance performance of the artificial hip joint prostheses. It means that, with good accuracy, the fatigue notch factor is equal to the geometrical stress concentration factor. In other words, the geometrical stress concentration factors can be used directly, in place of the fatigue notch factors, for calculating the effects of any stress increases, due to notches, on the fatigue strength of the material. For design purposes, however, the high notch sensitivity of the Ti-5Al-2.5Fe alloy means that notches should be avoided in areas of high stresses whenever it is possible.

The fatigue strength of the as-delivered material with brushed surface (720 N/mm²) was significantly higher than that of the as-delivered material with machined surface (560 N/mm²). Table 3.5.1.2 shows a comparison between these surface qualities, and, Figures 133 and 134 show optical photographs of machined and brushed surfaces. In Figure 133, numerous machining marks are clearly recognizable. These marks are entirely removed by the brushing procedure and the surface is plastically deformed (Fig. 134). From Table 3.4.1.2, it can be seen that the surface

roughness, as measured in the direction perpendicular to that of the machining marks, increased markedly after brushing. In spite of the deterioration in the surface quality, the brushed specimens have shown a dramatic increase in the value of the fatigue strength from 560 N/mm² to 720 N/mm² as compared to specimens with the machined surface.

Table 3.5.1.2. Comparison of surface finish.

	machined	brushed
R_a	0.7 µm	1.4 µm
R_t	35 µm	75 µm
HV20	320	320
σ_f	560 N/mm²	720 N/mm²

The results show clearly the beneficial effect of a surface treatment after machining.

The fatigue strength of the heat-treated material with brushed surface of 760 N/mm² was also higher than that of the as-delivered material with the same surface condition. The mechanical properties of the Ti-5Al-2.5Fe alloy showed therefore similar trends as in case of the Ti-6Al-4V alloy (see Chapter 3.2.4).

Based on the results of the fatigue tests of the Ti-5Al-2.5Fe alloy, two ways of improving the fatigue strength could be indicated.

Firstly, the fatigue strength of the material could be drastically improved by a surface treatment. The surface treatment should be aimed at removing any machining marks and at plastically deforming the surface layer. This task seems to be more important than assuring that the roughness of the surface of a finished product is kept below specified limits.

Secondly, an appropriate heat treatment leads also to an improvement of the mechanical properties. The as-delivered material had an equiaxed and the heat-treated material a bi-modal microstructure.

The heat-treated material was harder and stronger. As in the case of Ti-6Al-4V, the material with the bi-modal microstructure showed a higher high cycle fatigue strength (see Chapter 3.2.4).

The mechanical tests showed that the environment has a substantial influence on the fatigue strength of the Ti-5Al-2.5Fe alloy. The fatigue strength of the as-delivered material with brushed surface tested in air was 90 N/mm² higher compared to the material tested in the Ringer's solution. Thus, this result provides a justification for the claim that any assessments of the fatigue properties of the Ti-5Al-2.5Fe alloy have to be conducted under simulated working environment.

3.5.2. Microstructure

From the position of intensity peaks in the X-ray diffraction spectra, phases present in the as-delivered, quenched and the heat-treated material were identified. The alpha and beta phase were found in all the material conditions. The intermetallic phase TiFe was found in the heat-treated material (see Chapters 3.2.5 and 3.4.2).

It can be noticed from the X-ray spectra, Figures 113-115, that the position of the peaks associated with the β phase changes with the material condition. For example, the $(002)_\beta$-peak is found to lie at $2\theta \approx 57°$, at $2\theta \approx 57.7°$ or at $2\theta \approx 58.5°$ in case of the quenched, as-delivered and heat-treated material respectively. The shift in the position of the peaks is caused by different concentrations of iron in the β phases. With an increasing amount of Fe atoms, the unit cell of the β phase becomes smaller, which in turn leads to greater values of 2θ (see Chapter 3.2.1).

By comparing the relative heights of the α- and β-peaks in Figure 114, for quenched material, it can be seen that the $(011)_\beta$-peak is higher than the $(10\bar{1}1)_\alpha$-peak. Also, by comparing Figure 114 with Figure 113, for as-delivered material, it can be seen that the β-peaks are stronger in Figure 114. It can be therefore concluded that relatively large amount of the beta phase has been retained on quenching.

From a comparison of the relative heights of the peaks in the X-ray spectrum for the heat-treated material, Figure 115, it is apparent that the decomposition products of the β phase during aging of the quenched material are the α- and the TiFe-phase (see Chapter 3.2.5). The small peak at 2θ≈58° indicates that only a small amount of β is still present in the material after the entire heat treatment.

Fine precipitates were observed with the transmission electron microscope in the beta phase in the as-delivered and the quenched material (Fig. 120, 122a-b). Diffraction patterns obtained from the beta phase showed extensive diffuse streaking (Figures 120a and 122c). Such diffuse streaking effects are associated in the literature with the presence of the athermal omega phase [69, 70, 71, 72] (see Chapter 3.2.3). The athermal omega did not show in the X-ray diffraction spectra. This was presumably because of a low volume fraction of this phase in the material.

The microstructure of the as-delivered material was equiaxed (Fig. 116, 119). Such microstructure was expected from the knowledge of how the material was processed (see Chapters 3.2.4 and 3.3.1), and from the knowledge of different types of microstructures in the Ti-6Al-4V alloy (see Chapters 3.2.3. and 3.2.4). The presence of the athermal omega phase, however, represented the major difference between the Ti-5Al-2.5Fe and the Ti-6Al-4V alloy. The athermal omega played an important role during heat treatment of Ti-5Al-2.5Fe. In the quenched material, the athermal omega phase stabilized the beta phase, so that the beta phase was retained on quenching. A martensitic transformation of the retained beta phase was suppressed (Fig. 121 and 122). This behaviour of the Ti-5Al-2.5Fe alloy differs from that of the Ti-6Al-4V alloy described in the literature (see Chapters 3.2.3 and 3.3.4). In Ti-6Al-4V, the β phase transforms martensitically into the α' phase on quenching from the (α+β)-field.

It was shown in Chapter 3.4.2 that the fine lamellar structure in the heat-treated material occupied about 60% of the microstructure. Because of the fact that the lamellar structure originated directly from the retained beta phase, it can be concluded that the beta phase also occupied about 60% of the microstructure in the quenched material. Thus, in

the Ti-5Al-2.5Fe alloy is possible to retain a large amount of beta phase at room temperature, despite the low concentration of alloying elements. The material in this condition could have interesting mechanical properties. It can be imagined that the lamellar part of the bi-modal microstructure, and thus the mechanical properties of the heat-treated material can be easily influenced by the parameters of a heat treatment. As the beta phase in the quenched material does not transform martensitically, the size of the lamellae is directly correlated to the aging temperature and time. At high temperatures and long aging times, the lamellae should be coarse. At low temperatures and short annealing times, the lamellae should be very fine, and it may even be possible to create alpha precipitates in the retained beta phase. Such precipitates could significantly strengthen the beta phase.

The microstructure of the heat-treated material has not yet been described in the literature. It is therefore described in detail below.

The microstructure of the heat-treated material as seen in the electron microscope was bi-modal (Fig. 123, see also Chapter 3.2.4). The beta phase which had been retained in the quenched material, transformed into a fine lamellar structure during annealing. Phases present in the lamellar structure were determined on the basis of selected area diffraction patterns (see Chapter 3.4.2 and Fig. 125). The lamellar structure consisted predominantly of the alpha phase, and, the second product of the transformation was the intermetallic phase TiFe. A small amount of the beta phase could still be detected in the lamellar structure.

The analysis of the diffraction pattern from Figure 125b (presented in Chapter 3.4.2, Figures 125f-g) implies that the orientation relationship between the alpha and beta phase in the lamellar structure is as follows:

$$(0001)_\alpha \,||\, (110)_\beta \;,\; [11\bar{2}0]_\alpha \,||\, [100]_\beta .$$

According to the literature (see Chapter 3.2.3), the orientation relationship between the alpha and beta phase obeys the Burgers relation:

$$(0001)_\alpha \,||\, (110)_\beta \;,\; [11\bar{2}0]_\alpha \,||\, [111]_\beta .$$

In Figure 135, a schematic stereographic projection of the Burgers relation is shown. It can be seen that if the Burgers relation is satisfied, the orientation relationship shown in Figures 125f-125g is also approximately valid.

In Figure 126d, a dark-field photograph of the lamellar structure is shown which was taken with an operating reflexion belonging to the alpha phase. In the upper part of Figure 126d, a bending contour is recognizable. The bending contour is directly related to the operating reflection. The fact that the contour does not run through the centre of the photograph indicates that there is a difference of some degrees between ideal orientations of the alpha and beta phases which would give rise to the composite diffraction pattern in Figures 126b and 125b. It is therefore concluded that the orientation relationship from Figures 125f-125g can be seen as an approximate expression of the Burgers relation. The analysis in Chapter 3.4.2 showed that not only the beta phase but also the TiFe phase in the lamellar structure obeys the Burgers orientation relationship in respect to the alpha phase.

There was an orientation difference between adjacent lamellae of the alpha phase in the lamellar structure which resembled a twinned structure (Fig. 124). There was no relationship between the orientation of the lamellae and the orientation of the surrounding primary alpha grains.

The differences in the microstructures of the as-delivered and the heat-treated material explain why the heat-treated material had better mechanical properties (see Chapter 3.5.1). It is generally observed that materials which have high yield strength (or tensile strength), also show a high high-cycle-fatigue strength (e.g. [94]). In materials which have the same composition and similar microstructures, the yield strength increases with decreasing average grain size. This is expressed in the well known Hall-Petch relation (e.g. [116], p. 788):

$$\sigma = \sigma_o + Kd^{-1/2},$$

where

σ - yield strength

σ_o - extrapolated value of the yield strength as $d \to \infty$,

K - proportionality factor,

d - average grain diameter.

The as-delivered material had an equiaxed microstructure which consisted of alpha and beta grains. The average diameter of the alpha grains was 6.5 μm (see Chapter 3.4.2). The investigation of the dislocation structure in the fatigued material showed that there were no dislocations in the beta phase (see Chapter 3.4.3). The beta phase can therefore be regarded as harder then the alpha phase. This permits the assumption that the plastic flow of the material is initially controlled by the deformation of the alpha phase only. The microstructure of the heat-treated material was bi-modal. It consisted of primary alpha grains surrounded by fine lamellar structure. The primary alpha grains were approximately 7 μm in diameter, and therefore not much larger than the alpha grains in the as-delivered material. The lamellar structure occupied 60% of the microstructure in the heat-treated material. The thickness of the alpha lamellae was approximately 0.1 μm (see Chapter 3.4.2). A crude estimation of the average diameter of the alpha phase in the heat-treated material, which could be used in the Hall-Petch relation, is possible by applying the rule of mixtures:

$$d = d_l V_l + d_p V_p ,$$

where

d - average diameter,

d_l - size of alpha in lamellar structure; $d_l = 0.1$ μm,

V_l - amount of lamellar structure; $V_l = 0.6$,

d_p - size of primary alpha; $d_p = 7$ μm,

V_p - amount of primary alpha; $V_p = (1 - V_l) = 0.4$.

The estimation leads to the value of d=2.86 μm which is less than a half of the average diameter of the alpha phase in the as-delivered material. According to the Hall-Petch relation, the heat-treated material should have better mechanical properties than the as-delivered material. This was indeed confirmed experimentally.

3.5.3. Dislocations

It must be pointed out that that the aim of this part of the material investigation was to try to compare the dislocation structures in a fatigued titanium alloy with the dislocation structures of other metals described in the literature (see below, and Chapter 3.2.6). An in depth study of a development of dislocation structures during the fatigue process was not carried out. It appears that a different testing method, such as push-pull testing, should be used in that case, where a more accurate definition of the stress and deformation state can be achieved than in the case of a three-point bending test.

The currently-accepted picture of the role of dislocations in fatigue states that the so-called persistent slip bands play a major role in fatigue of fcc metals (see Chapter 3.2.6). An irregular dislocation structure, consisting of veins and bundles of edge dislocations, and, some screw dislocations, dominates during the first cycles of the deformation. Above a particular, well-defined threshold stress amplitude, new dislocation structures, called persistent slip bands (PSBs), start to emerge. The PSBs are well-ordered, ladder-like structures which consist of periodic walls of dislocation dipoles oriented perpendicular to the direction of the slip (Fig. 101). The volume fraction of the PSBs increases with the increase in the number of cycles. In other words, it is linearly dependent on the imposed plastic strain. The PSBs are believed to play a key role in the development of fatigue cracks. It has been established that the PSBs are softer than the vein structure, from which follows, that the PSBs accommodate the majority of the imposed plastic strain. This localization of the plastic deformation in PSBs leads to the formation of the extrusions on the surface of the fatigued specimens. Cracks initiate preferably on the site of the extrusions, because of the stress concentrations induced by the change in surface geometry, and then propagate along the PSBs in their early stage [98].

It is important to observe that if no PSBs are formed, the material can undergo a very large number of cycles. Because the PSBs are found to form above a well defined stress (or strain) amplitude, this critical stress can be regarded as the true fatigue limit [97]. This is best illustrated by the so-called cyclic stress-strain (css) curve which ex-

presses the dependence of the cyclic stress on cyclic plastic strain. Figure 136 shows a schematic css-curve for copper single crystals. At stress of approximately 25 MPa, there is a plateau in the curve which is associated with the presence of PSBs. Below this, so-called saturation stress, no PSBs are formed.

Unfortunately, the above outlined picture of the development of the dislocation structures in fatigued fcc metals can not be directly applied to metals with different crystallographic structures. In the case of bcc metals, like iron and niobium, it is found that the dislocation arrangements can differ substantially from those found in fcc metals [95, 99]. The differences are explained on the basis of the different mechanical properties of these metals. The mechanical behaviour of the bcc metals depends strongly on temperature and strain rate. In the low temperature range, the mobility of the screw dislocations (v_0) is low as compared to the mobility of the edge dislocations (v_T). Figure 137 shows schematically how a dislocation segment which is pinned at two points expands in the low and high temperature range. The low mobility of the screw dislocations impedes the dislocation propagation and multiplication. At low strain amplitudes, the more mobile edge dislocations draw out long screw dislocations and this process can be reversed repeatedly in a quasi-reversible fashion. Thus, a microyielding regime exists in which the strain is accommodated essentially by to-and-fro displacements of the mobile non-screw segments without microstructural changes. This regime manifests itself in the css-curve. Figure 138 depicts the css-curve of niobium single crystals. It can be recognized that at low plastic strain, there is a plateau in the curve. Analogous to fcc metals, this region in the css-curve can be associated with the fatigue limit. At higher strains, the lack of mobile dislocations causes early secondary glide. At this stage, the mobile edge dislocations draw out long screw dislocations in different slip systems. At not too low temperatures, the screw dislocations are sufficiently mobile to interact and form cell structures. It must be stressed that no PSBs are formed in the low temperature range. Cracks initiate in ill defined slip bands at the surface [99]. In the high temperature range, the mobility of the screw dislocations becomes comparable to the mobility of the edge dislocations and the fatigue behaviour of bcc metals can become quite similar to that of fcc metals. Under these conditions, PSBs with similar properties regarding

the strain localization and the initiation of cracks, and having the appearance of channels with comparatively few dislocations embedded in a matrix of veins, have been observed.

It has been previously mentioned that the microyielding regime appears to be associated with the fatigue limit. The to-and-fro gliding of the dislocation can proceed without microstructural changes only in the bulk material. At the surface, it is possible that the mobile, non-screw segment will be lost at some stage (Fig. 139). The resulting lack of mobile segments at the surface can be overcome by the activation of dislocations in the secondary slip system. In this case a cell structure can be expected to form, and accordingly, the surface regions to harden (this behaviour has been indeed confirmed experimentally [95]). The preferential hardening of the surface can lead to an increase in fatigue life, provided the hardened surface layer develops before cracks can form in surface slip-bands.

The investigation of dislocations in fatigued Ti-5Al-2.5Fe (see Chapter 3.4.3) led to the following results:

In the case of the as delivered material, no dislocations were found in the beta grains. This result is in agreement with literature on fatigued Ti-6Al-4V (see Chapter 3.2.6). All dislocations were confined to the alpha phase, where they formed parallel, elongated U-shaped loops (Fig. 127).

In the case of the heat-treated material, it was observed with scanning electron microscopy, that cracks initiated at slip lines in primary alpha grains (Fig. 131). This is in concordance with the literature on fatigued Ti-6Al-4V with an equiaxed microstructure, where cracks were found to originate in the alpha phase (see Chapter 3.2.6). The investigation of the dislocation structure in the transmission electron microscope showed that in the interior of the primary alpha grains the dislocations were arranged in parallel slip lines and also formed elongated U-shaped loops (Fig. 128 and 129).

The analysis of dislocations conducted in Chapter 3.4.3 and Figures 129 and 130, showed that the dislocations in the primary alpha grains in fatigued heat-treated material were confined to the prismatic $\{10\bar{1}0\}$-planes, and had the Burgers vectors of $^1/_3\langle 11\bar{2}0\rangle$. The majority of the dislocations had their Burgers vectors approximately parallel to their line directions. This means that they were screw dislocations (see Chapter 3.3.4). Small edge segments were found in dislocation loops, where they formed the mobile parts of the loops (Fig. 130). The shape of the loops, in the form of an elongated letter U, and the abundance of screw dislocations implies that edge dislocations were more mobile than the screw dislocations. The higher mobility of the edge dislocation in titanium has indeed been predicted in the literature [103].

From the description of dislocation structures in fatigued metals, and from the description of dislocations found in the primary alpha grains, it can be seen that the dislocation structure in fatigued Ti-5Al-2.5Fe have some similarities with the dislocation structures observed in body-centred cubic metals fatigued in the low temperature range. As in the case of bcc metals, the mobility of edge dislocations in the alpha phase is higher than the mobility of screw dislocations. The edge dislocations, therefore, draw out long straight screw dislocations. It is imaginable that at low stress levels, the strain could be accommodated by a to-and-fro gliding of edge dislocations in a quasi-reversible fashion. As with bcc metals, such a process could be associated with a fatigue limit. The to-and-fro movement of edge dislocations could also explain the increase of the fatigue strength due to a surface treatment. The surface treatment provided a plastically deformed layer which prevented the edge dislocations from escaping from the material. The gliding process of the edge segments could be maintained without activating a secondary slip system. However, carefully designed experiments, aimed in particular at measuring the css-curve (such as in [99]), would be needed in order to confirm these speculations.

At stress levels near to the fatigue strength of the Ti-5Al-2.5Fe alloy, the majority of the dislocations were concentrated in well defined slip lines, in what appeared to be the primary glide system. It seems that cracks originated at these slip lines. This finding is in contrast to

the behaviour of bcc metals where dislocations are usually arranged in cells, and cracks have been found to originate in ill defined slip bands.

It has been shown previously that the persistent slip bands play a crucial role in the fatigue of fcc metals. The PSBs consists of hard walls of edge dislocations, and a few screw dislocations which move between the walls (Fig. 140). In the case of copper single crystals, it is found that the saturation stress in the css-curve can be calculated from the following empirical equation [96]:

$$\tau_s = (2 \pm .3) Gb/[(1-\nu)d], \qquad (1)$$

where

τ_s - saturation stress,
G - shear modulus,
b - value of the Burgers vector,
ν - Poisson ratio,
d - distance between walls.

This equation expresses the stress required to force a screw dislocation between the walls of spacing d. It also enables a prediction of the fatigue strength, as no PSBs are found to form below the saturation stress.

By comparing Figure 140 with the picture of the dislocations found in the alpha grains (Fig. 128), it could be argued that the dislocation structure in the alpha grains resembles that in the PSBs. The slip lines can be regarded as hard walls, and there are few screw dislocations between the slip lines. The average spacing between the slip lines, as measured from Figure 128, is 0.37 µm. The shear modulus and the Poisson ratio for titanium is equal to 41 kN/mm² and 0.32 respectively (see Chapter 3.2.1). The value of the Burgers vector $^1/_3[11\bar{2}0]$ is 0.295 nm[18]. Using Equation (1), the value of τ_s is calculated to be

[18] The Burgers vector of the dislocations was found to be $\pm^1/_3[11\bar{2}0]$. The value (the length) of this Burgers vector is equal to the length of the unit cell vector a_α, i.e. b=0.295 nm (see Chapter 3.2.1.).

approximately equal to 96±14 N/mm². Unfortunately, this result can not be compared with data from the literature, as the fatigue of titanium has not yet been investigated to such a detail as e.g. that of copper. The stress τ_s can be however related to the applied external (tensile) stress σ. The stress τ_s is 'internal' in the sense that it acts parallel to the slip system of the dislocations. If a single crystal is loaded by an external tensile stress σ, in order to calculate the stresses τ which act on the particular slip systems, the stress σ has to be resolved into the slip systems according to the orientation of the crystal. In the case of a polycrystalline material, this is done with the help of the so-called Taylor factor. The stress τ are related to the externally applied stress σ according to the following equation:

$$\sigma = M\tau, \qquad (2)$$

where

σ - external stress,
M - Taylor factor,
τ - stress in the slip system.

The value of the Taylor factor for prismatic slip in polycrystalline titanium is equal to 5 [117]. Using Equation (2) for calculating the external stress for the value of τ equal to 96±14 N/mm², leads to the result of σ=480±70 N/mm². This value of σ can be compared with the fatigue strength of the material. It was found that the fatigue strength of the heat-treated material was 760 N/mm² (see Chapter 3.4.1). The comparison shows that the the value of the stress σ is approximately 60% of that of the fatigue strength. It can be therefore concluded that as much as 60% of the value of the fatigue strength of the heat-treated material, can be explained by gliding of screw dislocation between the slip lines. This is provided that the dislocation structure in the fatigued material can be regarded as similar to the persistent slip bands.

The picture of the dislocation structure in fatigued heat-treated material is similar to the dislocation structures found in plastically deformed Ti-Al single crystals [115]. The arrangement of screw disloca-

tions, in well defined slip lines, resembles dislocation pile-ups. It is pointed out in the literature that cracks can initiate at dislocation pile-ups [116, 118]. It is therefore interesting to estimate the stress which could cause a crack initiation in the material.

A pile-up exerts a large stress magnification at the head of the pile-up (at grain boundary) such that the stress on the leading dislocation is N-times the applied stress :

$$\tau_e = N\tau, \tag{3}$$

where

τ_e - stress on leading dislocation,
N - number of dislocations in the pile-up,
τ - applied stress.

The total number of (screw) dislocations in the pile-up (N) depends on the value of the applied stress (τ):

$$N = \pi d\tau/Gb, \tag{4}$$

where

d - grain diameter[19]; d=7 μm (see Chapter 3.4.2),
G - shear modulus; G=41 kN/mm^2,
b - Burgers vector; b=0.295 nm.

It can be assumed that the crack nucleation occurs if the stress τ_e exceeds a hypothetical, critical shear stress τ_c. The value of the stress τ_c was investigated in [118] for the case of monotonic tensile and compressive loading of Ti-8Al. It was found that the τ_c-value was approximately 38 kN/mm^2. Using Equations (3) and (4), a critical number of dislocations (N_c) in the pile-up can be calculated, which would cause the stress τ_e to equal the critical stress τ_c:

[19]It is assumed in this simple calculation that the length of the pile-up is equal to the average grain diameter.

$$N_c = \sqrt{(\tau_c d n / G b)}. \qquad (5)$$

The calculation leads to the value of N_c equal to 262. From the Equation (3), the critical number of dislocations can now be used for calculating the applied stress τ:

$$\tau = \tau_c / N_c. \qquad (6)$$

The calculated value of τ is 145 N/mm². Using the Taylor factor for calculating the external tensile stress (Equation (2)), leads to the value of σ equal to 725 N/mm². Surprisingly, this is very close to the value of the fatigue strength of the heat-treated material of 760 N/mm². This result indicates that the fatigue strength of the heat-treated material could be explained in terms of the formation of cracks at the end of dislocation pile-ups in the primary alpha grains. This is because of the fact that the value of σ has been calculated using the grain diameter of these grains (d=7 µm). If the value of the grain diameter was equal to that found in the as-delivered material (d=6.5 µm), the value of σ would be equal to 751 N/mm². If this value was taken as the fatigue strength of the as-delivered material, then it would be greater than that of the heat-treated material. This is in contradiction to the findings presented in Chapter 3.4.1, where it was shown that the opposite is the case. The contradiction disappears, however, when the average grain diameter of the entire microstructure of the heat-treated material is taken into account. It was estimated in Chapter 3.5.2 that the average grain diameter of the lamellar structure together with the primary alpha grains was 2.89 µm. The stress σ calculated with this value of the grain diameter is equal to 844 N/mm².

At this stage of the discussion, the shortcomings of the fatigue testing procedure, with regards to the rather theoretical considerations of the value of the fatigue strength, become apparent. The fatigue testing was primarily designed to determine the fatigue strength of the material with surface quality and in corrosive working environment of HERAMED prostheses. The last testing series (as-delivered material, without the Ringer's solution), has shown that the environment has had a substantial influence on the value of the fatigue strength (see Chapter 3.4.1). It seems therefore that the value of the fatigue strength of this last

testing series, of 810 N/mm², should be used for the comparison with the results obtained from the pile-up theory. It is apparent, that the values calculated with pile-up theory are close to the fatigue strength determined for the as-delivered material tested without the Ringer's solution. It is pointed out that this agreement is much better than the agreement between the fatigue strength and the result of the calculation based on the findings on persistent slip bands. It is therefore concluded that the fatigue strength of Ti-5Al-2.5Fe can be explained in terms of crack formation at dislocation pile-ups.

4. INTERRELATION OF STRESS ANALYSIS AND MATERIALS STUDY RESULTS

The mathematical and experimental modelling of the HERAMED prostheses showed that stresses in these prostheses can be calculated by using a simple model which relies on simple bending and beam on elastic foundation theory (see Chapter 2). This model is as accurate as the finite element analysis of the prostheses and it requires little effort in terms of computing resources, such as computing time and computing storage space.

The investigation of mechanical properties of the material of the prosthesis, the Ti-5AL-2.5Fe alloy, showed that its fatigue strength at 10^7 cycles and under simulated human body conditions amounted to 560 N/mm^2 (see Chapter 3). This investigation also showed that the material reacted as a perfectly notch sensitive material in respect to mild notches. This important finding means that in order to estimate the influence of stress concentrations on the fatigue performance of the prostheses, the theoretical, geometrical stress concentration factors can be used without any alternation. Thus, in the simple model the influence of stress concentrations due to the presence of transition radii along the axes of the HERAMED prostheses is calculated by simply multiplying the values of the stresses calculated for the prostheses without the transition radii by appropriate stress concentration factors. It was found that these factors can be in the best way estimated by using stress concentration factors from the literature (see Chapter 2).

With the knowledge of the fatigue properties of the material of the prostheses, the simple model can be used in order to predict the fatigue performance of the HERAMED prostheses under the conditions specified in DIN 58840 (see Chapter 2.2.2). Results of fatigue testing of some HERAMED prostheses are shown in Table 4.1 below. These results were obtained from reports on testing of the prostheses conducted by Staatliche Orthopädische Klinik in Munich (FRG) according to the method described in Chapter 2.2.2. They are a part of a data bank which is concerned with the HERAMED prostheses. One important item of information from these results of fatigue testing is that the prostheses always fail at the tension side. This feature is also found for standard prostheses [1].

Table 4.1. Results of fatigue testing of HERAMED prostheses.

Prosthesis	Transition radius [mm]	Section at embedding	Where broken	Number of cycles at load* 3100N	4600N	6200N
F055	1.	13	step 13	3000	820	-
F063	1.	13	step 10	3000	905	-
F076	1.	12	not broken	3000	1000	1000
F089	1.	14	step 11	3000	50	-
F092	1.	13	step 13	90	-	-
F094	1.	13	not known	115	-	-
F096	1.	13	step 11	172	-	-
F097	1.	12	step 12	3000	1000	34
G035	1.2	13	step 13	3100	27	-
G046	1.	12	step 9	3000	1000	120
G072	1.	12	not known	3000	22	-
G093	1.	9	not known	110	-	-

* Number of cycles x1000

In Table 4.2, results of the calculations of maximum stresses with the simple model for the prostheses shown in Table 4.1 are presented. In this calculations, the simple model was used with the embedding. Two values of stresses are shown for each value of the load. The first are the stresses without the and the second with the stress concentration factors. It has to be mentioned that only the maximum tensile stresses are shown in Table 4.2. This is because in real fatigue tests, the prostheses fail due to tensile stresses.

Table 4.2. Maximum tensile stresses for prostheses from Table 4.1 as calculated with the simple model.

Prosthesis	Maximum stress in N/mm ² due to load of 3100N	4600N	6200N	Step number
F055	303/539	451/800	-	13
F063	296/537	439/797	-	11
F076	257/429	382/621	515/837	12
F089	382/702	567/1042	-	12
F092	713/1258	-	-	13
F094	307/569	-	-	12
F096	429/746	-	-	11
F097	295/390	437/580	589/781	12
G035	453/691	672/1025	-	13
G046	266/524	396/778	533/1048	11
G072	502/784	745/1164	-	12
G093	397/710	-	-	9

The results in Table 4.1 show an interesting feature. The prostheses F063, F089, F096 and G046 failed below the embedding level. This means that it is very likely that in the case of these prostheses, the maximum stresses occurred in the embedding and not at the embedding level. The last column in Table 4.2 shows the section number at which the maximum stresses were predicted by the simple model. (The embedding levels were equal to that shown in Table 4.1). It can be seen that the simple model predicts correctly that the maximum stresses will occur in the embedding. However, the number of the section at which the maximum stresses are to be found is not exactly calculated. In the case of the prosthesis F063, for example, the model predicted the maximum stresses to occur at the section 11. The prosthesis F063, however, broke at the section 10.

This indicates that in real world, the embedding is 'softer' than that used in the model. Thus, the elasticity modulus of the embedding should be lower than that of PMMA of 3500 N/mm². By taking a two times lower value of this modulus of elasticity, the simple model predicts the number of the section with highest stresses in accordance with the experimental data.

By comparing Tables 4.1 and 4.2, the validity of the simple model can be checked. This is done by showing that the following statement is true or false:

> The simple model is correct if the prostheses survive the fatigue testing procedure for a given value of load, and, if the maximum factored stresses calculated with the simple model for these prostheses are lower than the fatigue strength of the material of 560 N/mm².

It can be seen from Table 4.2 that this statement is true. The maximum factored stress for the prostheses F055, F063, F076, F089, F097 and G046 were calculated as lower than 560 N/mm² for the value of the load equal to 3100 N. All these prostheses did not break after being fatigued with this load for $3*10^6$ cycles.

It is to be noted that the above statement defines the method in which the simple model can be used for predicting the performance of the HERAMED prostheses during the DIN-tests. Firstly, the stresses have to be calculated for any given load, and prosthesis under investigation. Secondly, if the maximum factored tensile stress is lower than 560 N/mm², then it is likely that the prosthesis will sustain the testing.

Two problems can be recognized in this method. Firstly, it was shown in the discussion of the photoelastic experiments that the error connected to the positioning of the prostheses during the DIN-test, can lead to an error in estimating the stresses in the range of ±20 percent (see Chapter 2.5.1). Thus, in order to accommodate this error, it is advisable to use a 20 percent lower value of the fatigue strength of the material, i.e, 450 N/mm², in the prediction of the performance of the prostheses.

This limit could be increased after more experience has been gained by using the simple model. In particular, the results from the simple model have to be compared with larger amount of data from fatigue testing of the prostheses than it was possible during the course of this work. Secondly, it can be seen from Tables 4.1 and 4.2 that some of the prostheses survived the testing procedure despite of the fact that the stresses calculated with the simple model were higher than 560 N/mm². The first reason for this is that the simple model calculates the stresses in the 'worst-case' scenario. In particular, the values of the stress concentration factors are overestimated (see Chapters 2.3.3 and 2.6.4). The second reason is that the prostheses are not tested for 10^7 cycles but either for $3*10^6$ or for 10^6 cycles. The fatigue strength for the last two numbers of cycles can be higher than that of 560 N/mm². From the results of the fatigue testing of the material conducted in this work, however, it can be seen that the difference between the fatigue strength at, for example, 10^6 cycles and that at 10^7 cycles is not large (see Chapters 3.4.1 and 3.5.1). If tested at the stress of 585 N/mm², some specimens broke only after $5*10^4$ cycles. From Table 4.1, it can be seen that the prosthesis F094 failed. The maximum factored stress for this prosthesis was calculated as 574 N/mm² (see Table 4.1). This is just above the value of the fatigue strength of the material at 10^7 cycles of 560 N/mm². Thus, instead of trying to find the values of fatigue strengths at $3*10^6$ and 10^6 cycles, it is easier and safer to use the fatigue strength of the material at 10^7 cycles in the prediction of the fatigue performance of the prostheses.

As the final remark, it has to be pointed out that by using of any mathematical model, the necessity of fatigue testing of the prostheses will not be eliminated. On the example of the simple model which was developed in this work, it can be seen that there could be prostheses, the maximum stresses of which are in the range of the fatigue strength of the material of these prostheses (see Table 4.2). By simple redesign measures, such as increasing of the value of the transition radius, or removing the transition radius all together, these maximum stresses can be brought under the value of the fatigue strength. In particular, if the second measure is used, the prostheses should be subjected to fatigue testing. This will provide more experimental data for comparison with the predictions made with the simple model, and, thus, it will show how reliable is this model.

5. CONCLUSION

Three mathematical models were developed in order to calculate stresses which occur in custom-made HERAMED prostheses during mechanical testing according to DIN 58840. Two of the models performed a three-dimensional stress analysis by using either the boundary element method or the finite element method. The third model was called the simple model and relied on a mixture of the simple bending theory, the beam-on-elastic-foundation theory and the finite element method. Results from the mathematical models were compared with results from three-dimensional photoelasticity by stress freezing. The use of three-dimensional scattered-light photoelasticity was also evaluated. On the basis of the theoretical and experimental results, it was found that stresses in the prostheses can satisfactorily be calculated with the simple model. The simple model was also much less expensive in terms of computer resources than both the boundary and finite element methods.

The high-cycle fatigue strength of the material of the prostheses: Ti-5Al5-2.5Fe, was investigated in three point bending tests in conditions, which approximated that of the human body. The material was perfectly notch sensitive in respect to mild notches. The fatigue strength can be improved by appropriate heat treatment and surface finish. Two different microstructures of the material were investigated using light microscopy, X-ray diffraction and transmission electron microscopy. They were described in detail. It was found that the formation of the athermal omega phase plays an important role during the heat treatement of the material. Dislocation structures introduced by the fatigue process into the material were also investigated. The majority of dislocations had a screw character and their Burgers vector was equal to $[11\bar{2}0]$. A simple explanation of the high-cycle fatigue strength was proposed on the basis of dislocation pile-up theory.

The application of the simple model together with the results obtained from the fatigue tests of the material enables the fatigue performance of the prostheses to be predicted. The accuracy with which such a prediction can be made, was discussed.

6. SUGGESTIONS FOR FUTURE WORK

Several areas which could be investigated in the future were identified while discussing the results of this work in Chapters 2.5 and 3.5. They are summarized below:

1. Experience has to be gained with the simple model. This should be done by comparing the results from the simple model with those from mechanical testing of the prostheses.

2. Stress concentration factors for stepped bars with irregular geometries of their cross sections need further investigation. Results can be obtained from complex FE-calculations and from 3D photoelasticity by stress freezing.

3. With the finite element method, the influence of non-linear embedding/prosthesis interface conditions, and of non-linear material behaviour of the embedding on the stresses in the prostheses can be estimated. The latter case has not yet been investigated in the literature.

4. The fatigue strength of Ti-5Al-2.5Fe can be improved by an appropriate heat treatment and surface finish. The optimum parameters for such treatments can be found. If a new material, or material with changed condition were to be used for the prostheses, new fatigue data for such a material would have to be provided by subjecting it to mechanical fatigue testing.

5. Little is known about dislocation structures in a fatigued titanium and its alloys. It seems, that they are different from that found in fcc and bcc metals. An investigation aimed directly at describing such dislocation structures would therefore contribute to our understanding of basic processes in fatigue of metals.

REFERENCES

1. Schlußbericht über vergleichende Tests an Hüftgelenkprothesen verschiedener Hersteller unter simulierenden Einsatzbedingungen, TÜV Rheinland, Köln, FRG, 1987
2. Morscher E., Zukunft der Hüftendoprothetik mit oder ohne Knochenzement?, Swiss Medicine, Volume 9, Nr. 6, 1987, pp. 27
3. Aldinger G., Kritische Analyse zementfreier Implantsysteme, Zementfreie Implantation von Hüftgelenksendoprothesen - Standortbestimmung und Tendenzen, Hauptthema I der 36. Jahrestagung der Vereinigung Nordwestdeutscher Orthopäden 1986, Herausgegeben von Refior H. J., Georg Thieme Verlag, Stuttgatrt · New York, 1987, pp. 181
4. Fifield R., New lives for painful hips, New Scientist, 10 December 1987, pp. 35
5. Patterson M., Ring Uncemented Hip Replacements. The Results of Revision, The Journal of Bone and Joint Surgery, Vol. 69-B, No. 3, May 1987, pp. 374
6. Pacheco V., Shelley P. & Wroblewski B. M., Mechanical Loosening of the Stem in Charnley Arthroplasties. Identification of "at Risk" Factors, The Journal of Bone and Joint Surgery, Vol. 70-B, No. 4, August 1988, pp. 596
7. Plitz W., Bergmann M., Quality Assurance of Custom-made Endoprostheses, First International Symposium on Custom-made Prostheses, Düsseldorf, F.R.G, October 1988
8. Weipert A., Aldinger G., Quality Assurance for Custom Made Endoprostheses, First International Symposium on Custom-made Prostheses, Düsseldorf, F.R.G., October 1988
9. Ranu H. S., Product Liability and Clinical Responsibility in Relation to the Use of Medical Devices and Orthopaedic Implants in the United States, C348/052, pp. 39
10. Crosbie G. A., Regulatory Control of Orthopaedic Implants in the UK: Department of Health Manufacturers Registration Scheme, Proceedings of the Institution of Mechanical Engineers, International Conference, The Changing Role of Engineering in Orthopaedics, IMechE 1989-5, London, C384/022, pp. 155
11. Walker P. S., Schneeweis D., Murphy S. & Nelson P., Strains and Micromotions of Press-fit Femoral Stem Prostheses, Journal Biomechanics, Volume 20, No. 7, 1987, pp. 693

12. Aldinger G., Küsswetter W., Sell St., Clinical Experience and Results of Custom Made Cementless Hip Stem, First International Symposium on Custom-Made Prostheses, Düsseldorf, F.R.G., October 1988
13. Selmitsch M., Panic B., Ten years experience with test criteria for fracture-proof anchorage stems of artificial hip joints, Engineering in Medicine, MEP Ltd., Volume 12, No. 4, 1983, pp. 185
14. DIN 58 840, Hüftgelenkprothesesn. Dauerschwingprüfung von metallischen Prothesenshäften, DK 616.728.2-77-034:620.178. 37, Beuth Verlag GmbH, Berlin, Januar 1986
15. BSI DD 91:1986, Daft for Development, Method for determination of endurance properties of stemmed femoral components of hip joint prostheses, British Standards Institution, London, 1986
16. Pauwels F., Biomechanics of the Locomotor Apparatus, Springer Verlag, Berlin Heidelberg New York, 1980, pp. 76
17. Taylor S. J. & Meswania J. M., Telemetry of strain in-vivo from proximal femoral replacement, Proceedings of the Institution of Mechanical Engineers, International Conference, The Changing Role of Engineering in Orthopaedics, IMechE 1989-5, London, C348/001, pp. 115
18. Ascenzi A., Boyde A., Portiglatti Barbos M. & Carnado S., Micro-Biomechanics vs Macro-Mechanics in Cortical Bone. A Micromechanical Investigation of Femurs Deformed by Bending, Journal of Biomechanics, Vol. 20, No. 11, 1987, pp. 1045
19. Rohlmann A., Mössner U. Bergmann G. & Kölbel R.,Finite-Element-Analysis and Experimental Investigation of Stresses in a Femur, Journal Biomedical Engineering, Vol. 4, July 1982, pp. 241
20. Huiskes R. & Chao E. Y. S., A Survey of Finite Element Analysis in Orthoppedic Biomechanics: The First Decade, Journal of Biomechanics, Vol. 16, No. 6, 1983, pp. 385
21. Carter D. R., Orr T. E. & Fyhrie D. P., Relationship between Loading History and Femoral Cancellous Bone Architecture, Journal of Biomechanics, Vol. 22, No. 3, 1989, pp. 231
22. Srinivasa L., Jayesekaran T., Blunck C. F. J., Selvam R. P., Development of Optimized Epoxy Graphite Implant for the Total Hip Join, ISA Transactions, Vol. 23, No. 2, 1984, pp. 7
23. Huiskes R., Weinanas H., Grootenbroer H. J., Dalstra M., Fudala B. & Sloof T. J., Adaptive Bone-Remodeling Theory Applied to Prosthetic-Design Analysis, Journal of Biomechanics, Vol. 20, No. 11/12, 1987, pp. 1135

24. Huiskes R., Some Fundamental Aspects of Human Joint Replacement, Acta Orthopaedica Scandinavica, Supplementum No. 185, 1980
25. Rohlmann A., Mossner U. and Bergmann G., The use of finite element analysis in assessment of endoprosthetic fixation, IMechE, C205/84, 1984, pp. 37
26. Bonfield W., Materials for the replacement of osteoarthritic hip joints, Metals and Materials, 3, 1987, pp. 712
27. Huiskes R., Janssen J. D. & Slooff T. J., Finite Element Analysis for Artificial Joint Fixation Problems in Orthopaedics, Finite Elements in Biomechanics, Edited by R. H. Gallagher, B. R. Simon, P. C. Johnson and J. F. Gross, John Wiley & Sons, Ltd, 1982, pp. 313
28. Fagan M. J. and Lee A. J. C., Role of the Collar on the Femoral Stem of Cemented Total Hip Replacements, Journal of Biomedical Engineering, Vol. 8, October 1986, pp. 295
29. Tarr R. R., Clarke I. C., Gruen T. A. and Sarimento A., Predictions of Cement-bone Failure Criteria: Three-dimensional Finite Element Models Versus Clinical Reality of Total Hip Replacement, Finite Elements in Biomechanics, Edited by R. H. Gallagher, B. R. Simon, P. C. Johnson and J. F. Gross, John Wiley & Sons, Ltd, 1982, pp. 345
30. Sih G. C., Matic P. & Berman A. T., Failure Prediction of Total Hip Prosthesis System, Journal of Biomechanics, Vol. 14, No. 12, 1981, pp. 833
31. Miles A. W., Crosby I. P., Rayment S. P. and Bannister G. C., The increasing role of instrumentation design and surgical technique in orthopaedic surgery, Proceedings of the Institution of Mechanical Engineers, International Conference, The Changing Role of Engineering in Orthopaedics, IMechE 1989-5, London, C348/018, pp. 103
32. Cheal E. J., Snyder B. D., Nunamaker D. M. and Hayes W. C., Trabecular Bone Remodeling Around Smooth and Porous Implants in Patellar Model, Journal of Biomechanics, Vol. 20, No. 11/12, 1987, pp. 1121
33. Brown T. D., Pedersen D. R., Radin E. L. and Rose R. M., Global Mechanical Consequences of Reduced Cement/Bone Coupling Rigidity in Proximal Femoral Arthroplasty: A Three-dimensional Finite Element Analysis, Journal of Biomechanics, Vol. 21, No. 2, 1988, pp. 115
34. Rohlmann A., Cheal E. J., Hayes W. C. and Bergmann G., A Nonlinear Finite Element Analysis of Interface Conditions in Porous Coated Hip Endoprostheses, Journal of Biomechanics, Vol. 21, No. 7, 1988, pp. 605

35. Brebbia C. A., Telles J. C. F. and Wrobel L. C., Boundary Element Techniques. Theory and Applications in Engineering., Springer-Verlag, Berlin, 1984

36. Zienkiewicz O.C., Methode der finiten Elemente, 2. Auflage, Carl Hanser Verlag München Wien, 1984, (Translation fom english, The Finite Element Method, McGraw-Hill, Maidenhead, England, 1977)

37. Bathe K.-J., Wilson E. L., Numerical Mehods in Finite Element Analysis, Prentice-Hall, Inc., Engelwood Clifs, New Jersey, U.S.A, 1976

38. PAFEC Data Preparation User Manual Level 7.1, PAFEC Ltd., Nottingham, England

39. PAFEC Theory Manual, PAFEC Ltd., Nottingham, England

40. PIGS User Manual Level 4.1, PAFEC Ltd., Nottingham, England

41. Hartmann F., Introduction to Boundary Elements. Theory and Applications, Springer-Verlag, Berlin Heidelberg, 1989

42. Cruse T. A., Application of the Boundary-Integral Equation Method to Three Dimensional Stress Analysis, Computer and Structures, Volume 3, Pergamon Press, Great Britain, 1973, pp. 509

43. Tan C. L. and Fenner R. T., Three-dimensional stress analysis by the boundary integral equation method, Journal of Strain Analysis, Vol. 13, No. 3, IMechE, October 1978, pp. 213

44. BEASY User Guide, Version 3.1, Computational Mechanics Publications, Southampton, U.K.

45. Shanley F. R., Strength of Materials, McGraw-Hill, Inc., New York, U.S.A., 1957

46. Fenner D. N., Engineering Stress Analysis: A Finite Element Approach with Fortran 77 Software, Ellis Horwood Ltd., Chichester, England, 1987

47. Malter H., Numerical Solutions for Beams on Elastic Foundations, Transactions ASCE, Paper No. 3042, March 1958, pp. 757

48. Huiskes R. and Schouten R. Y., The Effect of Interface Loosening on the Stress Distribution in Intramedullary Fixated Artificial Joints, Conference on Advances in Bioengineering, Chicago Nov. 1980, ASME 1980, pp. 213

49. Conte S. D. and de Boor C., Elementary Numerical Analysis. An Algorithmic Approach, McGraw-Hill Kogakusha, Ltd., Tokyo, Japan, 1972

50. Peterson, R. E., Stress Concentration Factors, John Wiley & Sons Inc., U.S.A., 1974

51. Wolf H., Spannungsoptik. Band 1. Grundlagen, 2. Auflage, Springer-Verlag, Berlin/Heidelberg, 1976
52. Kuske A and Robertson G., Photo-elastic Stress Analysis, John Wiley & Sons, Ltd., Chichester, U.K., 1977
53. Prüfbericht Nr.:01/86 HE, Staatliche Orthopädische Klinik München, Labor für Biomechanik und Experimentelle Orthopädie. Prüfstelle für Implantate, München, Februar 1986
54. Ascough J., A Review of the Scattered-light Method in Photoelasticity, International Journal on Optics and Lasers in Engineering, Edited by Butters J. N., Applied Science Publishers Ltd., Vol. 2, 1981, pp. 215
55. Jessop H. T., The Scattered Light Method of Exploration of Stresses in Two- and Three-Dimensional Models, British Journal of Applied Physics, Vol. 2, September 1951, pp. 249
56. Swinson W. F., Turner J. L. and Ranson W. F., Designing with Scattered-light Photoelasticity, Experimental Mechanics, Vol. 20, November 1980, pp. 397
57. Cheng Y. F., Some New Techniques for Scattered-light Photoelasticity, Experimental Mechanics, November 1963, pp. 275
58. Aderholdt R. W. and Swinson W. F., Establishing the Boundary Retardation with Respect to the Observed Fringes in Scattered-ligth Photoelasticity, Experimental Mechanics, November 1971, pp. 521
59. Frocht M. M. and Srinath L. S., A Non-destructive Method for Three Dimensional Photoelasticity, Proceedings Third U.S. Congress on Applied Mechanics, 1958, pp. 329
60. Bylica A., Sieniawski J.,Tytan i jego stopy, PWN, Warszawa, Poland, 1985
61. Steinemann S. G., Perren S. M., Titanium Alloys as Metallic Biomaterials, Titanium Science and Technology, Proceedings of the Fith International Conference on Titanium, Sept. 1984, Munich, FRG, Edited by G. Lütjering, U. Zwicker, W. Bunk, Deutsche Gesellschaft für Metallkunde,1985, pp. 1327
62. Welsch G., Lutjering G., Gazioglu K., Bunk W., Deformation Characteristics of Age Hardened Ti-6Al-4Al, Metallurgical Transactions A, Volume 8A, Jan. 1977, pp. 169
63. Burgers, W. G., On the Process of Transformation the Cubic Body Centered Modification into the Hexagonal Close Packed Modification of Zirconium, Physica, 1, 1934, pp. 299

64. Polmear I. J., Light Alloys, Metallury of Light Metals, Edward Arnold, 1981

65. Hammond C. & Kelly P. M., The Science, Technology and Application of Titanium, Edited by Jaffe R. I. & Promisel N. E., Pergamon Press, 1970, pp. 659

66. Duerig T. W., Albrecht J., Richter D. & Fischer P., Formation and Reversion of Stress Induced Martensite in Ti-10V-2Fe-3Al, Acta Metallurgica, Vol. 30, 1982, pp. 2161

67. Murakami Y., Izumi O., Nishimura T., Phase Transformations and Heat Treatment in Ti Alloys, Titanium Science and Technology, Proceedings International Conference on Titanium, Edited by Lütjering G., Zwicker U., Bunk W, Deutsche Gesellschaft für Metallkunde, Vol. 3, 1985, pp. 1403

68. Oka M., Lee C. S., Shimizu K., Transmission Electron Microscopy Study of Face-Centred Orthorombic Martensite in Ti-12.6 Pct. V Alloy, Metallurgical Transactions, Vol. 3, Jan. 1972, pp. 37

69. Williams J. C., de Fontaine D., Paton N. E., The Omega Phase as an Example of an Unusual Shear Transformation, Metallurgical Transactions, Vol. 4, December 1973, pp. 2701

70. Duerig T. W., Terlinde G. T., & Williams J. C, The Omega Phase Reaction in Titanium Alloys, Proceedings of the 4th Conference on Titanium, Kyoto, Japan, 1980, pp. 1299

71. De Fontaine D., Paton N. E., & Williams J. C., The Omega Phase Transformation in Titanium Alloys as an Example of Displacement Controlled Reactions, Acta Metallurgica, Vol. 19, November 1971, pp. 1153

72. Sass S. L., The Omega Phase in a Zr-25 AT.% Ti Alloy, Acta Metallurgica, Vol. 17, July 1969, pp. 813

73. Lütjering G., Gysler A., Fatigue. Crytical Review, Titanium Science and Technology, Proceedings of the Fith International Conference on Titanium, Sept. 1984, Munich, FRG, Edited by G. Lütjering, U. Zwicker, W. Bunk, Deutsche Gesellschaft für Metallkunde, 1985, pp. 1327

74. Peters M., Gysler A., & Lütjering G., Influence of the Microstructure on the Fatigue Behaviour of Ti-6Al-4V, Titanium 80, Science and Technology, Proceedings of the 4th Conference on Titanium, Kyoto, Japan, AIME, 1980, pp. 1777

75. Gilmore C. M., & Iman M. A., Fatigue Failure in Annealed Ti-6Al-4V Microstructures, Titanium Science and Technology, Proceedings of the 3rd Conference on Titanium, Moscow, USSR, May 1976, English edition edited by Williams J. C., & Belov A. F., 1982, pp 637

76. Bowen A. W. & Stubbington C. A., The Effect of Heat Treatment on the Fatigue Strength of Ti-6Al-4V, Titanium Science and Technology, Proceedings of the 3rd Conference on Titanium, Moscow, USSR, May 1976, English edition edited by Williams J. C., & Belov A. F., 1982, pp. 1989

77. Rüdiger K., Fischer D., Relationship Between Primary Alpha Content, Tensile Properties and High Cycle Fatigue Behaviour of Ti-6Al-4V, Titanium Science and Technology, Proceedings of the Fith International Conference on Titanium, Sept. 1984, Munich, FRG, DGM, 1985, pp. 2123

78. Wagner L., Gerdes C., & LÜtjering G., Influence of the Surface Treatment on the Fatigue Strength of Ti-6Al-4V, Titanium Science and Technology, Proceedings of the Fith International Conference on Titanium, Sept. 1984, Munich, FRG, Edited by G. Lütjering, U. Zwicker, W. Bunk, Deutsche Gesellschaft für Metallkunde, 1985, pp. 2147

79. Hertzberg R. W., Deformation and Fracture Mechanics of Engineering Materials, 3rd edition, John Wiley & Sons, New York, 1989

80. Zwicker U., Bühler K. & Müller R., Mechanical Properties and Tissue Reactions of a Titanium Alloy for Implant Material, Titanium 80, Science and Technology, Proceedings of the 4th Conference on Titanium, Kyoto, Japan, AIME, 1980, pp. 505

81. Lupton D., Schusser U., Kramer K.-H., Ti5Al2.5Fe as a Material for Endoprosthetics, Proposal for ISO Specification 5832, W. C. Heraeus GmbH, Hanau, FRG, 1987

82. Steinemann S. G., Perren S. M., Titanium Alloys as Metallic Biomaterials, Titanium Science and Technology, Proceedings of the Fith International Conference on Titanium, Sept. 1984, Munich, FRG, Edited by G. Lütjering, U. Zwicker, W. Bunk, Deutsche Gesellschaft für Metallkunde, 1985, pp. 1327

83. TÜmler H. P., Thull R., Surface Properties of Titanium and its Alloys-Mechanical and Electrochemical Investigation, Titanium Science and Technology, Proceedings of the Fith International Conference on Titanium, Sept. 1984, Munich, FRG, Edited by G. Lütjering, U. Zwicker, W. Bunk, Deutsche Gesellschaft für Metallkunde, 1985, pp. 1335

84. Zwicker U., Etzold U. & Moser Th., Abrasive Properties of Oxide Layers on TiAl5Fe2.5 in Contact with High Density Polyethylene, Titanium Science and Technology, Proceedings of the Fith International Conference on Titanium, Sept. 1984, Munich, FRG, Edited by G. Lütjering, U. Zwicker, W. Bunk, Deutsche Gesellschaft für Metallkunde, 1985, pp. 1343

85. Breme J., Heimke G., Corrosion Fatigue Test of TiAl5Fe2.5 Hip Implant Under High Stresses, Titanium Science and Technology, Proceedings of the Fith International Conference on Titanium, Sept. 1984, Munich, FRG, Edited by G. Lütjering, U. Zwicker, W. Bunk, Deutsche Gesellschaft für Metallkunde, 1985, pp. 1351

86. Thull R., Pesch H. J., Longterm Behaviour of Titanium and Titanium Allos as Medical Implant Material, Titanium Science and Technology, Proceedings of the Fith International Conference on Titanium, Sept. 1984, Munich, FRG, Edited by G. Lütjering, U. Zwicker, W. Bunk, Deutsche Gesellschaft für Metallkunde, 1985, pp. 1359

87. Hohmann D., Legal H., Application of Titanim Alloys for Orthopaedic Surgery, Titanium Science and Technology, Proceedings of the Fith International Conference on Titanium, Sept. 1984, Munich, FRG, Edited by G. Lütjering, U. Zwicker, W. Bunk, Deutsche Gesellschaft für Metallkunde, 1985, pp. 1365

88. Steinemann S. G., Corrosion of Titanium and Titanium Alloys for Surgical Implants, Titanium Science and Technology, Proceedings of the Fith International Conference on Titanium, Sept. 1984, Munich, FRG, Edited by G. Lütjering, U. Zwicker, W. Bunk, Deutsche Gesellschaft für Metallkunde, 1985, pp. 1373

89. Borowy K.-H., Kramer K.-H., On the Properties of a New Titanium Alloy (TiAl5Fe2.5) as Implant Material, Titanium Science and Technology, Proceedings of the Fith International Conference on Titanium, Sept. 1984, Munich, FRG, Edited by G. Lütjering, U. Zwicker, W. Bunk, Deutsche Gesellschaft für Metallkunde, 1985, pp. 1381

90. Merget M., Aldinger F., Influence of Technological Parameters on the Fatigue Strength of Ti5Al2.5Fe - A New Material for Endoprostheses, Titanium Science and Technology, Proceedings of the Fith International Conference on Titanium, Sept. 1984, Munich, FRG, Edited by G. Lütjering, U. Zwicker, W. Bunk, Deutsche Gesellschaft für Metallkunde, 1985, pp. 1393

91. Zitter H., Korrosionsverhalten und Biokompatibilität von Titanlegierungen für Implantate, Werkstoffe und Korrosion, 39, 1988, pp. 574

92. Breme J., Schade W., Phase Transformation in TiAl5Fe2.5 Alloy, Titanium Science and Technology, Proceedings of the Fith International Conference on Titanium, Sept. 1984, Munich, FRG, Edited by G. Lütjering, U. Zwicker, W. Bunk, Deutsche Gesellschaft für Metallkunde, 1985, pp. 1487

93. Adachi S., Wagner L. & Lütjering G., Influence of Microstructure and Mean Stress on Fatigue Strength of Ti-6Al-4V, Titanium Science and Technology, Proceedings of the Fith International Conference on Titanium, Sept. 1984, Munich, FRG, Edited by G. Lütjering, U. Zwicker, W. Bunk, Deutsche Gesellschaft für Metallkunde, 1985, pp. 2139

94. Buch A., Fatigue Strength Calculation, Materials Science Surveys No. 6, Trans Tech Publications, Trans Tech SA, Aedermannsdorf, Switzerland, 1988

95. Mughrabi H., Dislocations in Fatigue, Dislocations and Properties of Real Materials, Proceedings of Conference, London, December 1984, The Institute of Metals, London 1985, pp. 244

96. Brown L. M., Dislocations and the Fatigue Strength of Metals, Dislocation Modelling of Physical Systems, Proceedings of the International Conference, Gainesville, Florida USA, June 1980, Edited by M. F. Ashby, R. Bullough, C. S. Hartley & J. P. Hirth, Pergamon Press, 1981, pp. 51

97. Rémy L., Cyclic Deformation and Crack Initiation Processes, Fatigue 84, Proceedings 2nd International Conference on Fatigue, Birmingham, September 1984, Chameleon Press Ltd, London, UK, EMAS, 1984, pp. 15

98. Lukás P., Models for ΔK_{th} and Near-Threshold Fatigue Crack Growth, Fatigue 84, Proceedings 2nd International Conference on Fatigue, Birmingham, September 1984, Chameleon Press Ltd, London, UK, EMAS, 1984, pp. 479

99. Mughrabi H., Herz K. & Stark X., Cyclic Deformation and Fatigue Behaviour of α-Iron Mono- and Polycrystals, International Journal of Fracture, Vol. 17, No. 2, April 1981, pp. 193

100. Partrige P. G. & Pell C. J., Effect of Cyclic Stress on Unalloyed Polycrystalline Titanium, The Science, Technology and Application of Titanium, Edited by Jaffe R. I. & Promisel N. E., Pergamon Press, 1970, pp. 517

101. MacDonald D. E. & Wood W. A., Fatigue Mechanisms in Titanium, Titanuim Science and Technology, Proceedings of 2nd International Conference, Cambridge, Massachusetts, May 1972, Edited by Jaffe R. I. and Burte H. M., Plenum Press, 1973, pp. 1219

102. Takemoto T., Jing K. L., Tsakalakos T., Weissmann S. & Kramer I. R., The Importance of Surface Layer on Fatigue Behaviour of a Ti-6Al-4V Alloy, Metallurgical Transactions A, Volume 14A, January 1983, pp. 127

103. Vitek V., Effect of Dislocation Core Structure on the Plastic Properties of Metallic Materials, Dislocations and Properties of Real Materials, Proceedings of Conference, London, December 1984, The Institute of Metals, London 1985, pp. 30

104. QS-Richtlinie Nr. 4801, Heraeus PSM-QS, W. C. Heraeus GmbH, Hanau, W. Germany, January, 1987

105. QS-Richtlinie Nr. 032601, Heraeus PSM-QS, W. C. Heraeus GmbH, Hanau, W. Germany, January, 1987

106. Hüftgelenkprothesen. Dauerschwingprüfung von metallischen Prothesenschäften, DIN 58 840, Deutsche Norm, DK 616.728.2-77-034 : 620.178.37, Beuth Verlag GmbH,Berlin, January 1986

107. Peterson R. E., Stress Concentration Factors, John Wiley & Sons, U.S.A., 1974

108. Standard Methods for Testing of Metalic Materials. E 8M., Annual Book of ASTM, American Society for Testing and Materials, U.S.A., Vol. 03.01, 1987, pp. 199

109. International Tables for X-Ray Crystallography, The International Union of Crystallography, Kynoch Press, Birmingham, England, 1952

110. Spurling R. A., A Techinque for Preparing Thin Foils of Ti and Ti Alloys for Transmission Electron Microscopy, Metallurgical Transactions A, Vol. 6A, 1975, pp. 1660

111. Edington J. W., Practical Electron Microscopy in Material Science. Monograph Two. Electron Diffraction in the Electron Microscope, Philips Technical Library, Macmillan Press, 1975

112. Edington J. W., Practical Electron Microscopy in Material Science. Monograph Three. Interpretation of Transmission Electron Micrographs, Philips Technical Library, Macmillan Press, 1975

113. Duwez P. & Taylor L., The structure of Intermediate Phases in Alloys of Titanium with Iron, Cobalt, and Nickel, Transactions AIME, Vol. 188, September 1950, pp. 1173

114. Banerjee D., Rhodes C. G. & Williams J. C., On the Nature of α/β Interfaces in Titanium Alloys, Titanium Science and Technology, Proceedings of the Fith International Conference on Titanium, Sept. 1984, Munich, FRG, Edited by G. Lütjering, U. Zwicker, W. Bunk, Deutsche Gesellschaft für Metallkunde, 1985, pp. 1597

115. Cass, T. R., Slip Modes and Dislocation Substructures in Titanium and Titanium-Aluminum Single Crystals, The Science, Technology and Application of Titanium, Edited by Jaffe R. I. & Promisel N. E., Pergamon Press, 1970, pp. 459

116. Hirth J. P. & Lothe J., Theory of Dislocations, Second Edition, John Wiley & Sons, USA, 1982

117. Conrad H., Doner M., and De Meester B., Deformation and Fracture. Critical Review., Proceedings of 2nd International Conference, Cambridge, Massachusetts, May 1972, Edited by Jaffe R. I. and Burte H. M., Plenum Press, 1973, pp. 969

118. Terlinde G. and Luetjering G., Influence of Grain Size and Age-Hardening on Dislocation Pile-Ups and Tensile Fracture for a Ti-Al Alloy, Metallurgical Transactions A, ASM, Volume 13A, July 1982, pp. 1283

LIST OF TABLES

LIST OF FIGURES

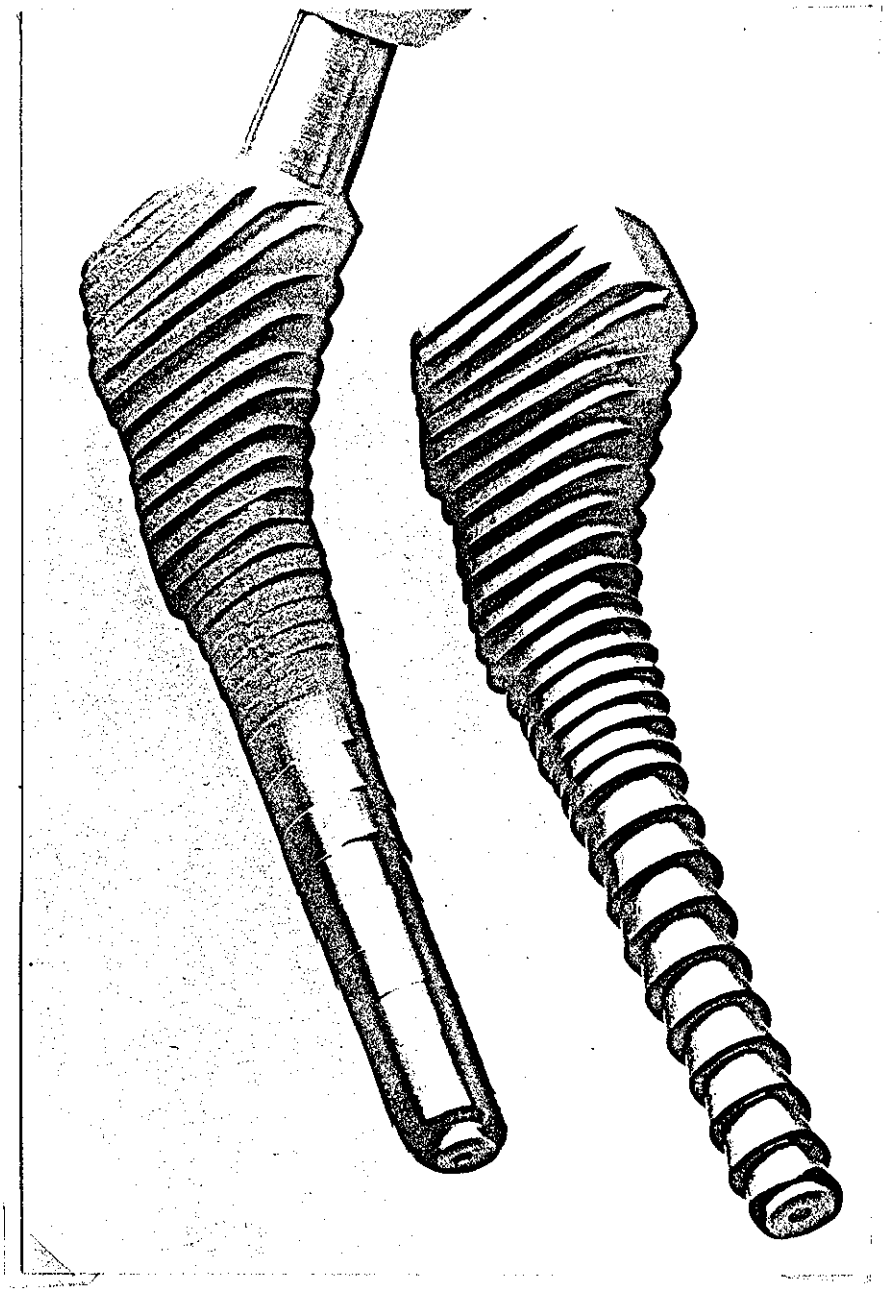

Figure 1. HERAMED-CAT prosthesis (left) with the preparation tool, the broach (right).

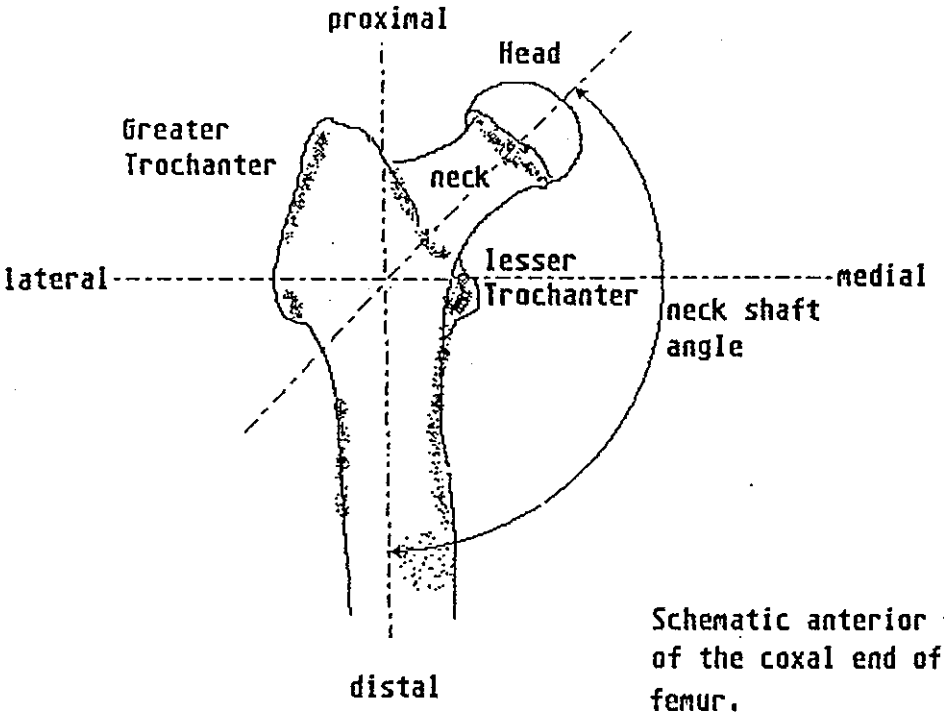

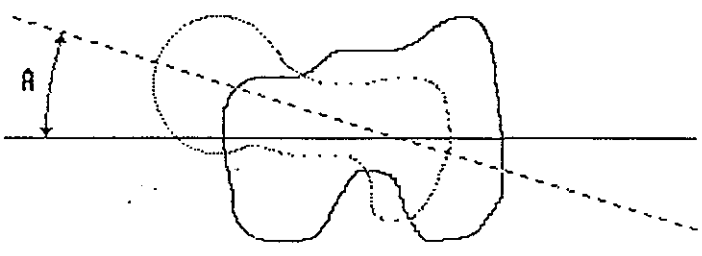

The angle of femoral torsion, A, is the angle between the axis of the head and neck, and that of the distal end of the bone.

Figure 2. Schematic drawing of a femur. Explanation of medical terms used in the text.

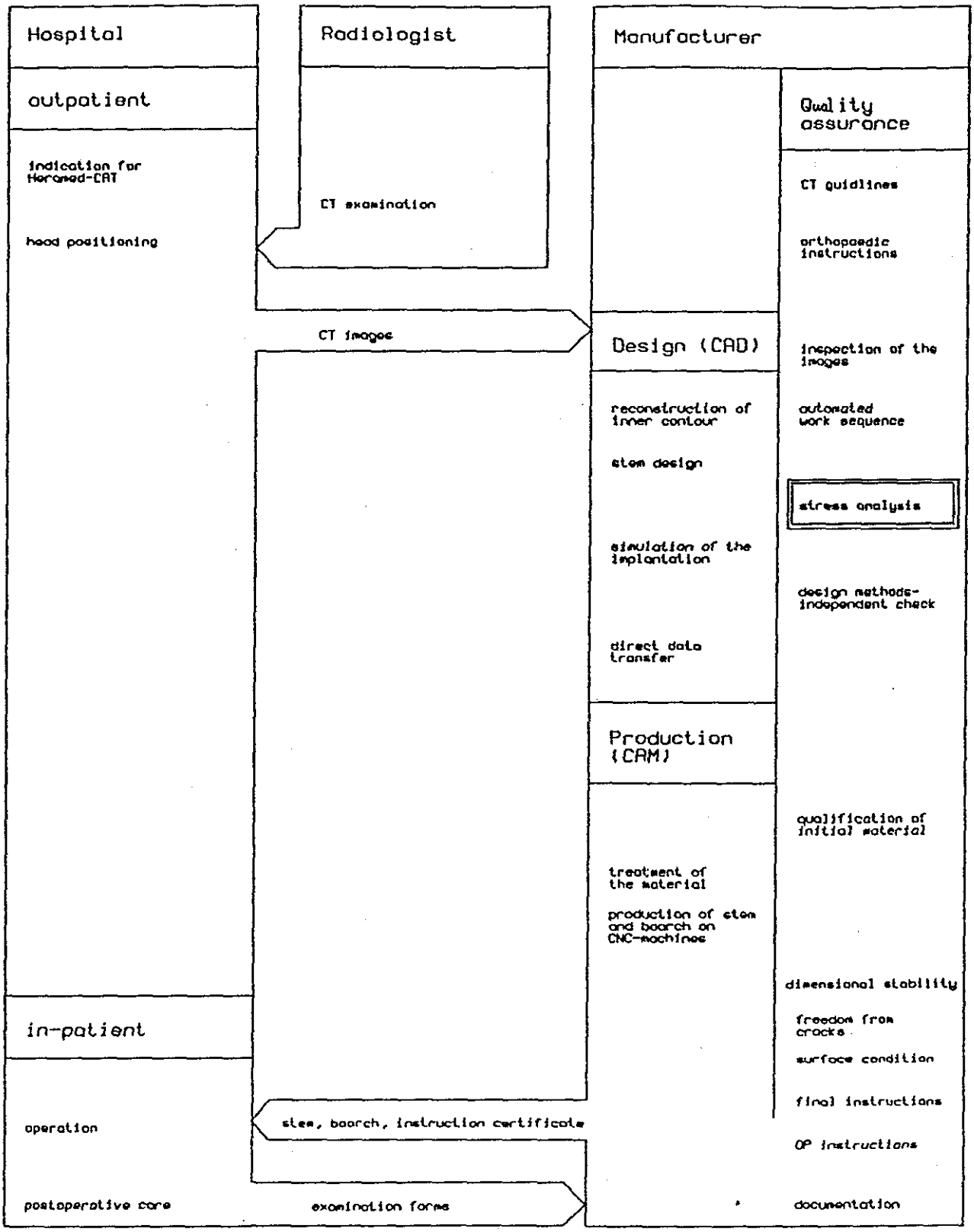

Figure 3. Schematic flow-chart of activities connected with the design and manufacture of HERAMED prostheses.

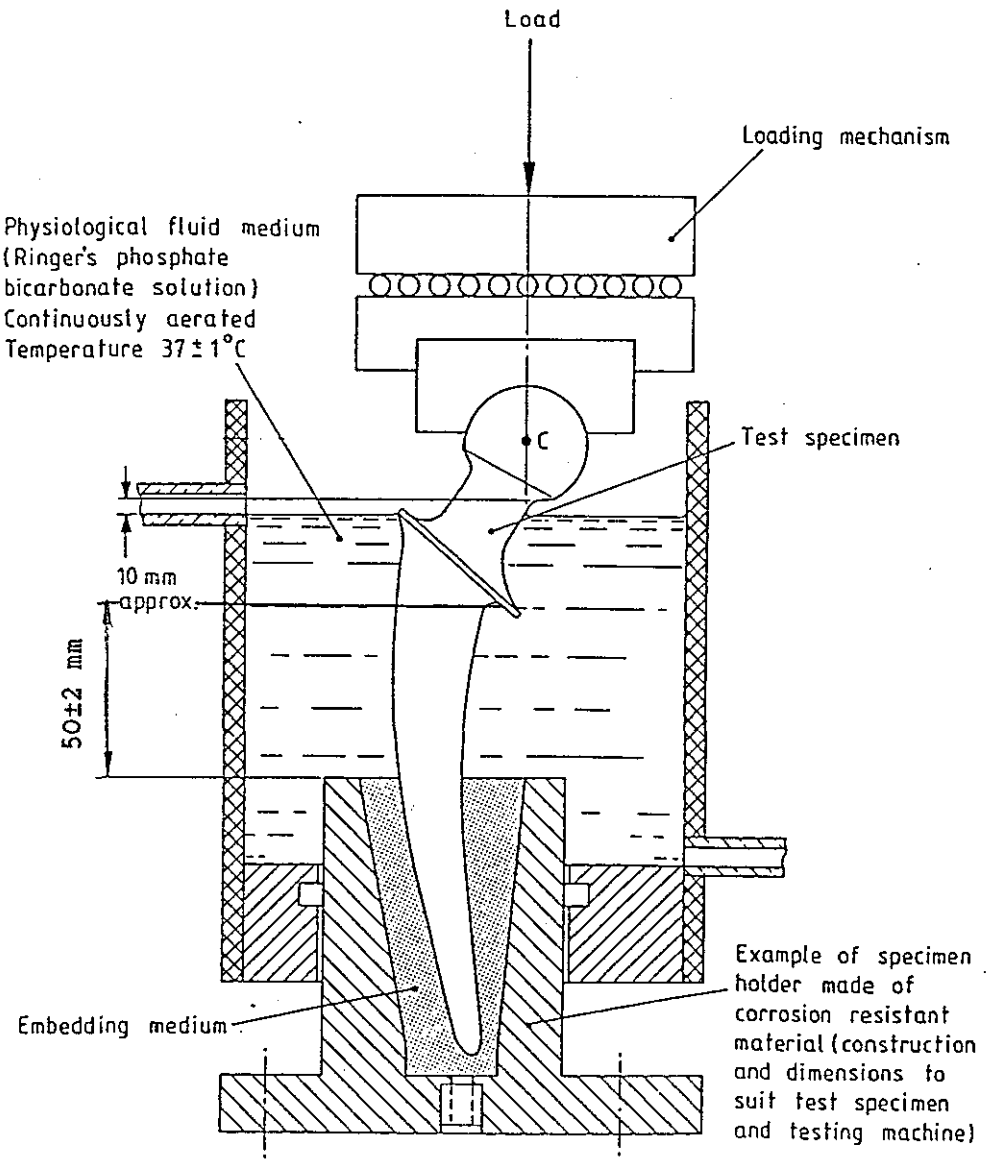

Figure 4. General arrangement of prostheses for testing.

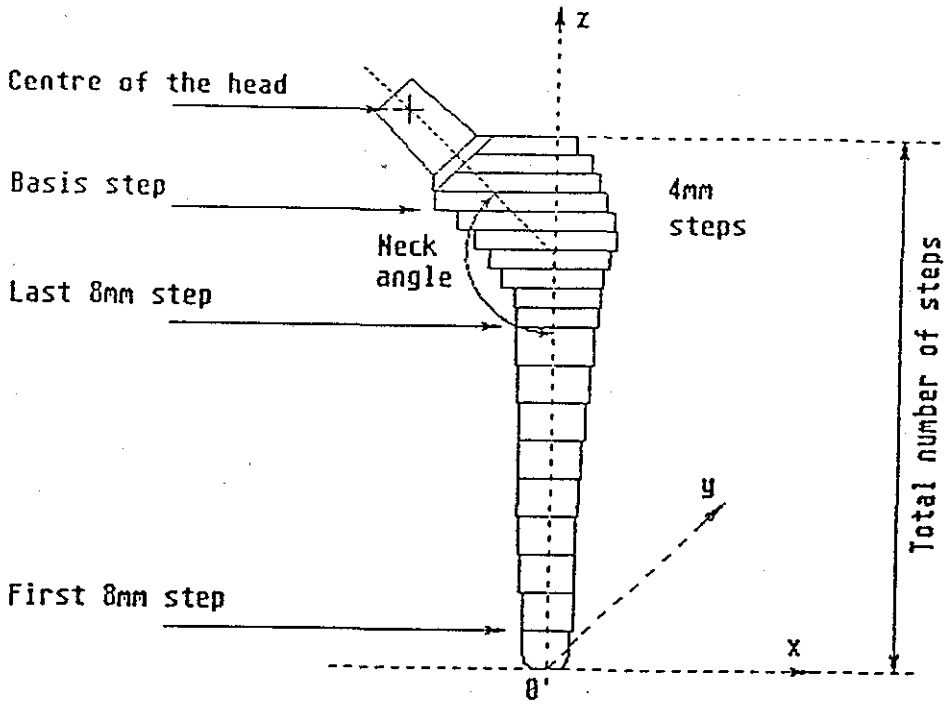

Figure 5. Schematic drawing of prosthesis. Explanation of terms used in the geometrical input file.

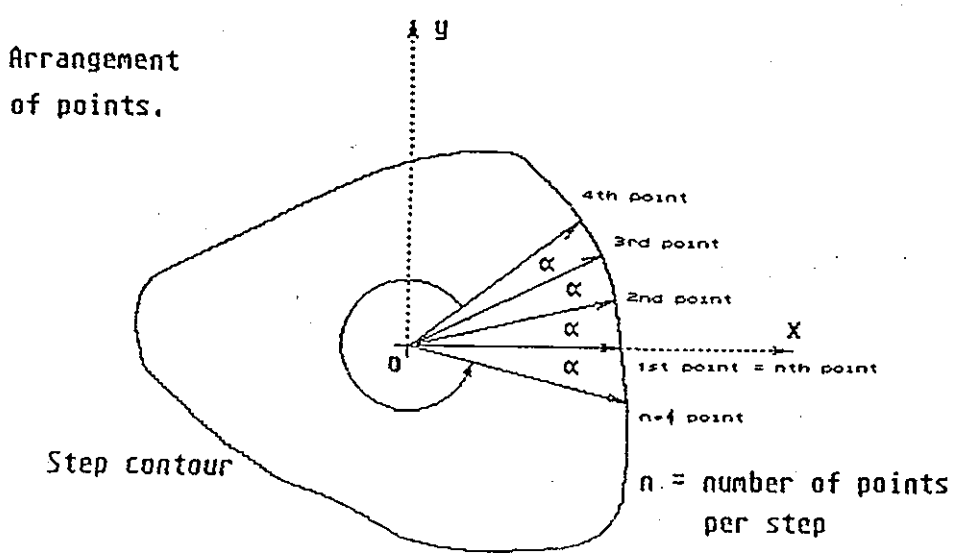

Figure 6. Way of defining points along contours of cross sections.

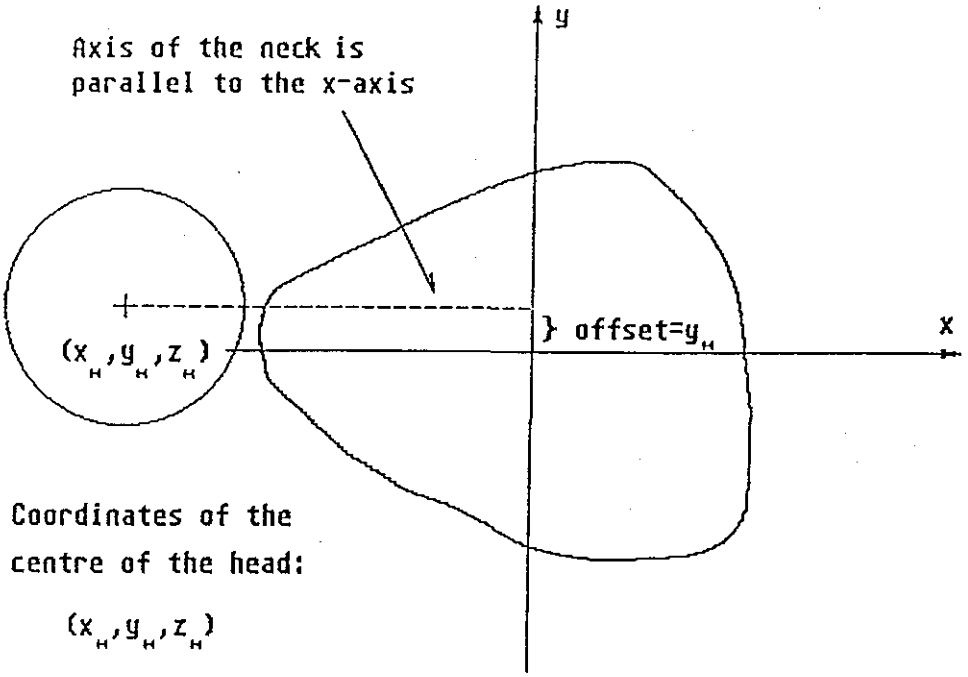

Figure 7. Definition of the offset of the neck of the prosthesis.

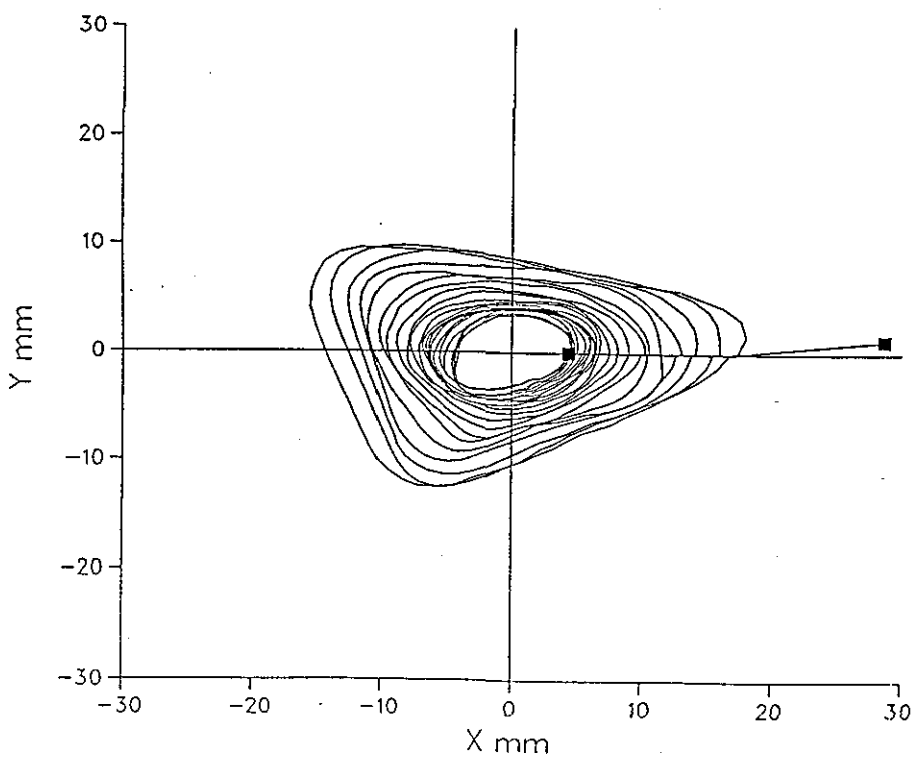

Figure 8. Shape of the contours of the prosthesis G035.

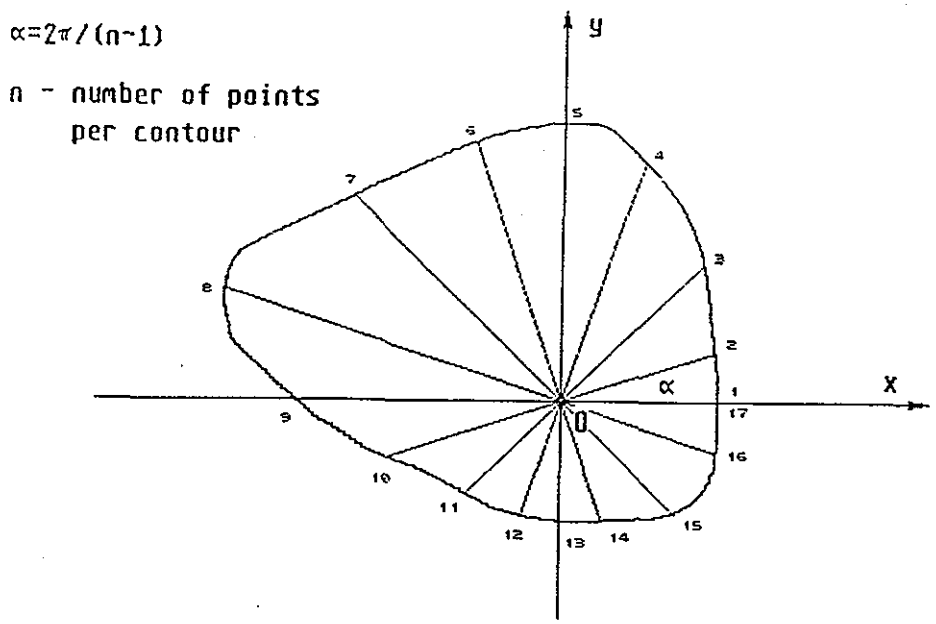

Figure 9. Schematic drawing of a contour showing the uneven distribution of points in the geometry file.

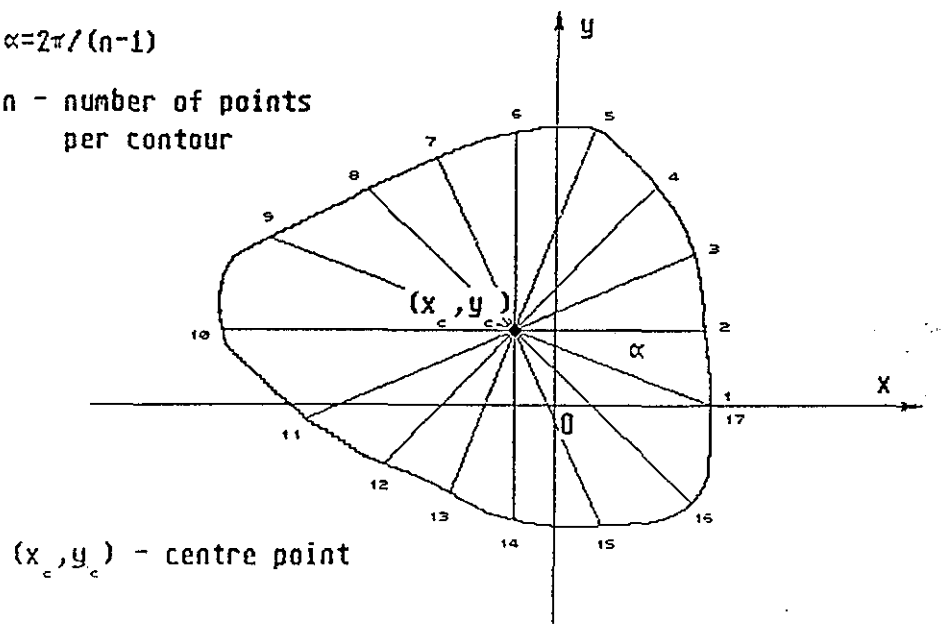

Figure 10. Change to the distribution of points caused by subroutine SECT.

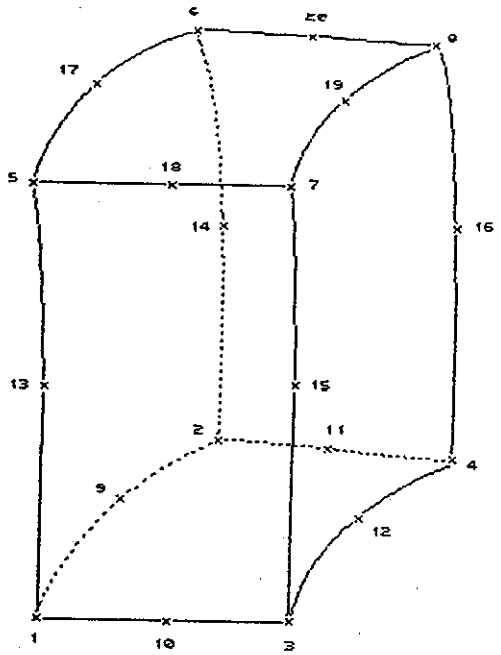

Figure 11. The twenty-noded brick element for three dimensional finite element analysis and its topology.

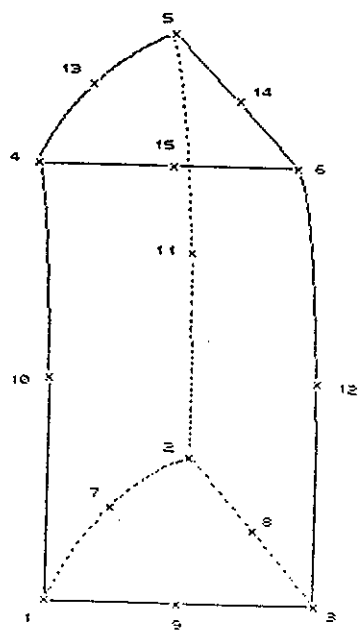

Figure 12. The fifteen-noded prism element for three dimensional finite element analysis and its topology.

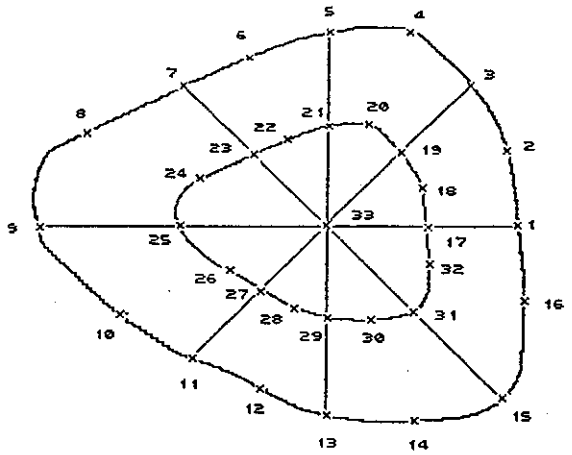

Figure 13. Schematic drawing of the definition of nodes of the stem of the prosthesis.

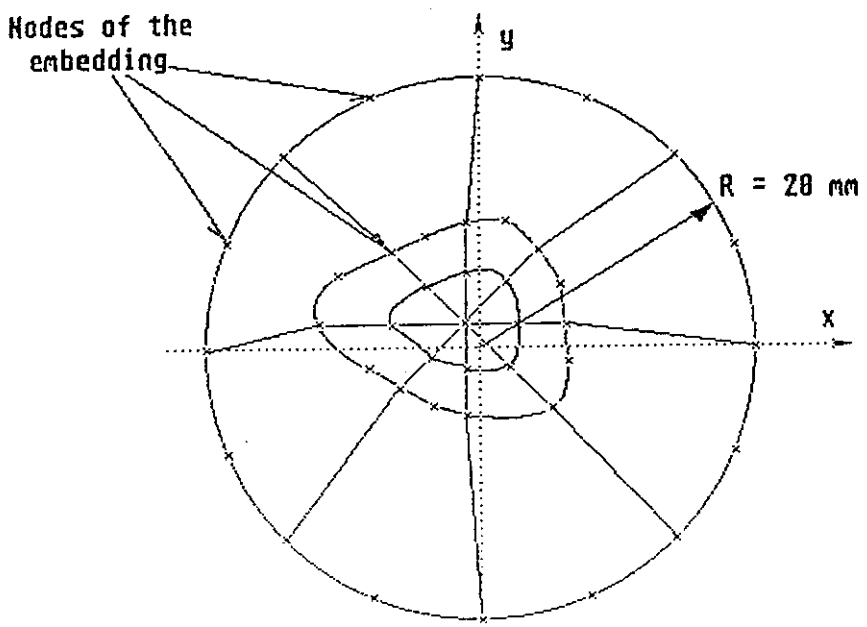

Figure 14. Schematic drawing of the definition of nodes of the embedding.

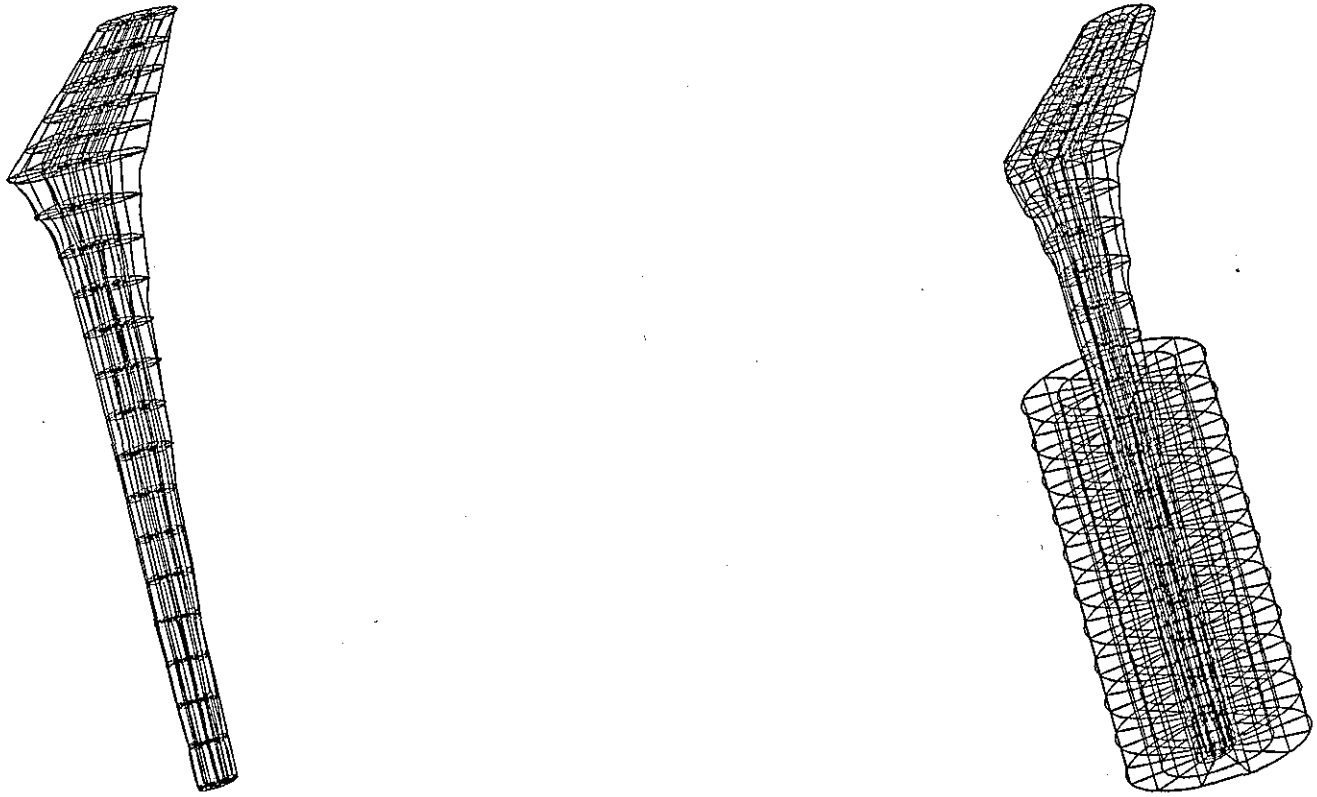

Figure 15. FEM-model of the prosthesis F076 and the prosthesis with the embedding.

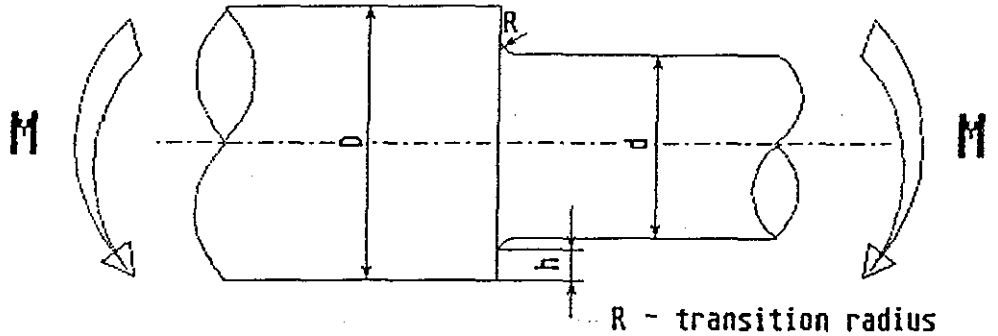

R - transition radius
h - height of the shoulder
M - bending moment
D, d - diameters

Stress concentration factor K_T

$$K_T = \frac{\sigma_{max}}{\sigma} ,$$

where

$$\sigma = \frac{32M}{\pi d^3} ,$$

σ_{max} - maximum stress in the transition radius.

Figure 16. Circular bar with a fillet. Definition of stress concentration factor.

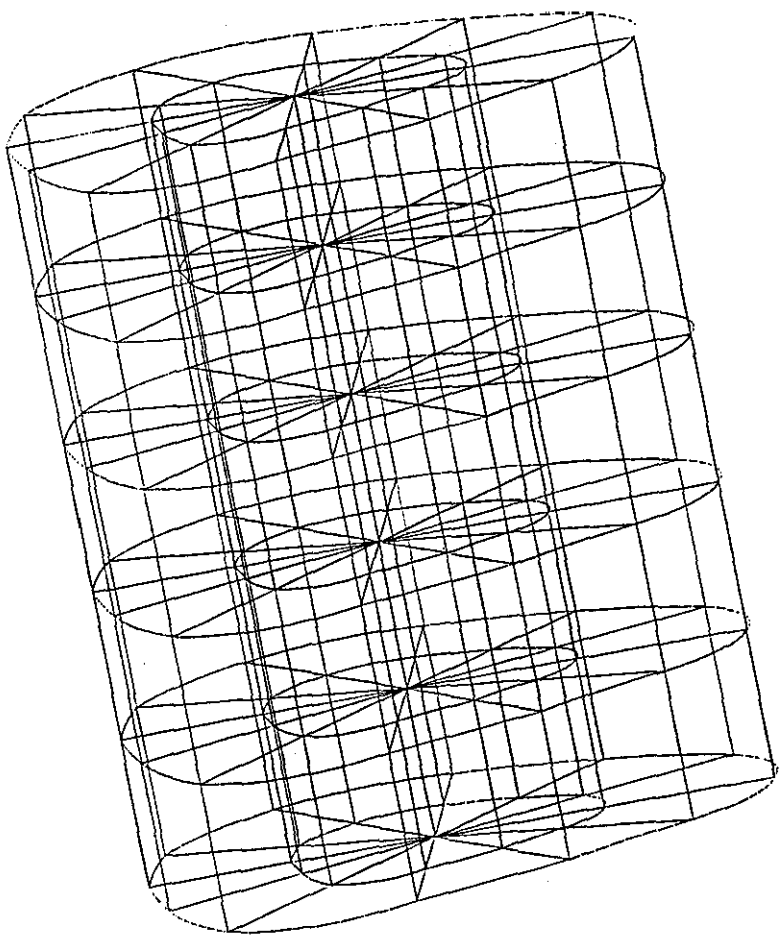

Figure 17. FEM-model of the section 12 of the prosthesis F076 with no transition radius as generated by the subroutine COSCF0.

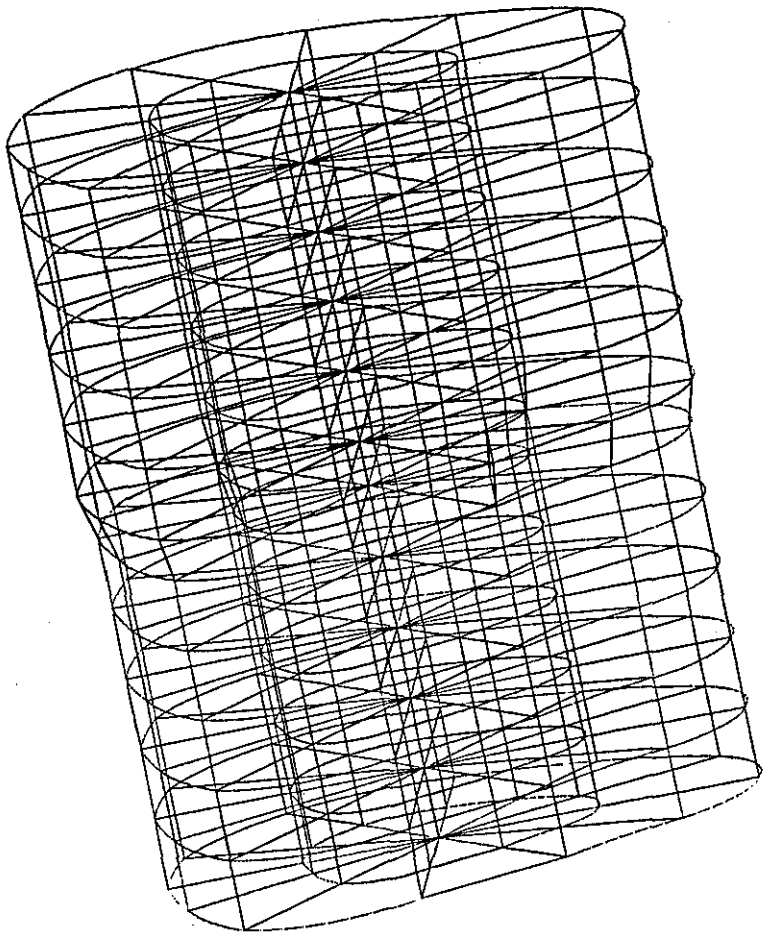

Figure 18. FEM-model of the section 12 of the prosthesis F076 with one third of the transition radius as generated by the subroutine COSCF1.

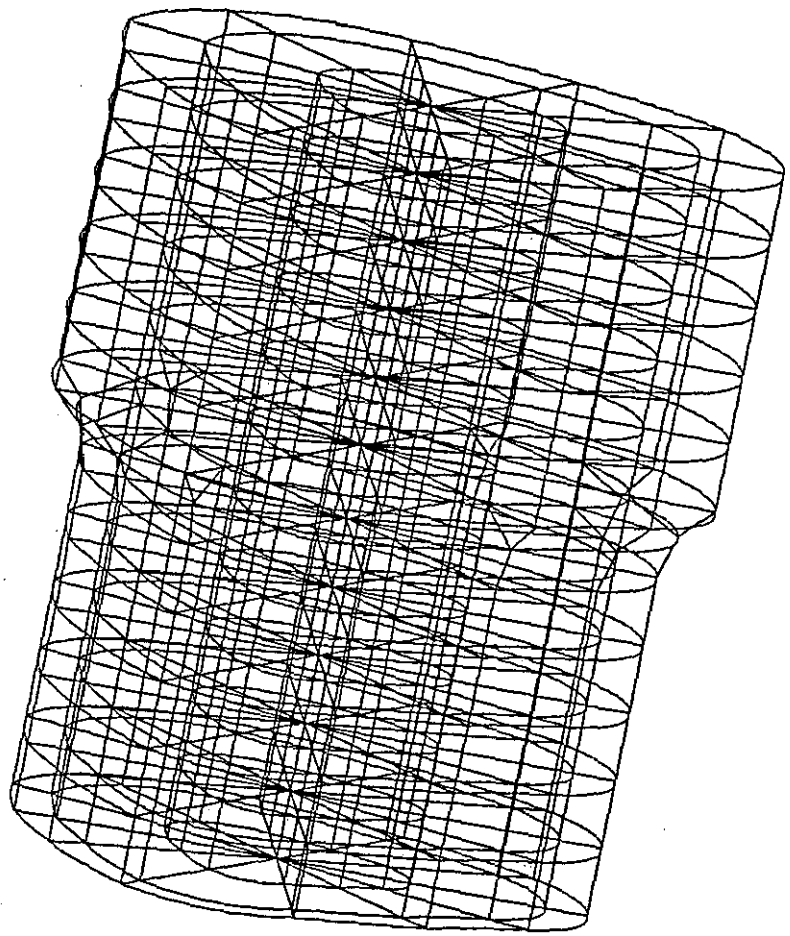

Figure 19. FEM-model of the section 12 of the prosthesis F076 with two thirds of the transition radius as generated by the subroutine COSCF2.

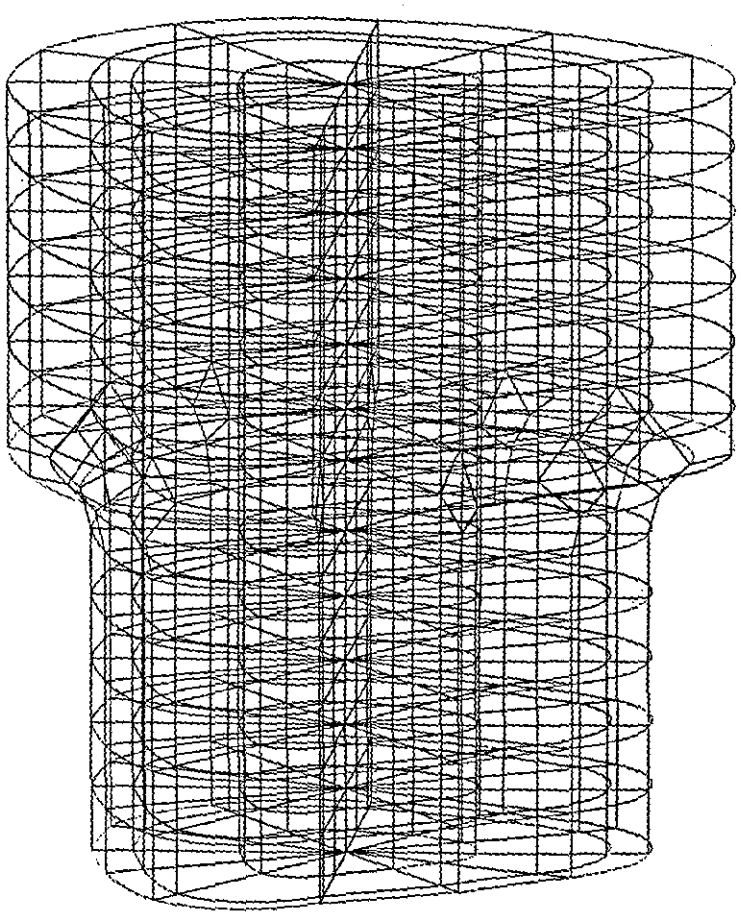

Figure 20. FEM-model of the section 12 of the prosthesis F076 with the whole transition radius as generated by the subroutine COSCF3.

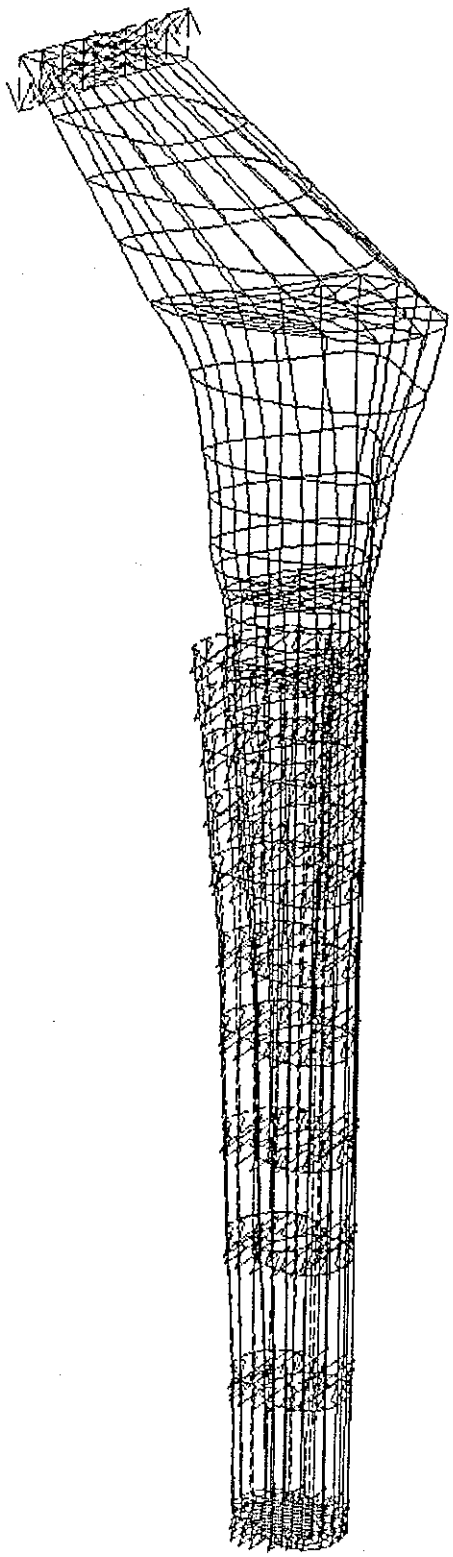

Figure 21. BEM-model of the prosthesis FØ76.

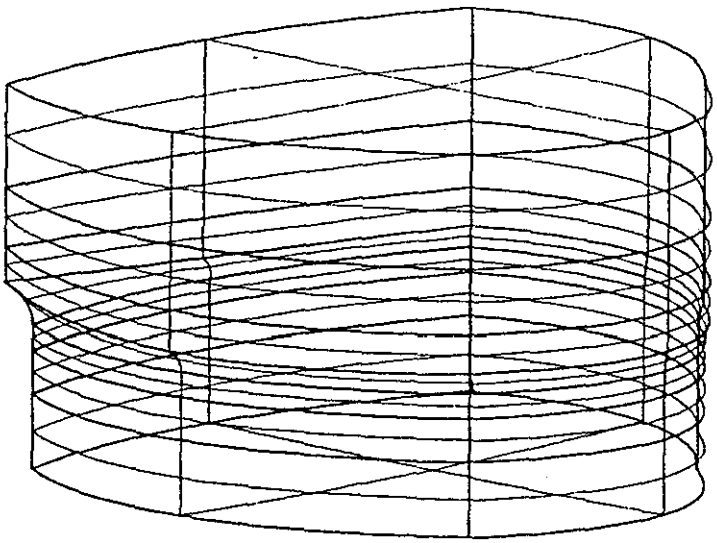

Figure 22. BEM-model of a section with the transition radius.

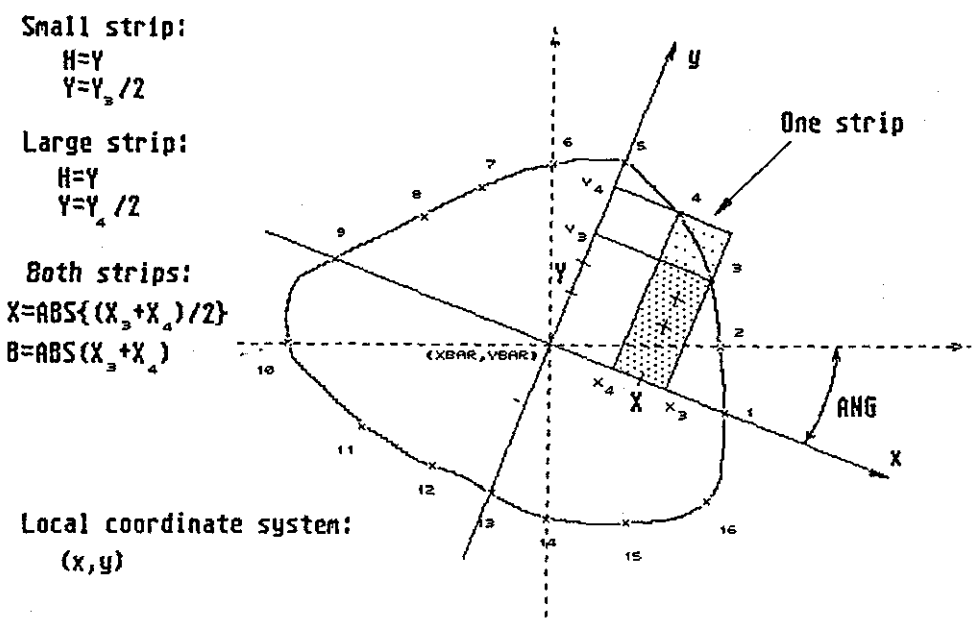

Figure 23. Division of sections into strips in order to calculate the geometrical properties these sections.

P - load
S - shear force
F - axial force
BETA - tilt angle
ZL - distance from centre of the head
Y_o - offset
T - torsion moment

S=P*SIN(BETA)
F=P*COS(BETA)
T=S*Y_o

x,y,z - global coordinate system
x_p,y_p,z_p - coordinate system of prosthesis

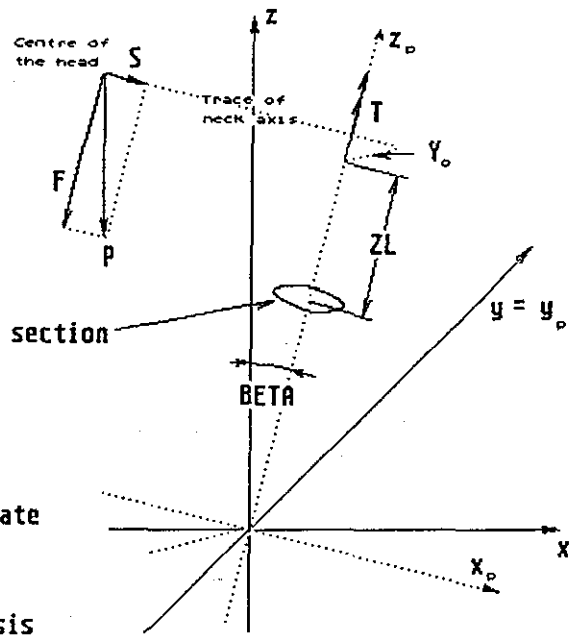

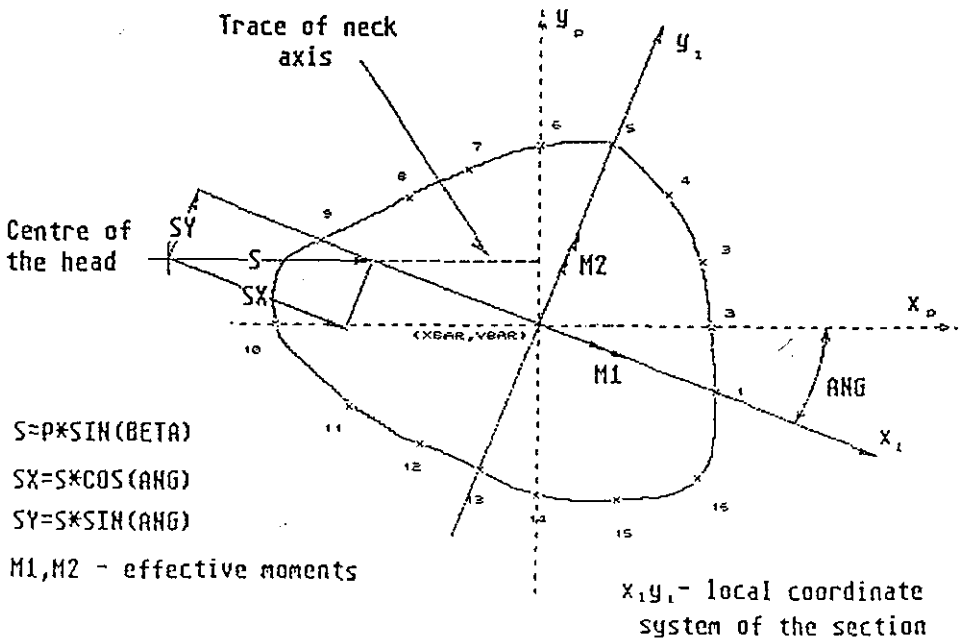

S=P*SIN(BETA)
SX=S*COS(ANG)
SY=S*SIN(ANG)
M1,M2 - effective moments

x_1y_1 - local coordinate system of the section

Figure 24. Schematic representation of forces acting on the prosthesis globally and on one of the sections.

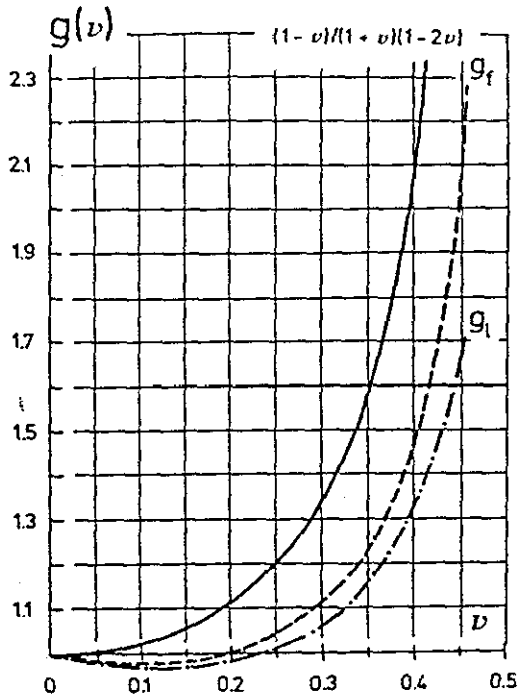

Figure 25. Functions used for calculating the stiffness of the embedding in the simple model [24].

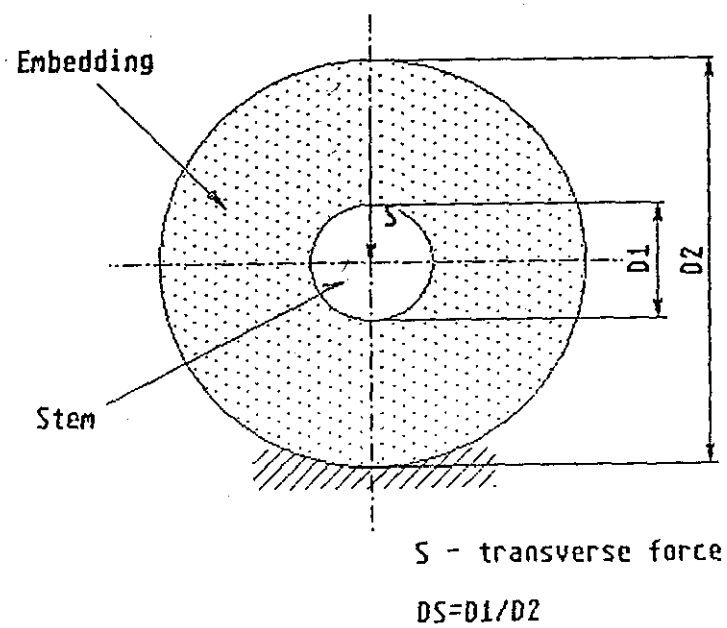

Figure 26. Circular ring subjected to a transverse loading.

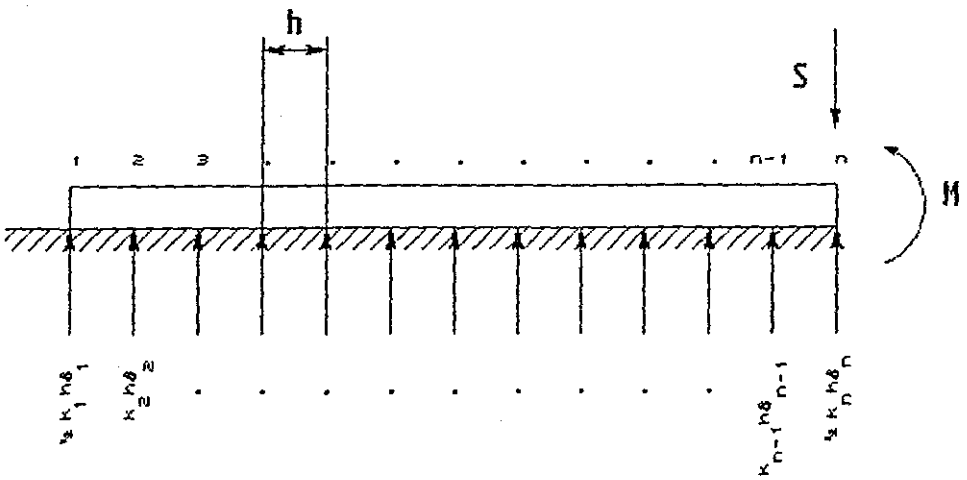

S - transverse force
M - bending moment
h - step width
δ_i - displacement in point i
i=1,.....,n
k_i - stiffness of spring i

Figure 27. Beam on elastic foundation. Approximation of the prosthesis in the embedding.

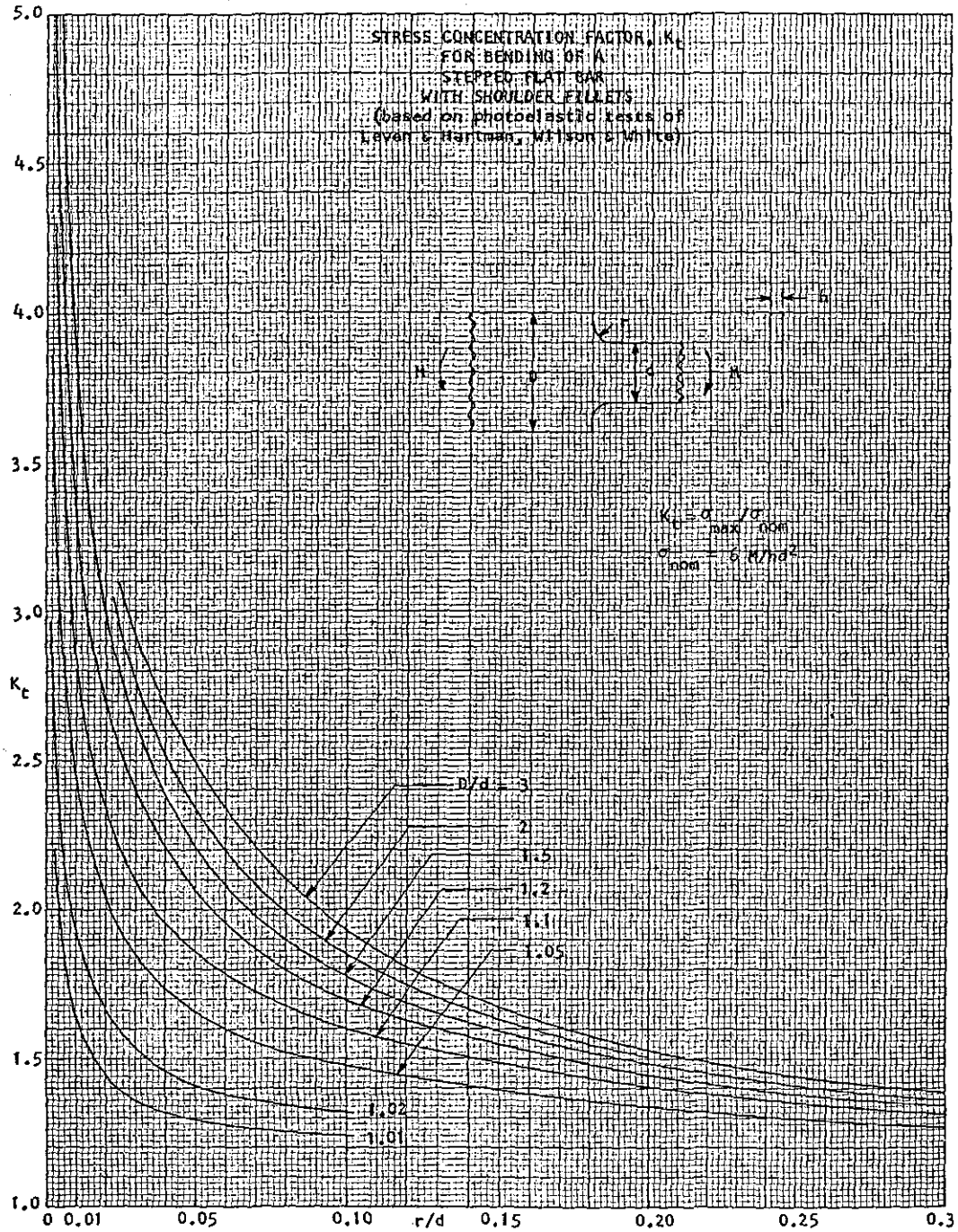

Figure 28. Stress concentration factor, K_t, for bending of a stepped flat bar with a shoulder fillet [49].

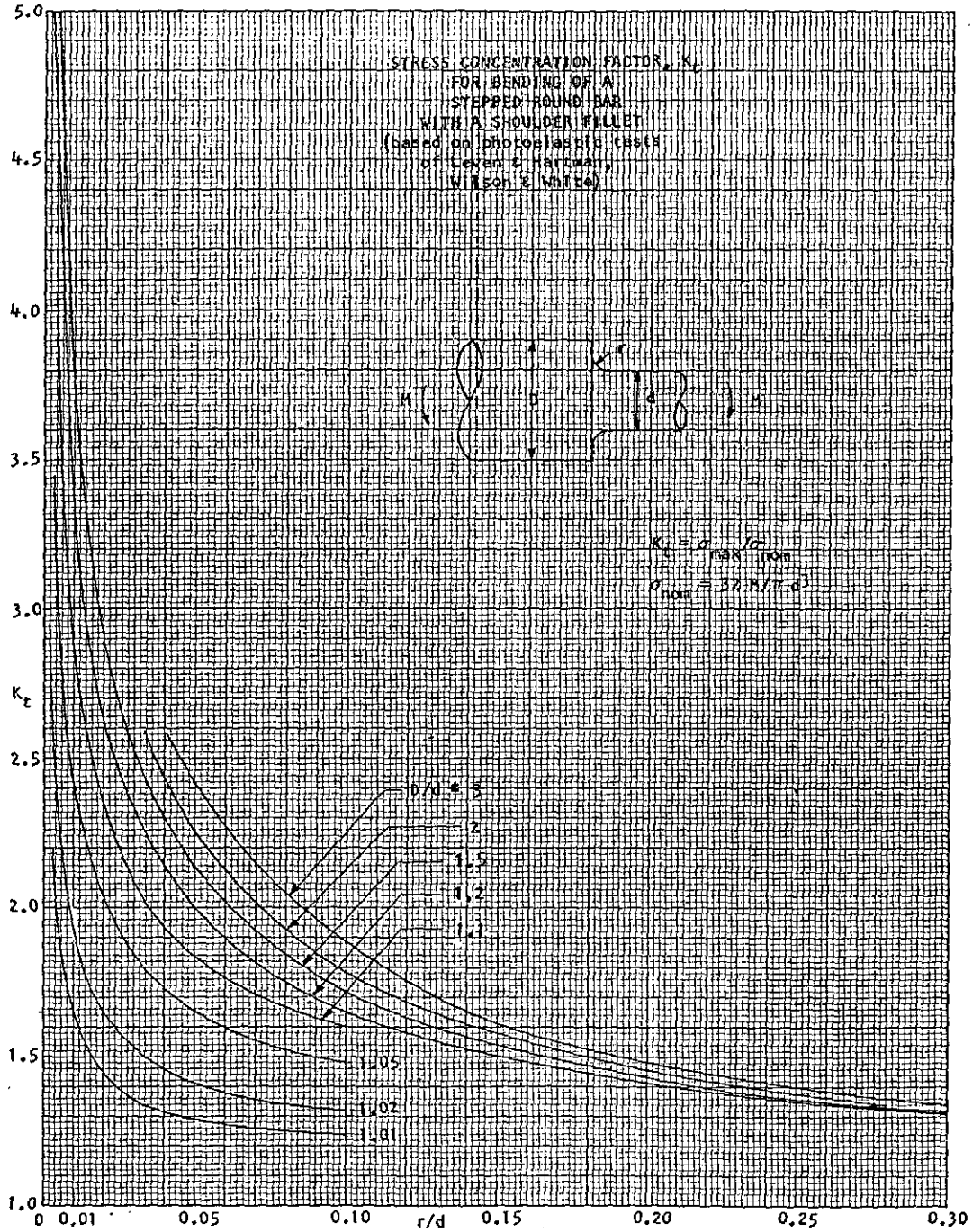

Figure 29. Stress concentration factor, K_t, for bending of a stepped round bar with a shoulder fillet [49].

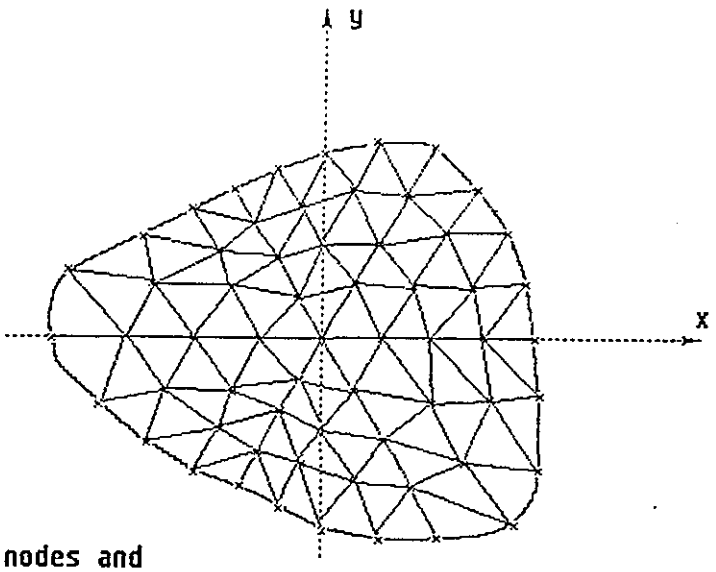

Figure 30. Division of sections in triangular elements in the subroutine TORO.

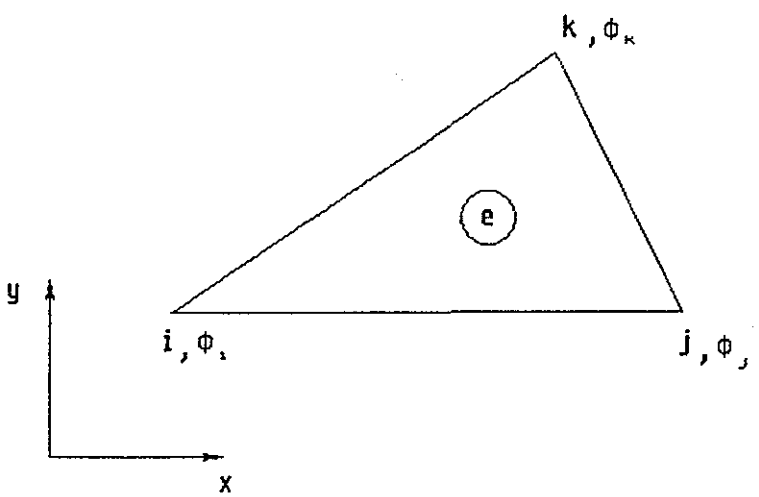

Figure 31. The triangular element used in the subroutine TORO.

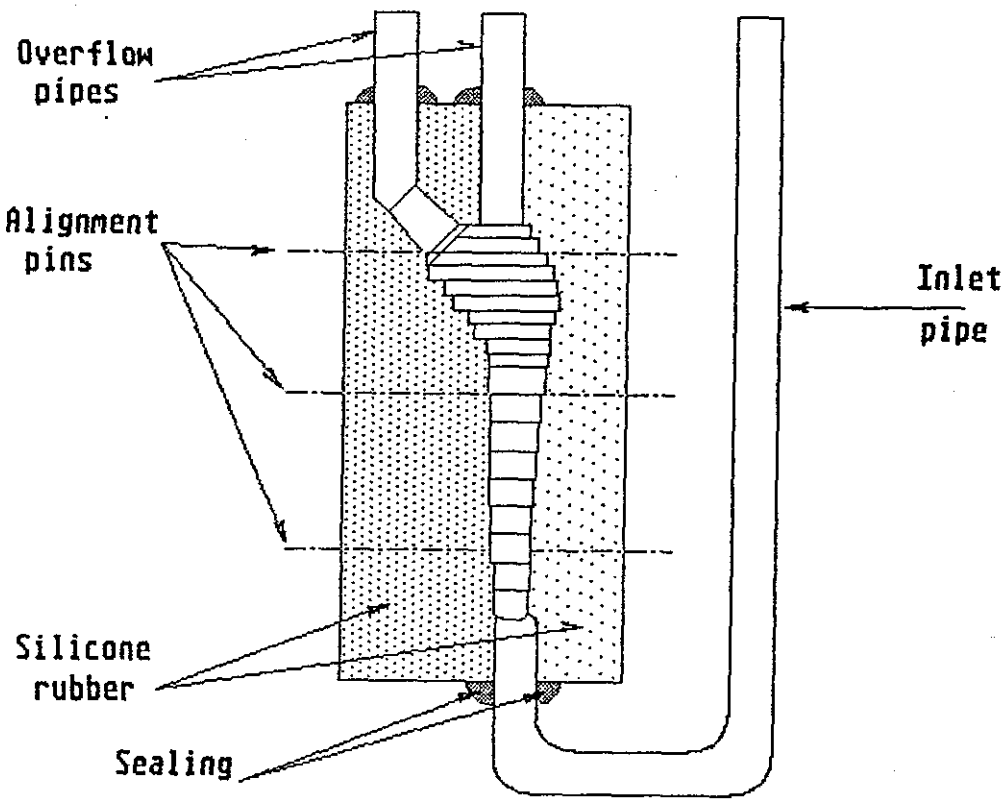

Figure 32. Schematic drawing of an assembled mould ready for ascending casting.

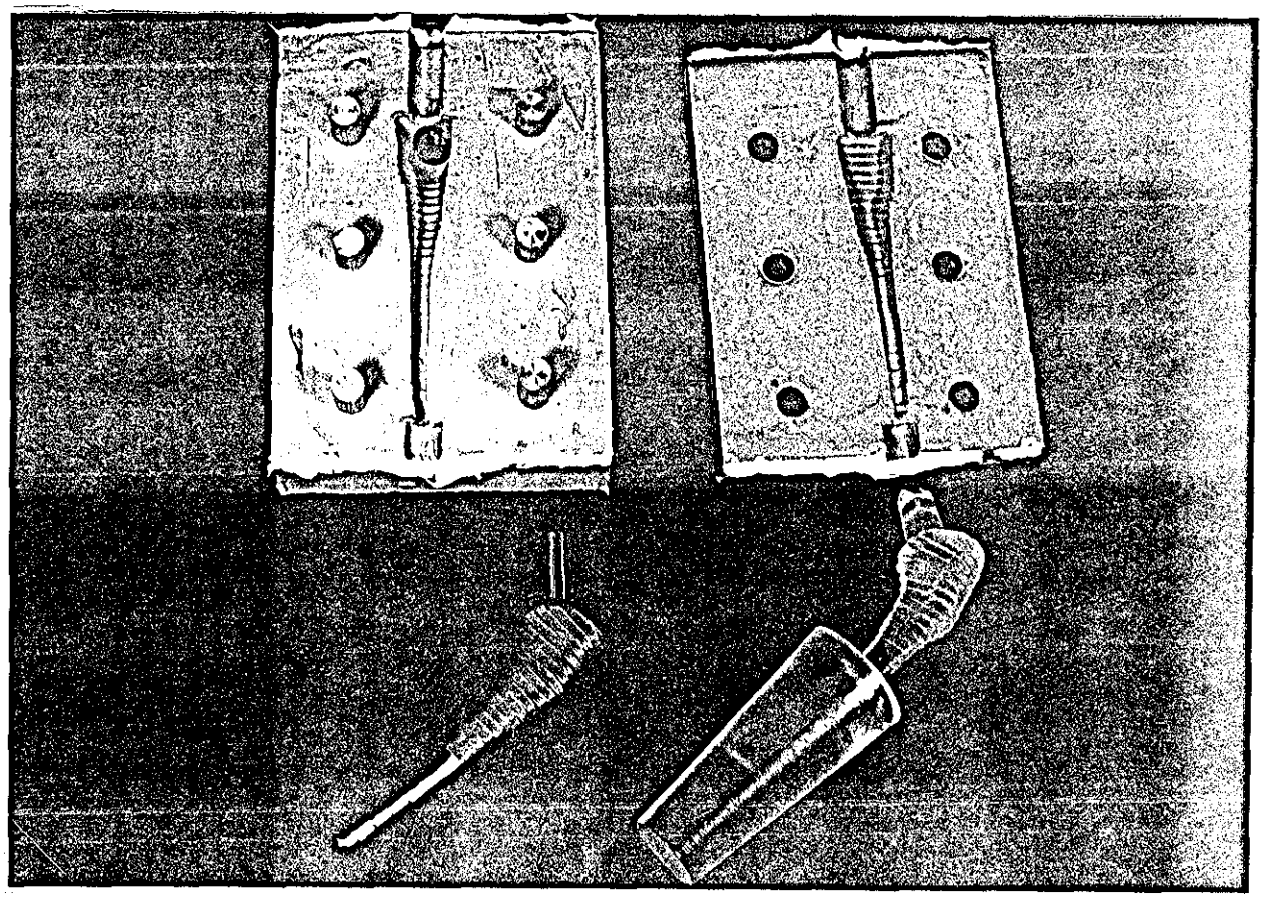

Figure 33. Photograph showing the mould, the photoelastic model and the prosthesis G035.

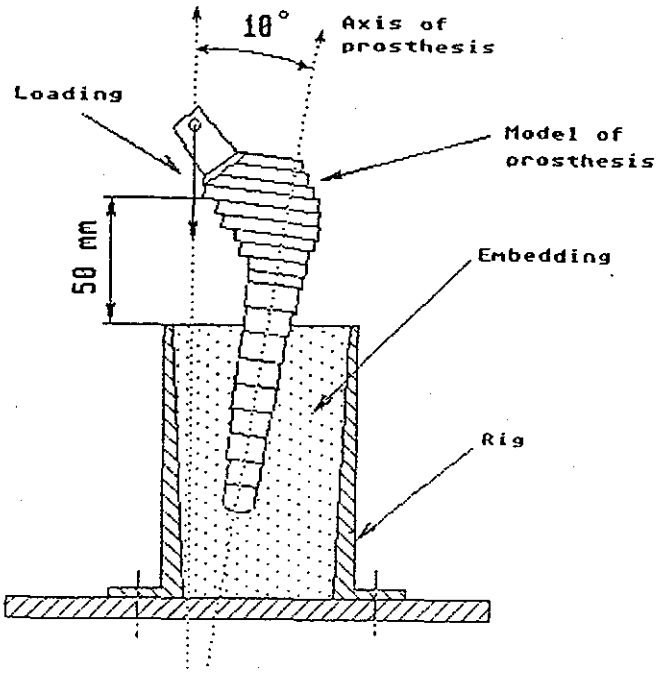

Figure 34. Schematic drawing of the photoelastic model in the loading rig.

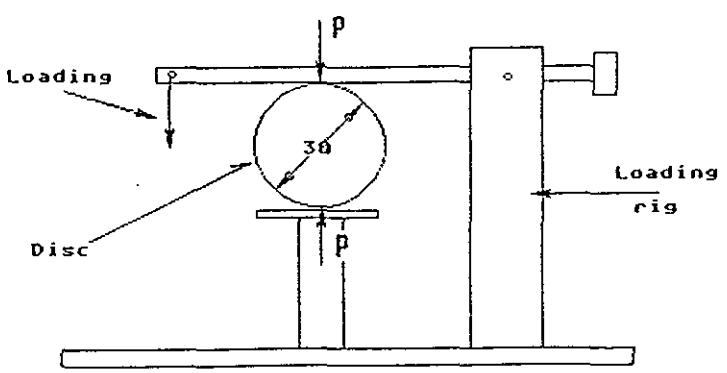

Figure 35. Schematic drawing of the disc in the loading rig.

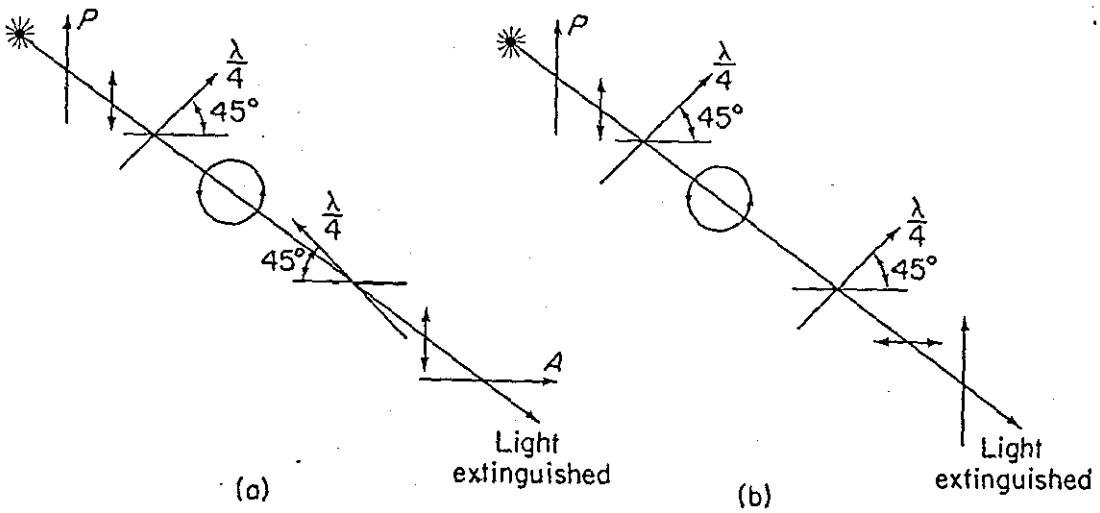

Figure 36. The circular polariscope (schematically). (a) Crossed arrangement (dark-field mode). (b) Parallel arrangement (bright-field mode).

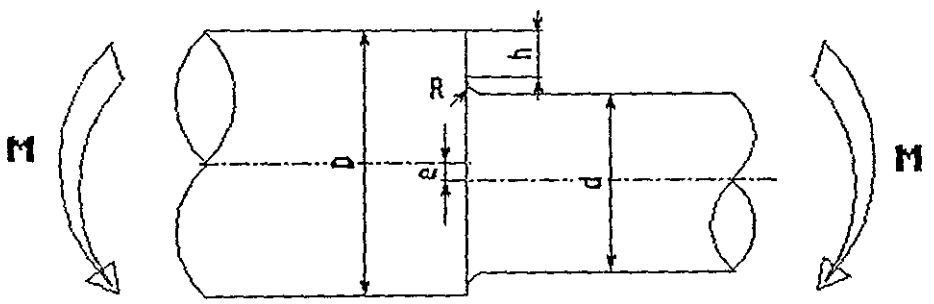

M - bending moment
D - diameter; D=30 mm
d - diameter; d=20 mm
R - transition radius
h - hight of the shoulder
e - eccentricity

Figure 37. Eccentric specimen used in scattered-light photoelastic experiments.

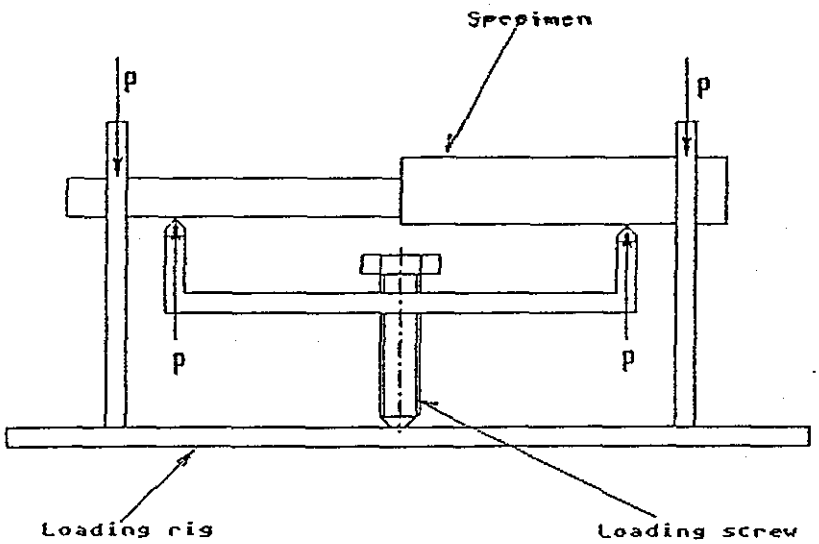

Figure 38. Schematic drawing of the loading rig used in scattered-light experiments.

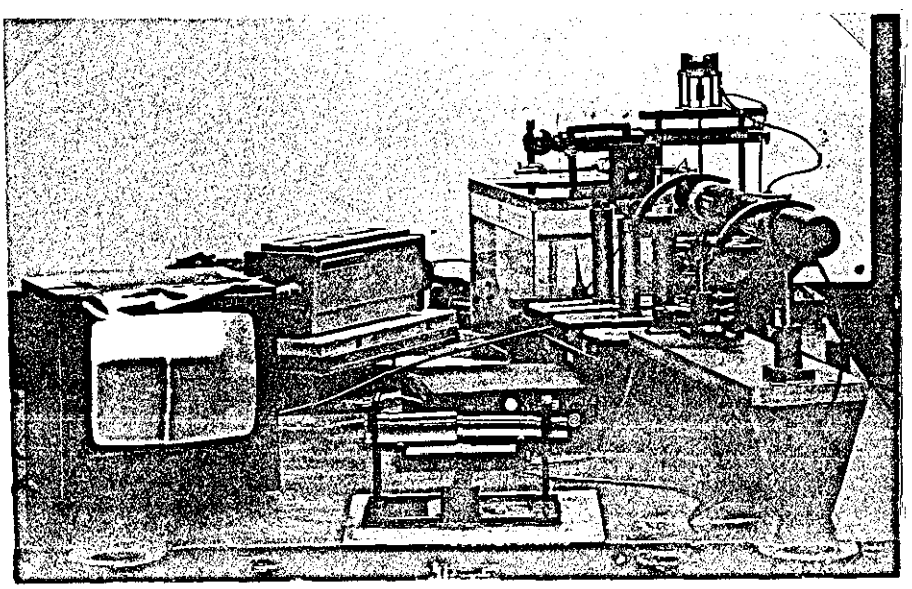

Figure 39. Experimental set-up in scattered light photoelasticity.

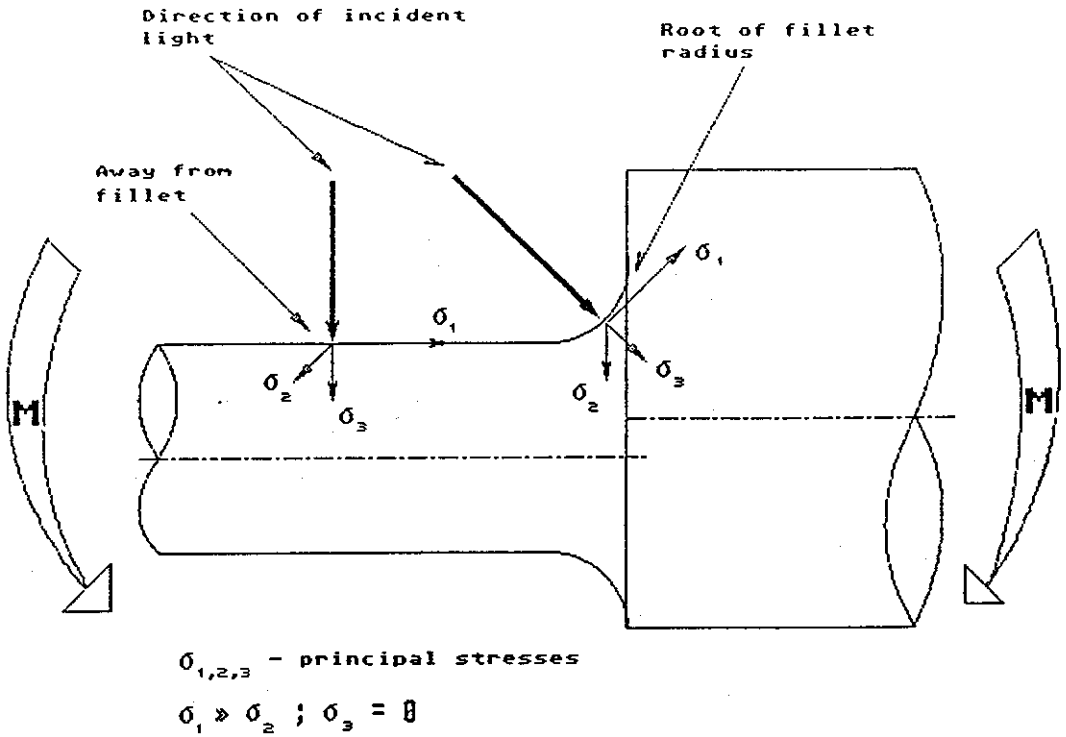

Figure 40. Directions of incident light in scattered-light experiments.

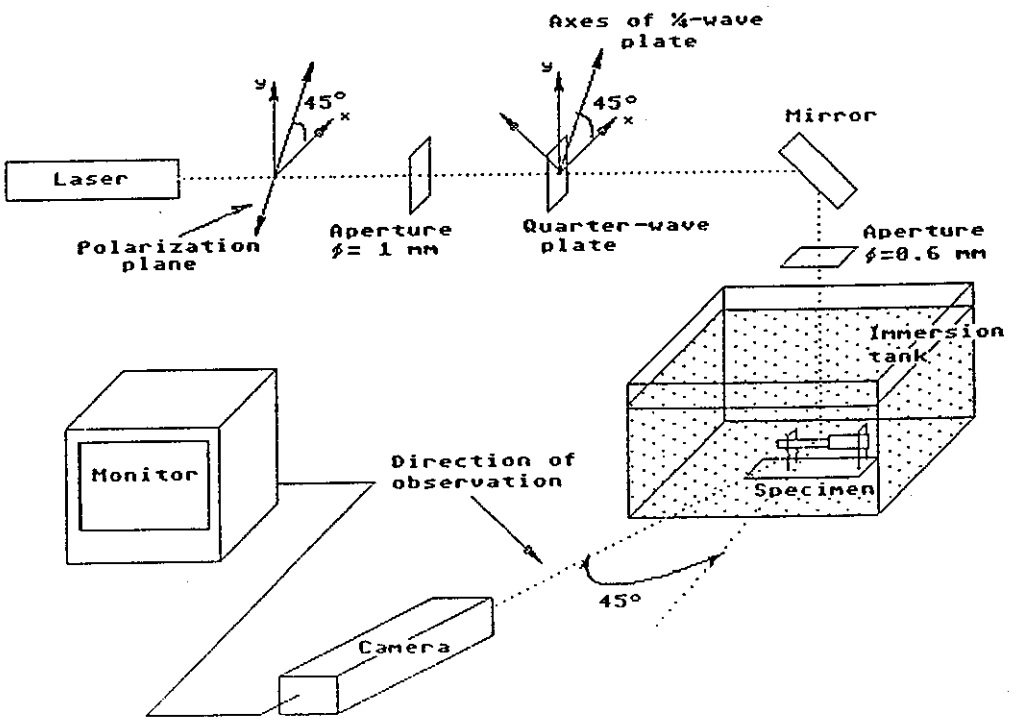

Figure 41. Schematical drawing of the set-up used in the experiments with scattered-light.

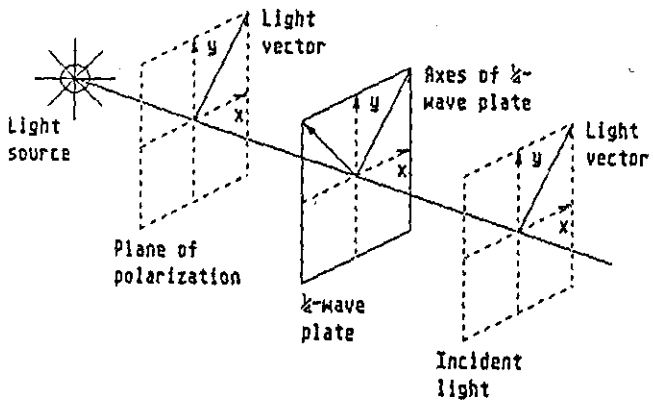

Initial position

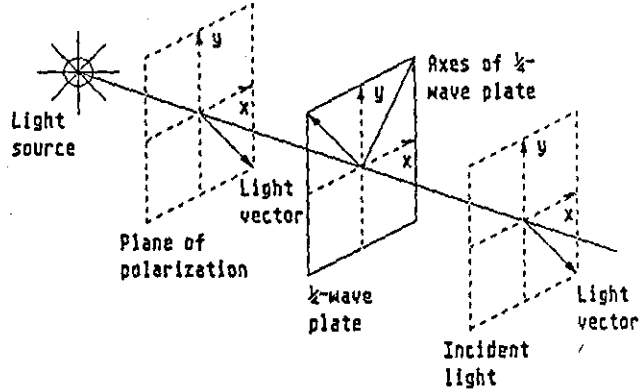

Laser rotated by 90°

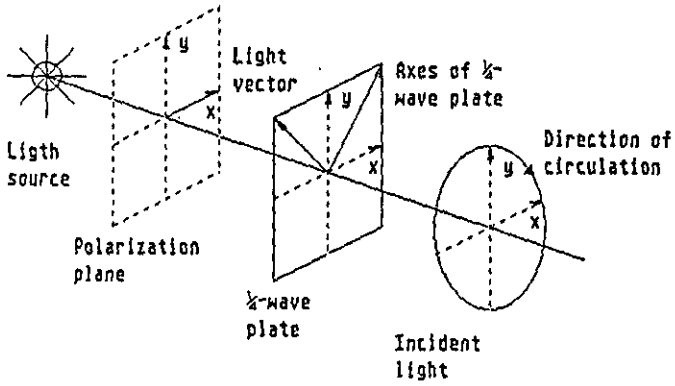

Laser rotated by 45°

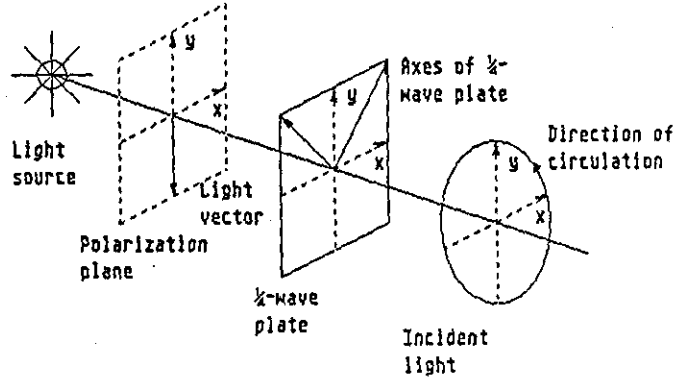

Laser rotated by 135°

Figure 42. Direction of polarisation of the incident light in dependence on the position of the laser.

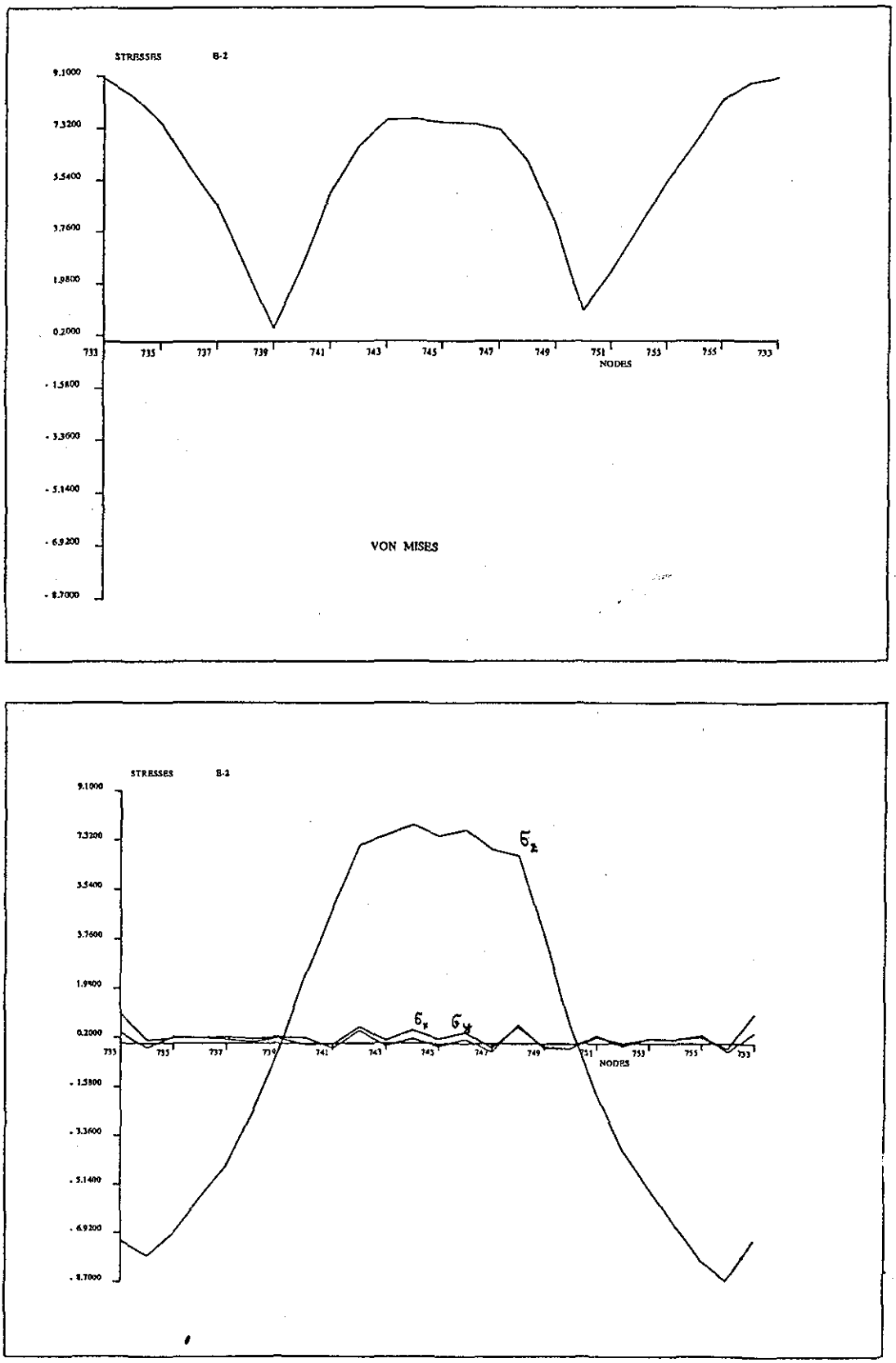

Figure 43. Direct and von Mises stresses along a contour above the embedding level.

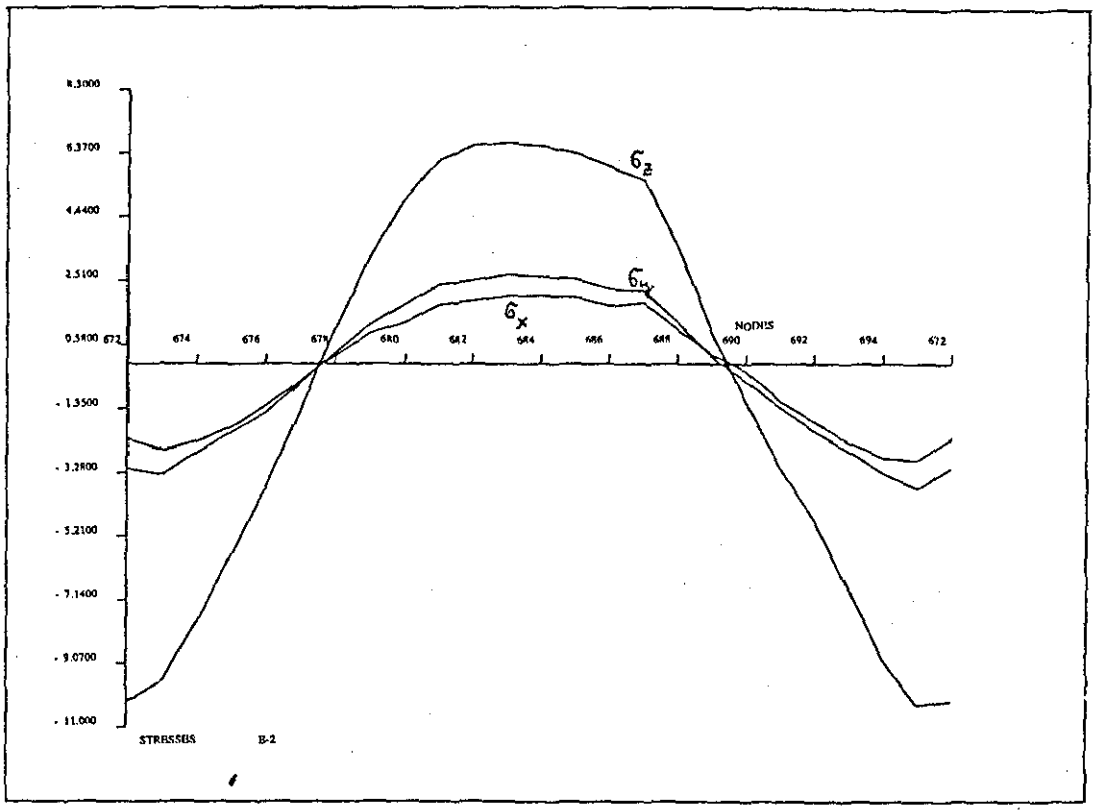

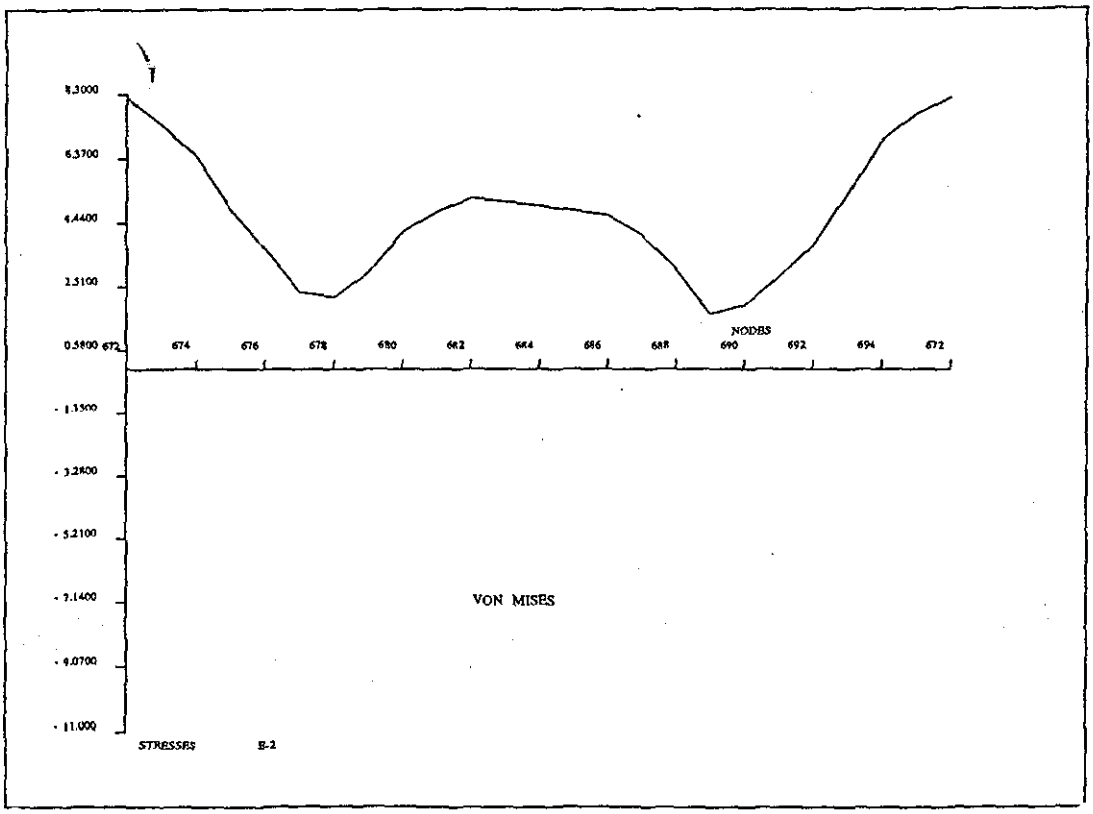

Figure 44. Direct and von Mises streses along a contour at the embedding level.

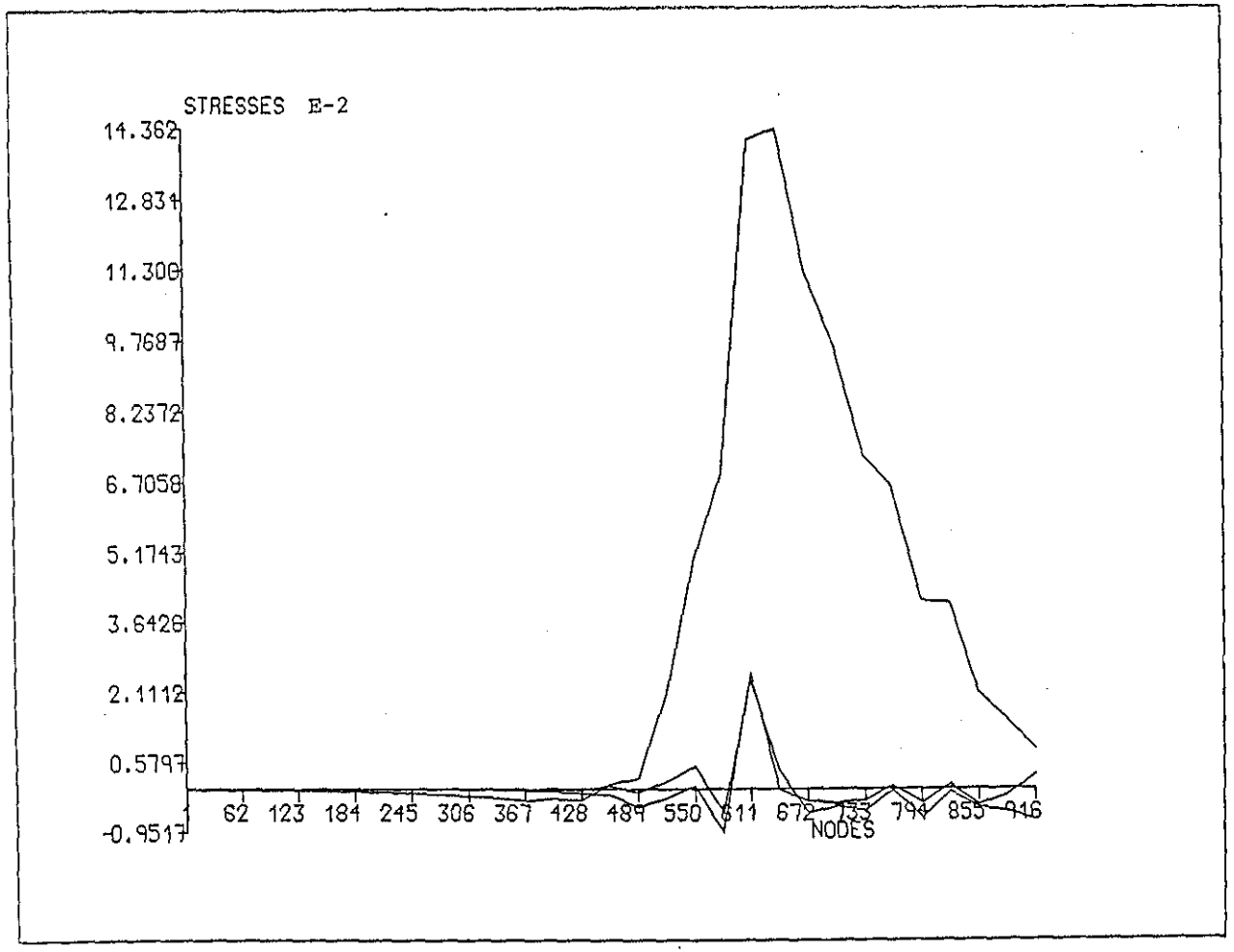

Figure 45. Direct stresses on the lateral (tension) side of the prosthesis F063. Results from the FEM-model for comparison with the results from the photoelastic experiments.

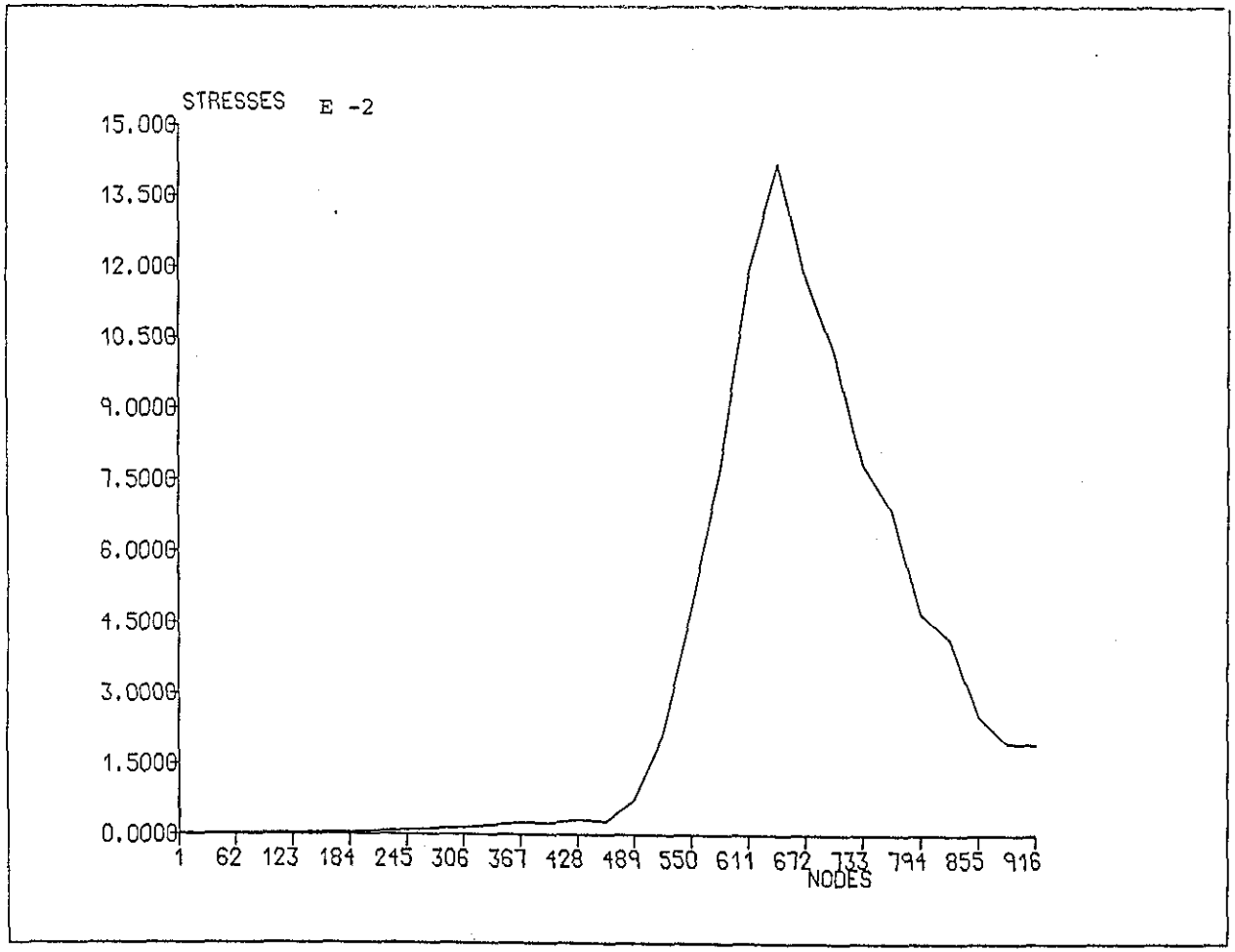

Figure 46. Von Mises stress on the lateral (tension) side of the prosthesis FØ63. Results from the FEM-model for comparison with the results from the photoelastic experiments.

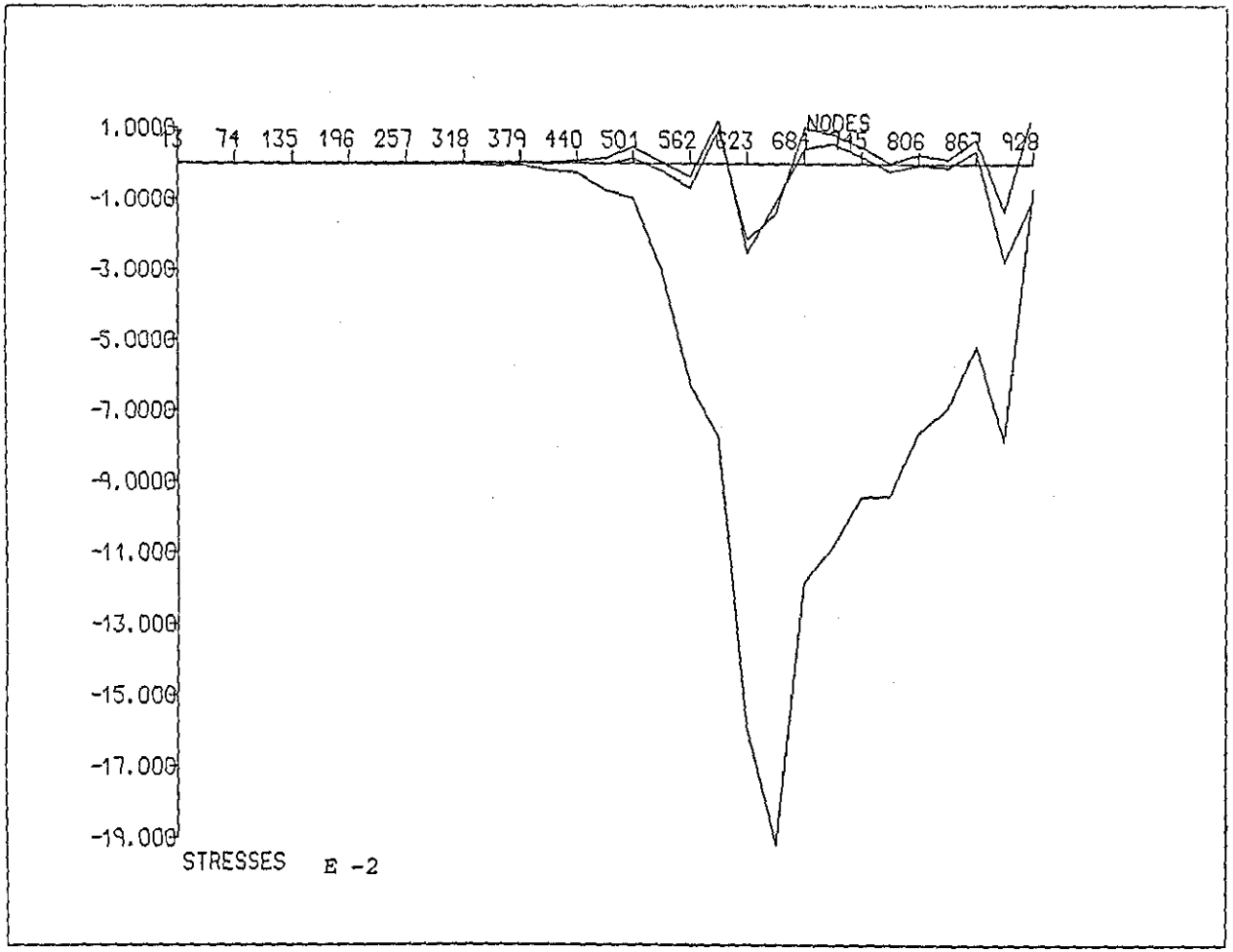

Figure 47. Direct stresses on the medial (compression) side of the prosthesis F063. Results from the FEM-model for comparison with the results from the photoelastic experiments.

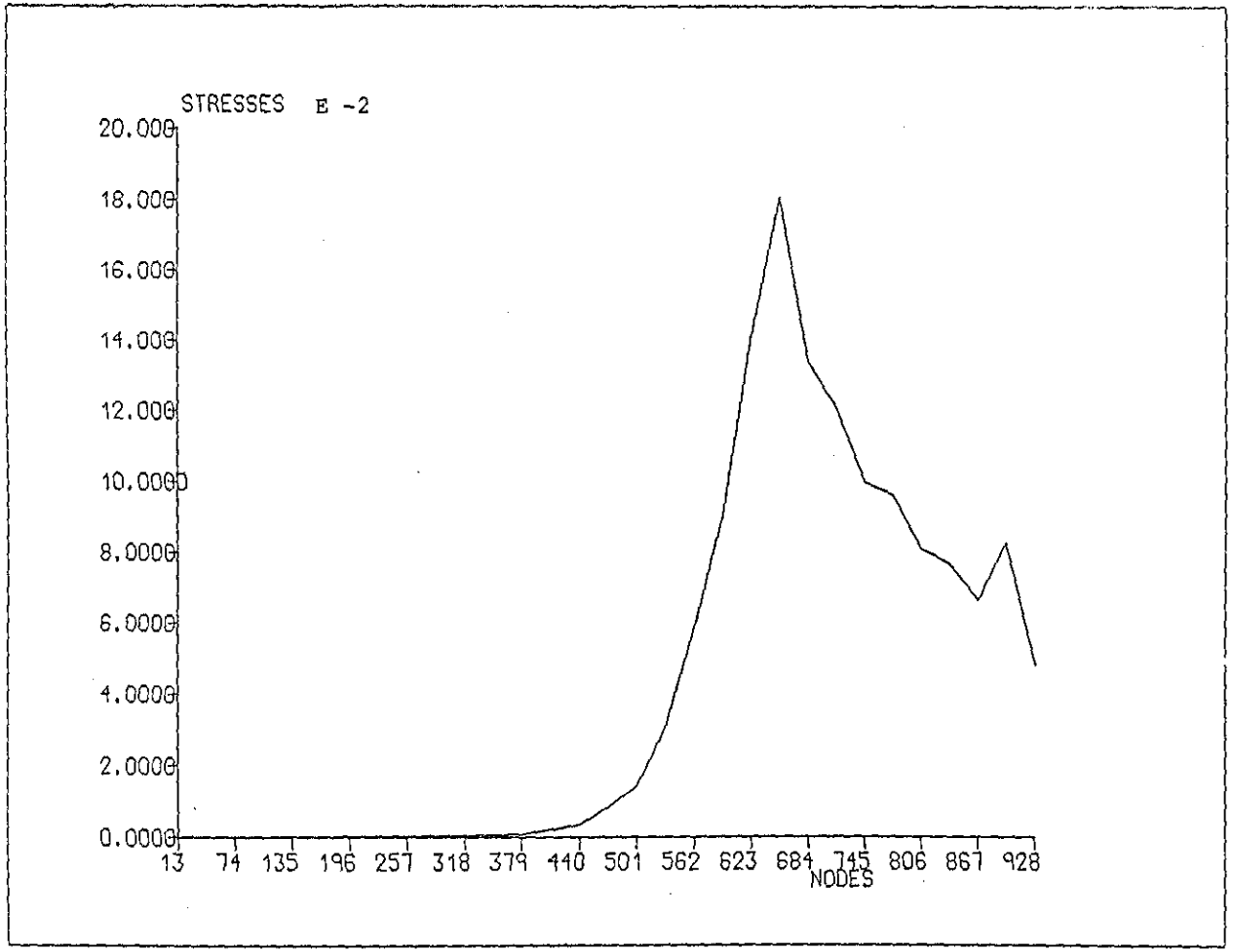

Figure 48. Von Mises stress on the medial (compression) side of the prosthesis F063. Results from the FEM-model for comparison with the results from the photoelastic experiments.

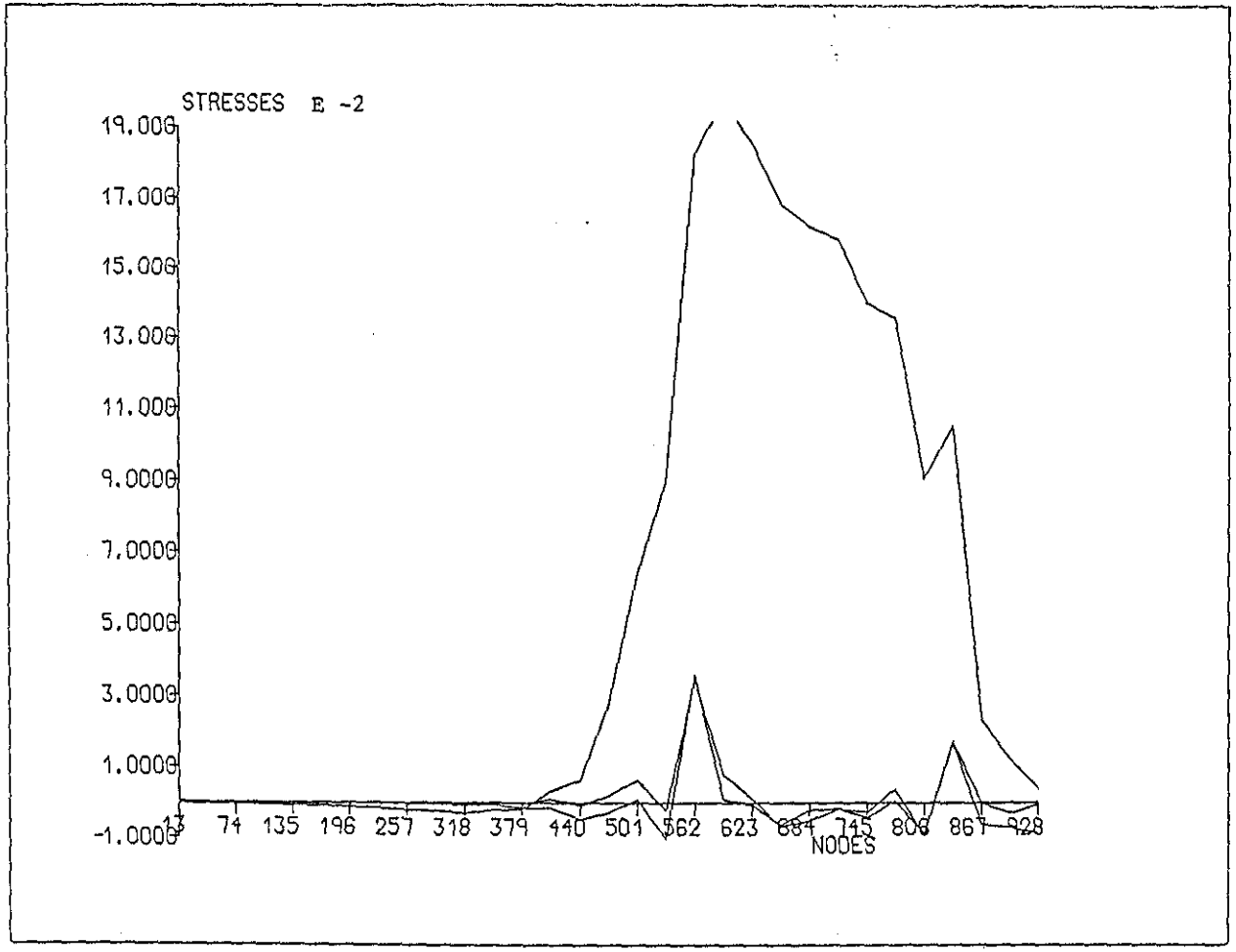

Figure 49. Direct stresses on the lateral (tension) side of the prosthesis F076. Results from the FEM-model for comparison with the results from the photoelastic experiments.

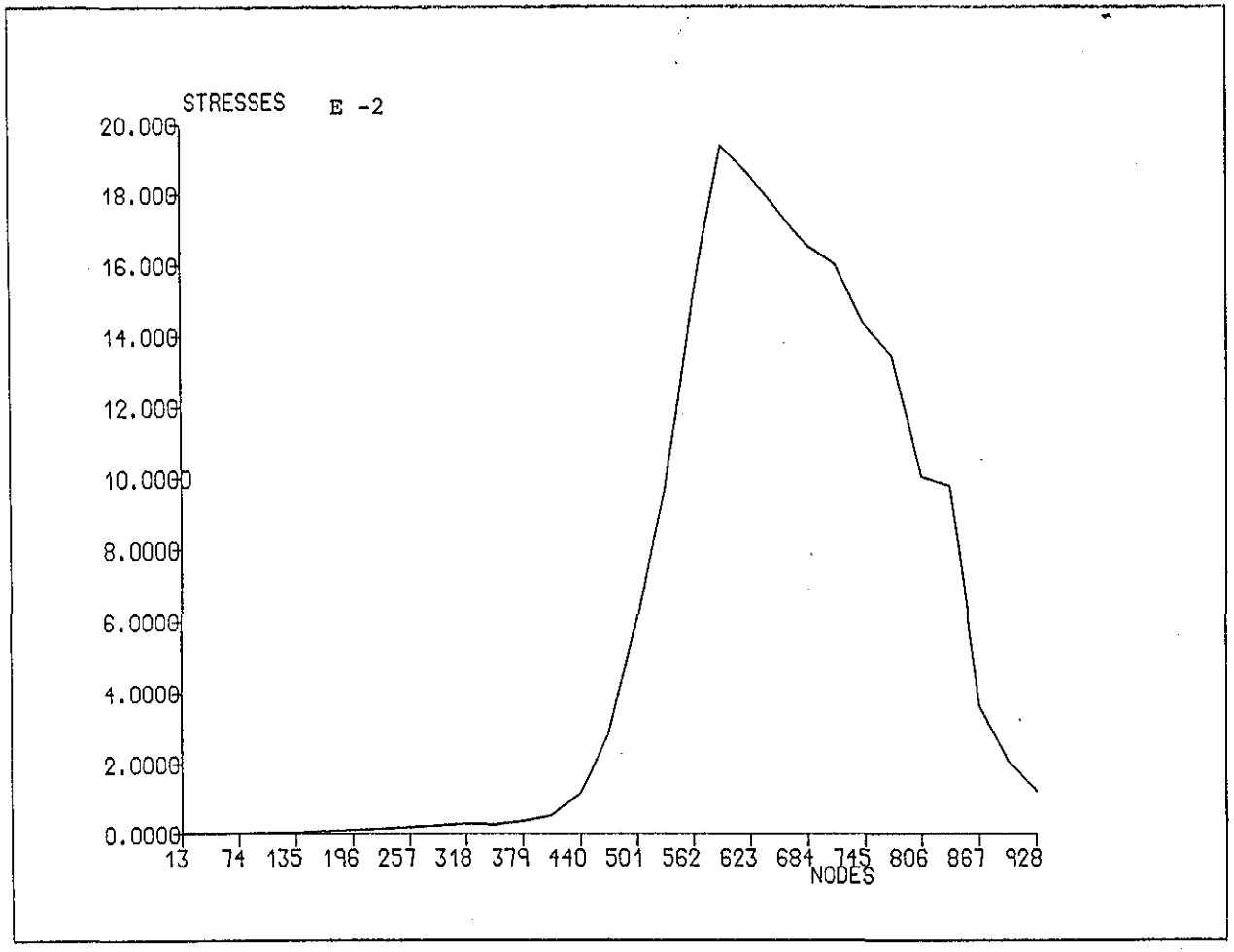

Figure 50. Von Mises stress on the lateral (tension) side of the prosthesis F076. Results from the FEM-model for comparison with the results from the photoelastic experiments.

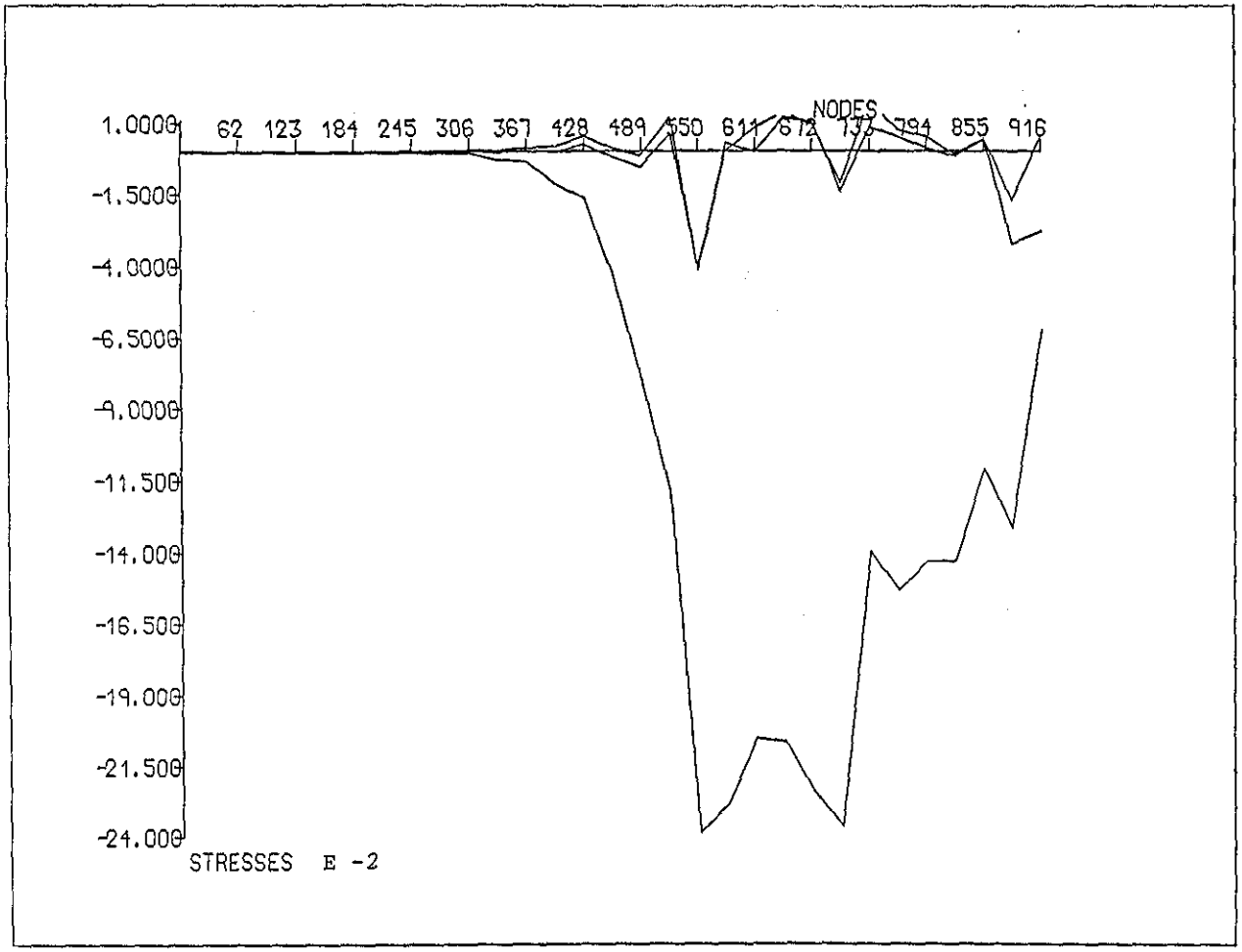

Figure 51. Direct stresses on the medial (compression) side of the prosthesis FØ76. Results from the FEM-model for comparison with the results from the photoelastic experiments.

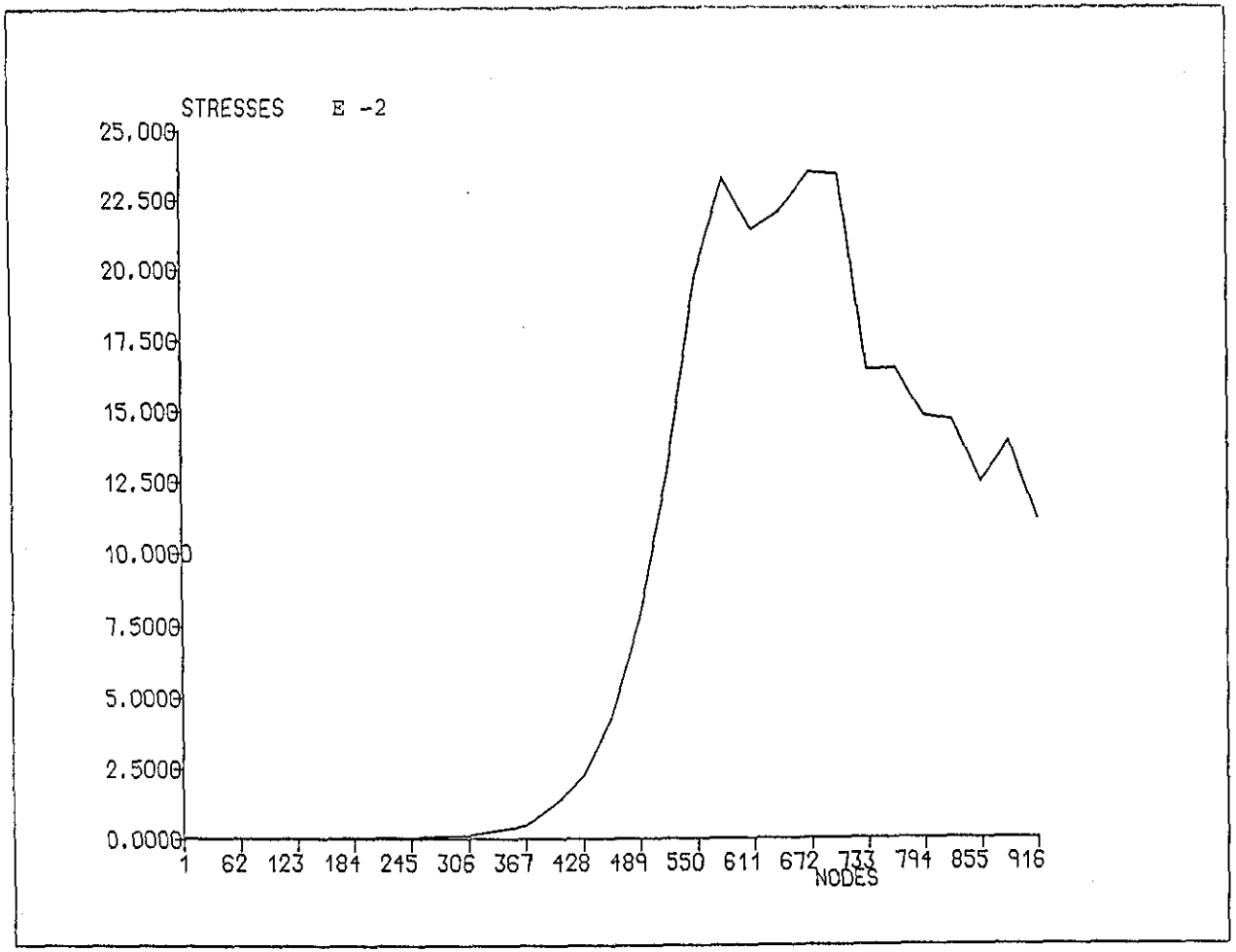

Figure 52. Von Mises stress on the medial (compression) side of the prosthesis FØ76. Results from the FEM-model for comparison with the results from the photoelastic experiments.

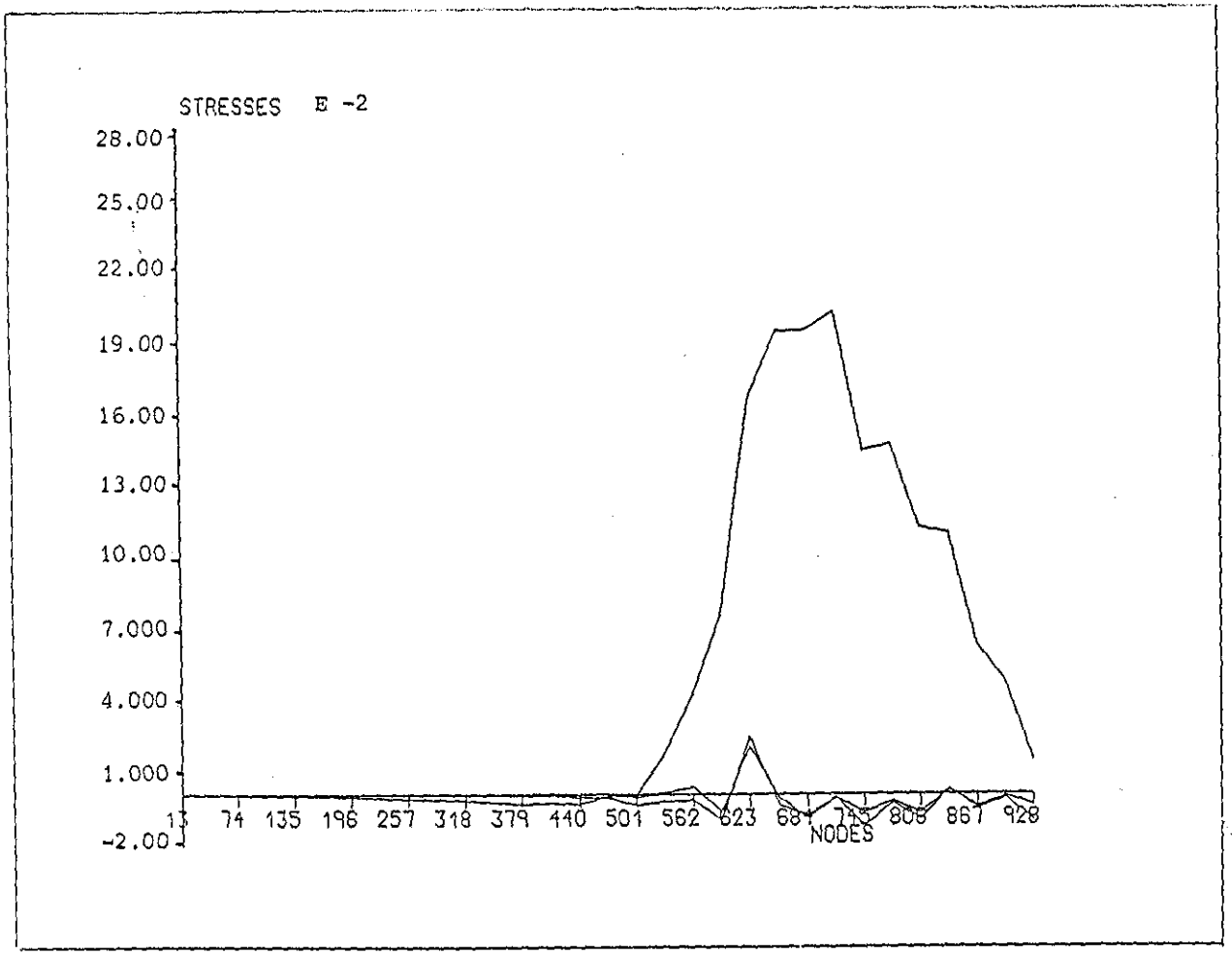

Figure 53. Direct stresses on the lateral (tension) side of the prosthesis G035. Results from the FEM-model for comparison with the results from the photoelastic experiments.

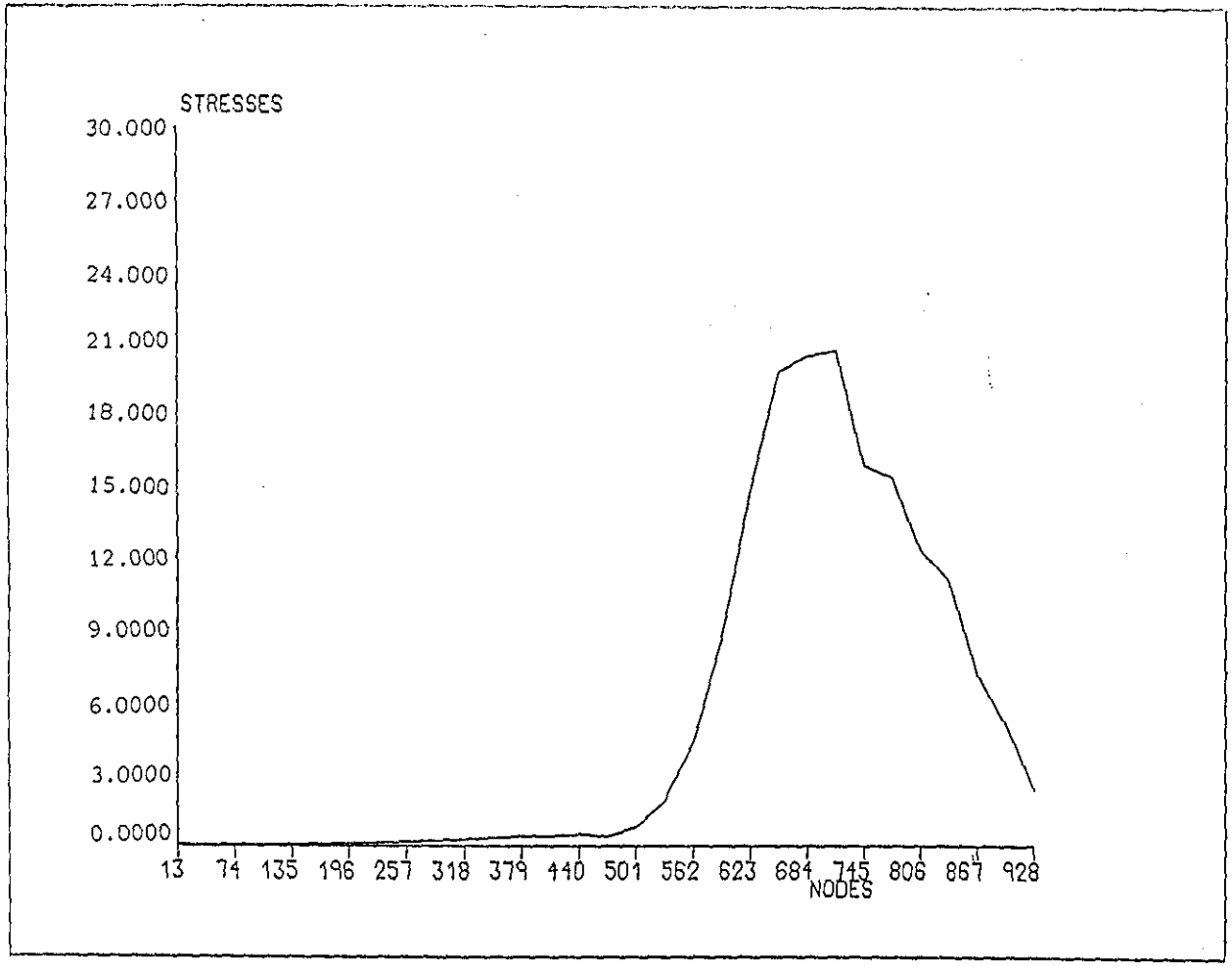

Figure 54. Von Mises stress on the lateral (tension) side of the prosthesis GØ35. Results from the FEM-model for comparison with the results from the photoelastic experiments.

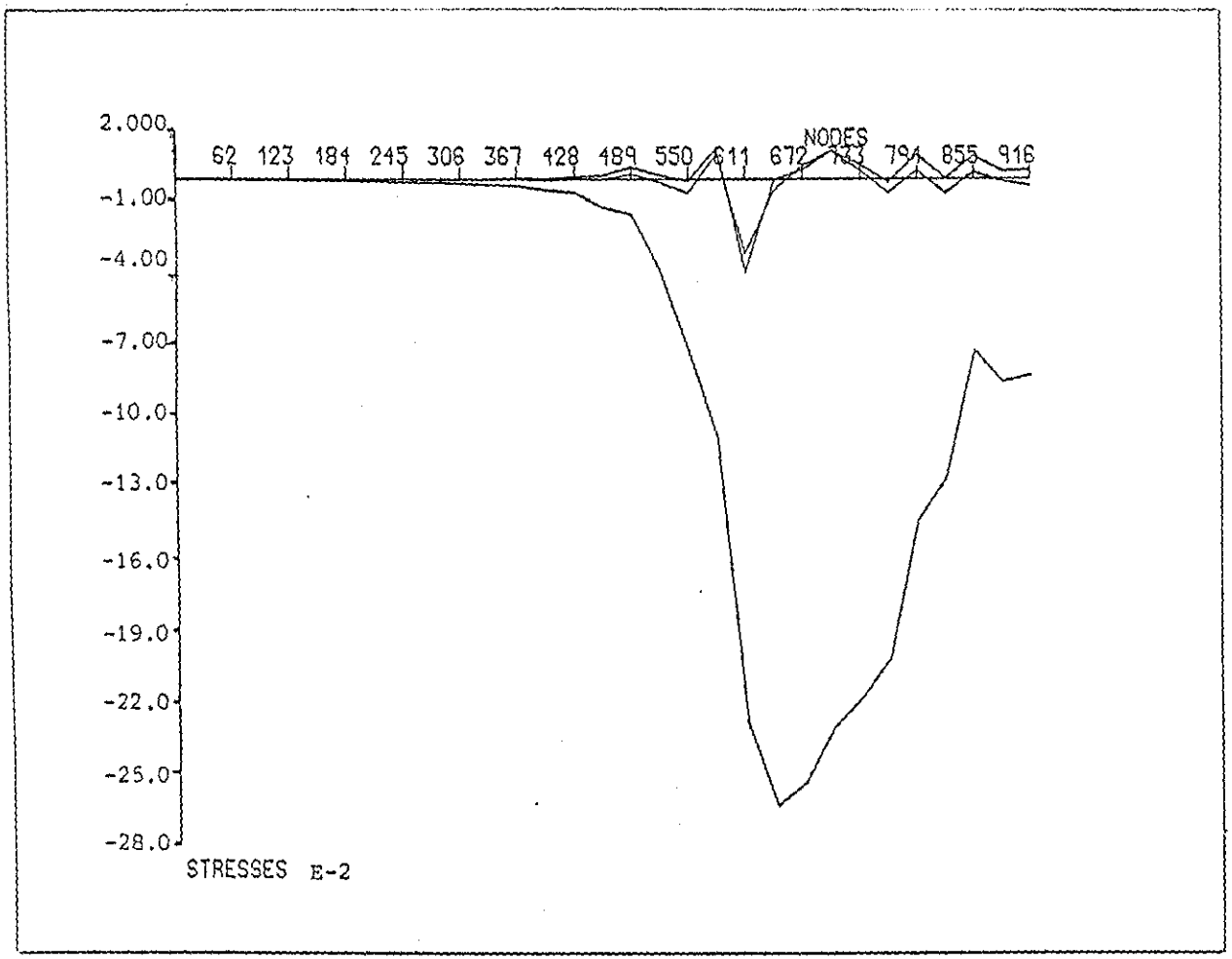

Figure 55. Direct stresses on the medial (compression) side of the prosthesis G035. Results from the FEM-model for comparison with the results from the photoelastic experiments.

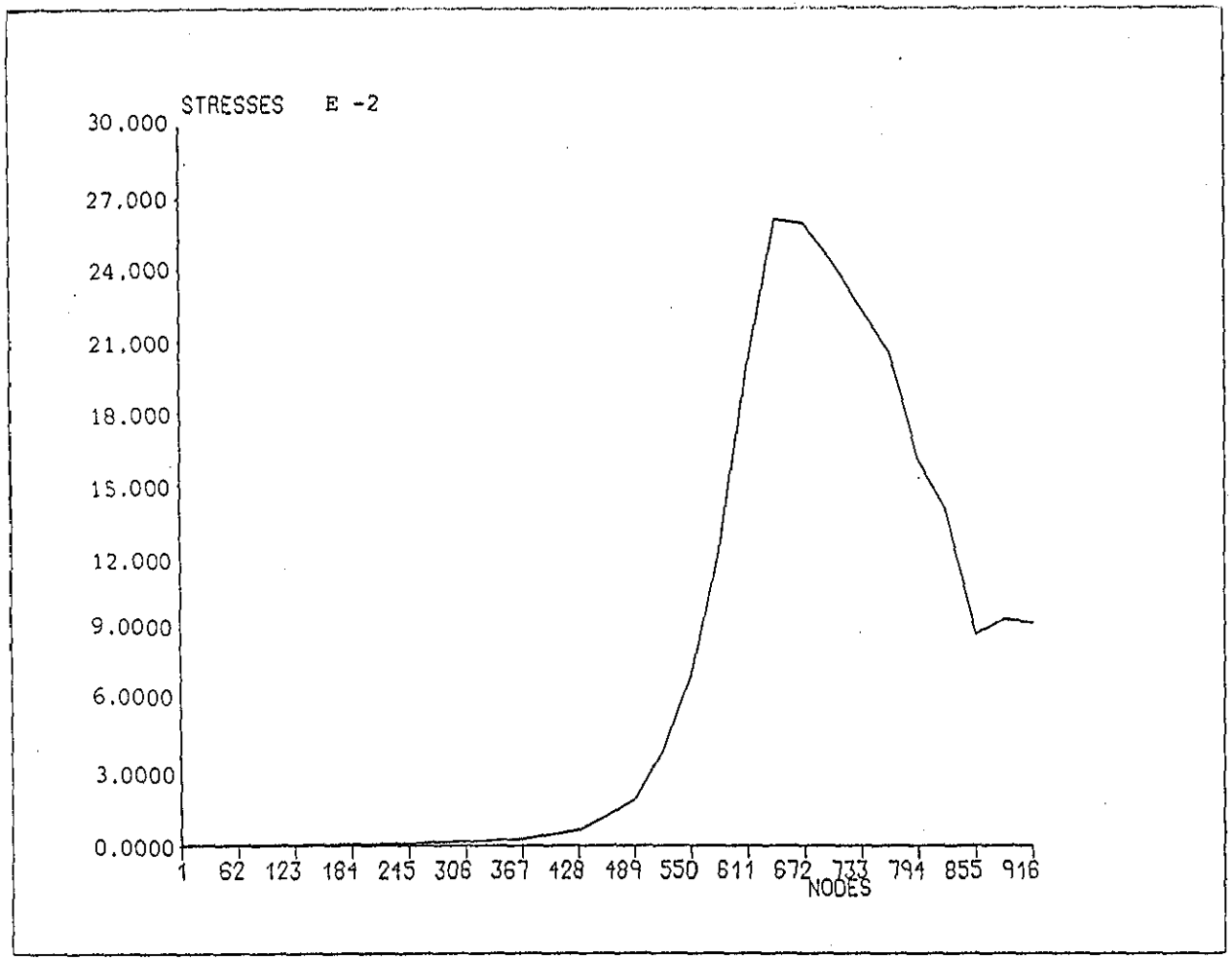

Figure 56. Von Mises stress on the medial (compression) side of the prosthesis G035. Results from the FEM-model for comparison with the results from the photoelastic experiments.

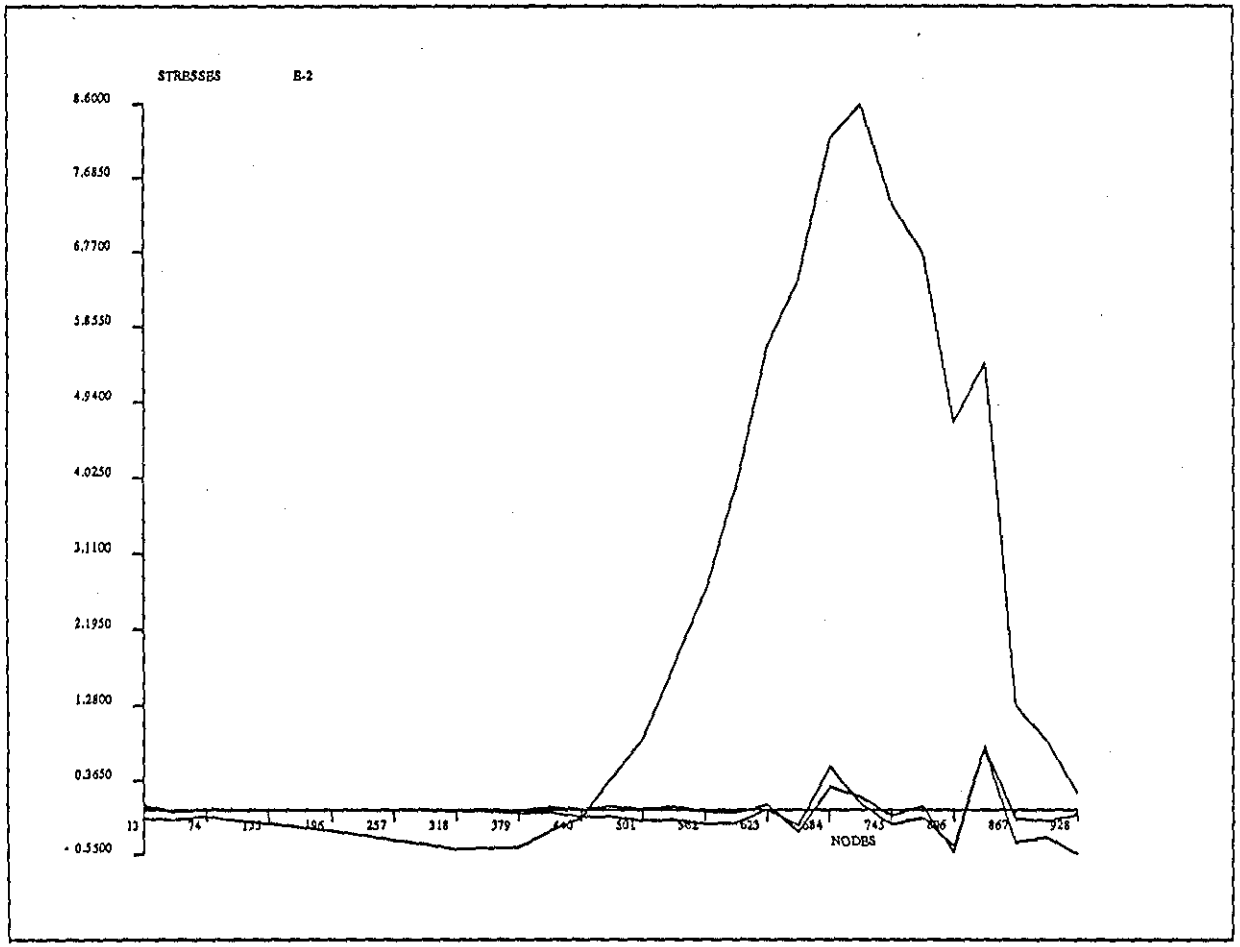

Figure 57. Direct stresses on the lateral (tension) side of the prosthesis FØ76. Load equal to 1N, and, modulus of elasticity of the embedding 32 times lower than that of the prosthesis.

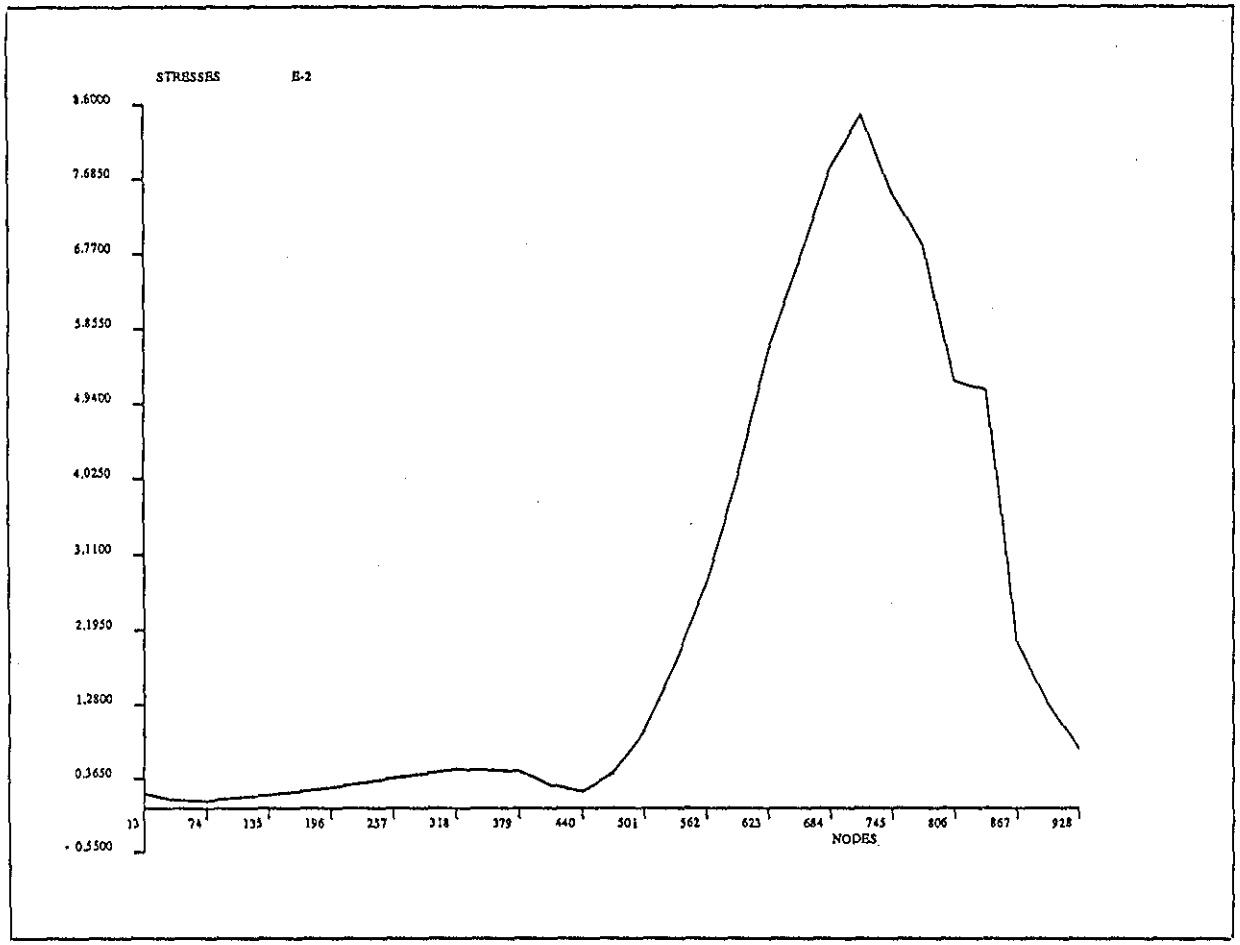

Figure 58. Von Mises stress on the lateral (tension) side of the prosthesis FØ76. Load equal to 1N, and, modulus of elasticity of the embedding 32 times lower than that of the prosthesis.

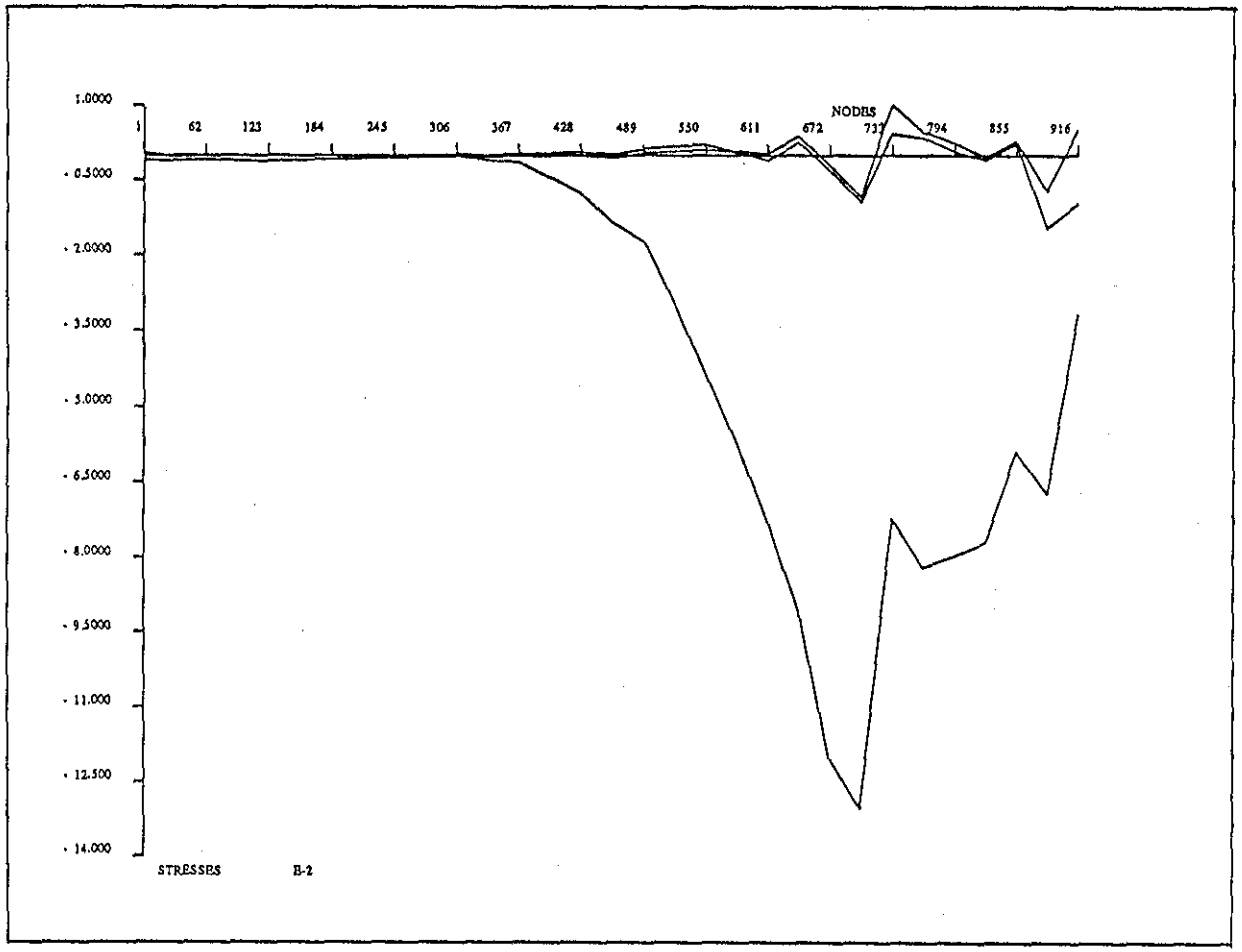

Figure 59. Direct stresses on the medial (compression) side of the prosthesis F076. Load equal to 1N, and, modulus of elasticity of the embedding 32 times lower than that of the prosthesis.

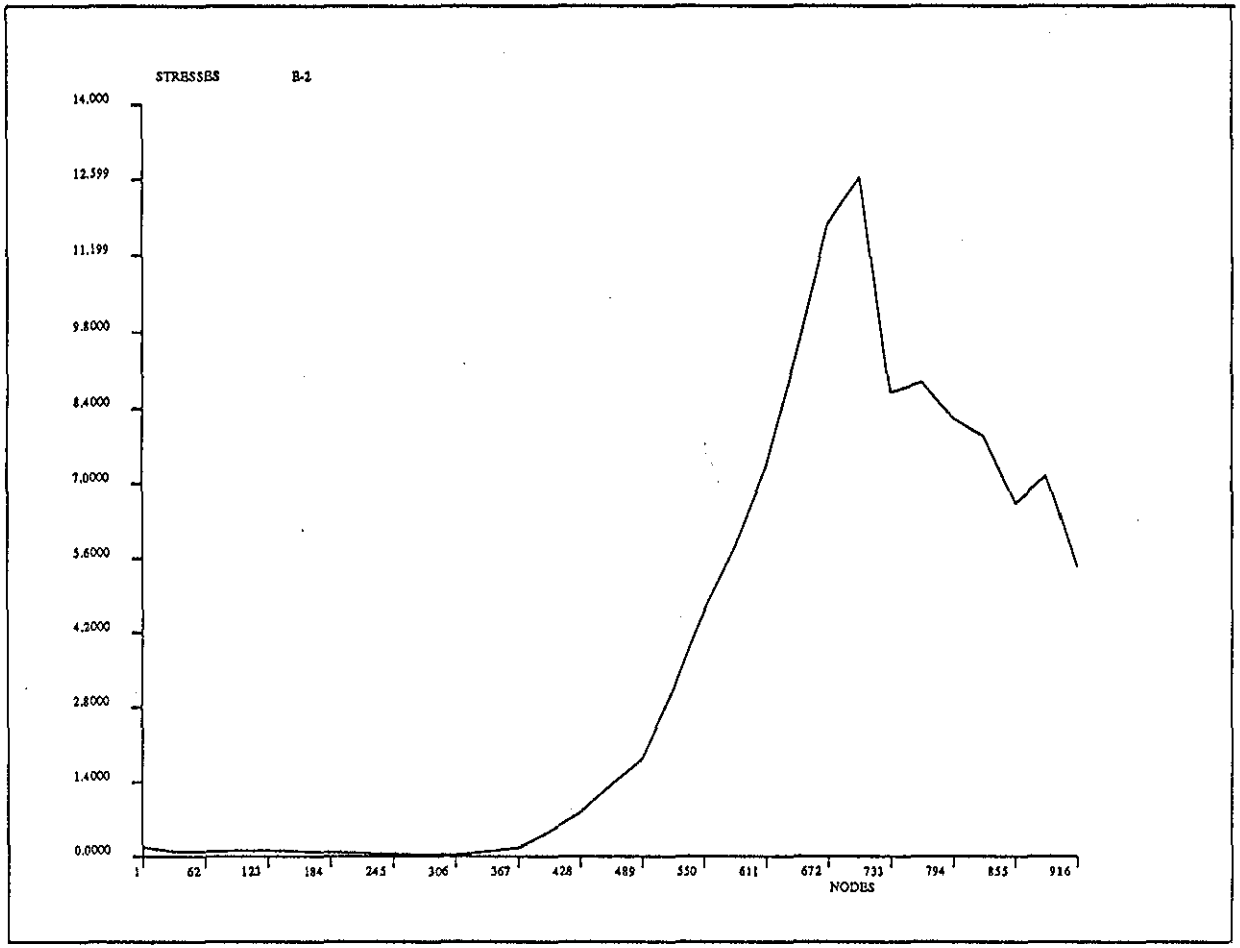

Figure 60. Von Mises stress on the medial (compression) side of the prosthesis FØ76. Load equal to 1N, and, modulus of elasticity of the embedding 32 times lower than that of the prosthesis.

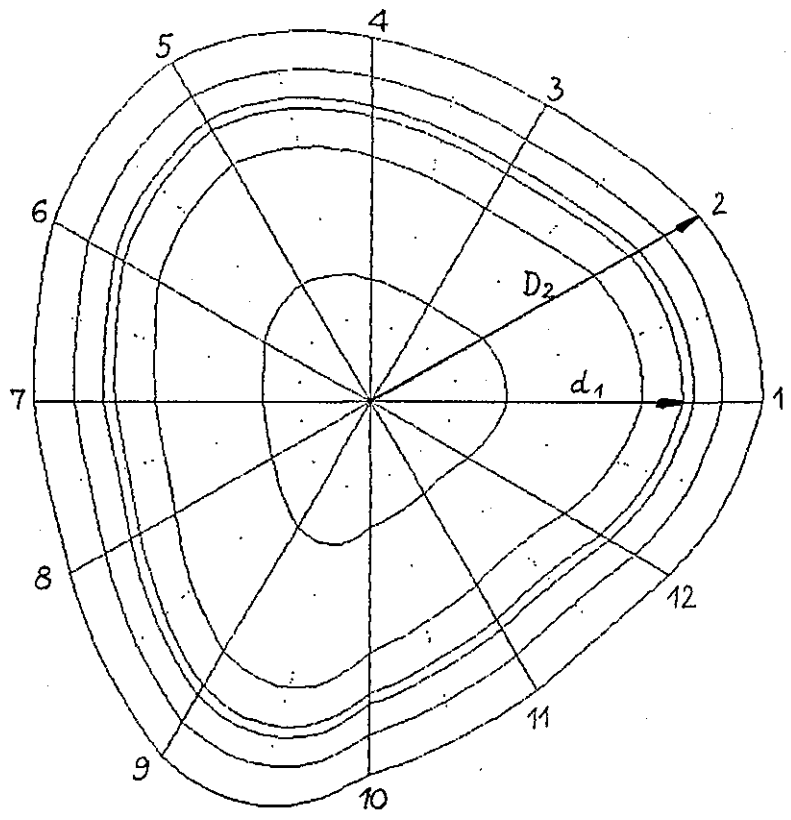

Figure 61. Geometry of the section 12 of the prosthesis F076 modelled with the program COSCF.

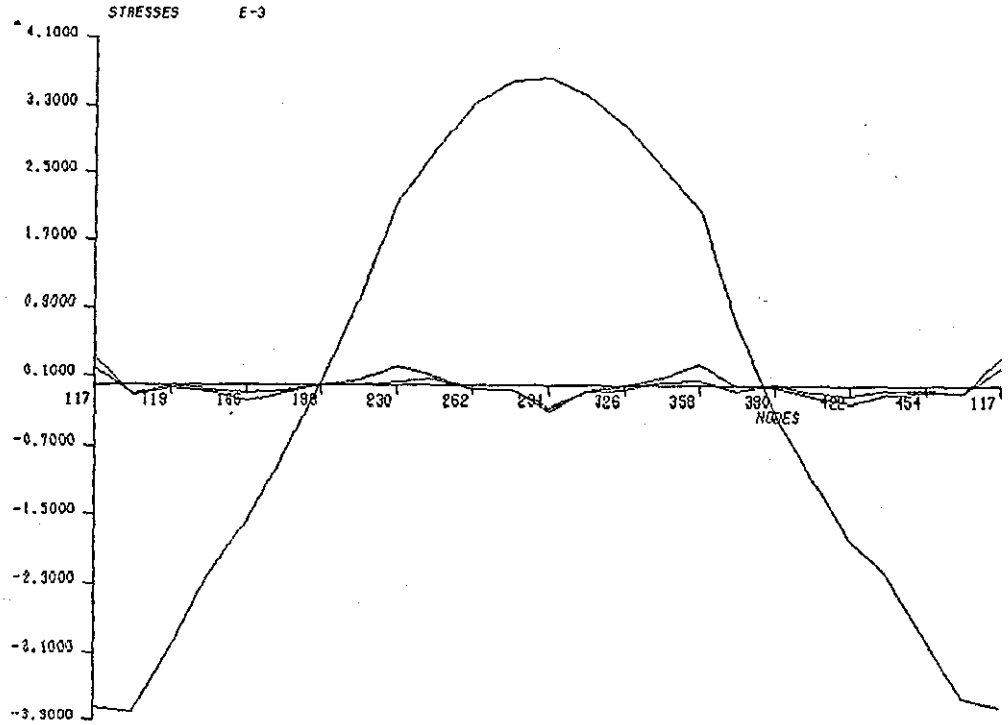

Figure 62. Direct stresses along the contour of the section 12 of the prosthesis F076 without the transition radius.

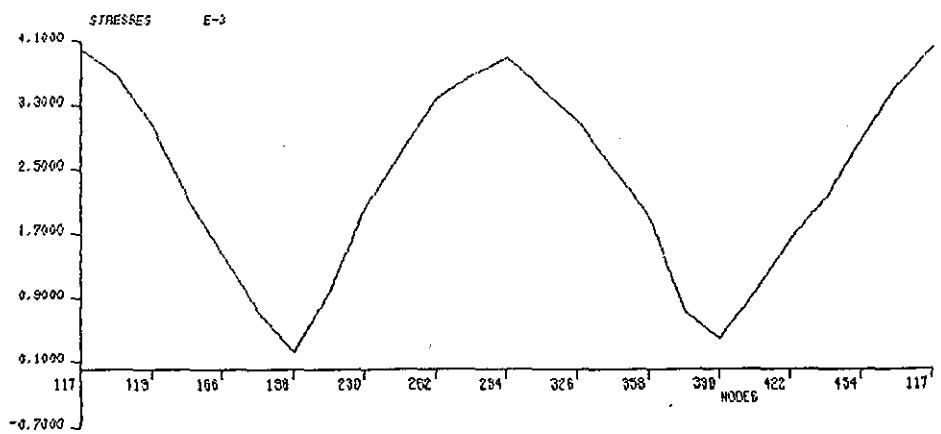

Figure 63. Von Mises stresses along the contour of the section 12 of the prosthesis F076 without the transition radius.

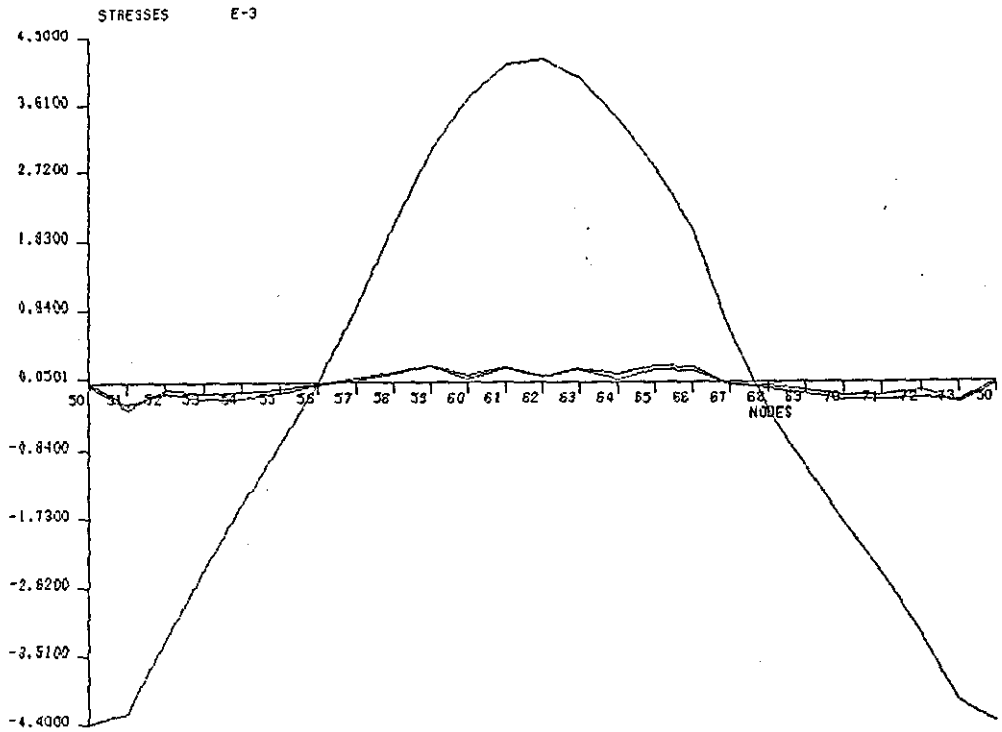

Figure 64. Direct stresses along the contour of the section 12 of the prosthesis FØ76 with one third of the transition radius.

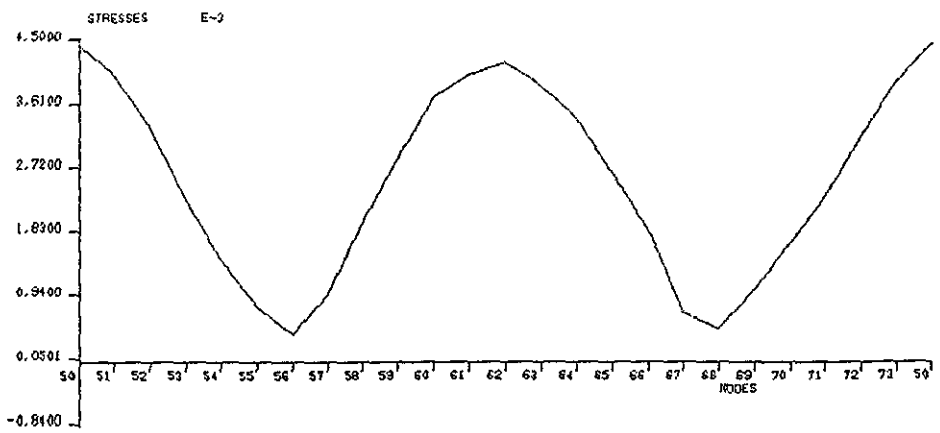

Figure 65. Von Mises stresses along the contour of the section 12 of the prosthesis FØ76 with one third of the transition radius.

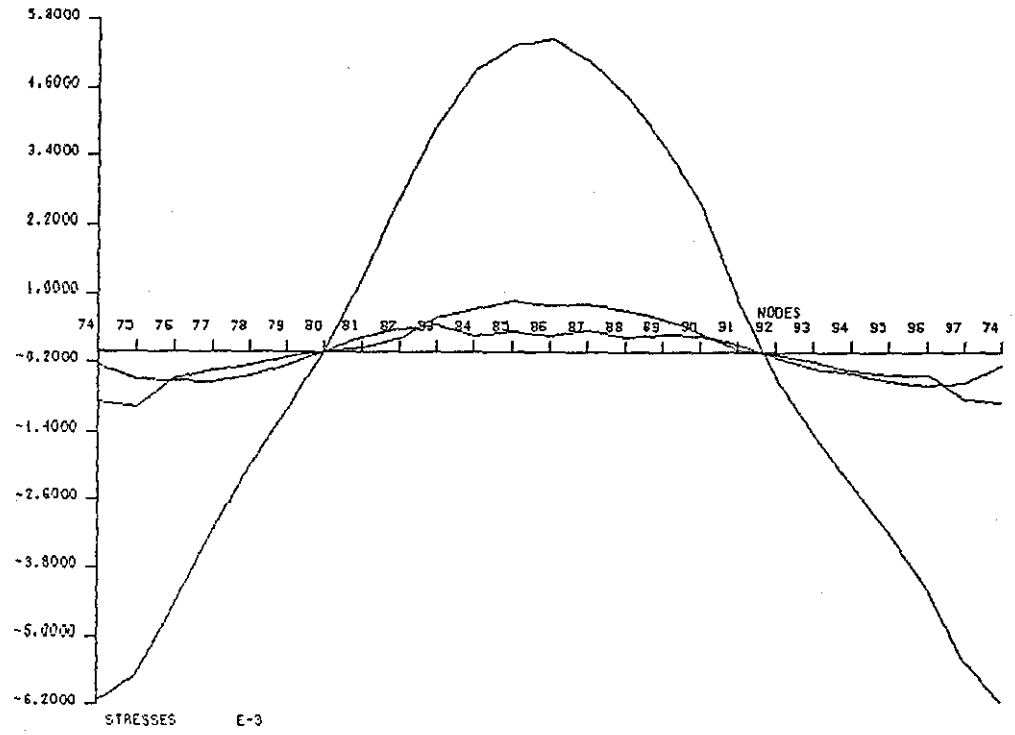

Figure 66. Direct stresses along the contour of the section 12 of the prosthesis FØ76 with two thirds of the transition radius.

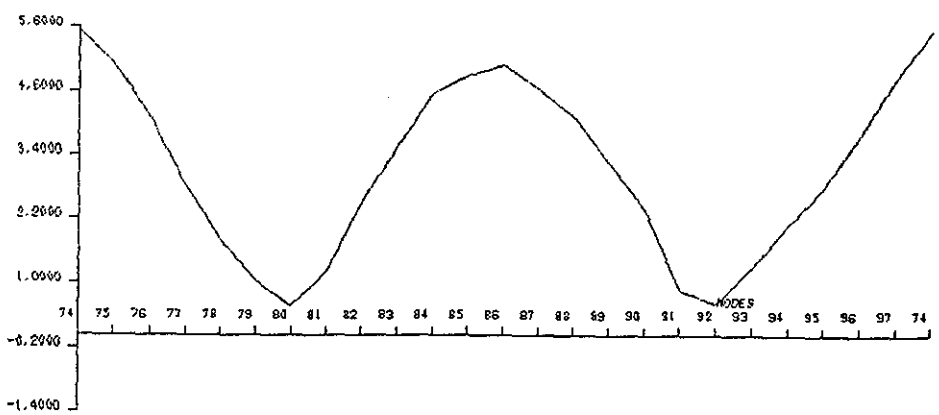

Figure 67. Von Mises stresses along the contour of the section 12 of the prosthesis FØ76 with two thirds of the transition radius.

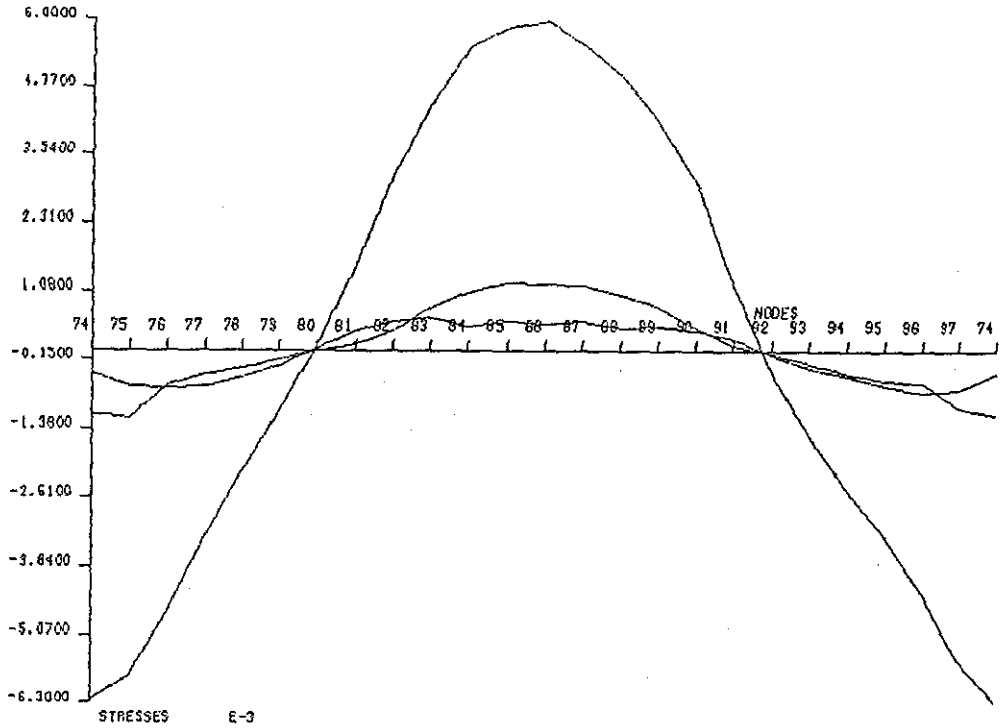

Figure 68. Direct stresses along the contour of the section 12 of the prosthesis F076 with the whole transition radius.

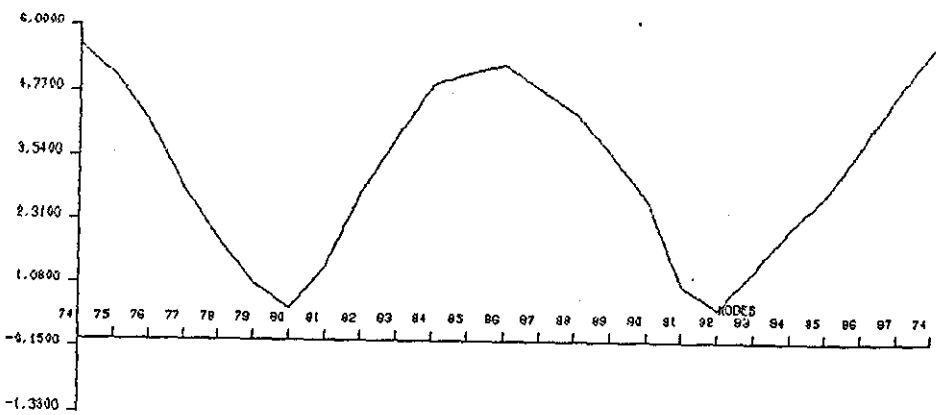

Figure 69. Von Mises stresses along the contour of the section 12 of the prosthesis F076 with the whole transition radius.

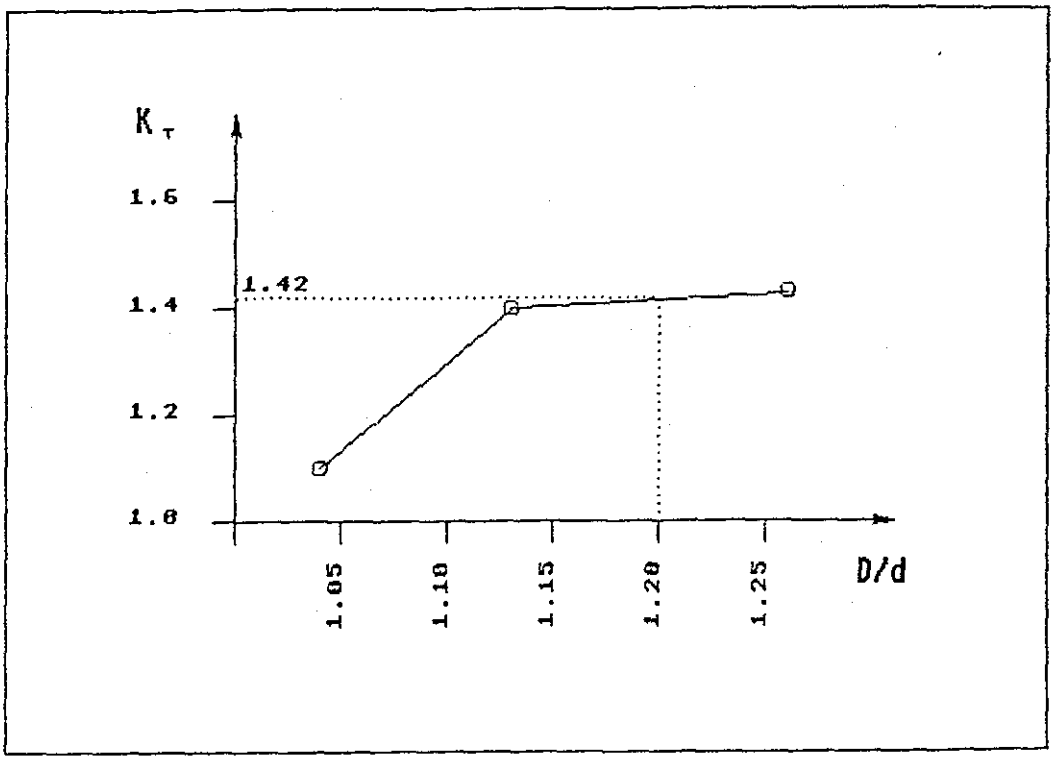

Figure 70. Stress concentration factors for the point 1 of the section 12 of the prosthesis F076.

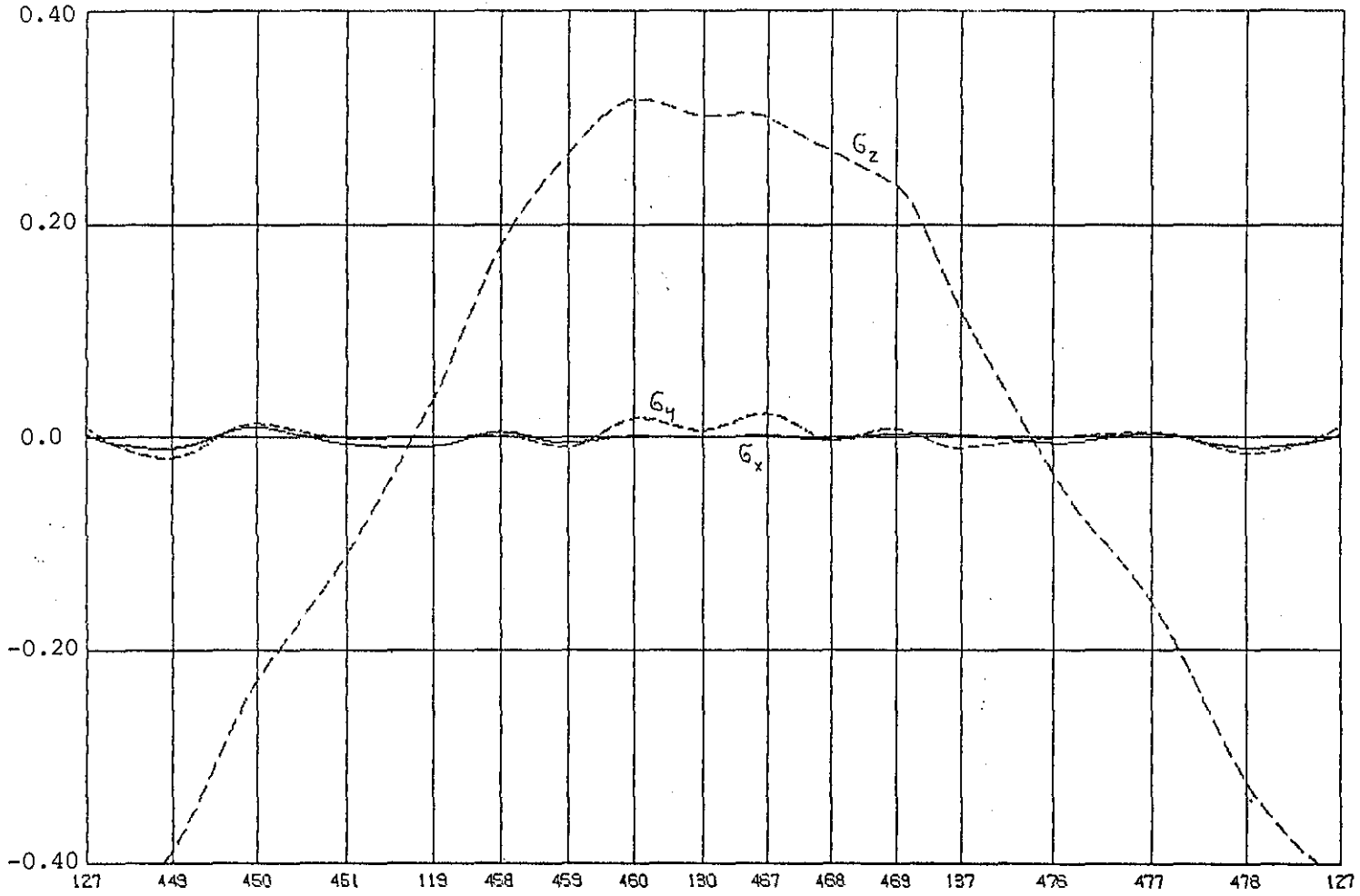

Figure 71. BEM-model. Direct stresses along the contour of a section above the embedding level.

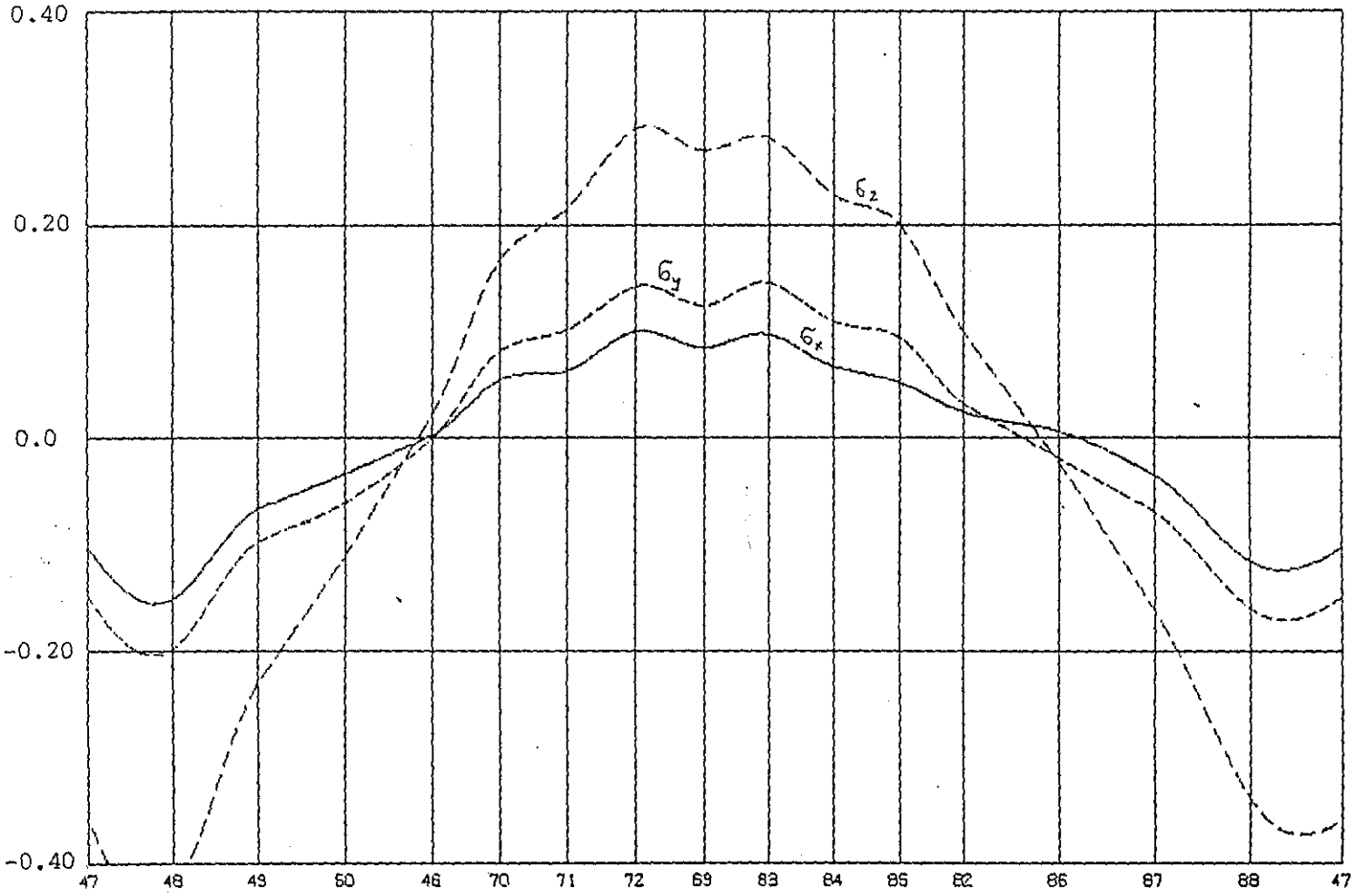

Figure 72. BEM-model. Direct stresses along the contour of a section at the embedding level.

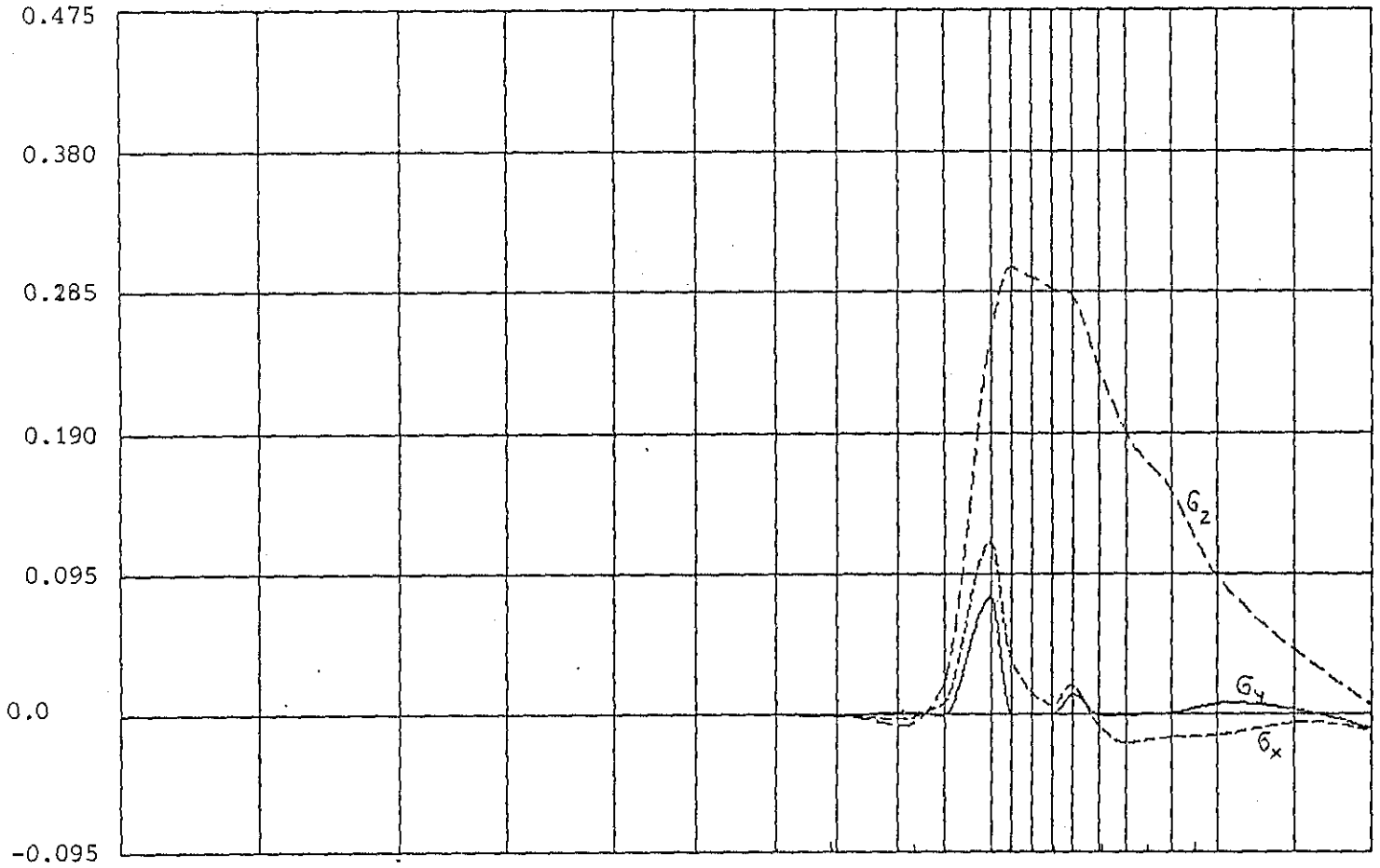

Figure 73. BEM-model. Direct stresses on the lateral (tension) side of the prosthesis F076.

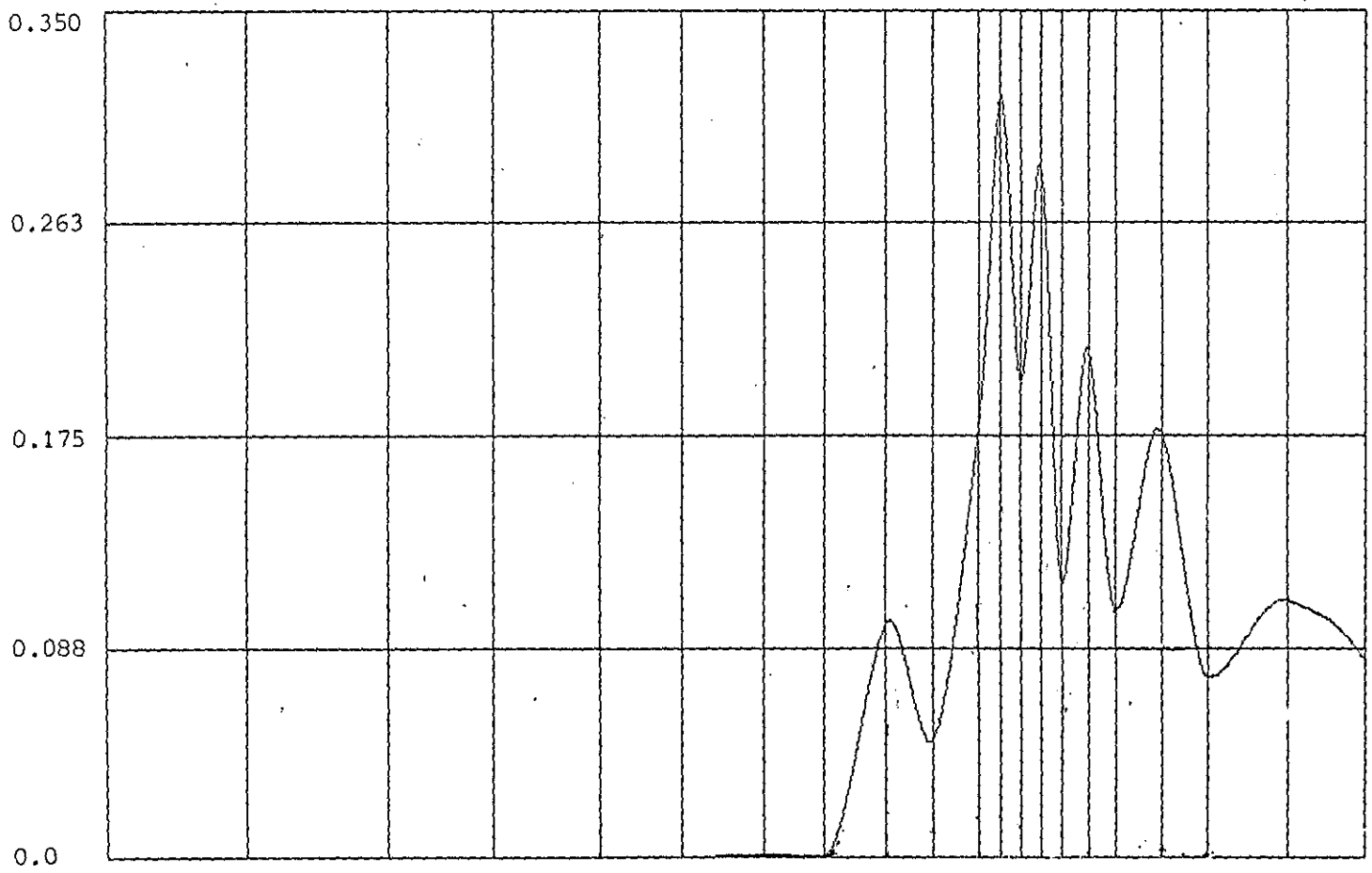

Figure 74. BEM-model. Von Mises stress on the lateral (tension) side of the prosthesis F076.

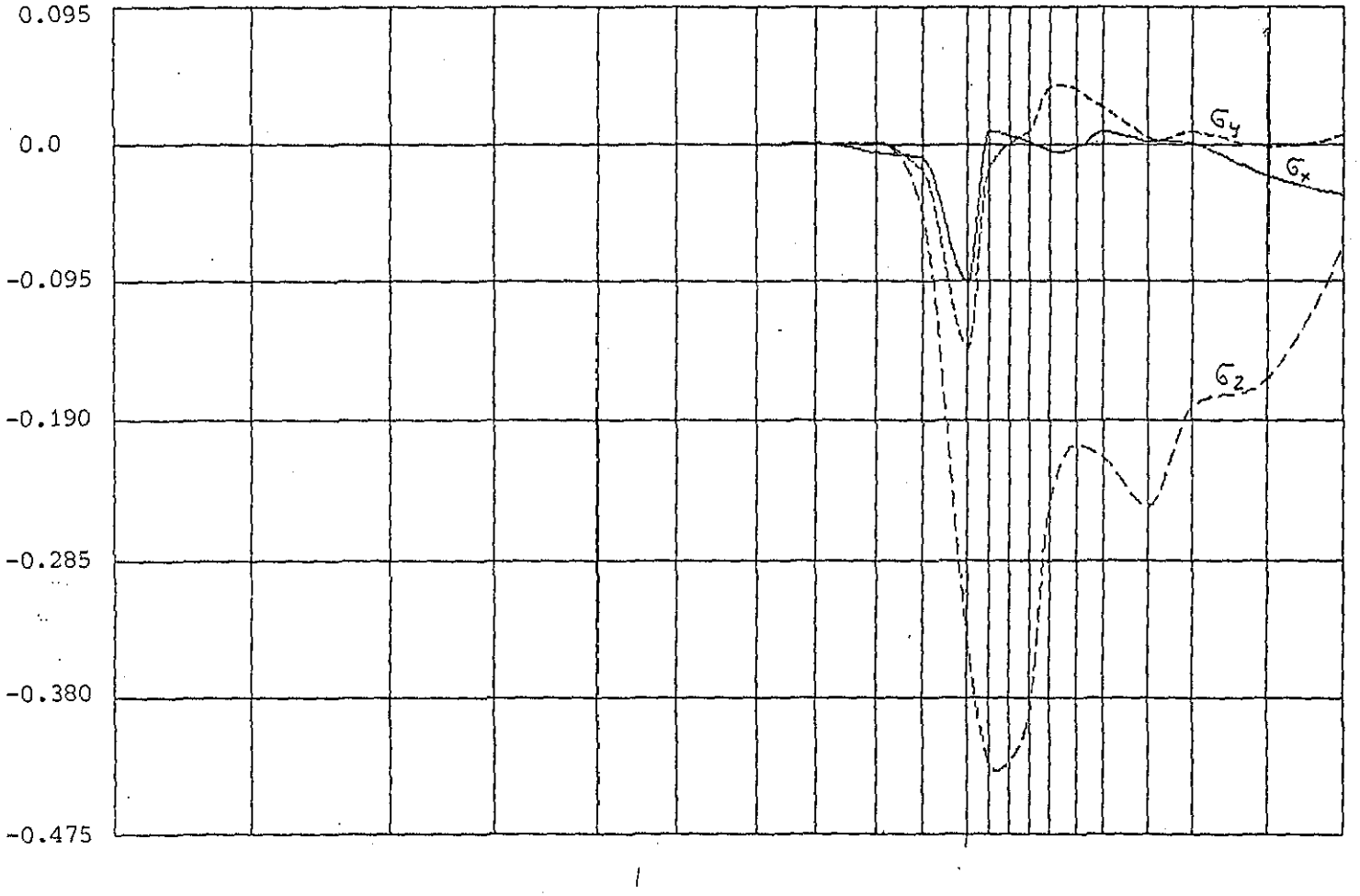

Figure 75. BEM-model. Direct stresses on the medial (compression) side of the prosthesis F076.

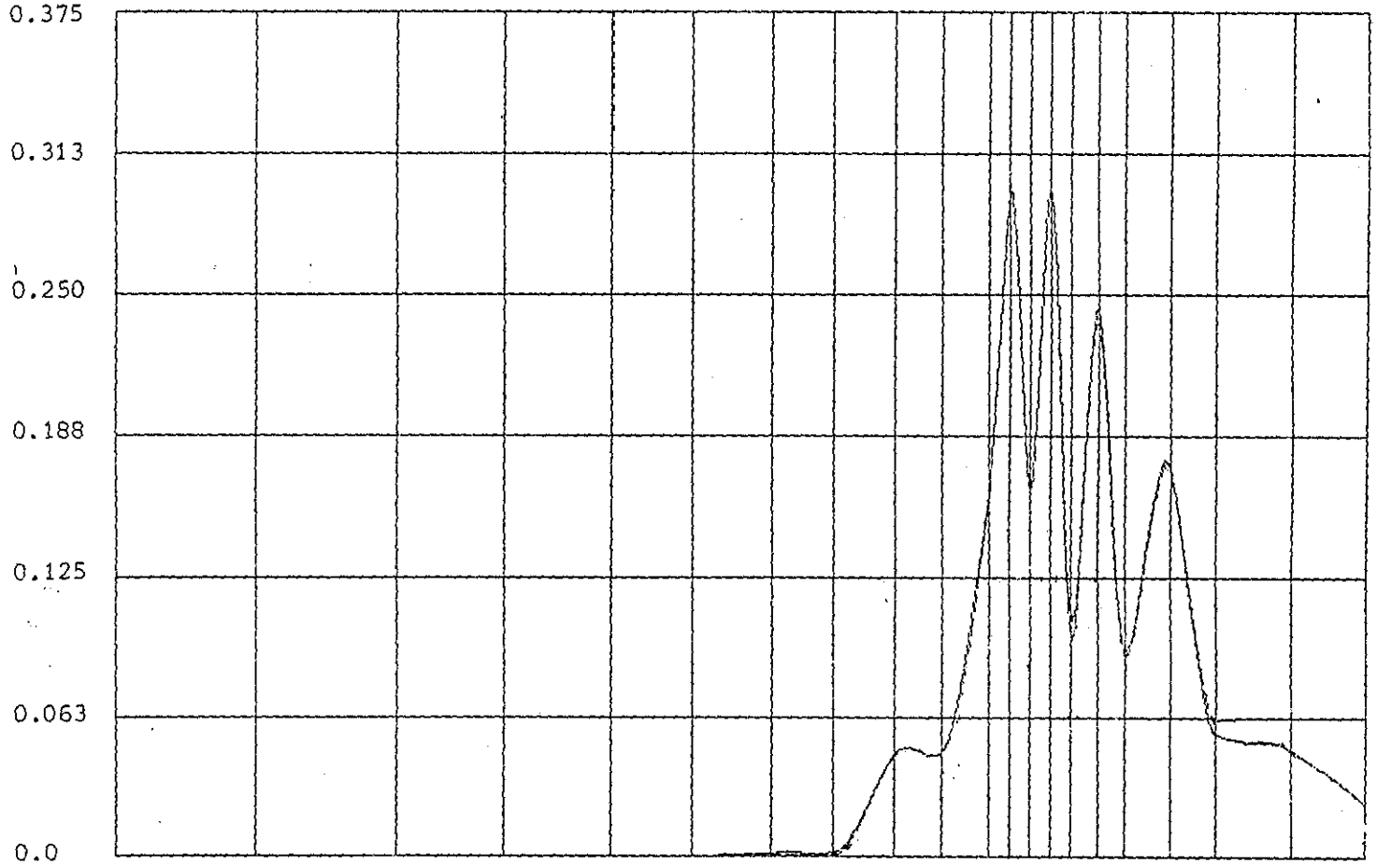

Figure 76. BEM-model. Von Mises stress on the medial (compression) side of the prosthesis F076.

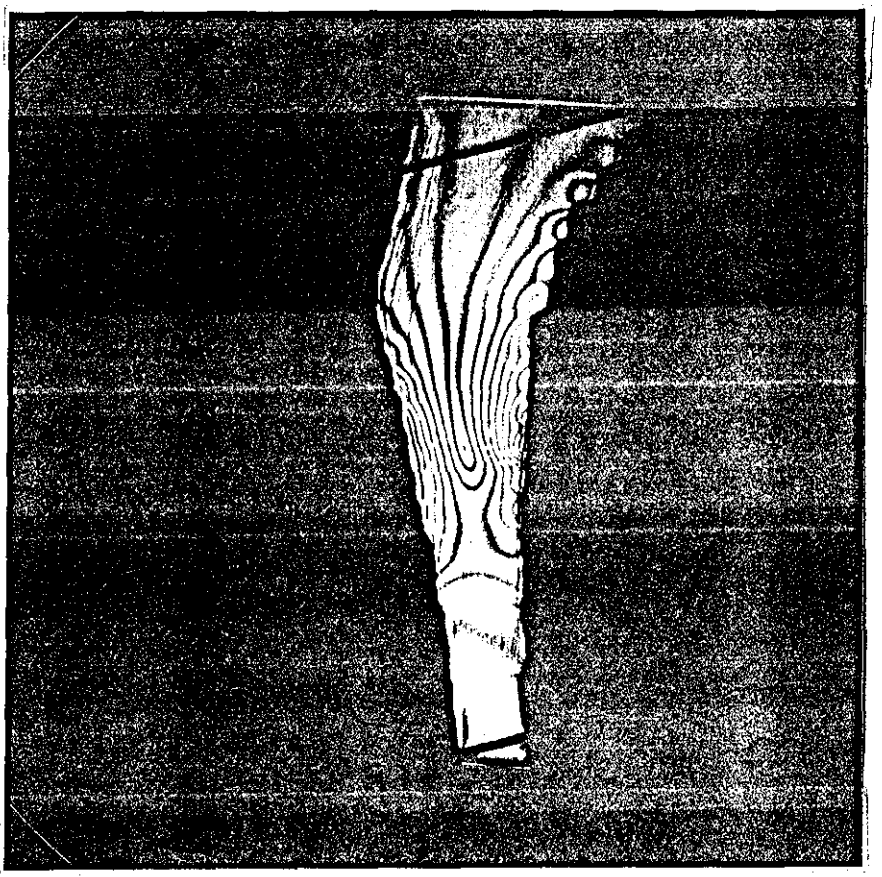

Figure 77. Example of a typical pattern of isochromatics in a slice machined from a photoelastic model of one of the prosthesis.

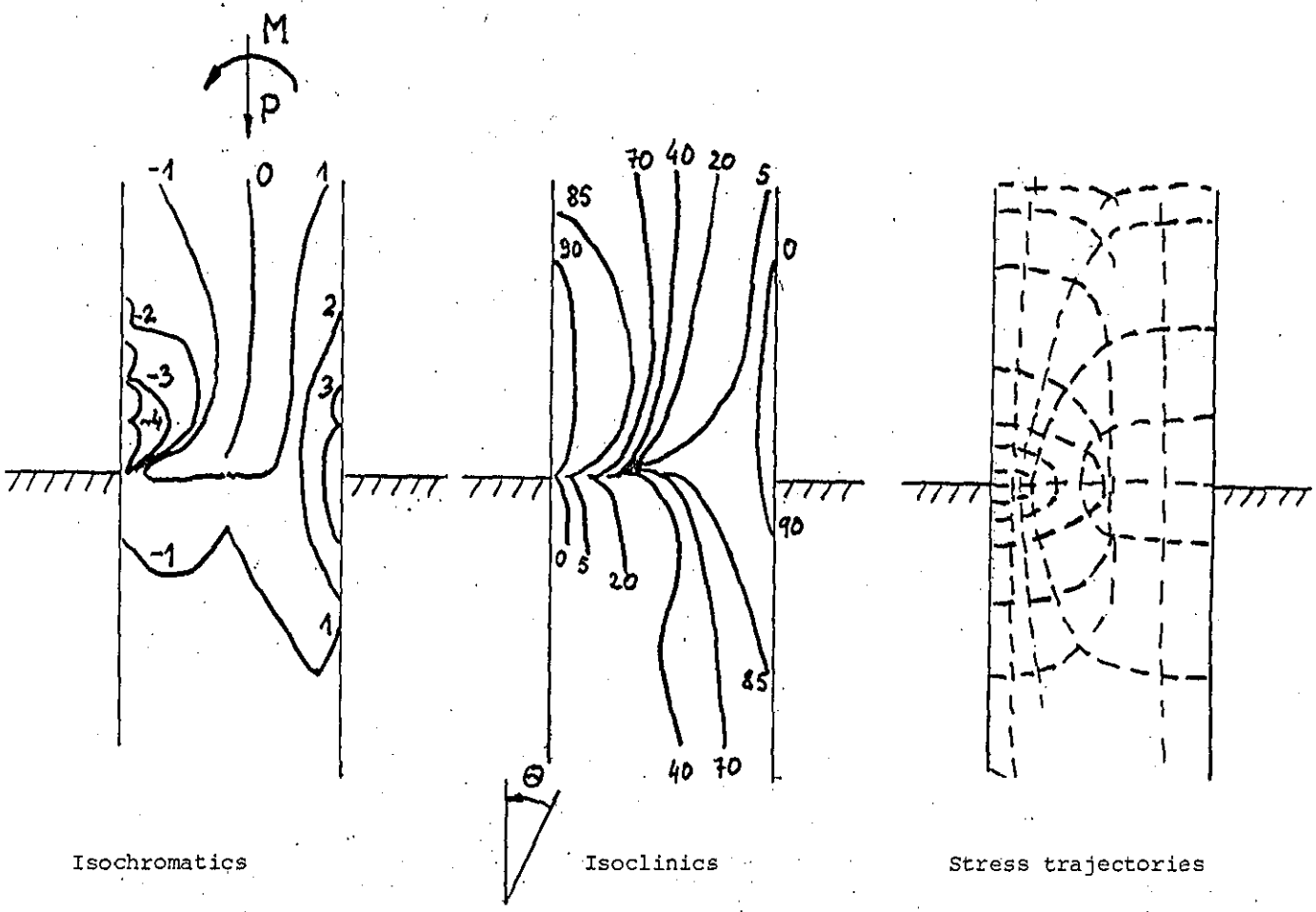

Figure 78. Schematic drawing of isochromatics, isoclinics and stress trajectories in a slice machined from a photoelastic model.

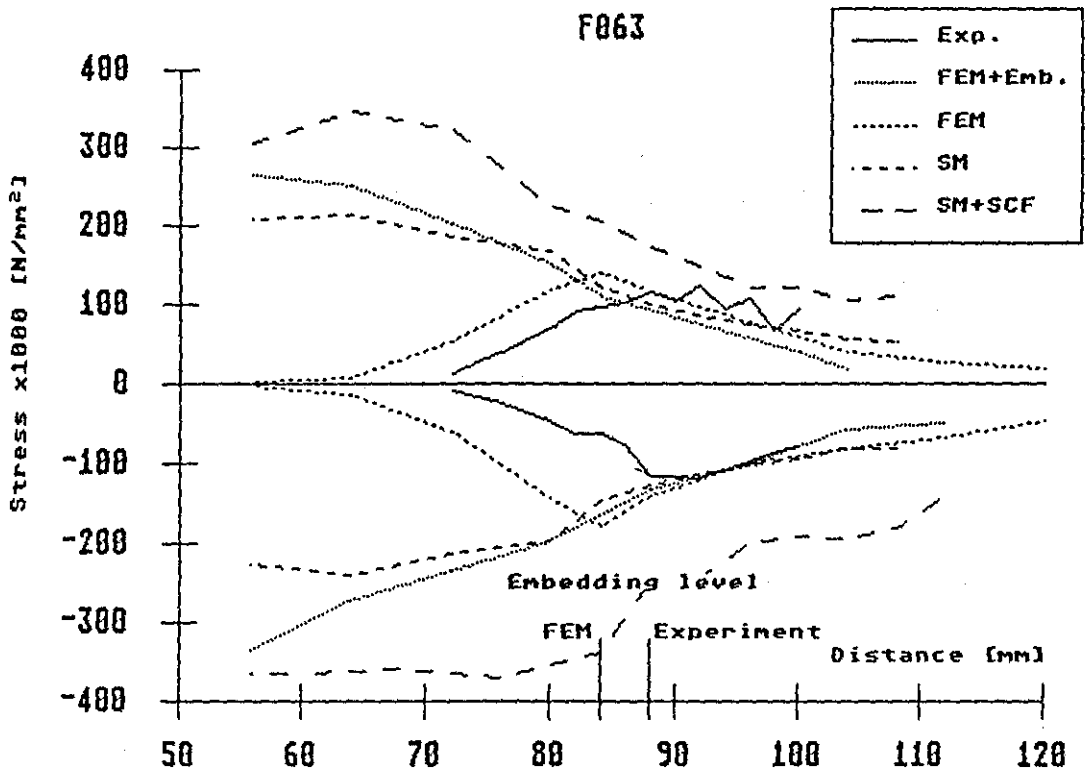

Figure 79. Comparison of the results from photoelastic experiments, the FEM-model and the simple model for the prosthesis F063.

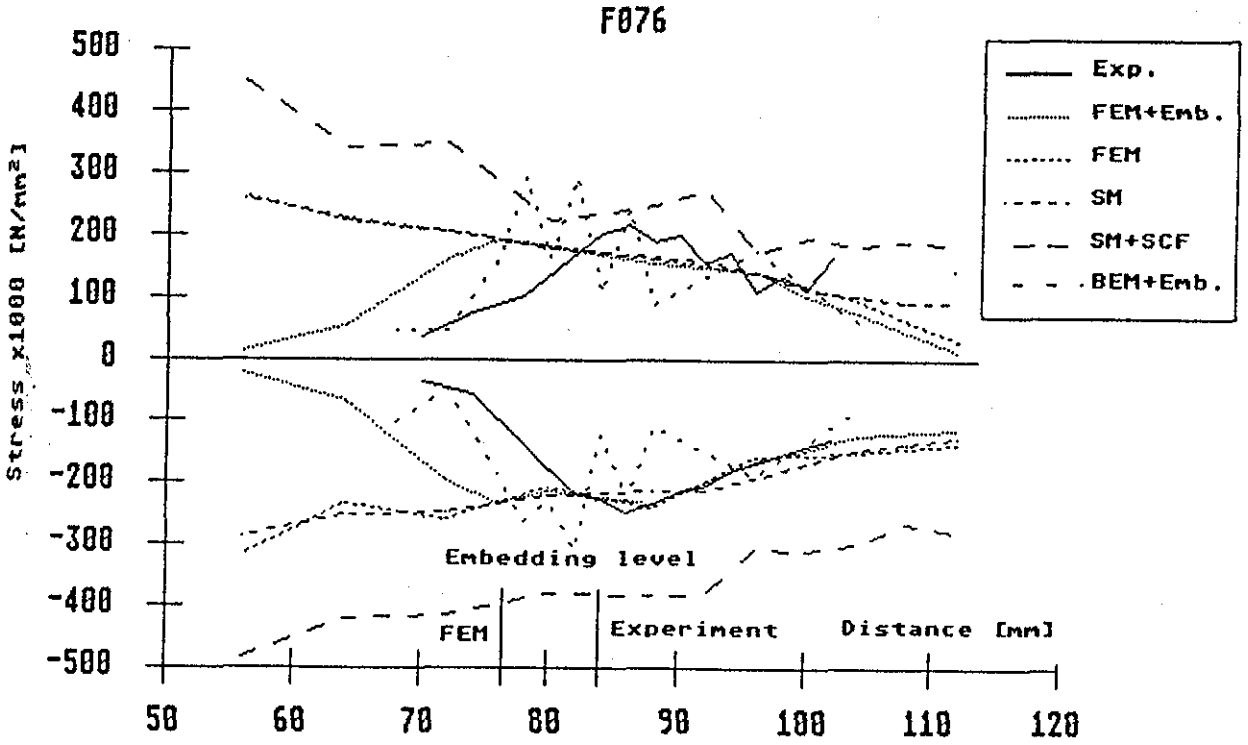

Figure 80. Comparison of the results from photoelastic experiments, the FEM-model, the BEM-model and the simple model for the prosthesis F076.

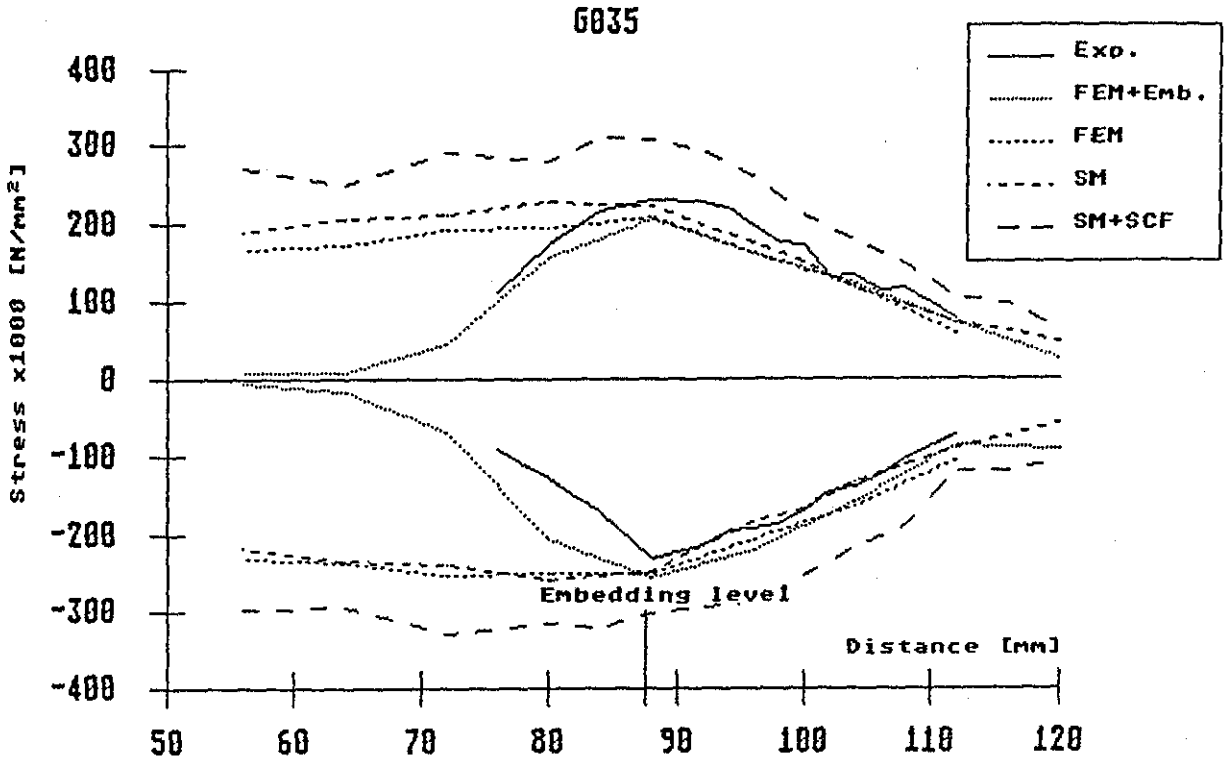

Figure 81. Comparison of the results from photoelastic experiments, the FEM-model and the simple model for the prosthesis G035.

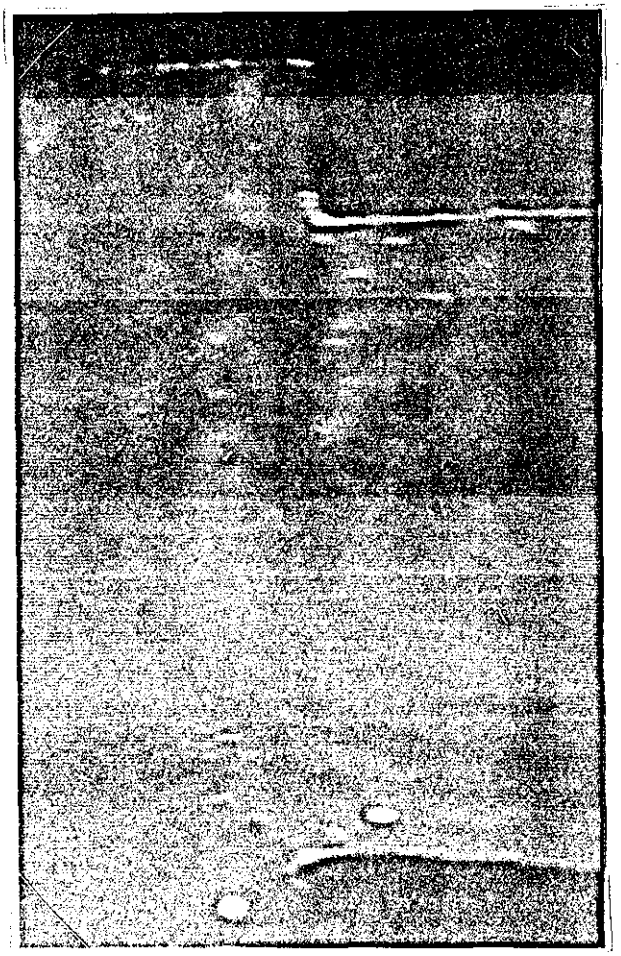

Figure 82. Example of a pattern observed with scattered-light photoelasticity. This pattern was obtained on concentric specimen with 5 mm fillet radius using a thin pencil of light propagating perpendicular to the surface of the specimen.

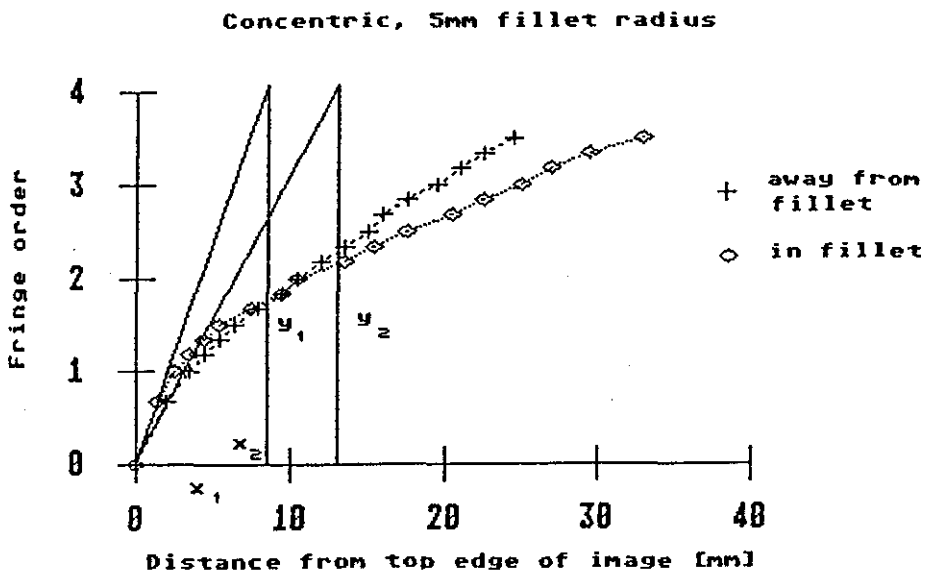

Figure 83. Example of the results obtained with scattered-light photoelasticity for one of the specimens.

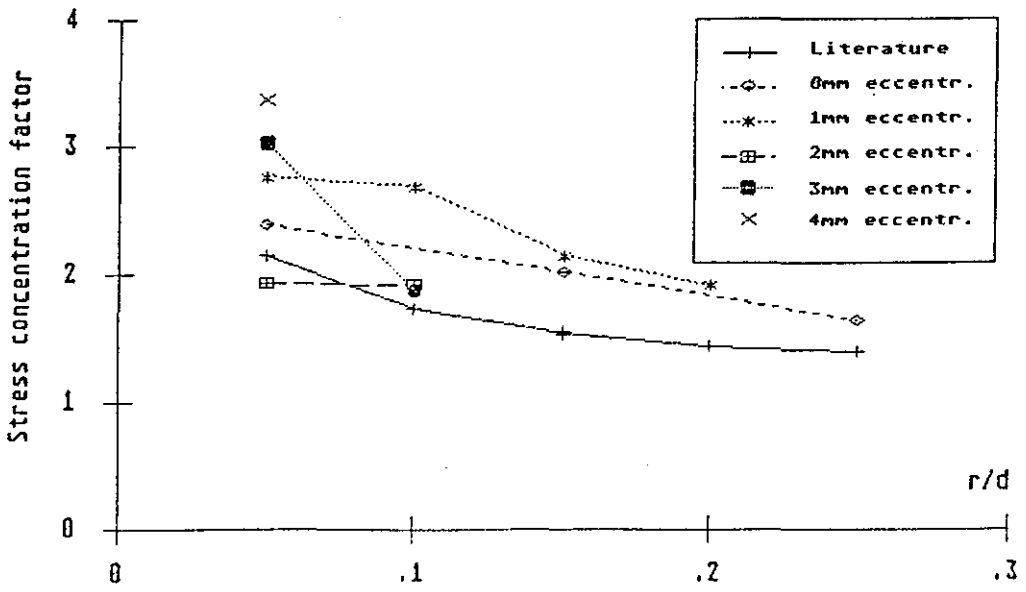

Figure 84. Stress concentration factors (K_T) obtained with scattered-light photoelasticity.

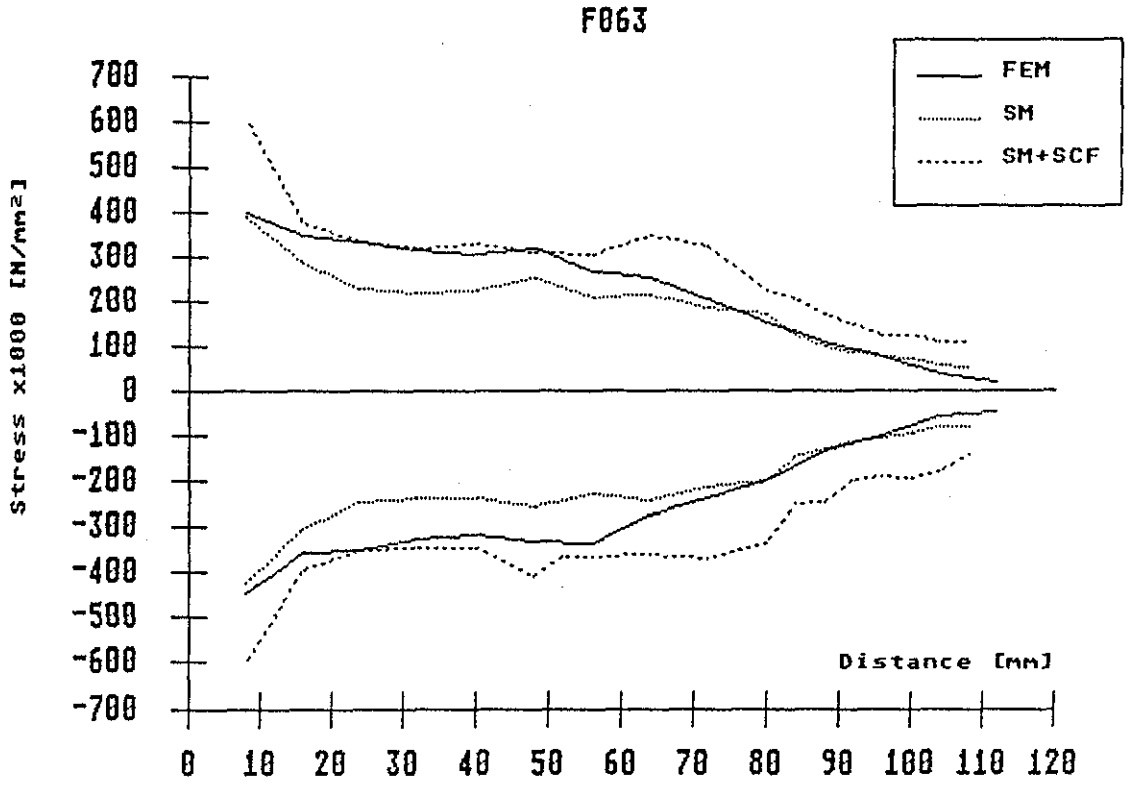

Figure 85. Comparison of the results from the FEM-model with that from the simple model for prosthesis F063 without the embedding.

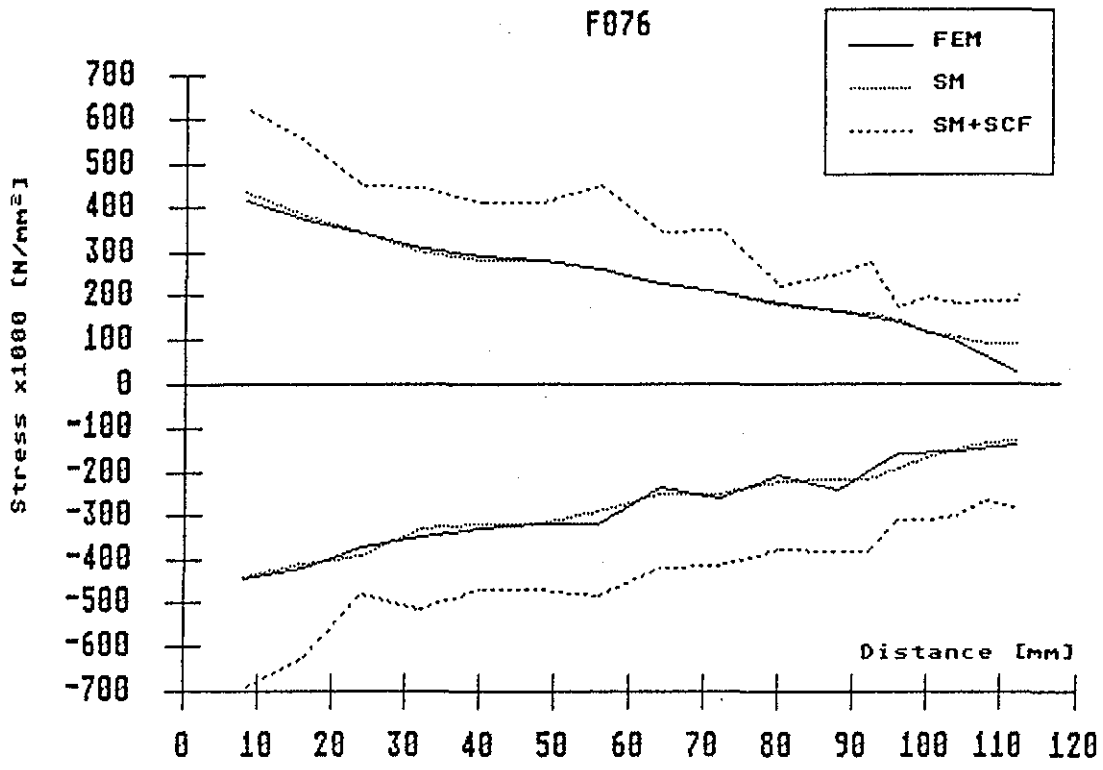

Figure 86. Comparison of the results from the FEM-model with that from the simple model for prosthesis F076 without the embedding.

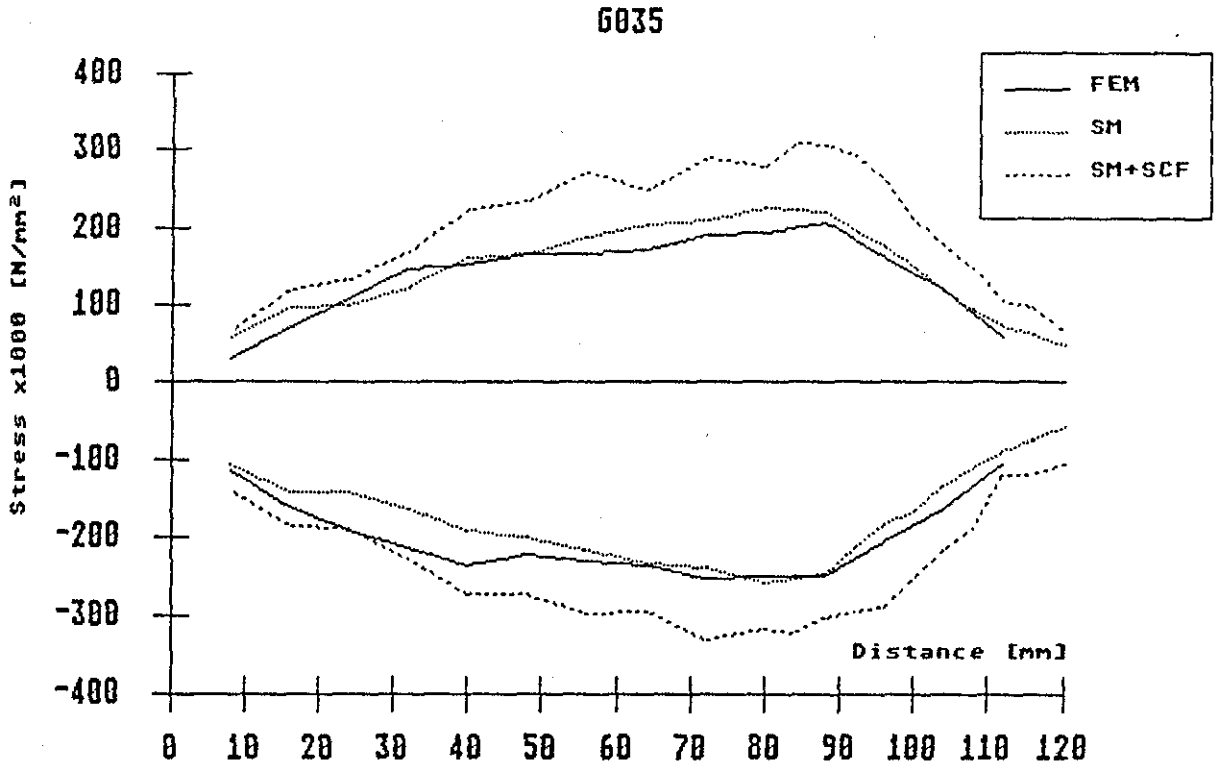

Figure 87. Comparison of the results from the FEM-model with that from the simple model for prosthesis G035 without the embedding.

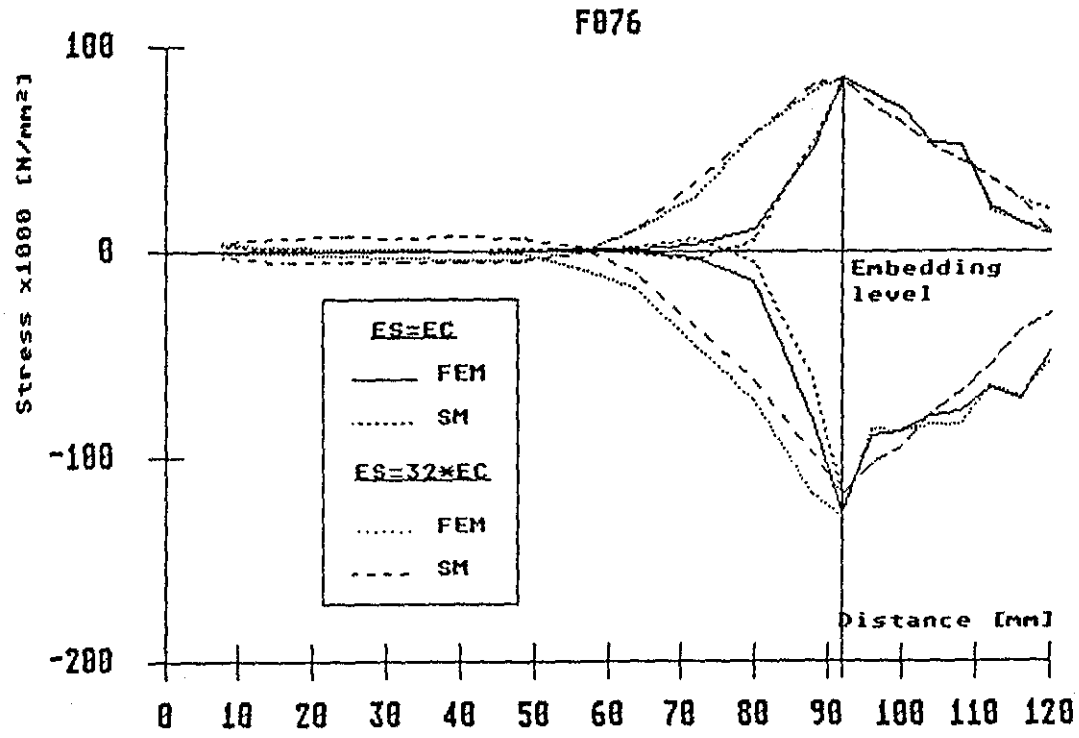

Figure 88. Comparison of the results form the simple model and the FEM-model. Different values of the modulus of elasticity of the embedding (EC) and of the prosthesis (ES).

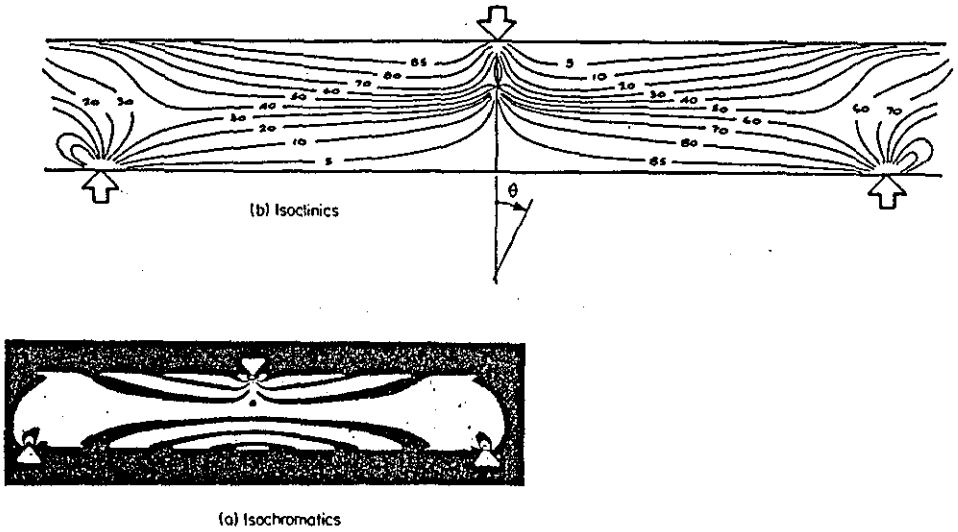

Figure 89. Isochromatics and isoclinics in a uniform bar subjected to three point bending [52].

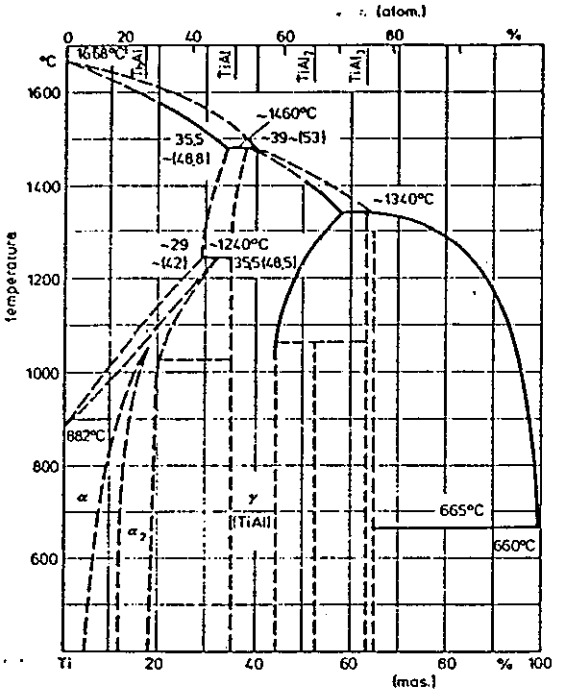

Figure 90. Phase diagram Ti-Al [60].

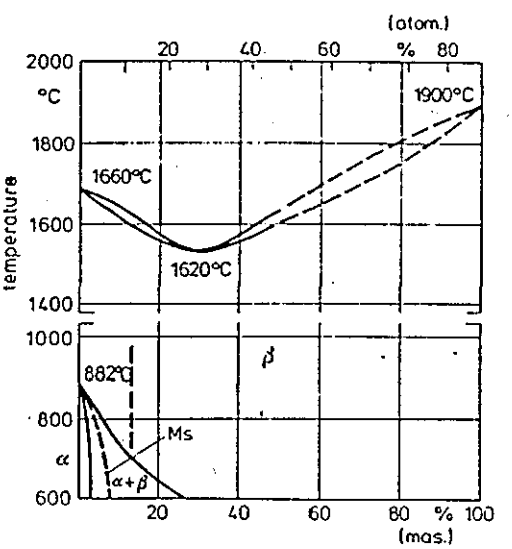

Figure 91. Phase diagram Ti-V [60].

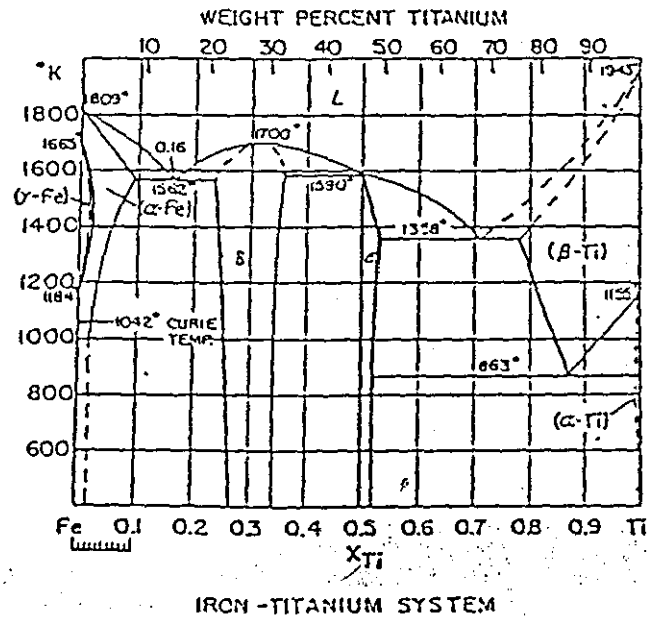

Figure 92. Phase diagram Fe-Ti.

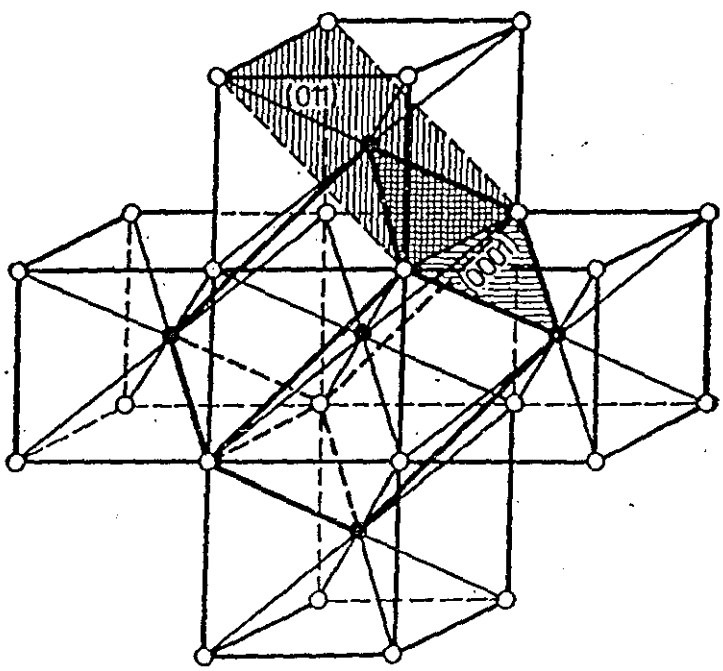

Figure 93. Orientations of unit cells Ti_α and Ti_β during the allotropic transformation [60].

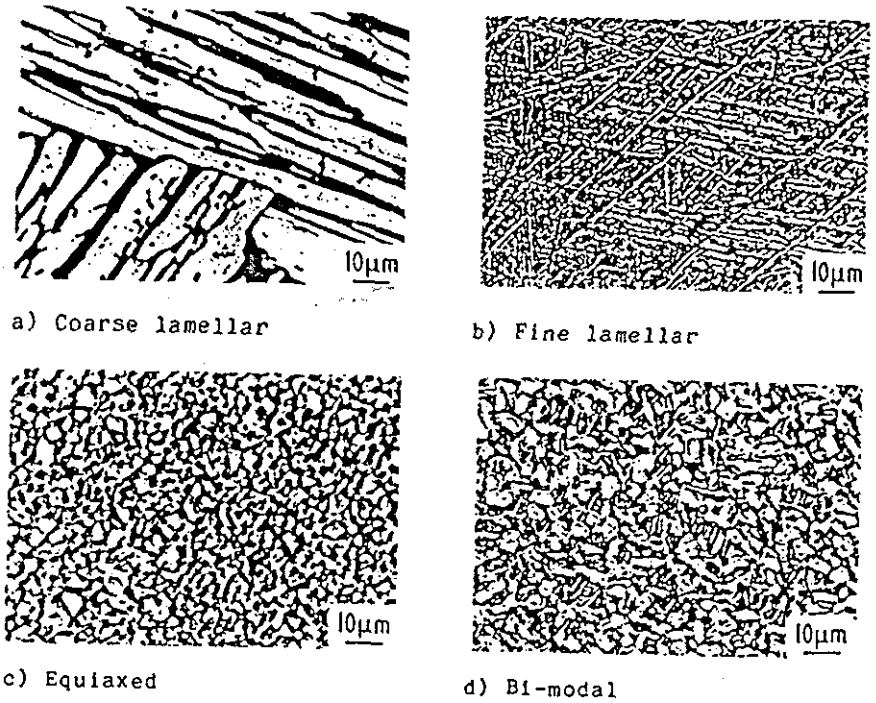

a) Coarse lamellar

b) Fine lamellar

c) Equiaxed

d) Bi-modal

Figure 94. Microstructures in Ti-6Al-4V [73].

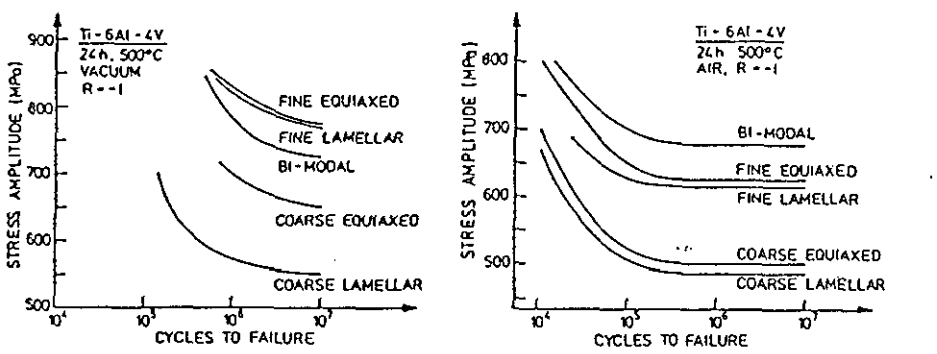

a) Vacuum tests

b) Air tests

Figure 95. Influence of different microstructures and test environments on HCF strength [73].

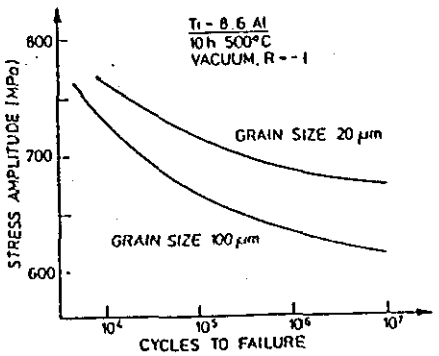

Figure 96. Influence of grain size on HCF strength [73].

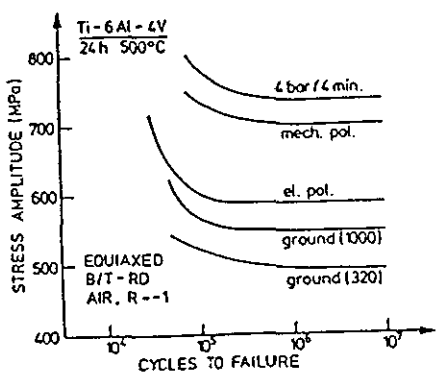

Figure 97. Influence of surface treatment on HCF strength [73].

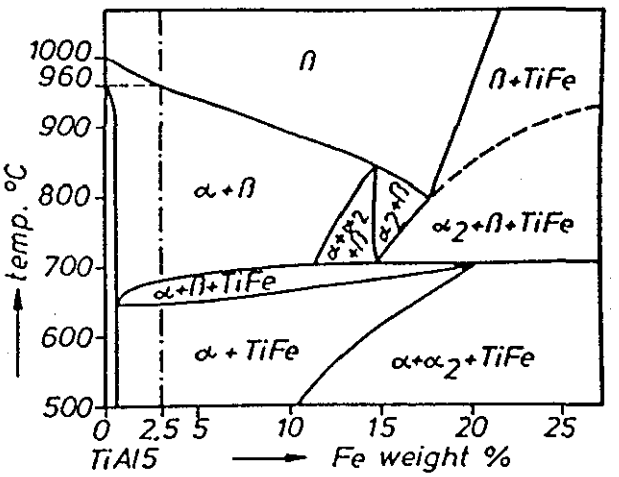

Figure 98. Concentration section of the Ti-5Al-2.5Fe-diagram at 5 % wt. Al [80].

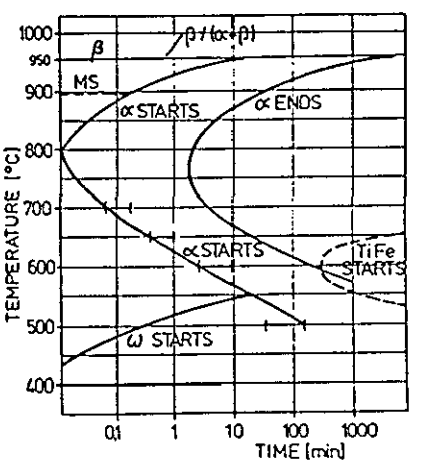

Figure 99. TTT-diagram of Ti-5Al-2.5Fe (schematically) [92].

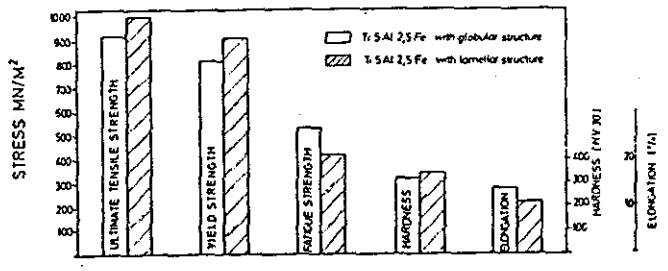

Figure 100. Mechanical properties of different Ti-5Al-2.5Fe microstructures [81].

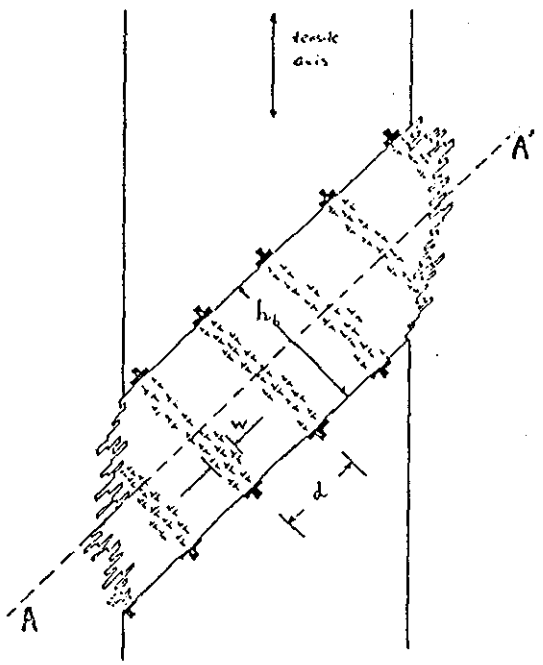

Figure 101. Schematic diagram of persistent slip band [96].

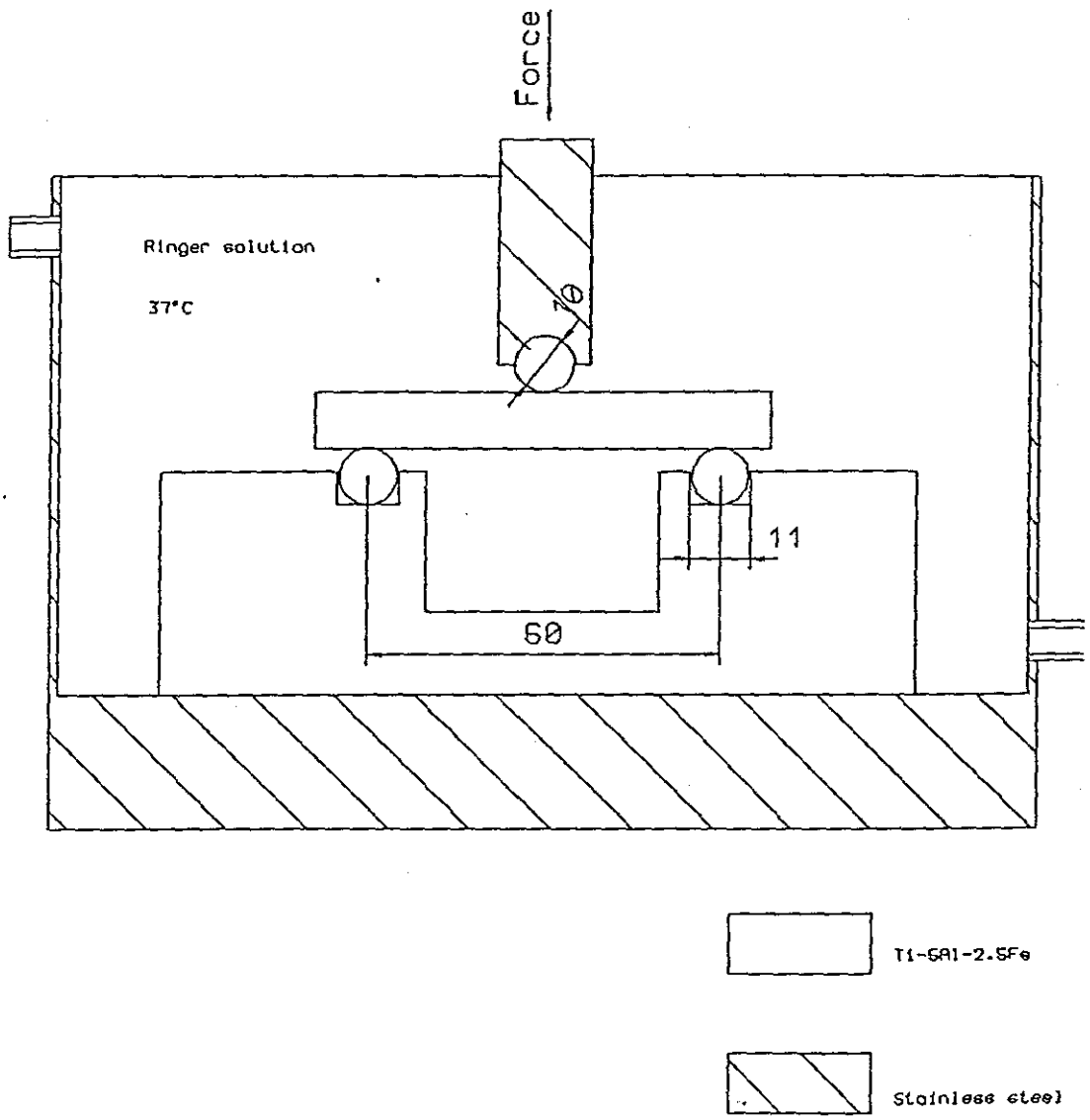

Figure 102. Schematic drawing of the testing rig.

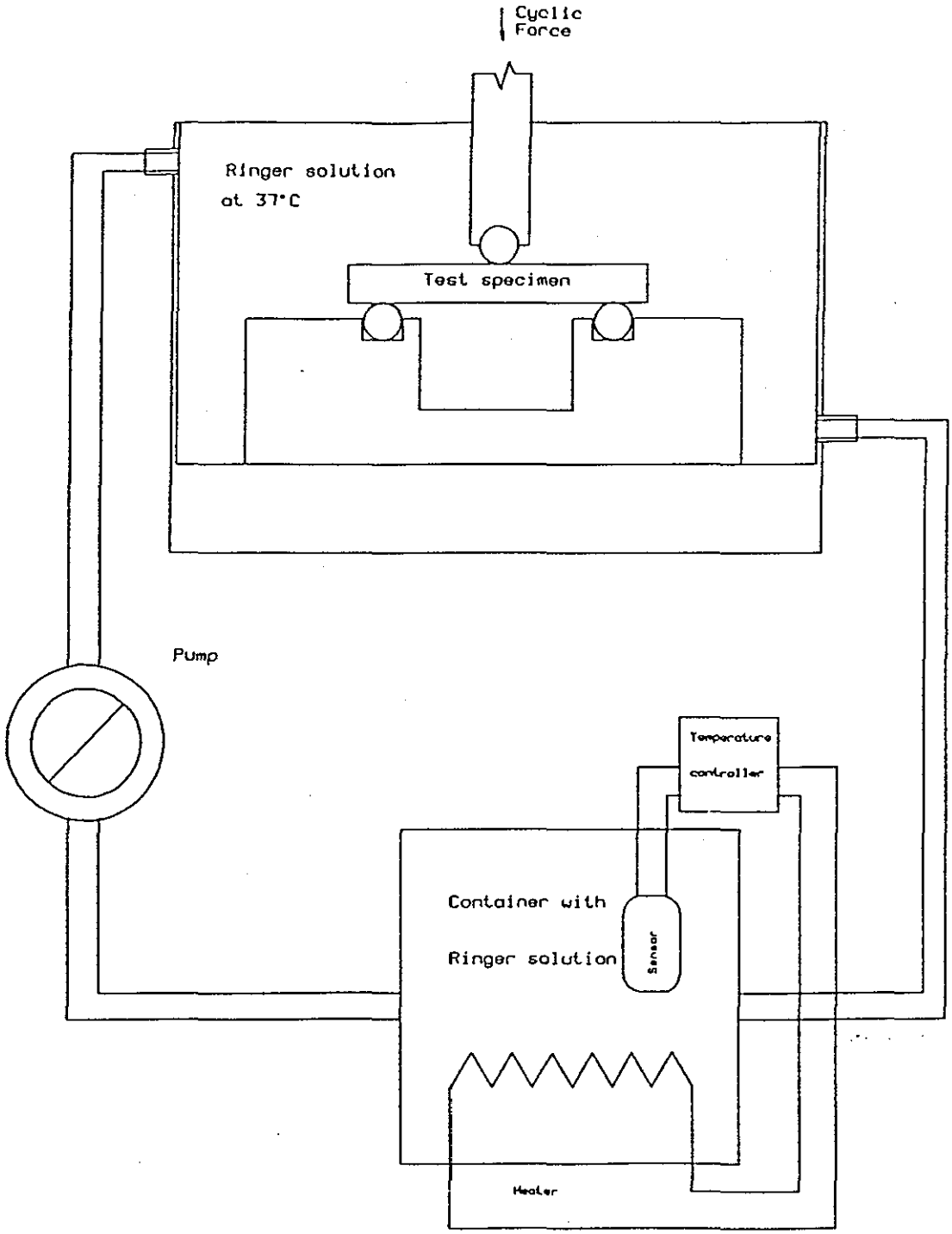

Figure 103. Schematic drawing of the set-up for mechanical testing of the material.

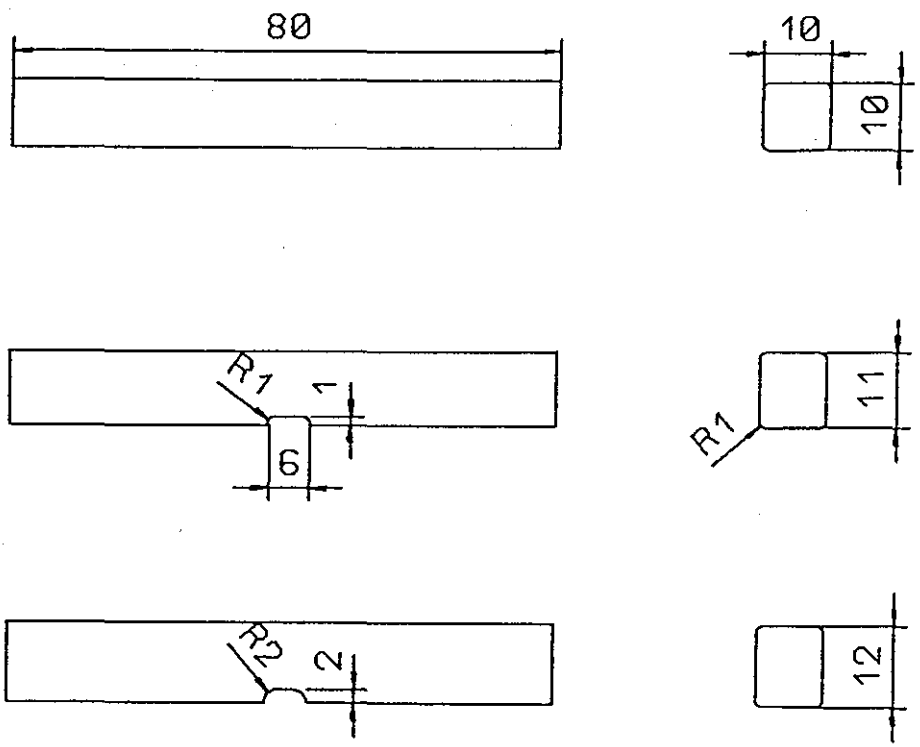

Figure 104. Shapes of the test specimens.

	Reflection	Burgers vectors of perfect dislocations ($\times\frac{1}{3}$)									
		$\pm[11\bar{2}0]$	$\pm[\bar{1}2\bar{1}0]$	$\pm[\bar{2}110]$	$\pm[11\bar{2}3]$	$\pm[\bar{1}2\bar{1}3]$	$\pm[\bar{2}113]$	$\pm[11\bar{2}\bar{3}]$	$\pm[\bar{1}2\bar{1}\bar{3}]$	$\pm[\bar{2}11\bar{3}]$	$\pm[0003]$
1	$10\bar{1}0$	±1	0	∓1	±1	0	∓1	±1	0	∓1	0
	$01\bar{1}0$	±1	±1	0	±1	±1	0	±1	±1	0	0
	$\bar{1}100$	0	±1	±1	0	±1	±1	0	±1	±1	0
2	0002	0	0	0	±2	±2	±2	∓2	∓2	∓2	±2
3	$10\bar{1}1$	±1	0	∓1	±2	±1	0	0	∓1	∓2	±1
	$10\bar{1}\bar{1}$	±1	0	∓1	0	∓1	∓2	±2	±1	0	∓1
	$01\bar{1}1$	±1	±1	0	±2	±2	±1	0	0	∓1	±1
	$01\bar{1}\bar{1}$	±1	±1	0	0	0	∓1	±2	±2	±1	∓1
	$\bar{1}101$	0	±1	±1	±1	±2	±2	∓1	0	0	±1
	$\bar{1}\bar{1}0\bar{1}$	0	±1	±1	∓1	0	0	±1	±2	±2	∓1
4	$10\bar{1}2$	±1	0	±1	±3	±2	±1	∓1	∓2	∓3	±2
	$10\bar{1}\bar{2}$	±1	0	±1	∓1	∓2	∓3	±3	±2	±1	∓2
	$01\bar{1}2$	±1	±1	0	±3	±3	±2	∓1	∓1	∓2	±2
	$01\bar{1}\bar{2}$	±1	±1	0	∓1	∓1	∓2	±3	±3	±2	∓2
	$\bar{1}102$	0	±1	±1	±2	±3	±3	∓2	∓1	∓1	±2
	$\bar{1}10\bar{2}$	0	±1	±1	∓2	∓1	∓1	±2	±3	±3	∓2
5	$11\bar{2}0$	±2	±1	∓1	±2	±1	∓1	±2	±1	∓1	0
	$\bar{1}2\bar{1}0$	±1	±2	±1	±1	±2	±1	±1	±2	±1	0
	$\bar{2}110$	∓1	±1	±2	∓1	±1	±2	∓1	±1	±2	0
6	$10\bar{1}3$	±1	0	∓1	±4	±3	±2	∓2	∓3	∓4	±3
	$10\bar{1}\bar{3}$	±1	0	∓1	∓2	∓3	∓4	±4	∓3	±2	∓3
	$01\bar{1}3$	±1	±1	0	±4	±4	±3	∓2	±4	∓3	±3
	$01\bar{1}\bar{3}$	±1	±1	0	∓2	∓2	∓3	±4	∓2	±3	∓3
	$\bar{1}103$	0	±1	±1	±3	±4	±4	∓3	±4	∓2	±3
	$\bar{1}10\bar{3}$	0	±1	±1	∓3	∓2	∓2	±3	∓2	±4	∓3
7	$11\bar{2}2$	±2	±1	∓1	±4	±3	±1	0	∓1	∓3	±2
	$11\bar{2}\bar{2}$	±2	∓1	∓1	0	∓1	∓3	±4	±3	±1	∓2
	$\bar{1}2\bar{1}2$	±1	±2	±1	±3	±4	±3	∓1	0	∓1	±2
	$\bar{1}2\bar{1}\bar{2}$	±1	±2	±1	∓1	0	∓1	±3	0	±3	∓2
	$\bar{2}112$	∓1	±1	±2	±1	±3	±4	∓3	±3	0	±2
	$\bar{2}11\bar{2}$	∓1	±1	±2	∓3	∓1	0	±1	±1	±4	∓2

Figure 105. Values of $g \cdot b$ for the first seven reflections in the chp crystal structure [112].

Maximum load F_{max} [N]	Mean load F_{mean} [N]	Maximum stress σ_{max} [N/mm²]	Number of cycles N * 1000
8000	4200	720	47.7
8000	4200	720	44.5
7000	3675	630	47.0
7000	3675	630	84.1
7000	3675	630	63.4
6500	3413	585	124.4
6500	3413	585	51.1
6250	3281	562	21 414.0*
6250	3281	562	22 588.4*
6250	3281	565	20 112.0*
6000	3150	540	20 020.0*
6000	3150	540	20 829.8*
6000	3150	540	20 100.0*

* - did not break

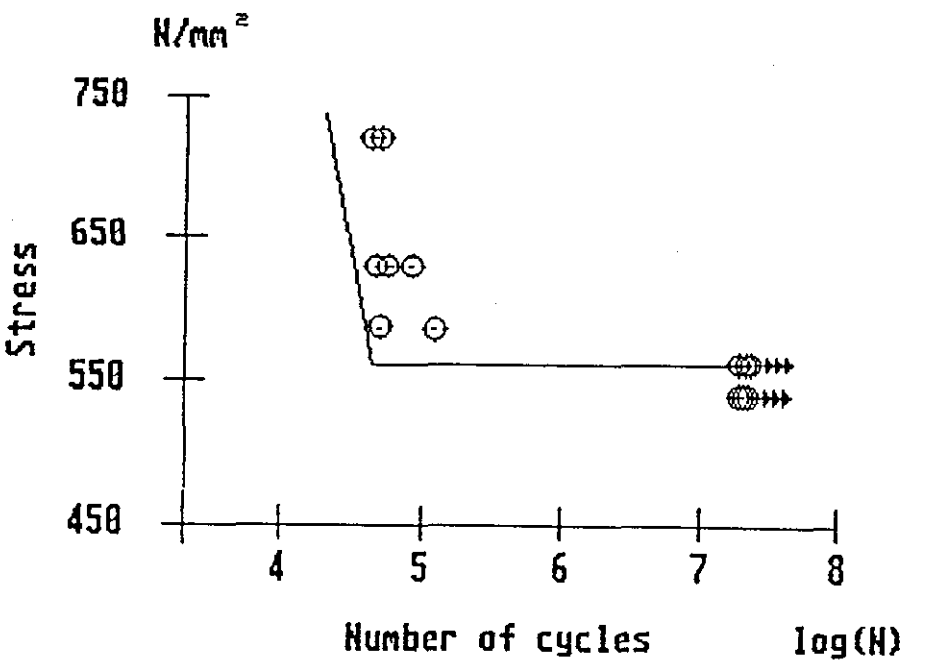

Figure 106. Results of fatigue testing. As-delivered material with machined surface.

Maximum load F_{max} [N]	Mean load F_{mean} [N]	Maximum stress σ_{max} [N/mm²]	Number of cycles N * 1000
6000	3150	540	11.1
6000	3150	540	12.0
5500	2863	495	42.1
5500	2863	495	24.7
5500	2863	495	39.8
5000	2625	450	140.3
5000	2625	450	146.8
5000	2625	450	245.3
4725	2481	425	4 839.5
4500	2363	405	10 122.2*
4500	2363	405	10 540.4*
4500	2363	405	10 645.6*

* - did not break

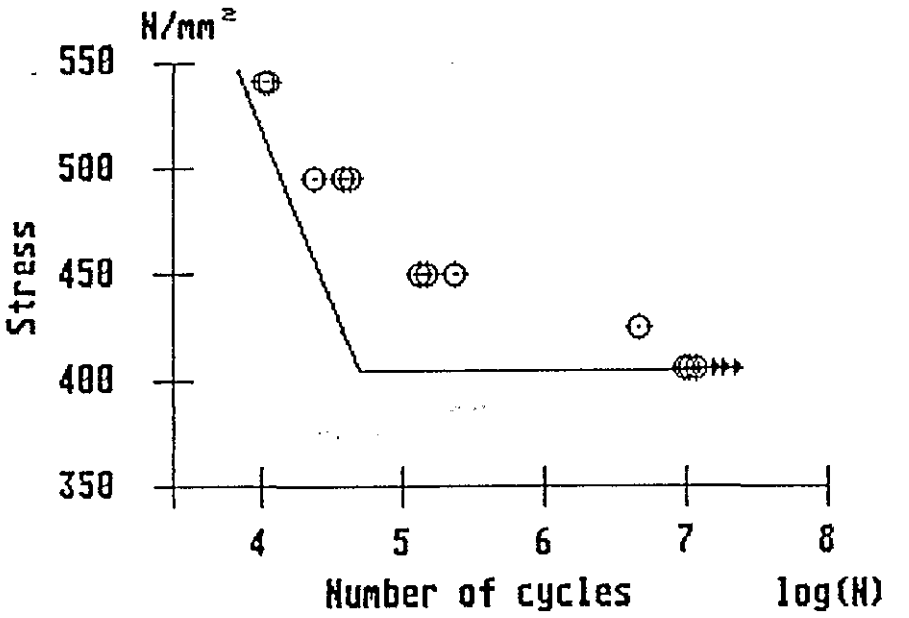

Figure 107. Results of fatigue testing. As-delivered material with 2 mm notch.

Maximum load F_{max} [N]	Mean load F_{mean} [N]	Maximum stress σ_{max} [N/mm²]	Number of cycles N * 1000
6000	3150	540	13.2
5500	2863	495	38.8
5500	2863	495	34.3
5000	2625	450	34.4
4500	2363	405	79.8
4500	2363	405	73.4
4500	2363	405	49.6
4000	2100	360	124.2
4000	2100	360	169.5
4000	2100	360	10 608.7*
3500	1838	315	10 372.5*
3500	1863	315	10 611.0*
3500	1863	315	24 030.1*

* - did not break

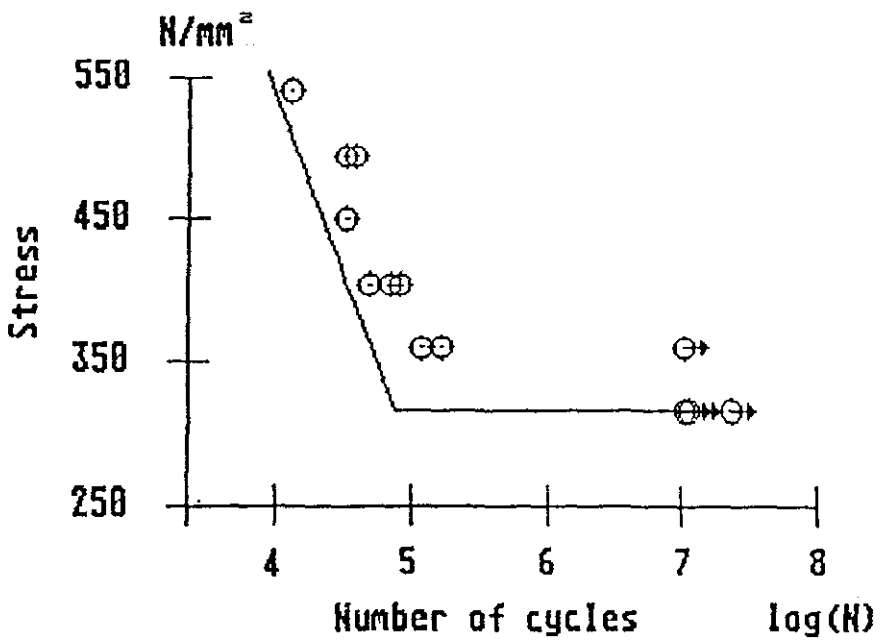

Figure 108. Results of fatigue testing. As-delivered material with 1 mm notch.

Maximum load F_{max} [N]	Mean load F_{mean} [N]	Maximum stress σ_{max} [N/mm²]	Number of cycles N * 1000
10000	5250	900	42.6
10000	5250	900	44.0
9000	4725	810	7 977.6
9000	4725	810	71.9
9000	4725	810	179.5
8750	4593	787	12 432.9*
8750	4593	787	2 826.0
8500	4463	765	12 526.7*
8500	4463	765	993.4
8000	4200	720	14 877.8*
8000	4200	720	15 037.1*
8000	4200	720	16 637.9*

* - did not break

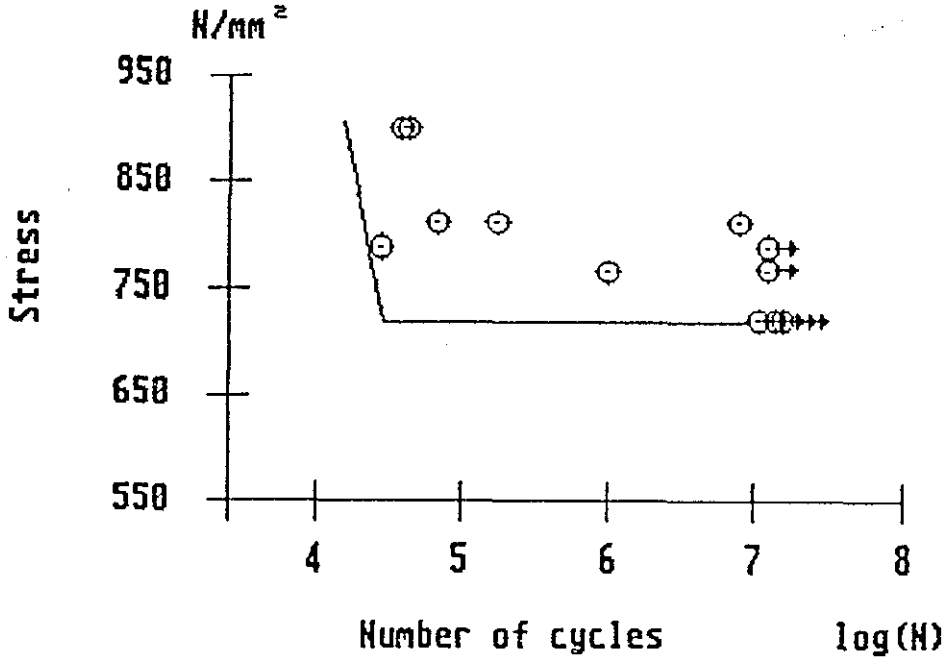

Figure 109. Results of fatigue testing. As-delivered material with brushed surface.

Maximum load F_{max} [N]	Mean load F_{mean} [N]	Maximum stress σ_{max} [N/mm²]	Number of cycles N * 1000
9500	5000	855	173.2
9500	5000	855	215.0
9000	4725	810	10 371.1*
9000	4725	810	128.0
9000	4725	810	115.0
8750	4593	787	193.3
8750	4593	787	163.3
8750	4593	787	10 191.3*
8500	4463	765	12 422.8*
8500	4463	765	12 619.7*
8500	4463	765	10 129.2*
8000	4200	720	10 994.0*
8000	4200	720	12 323.8*
8000	4200	720	11 944.0*

* - did not break

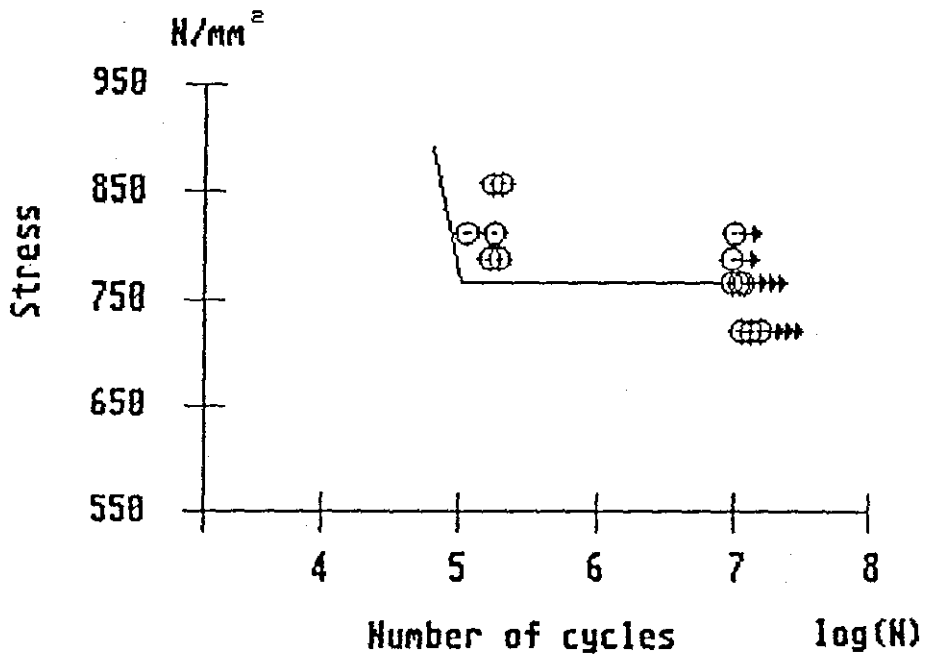

Figure 110. Results of fatigue testing. Heat-treated material with brushed surface.

Maximum load F_{max} [N]	Mean load F_{mean} [N]	Maximum stress σ_{max} [N/mm²]	Number of cycles N * 1000
10000	5250	900	6 350.9
10000	5250	900	112.8
9500	5000	855	12 328.7*
9500	5000	855	12 817.1*
9500	5000	855	279.7
9500	5000	855	346.7
9000	4725	810	10 023.2*
9000	4725	810	11 799.4*
9000	4725	810	12 360.9*
9000	4725	810	12 430.9*
8500	4463	765	12 351.2*
8000	4200	720	12 757.4*

* - did not break

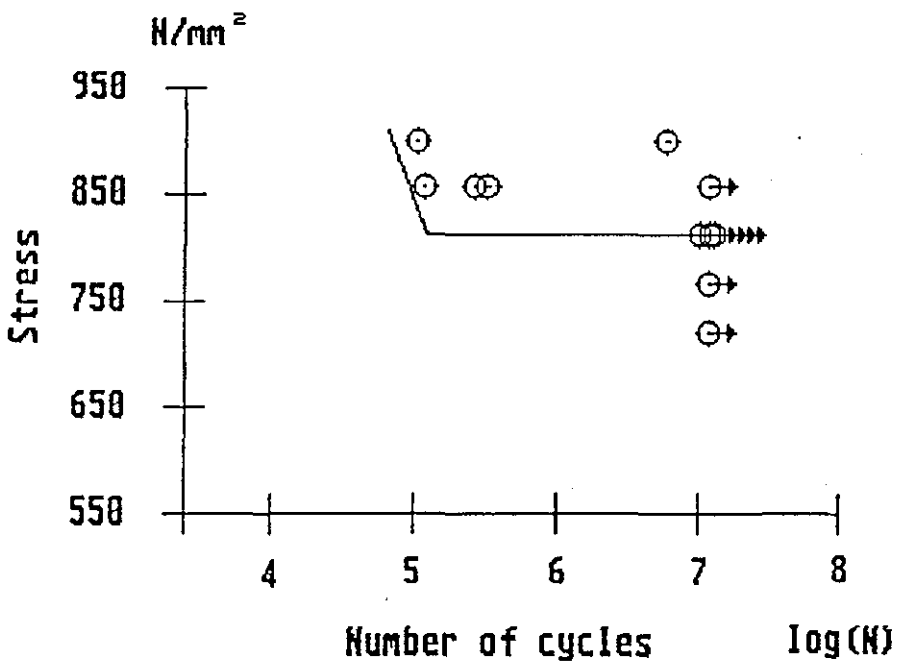

Figure 111. Results of fatigue testing. As-delivered material with brushed surface and without the Ringer's solution.

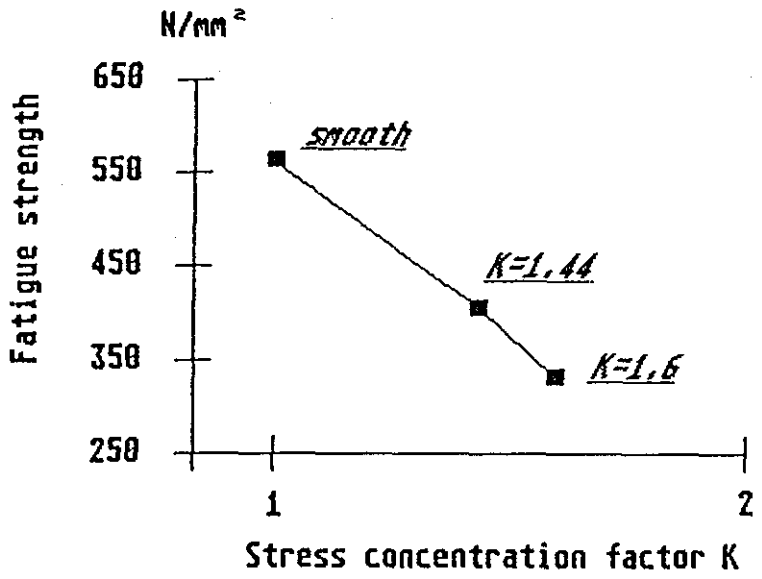

Figure 112. Influence of stress concentration factor on fatigue strength of Ti-5Al-2.5Fe (in Ringer's solution at 37°C).

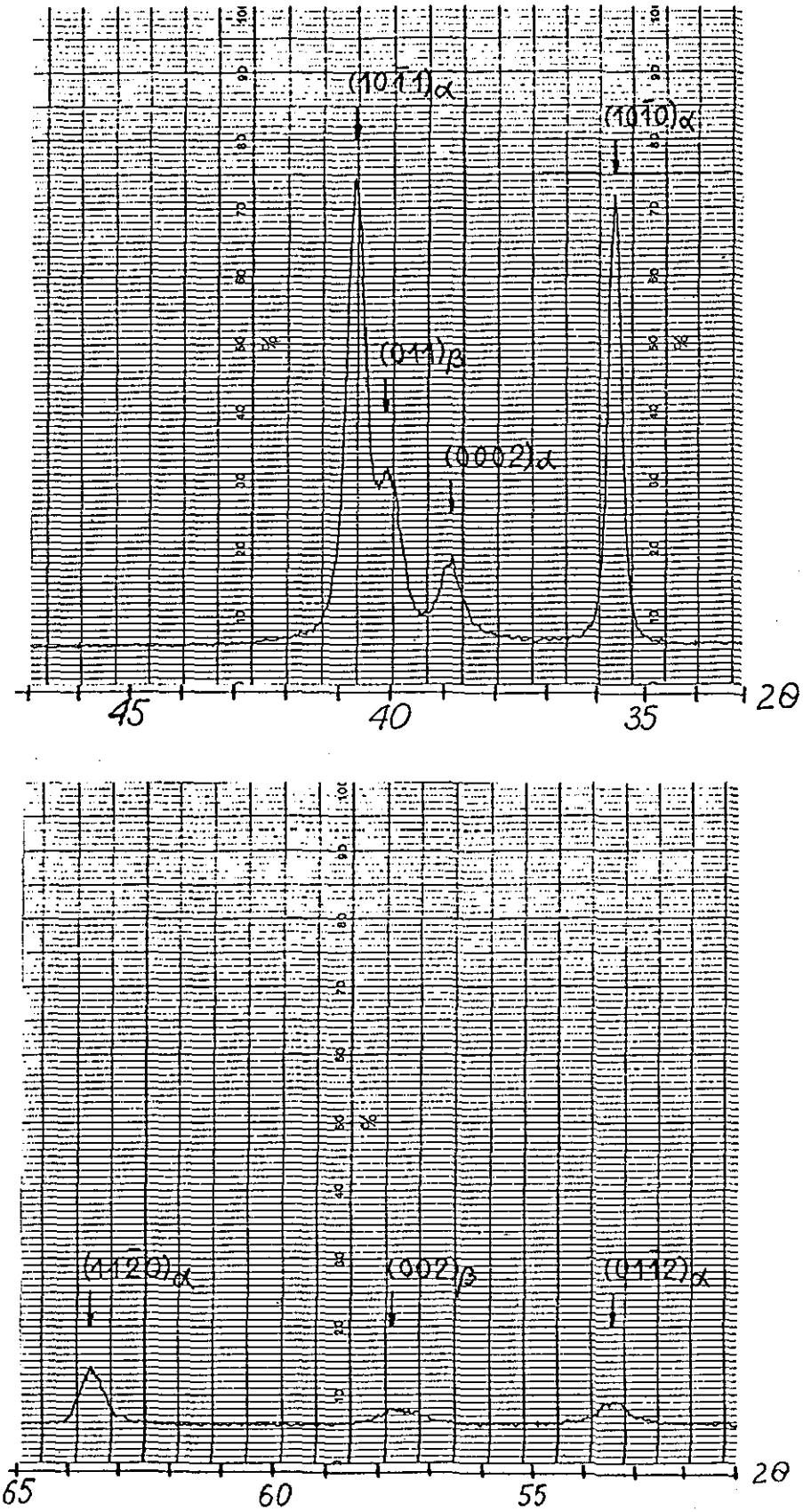

Figure 113. X-ray spectrum of the as-delivered material.

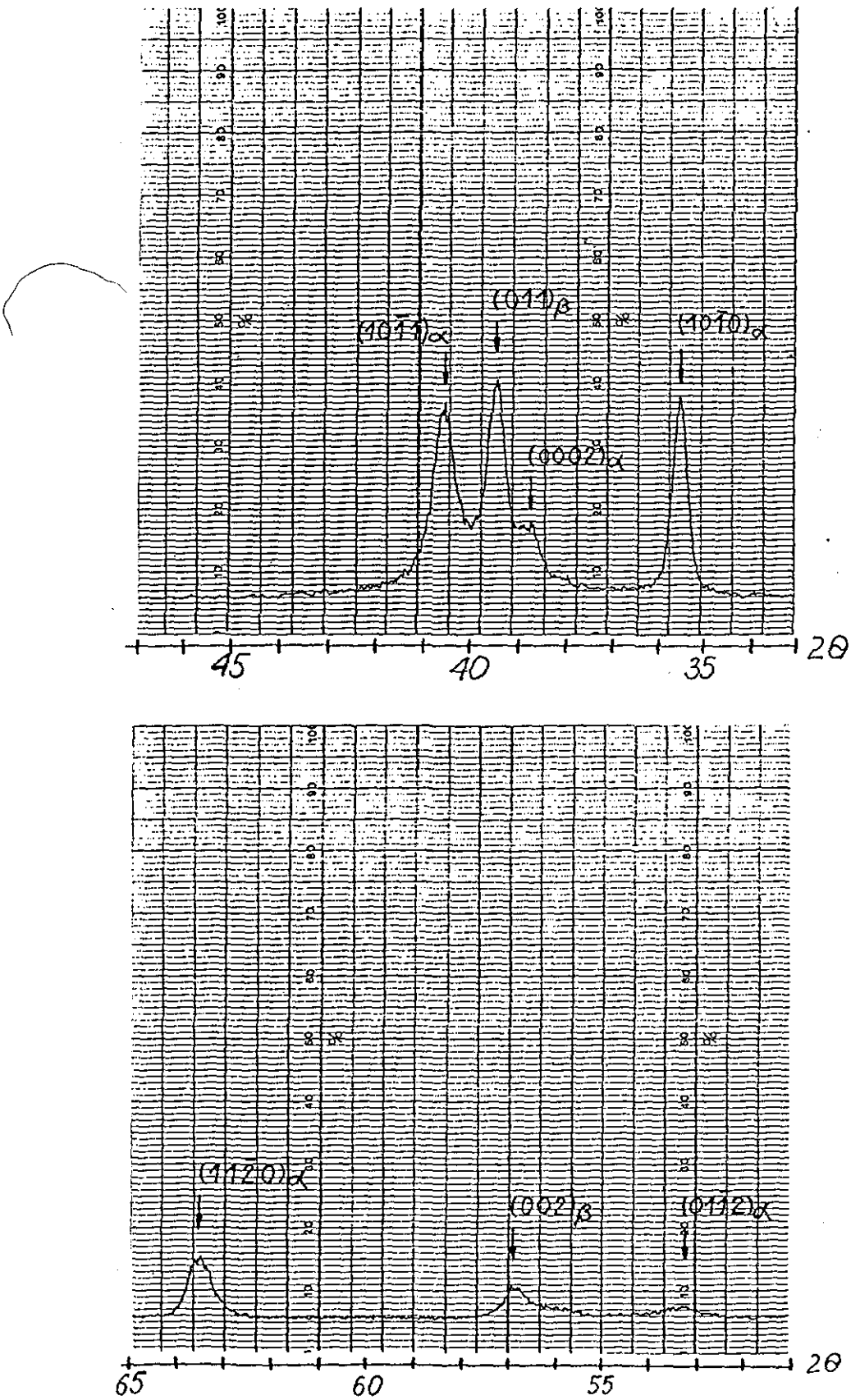

Figure 114. X-ray spectrum of the quenched material.

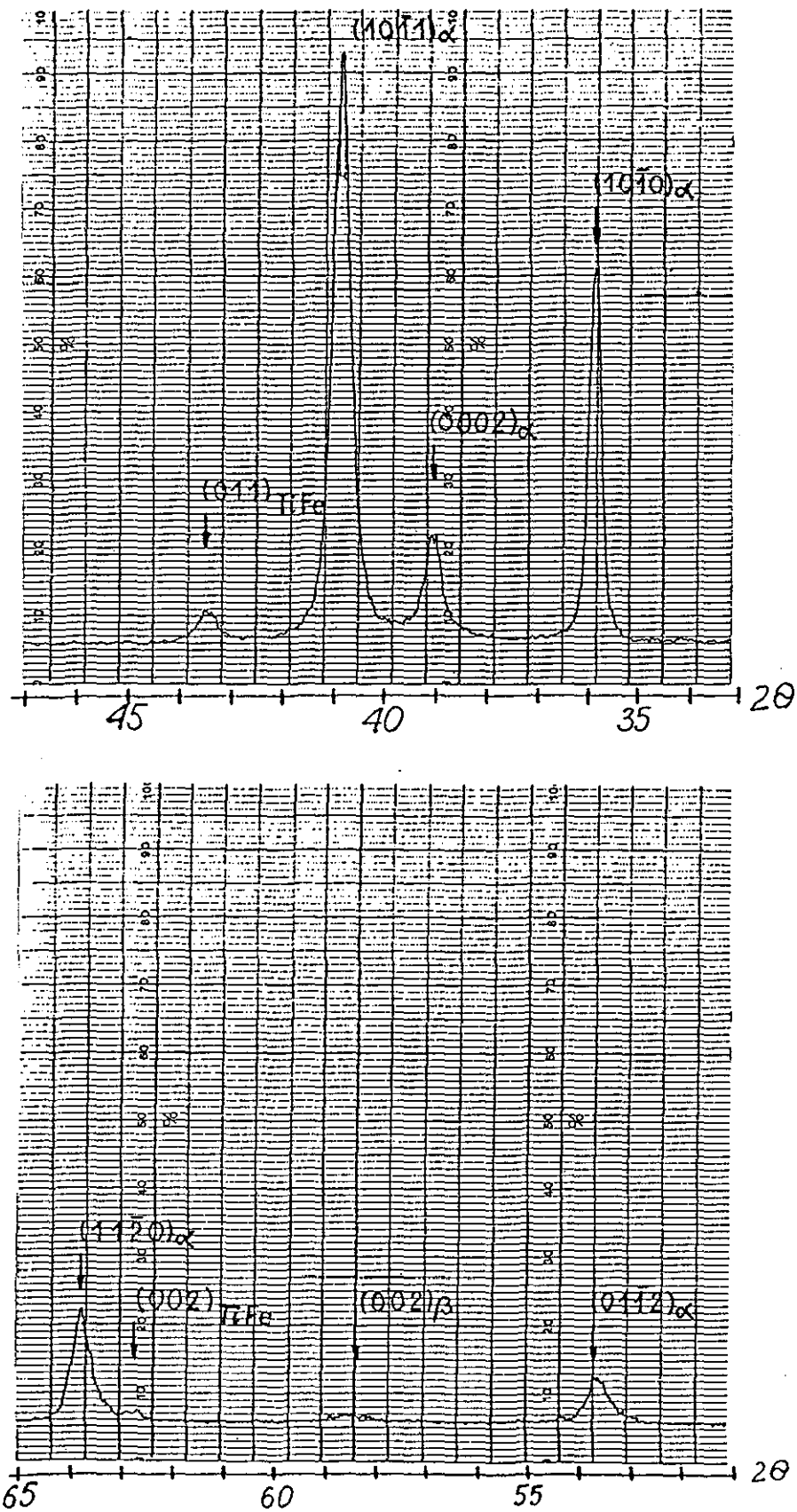

Figure 115. X-ray spectrum of the heat-treated material.

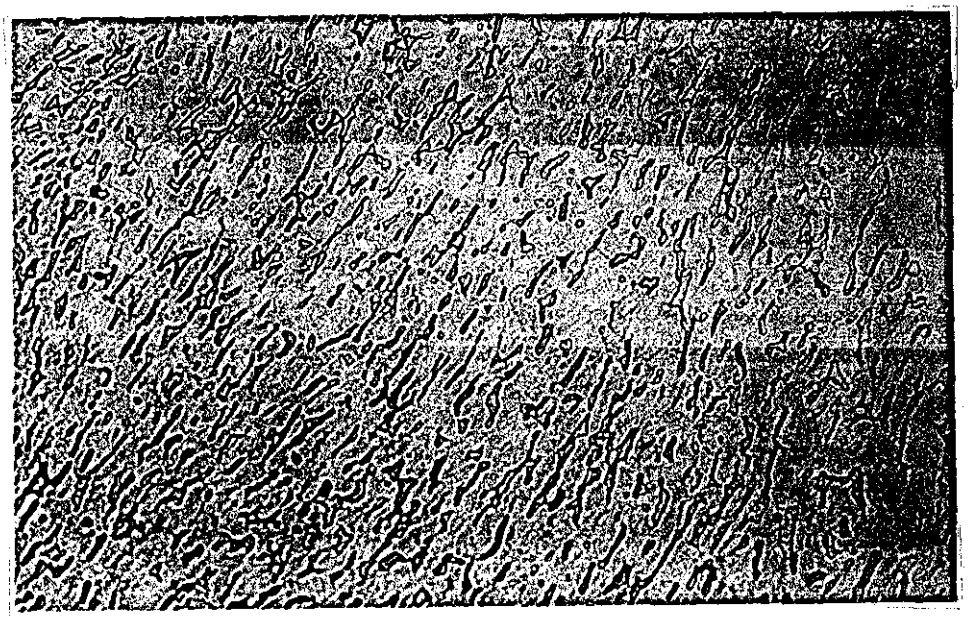

Figure 116. Microstructure of the as-delivered material as seen in optical microscope (X1000).

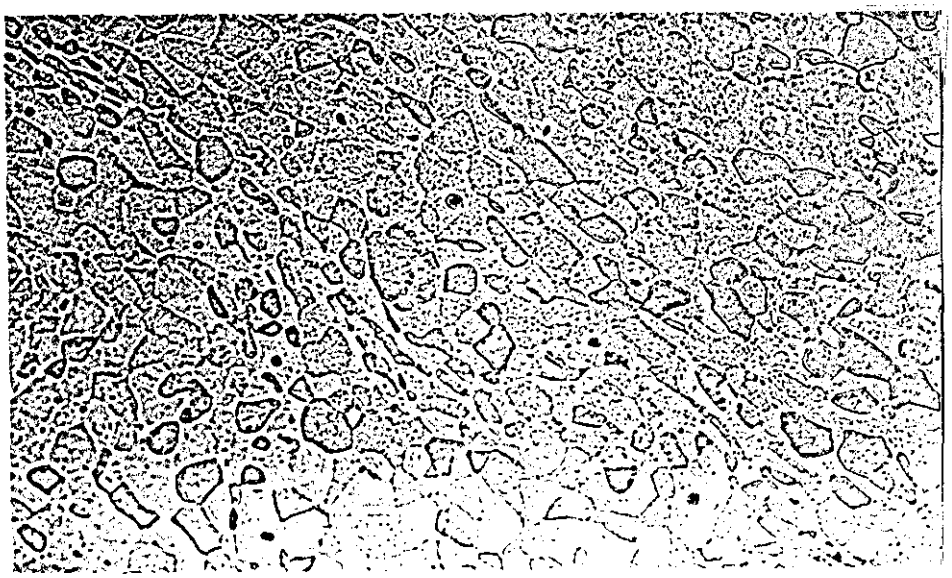

Figure 117. Microstructure of the quenched material as seen in optical microscope (X1000).

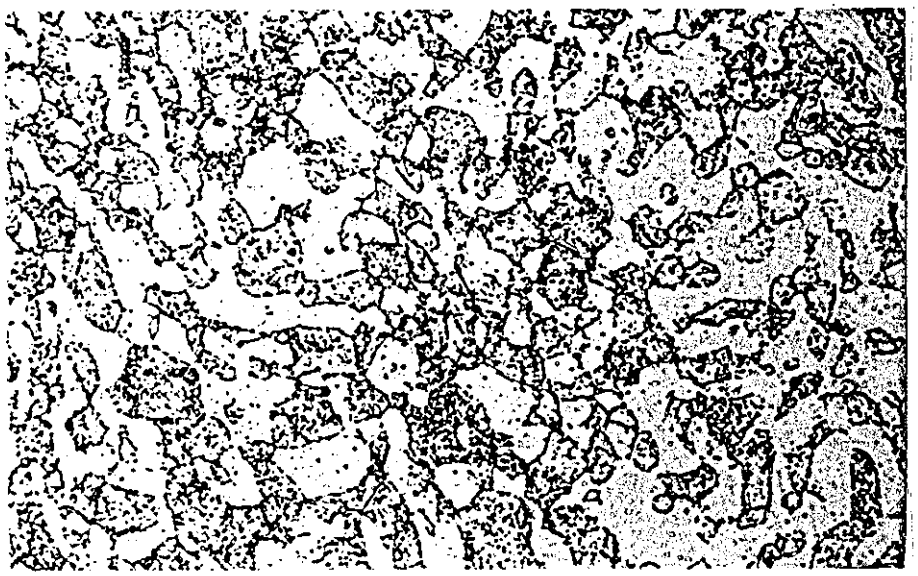

Figure 118. Microstructure of the heat-treated material as seen in optical microscope (X1000).

Figure 119. TEM micrograph of the microstructure in the as-delivered material (X10,000).

(a) Region near a grain boundary between beta (left) and alpha (right) phases (X132,000).

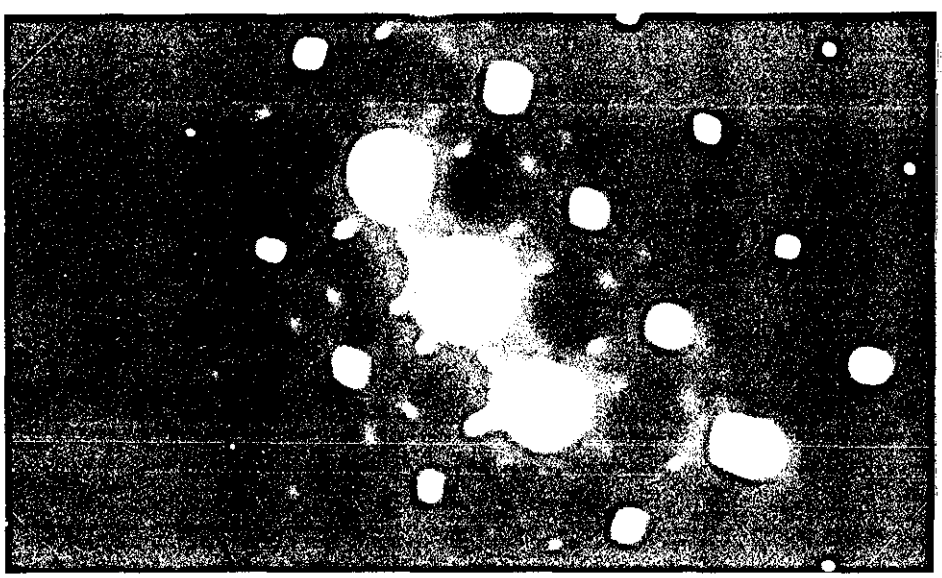

(b) Diffraction pattern of the beta phase. Beam direction B=[100].

Figure 120. TEM micrograph of the as-delivered material.

Figure 121. TEM micrograph of the microstructure in the quenched material (X6600).

(a) Morphology of beta phase (X66,000).

Figure 122. TEM micrographs of beta phase in the quenched material.

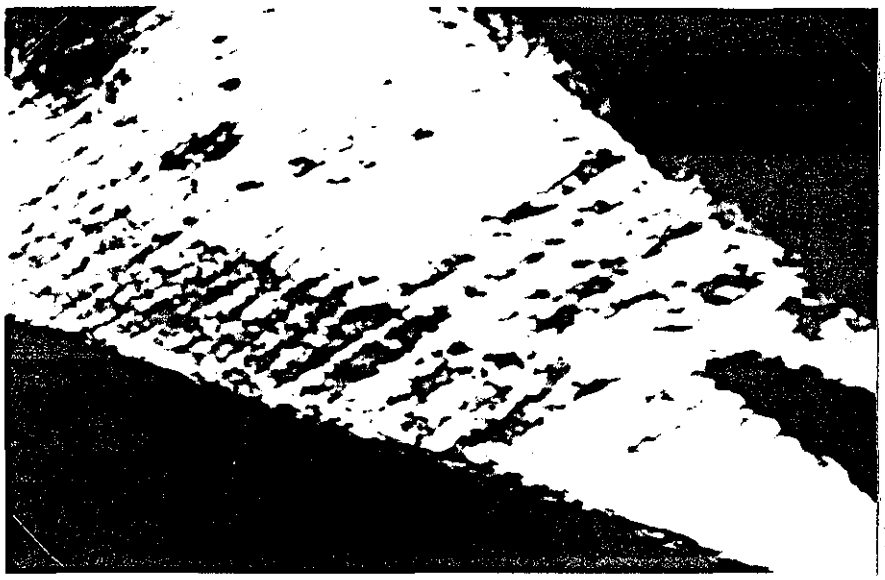

(b) Morphology of beta phase (X132,000).

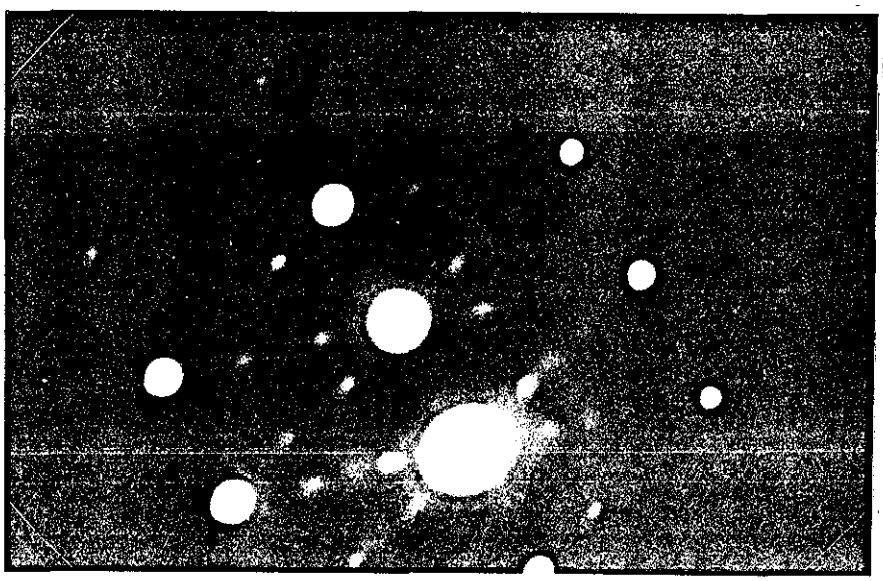

(c) Diffraction pattern (B=[023]).

Figure 122. TEM micrographs of beta phase in the quenched material.

Figure 123. TEM micrograph of the microstructure in the heat-treated material (X10,000).

(a) Bright-field (X66,000).

Figure 124. TEM micrpgraphs of the microstructure in the heat-treated material.

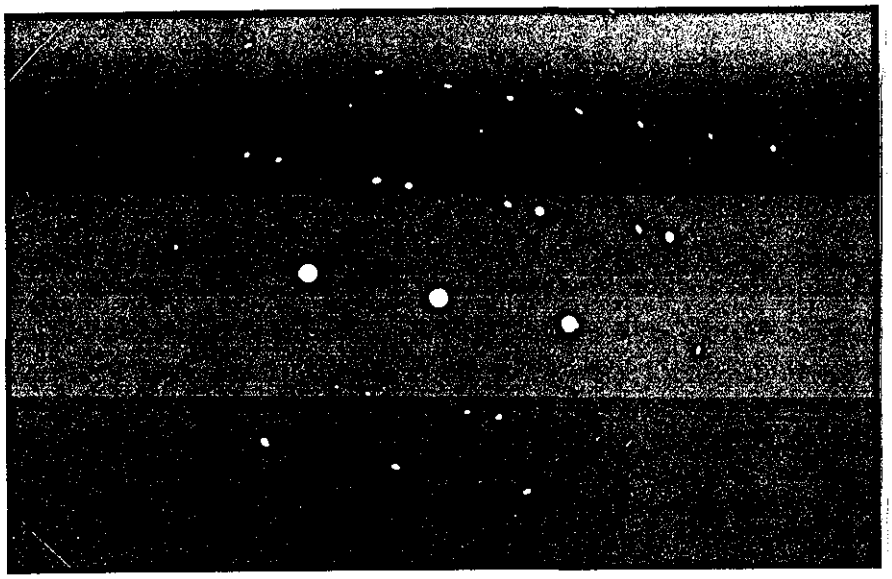

(b) Diffraction pattern.

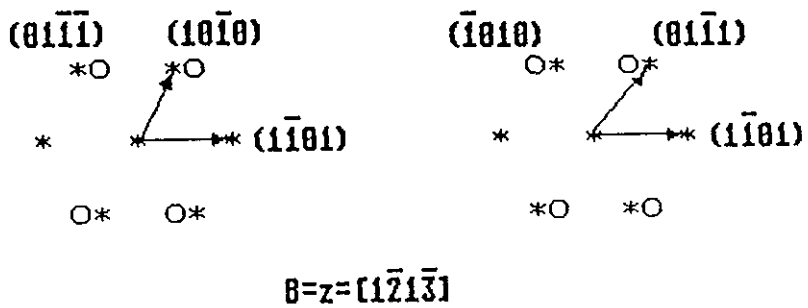

(c) Indexed, theoretical diffraction pattern.

Figure 124. TEM micrpgraphs of the microstructure in the heat-treated material.

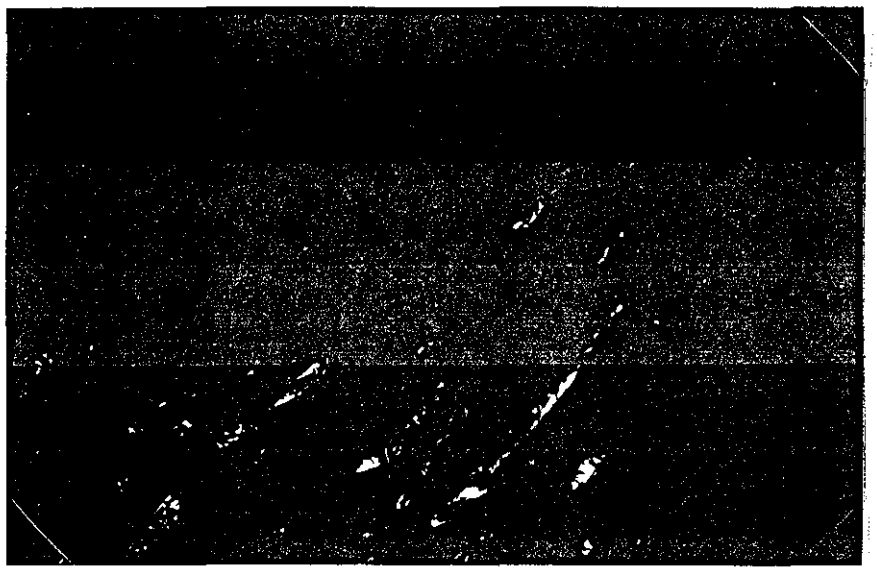

(d) Dark-field with one of the reflections (X66,000).

(e) Dark-field with different operating reflection (X66,000).

Figure 124. TEM micrographs of the microstructure in the heat-treated material.

(a) Bright-field (X66,000).

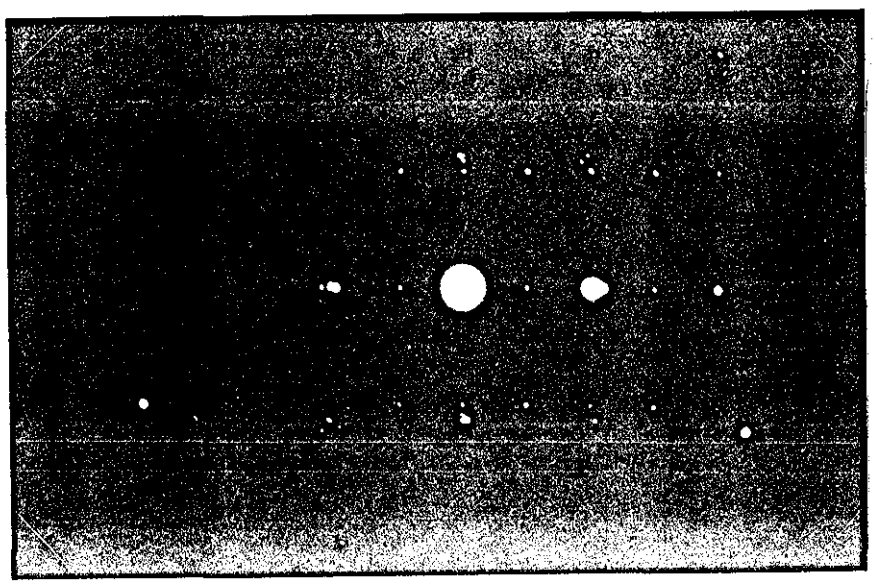

(b) Diffraction pattern.

Figure 125. TEM micrographs of the lamellar structure in the heat-treated material.

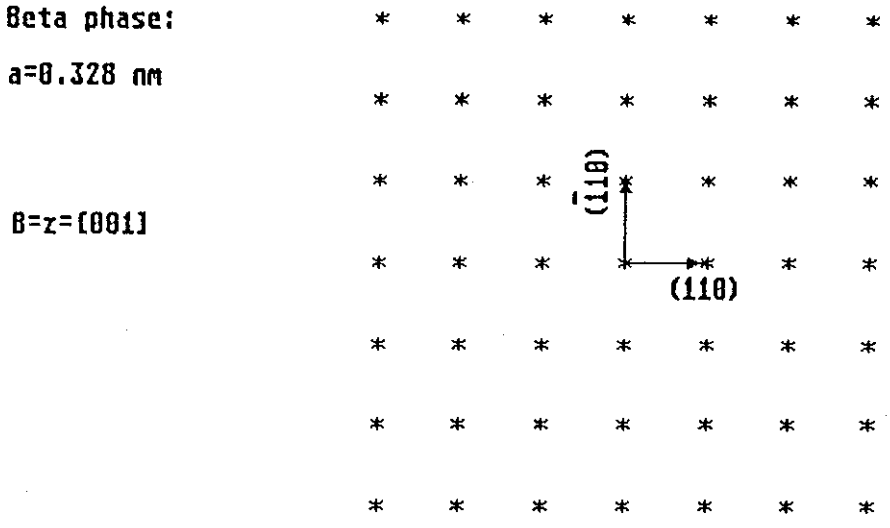

(c) Theoretical diffraction pattern of the beta phase.

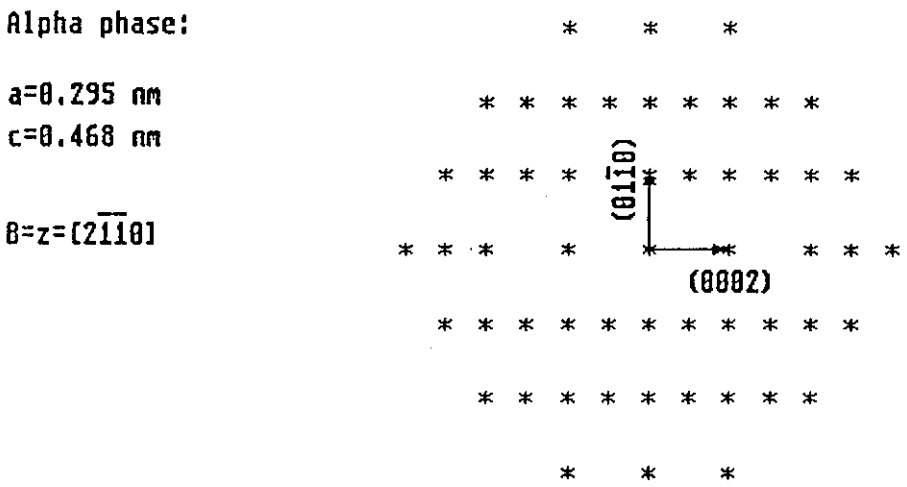

(d) Theoretical diffraction pattern of the alpha phase.

Figure 125. TEM micrographs of the lamellar structure in the heat-treated material.

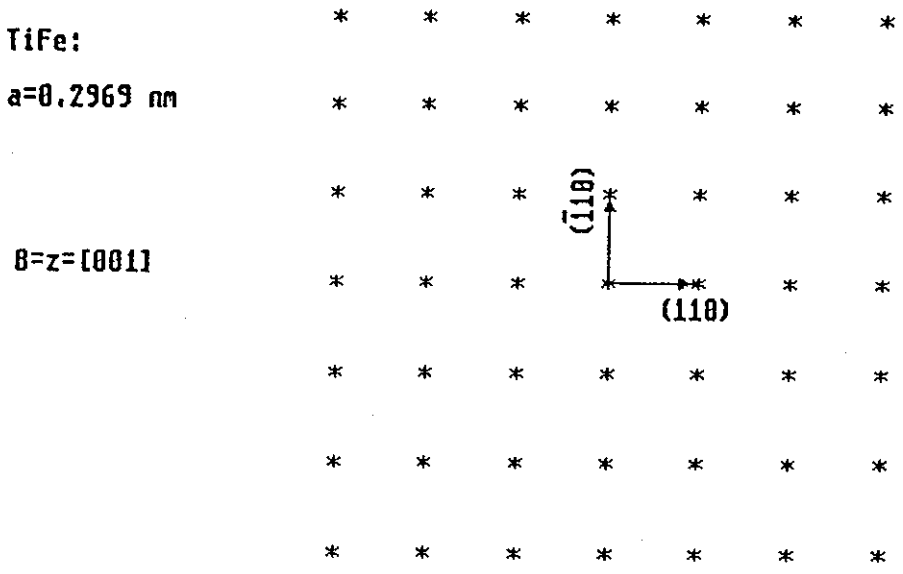

(e) Theoretical diffraction pattern of TiFe.

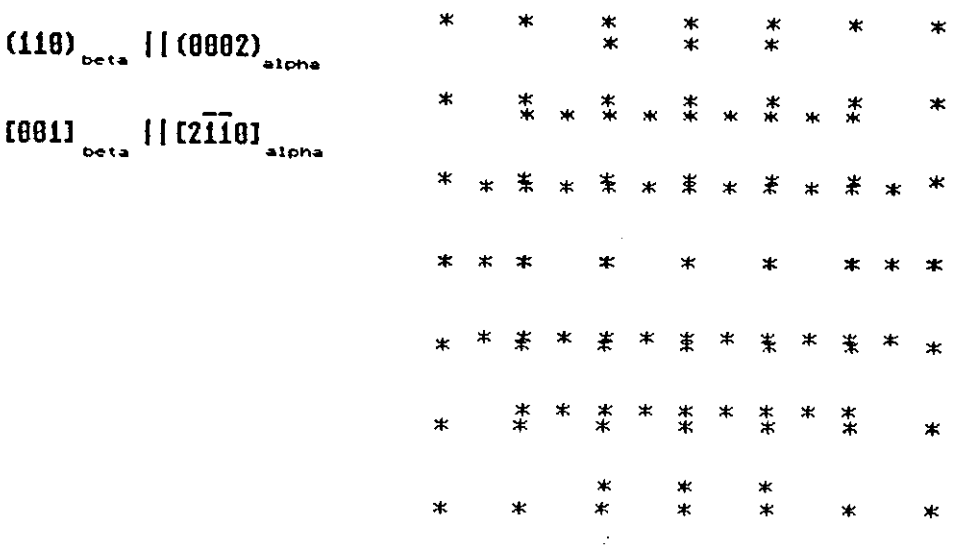

(f) Superimposed diffraction patterns of the beta and alpha phases.

Figure 125. TEM micrographs of the lamellar structure in the heat-treated material.

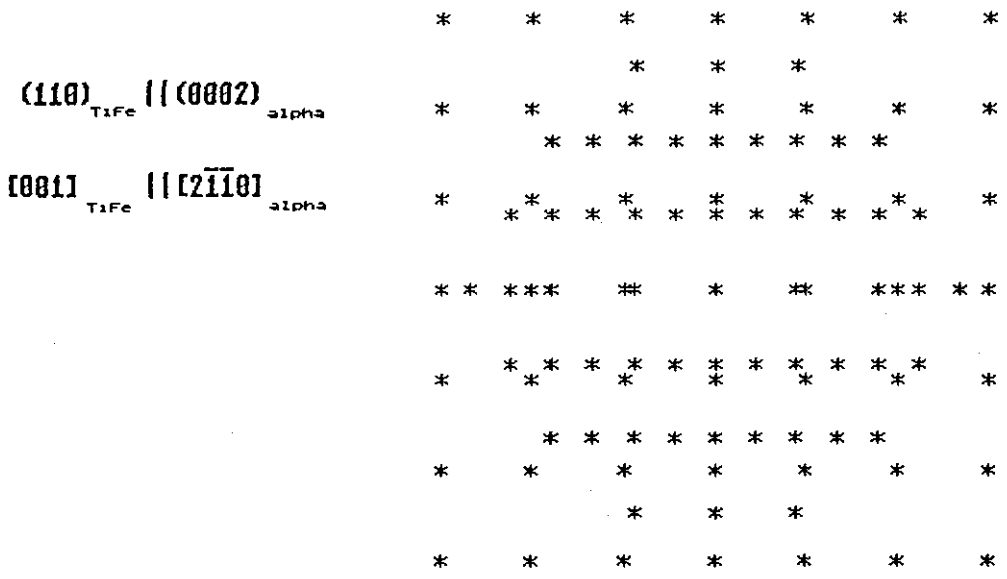

(g) Superimposed diffraction patterns of the alpha and TiFe phases.

Figure 125. TEM micrographs of the lamellar structure in the heat-treated material.

(a) Bright-field (X100,000).

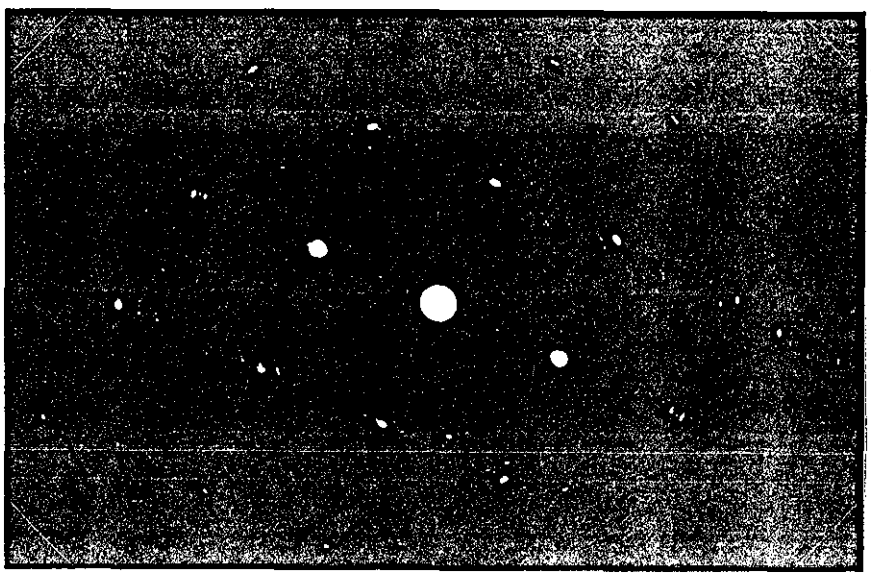

(b) Diffraction pattern.

Figure 126. TEM micrographs of the lamellar structure in the heat-treated material.

(c) Dark-field with operating reflection belonging to the beta phase.

(d) Dark-field with operating reflection belonging to the alpha phase.

Figure 126. TEM micrographs of the lamellar structure in the heat-treated material.

Figure 127. Dislocations in fatigued, as-delivered material. Alpha phase (X150,000).

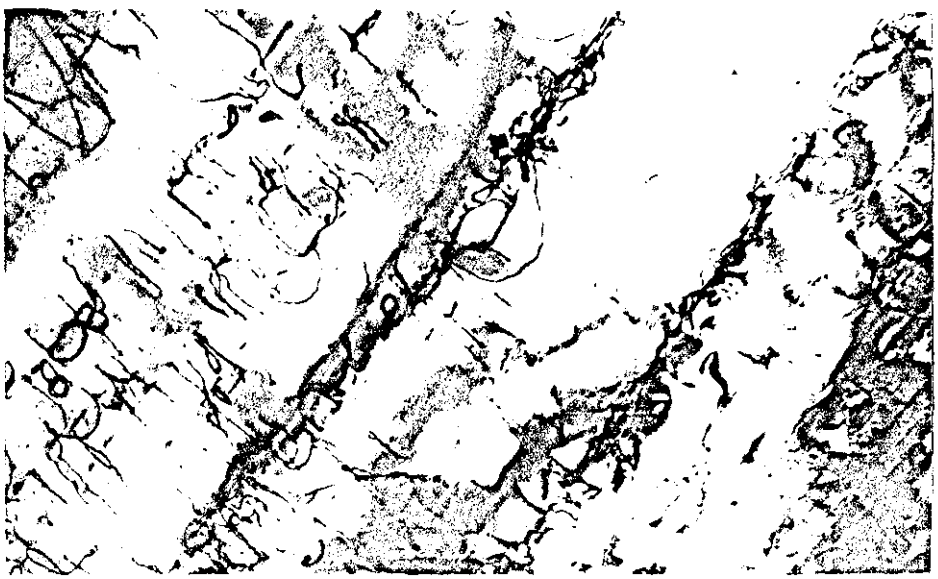

Figure 128. Dislocations in fatigued, heat-treated material. Alpha phase (X26,000).

(a) $\vec{B}=[1\bar{2}10]$; operating reflection $g=(10\bar{1}0)$. X100,000.

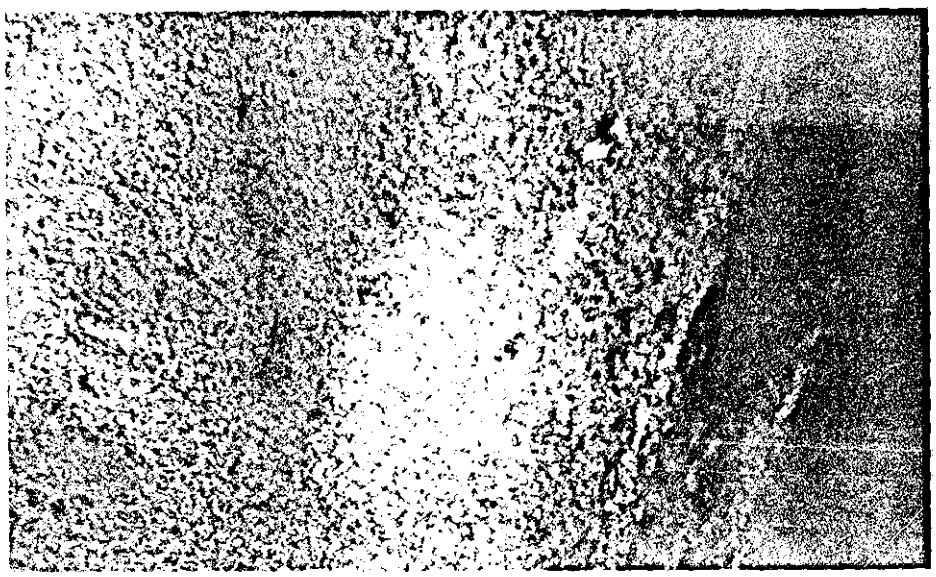

(b) $\vec{B}=[1\bar{2}10]$; operating reflection $g=(0001)$. X100,000.

Figure 129. Dislocation loop seen with different operating reflections under two beam conditions.

(c) $\mathbf{B}=[0\bar{1}11]$; operating reflection $g=(01\bar{1}2)$. X100,000.

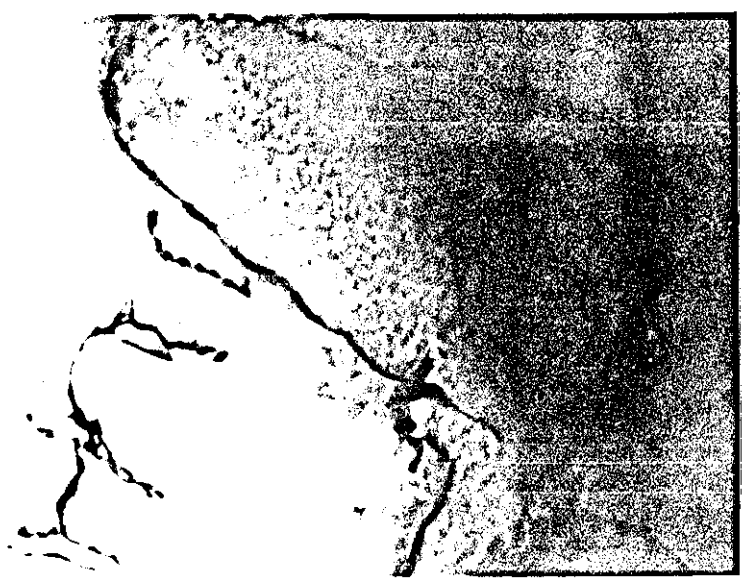

(d) $\mathbf{B}=[\bar{1}\bar{1}20]$; operating reflection $g=(\bar{1}10\bar{1})$. X100,000.

Figure 129. Dislocation loop seen with different operating reflections under two beam conditions.

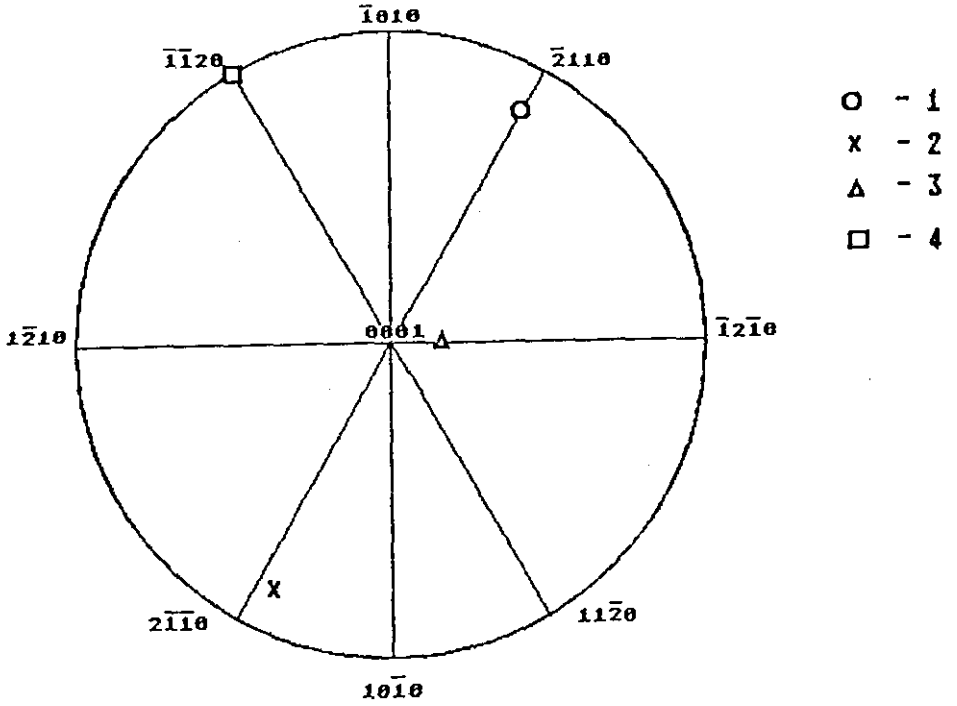

(a) Stereographic projection.

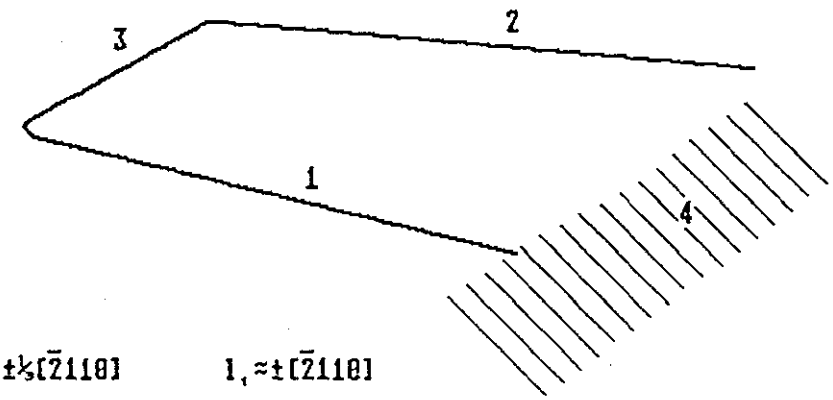

$\mathbf{b}_1 = \pm\frac{1}{3}[\bar{2}110]$ $\quad l_1 \approx \pm[\bar{2}110]$

$\mathbf{b}_2 = \pm\frac{1}{3}[\bar{2}110]$ $\quad l_2 \approx \pm[\bar{2}110]$

$\mathbf{b}_3 = \pm\frac{1}{3}[\bar{2}110]$ $\quad l_3 \approx \pm[0001]$

$\mathbf{b}_4 = \pm\frac{1}{3}[11\bar{2}0]$ $\quad l_4 \approx \pm[11\bar{2}0]$

(b) Schematic drawing of the dislocation loop from Figure 129.

Figure 130. Line directions of the dislocations from Figure 129.

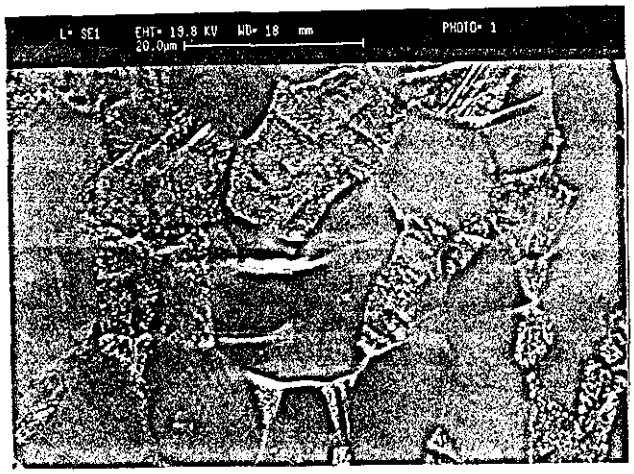

Figure 131. Crack initiation at the surface of the heat-treated material.

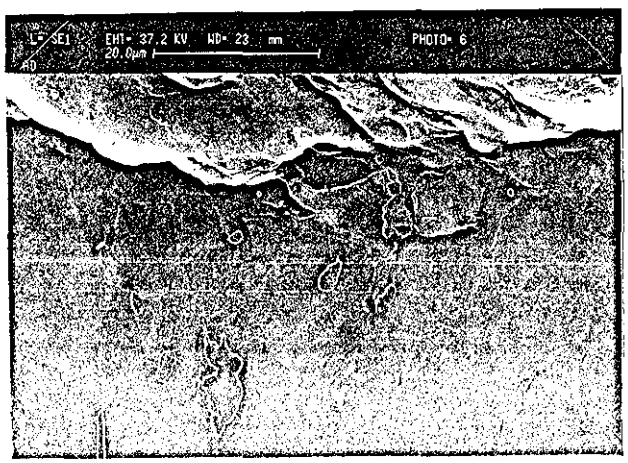

Figure 132. Crack initiation at the surface of the as-delivered material.

Figure 133. Optical micrograph of machined surface (X20).

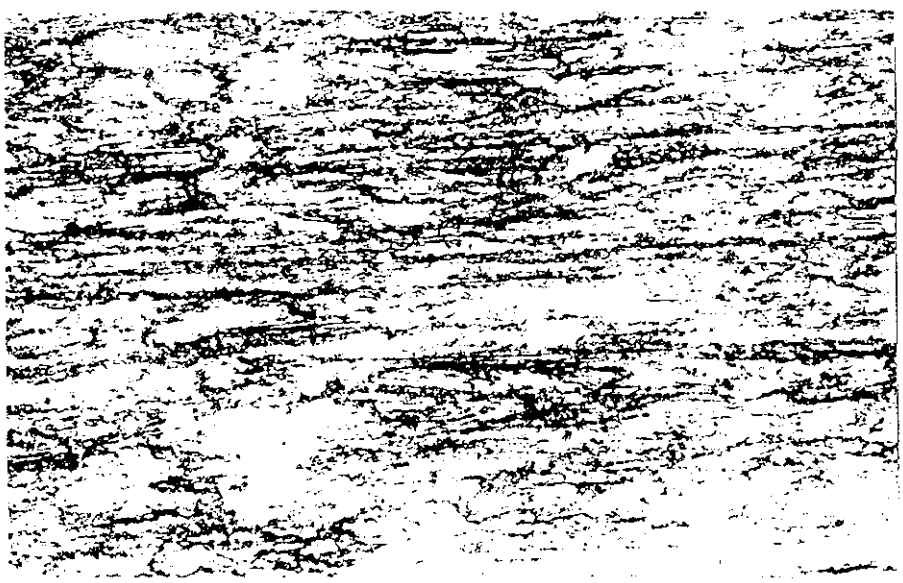

Figure 134. Optical micrograph of brushed surface (X20).

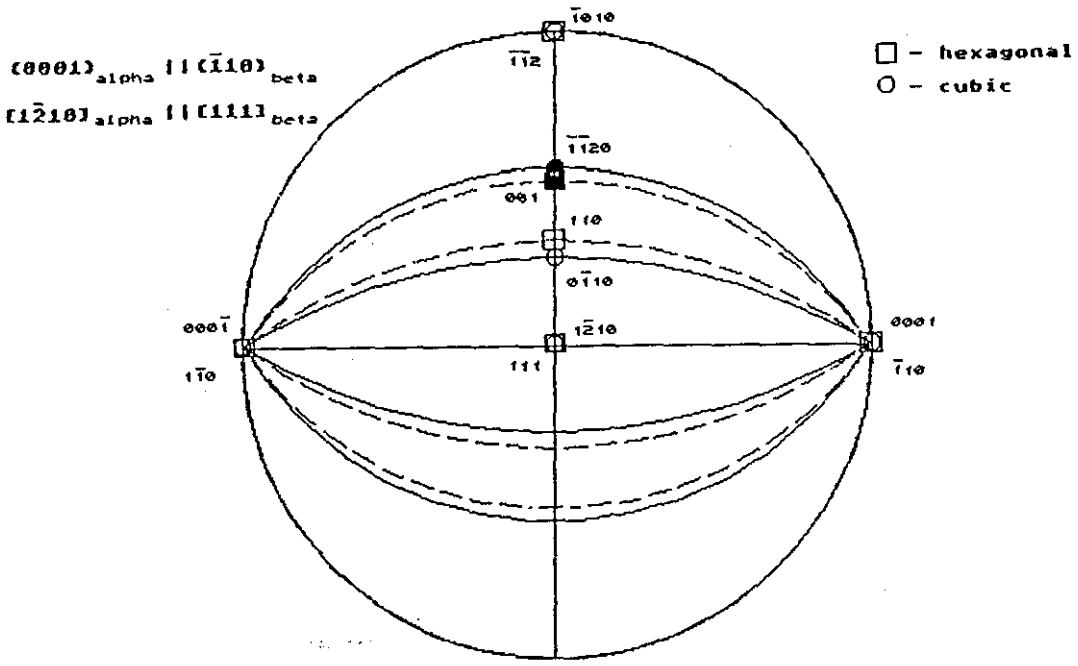

Figure 135. Schematic stereographic projection showing that in the Burgers relation, the [001] direction of the beta phase is close to the [1120] direction of the alpha phase.

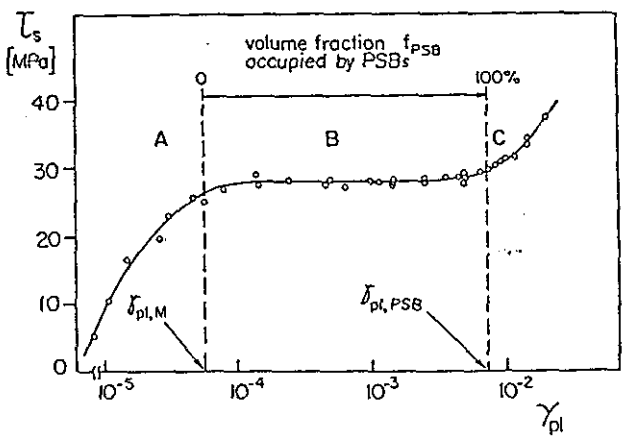

Figure 136. Schematic css-curve for copper single crystals [95].

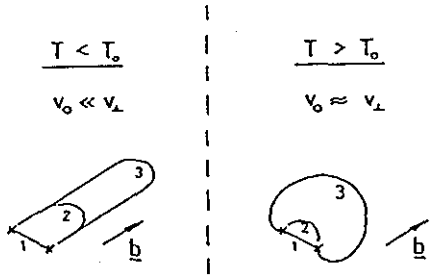

Figure 137. Schematic picture of a dislocation loop in bcc metals in different temperature ranges.

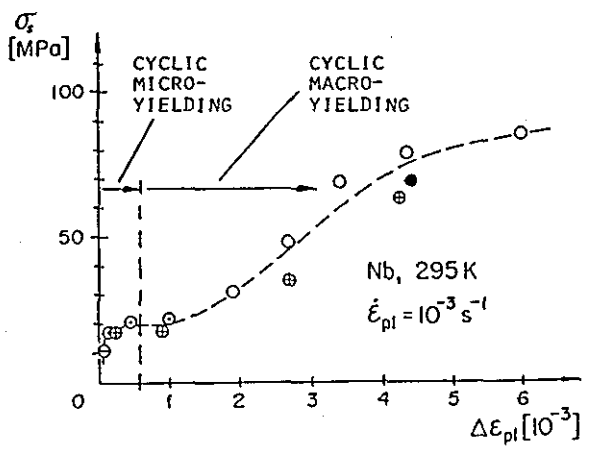

Figure 138. Schematic css-curve for niobium single crystals [99].

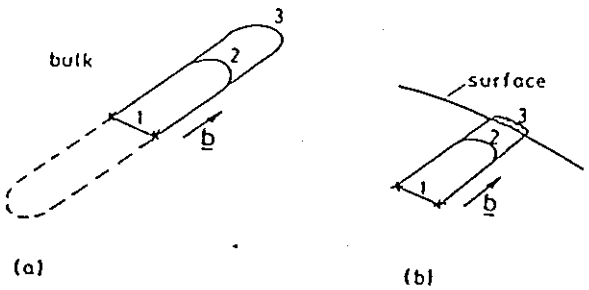

Figure 139. Low amplitude dislocation mechanisms in fatigued bcc metals [95]. (a) Interior. (b) Near surface.

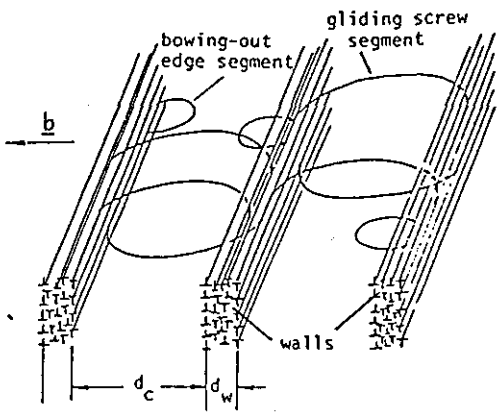

Figure 140. Schematic picture of the arrangement of dislocations in persistent slip bands.